ISSN : 2349-6495(P) | 2456-1908 (O)

International Journal of Advanced Engineering Research and Science

(IJAERS)

An Open Access Peer-Reviewed International Journal

Journal DOI: 10.22161/ijaers

Issue DOI: 10.22161/ijaers.134

AI PUBLICATIONS

Vol.- 13 | Issue - 4 | Apr 2026

editor.ijaers@gmail.com | editor@ijaers.com | https://www.ijaers.com/

International Journal of Advanced Engineering Research and Science (IJAERS)

(ISSN: 2349-6495(P)| 2456-1908(O))

DOI: 10.22161/ijaers

Vol-13, Issue-4

April, 2026

Publisher

AI Publication

Email: editor.ijaers@gmail.com; editor@ijaers.com

Web: www.ijaers.com

International Editorial/ Reviewer Board

Editor in Chief

- **Dr. Swapnesh Taterh (Chief-Editor),** Amity University, Jaipur, India

Cheif Executive Editor

- **S. Suman Rajest,** Vels Institute of Science, Technology & Advanced Studies, India
  chief-executive-editor@ijaers.com

Associate Editors

- **Dr. Ram Karan Singh,** King Khalid University, Guraiger, Abha 62529, Saudi Arabia
- **Dr. Shuai Li,** University of Cambridge, England, Great Britain

Editorial Member

- **Behrouz Takabi,** PhD, Texas A&M University, Texas, USA
- **Dr. Gamal Abd El-Nasser Ahmed Mohamed Said,** Port Training Institute (PTI), Arab Academy For Science, Technology and Maritime Transport, Egypt
- **Dr. Hou, Cheng-I ,** Chung Hua University, Hsinchu Taiwan
- **Dr. Ebrahim Nohani,** Islamic Azad University, Dezful, IRAN.
- **Dr. Ahmadad Nabih Zaki Rashed,** Menoufia University, EGYPT
- **Dr. Rabindra Kayastha ,** Kathmandu University, Nepal
- **Dr. Dinh Tran Ngoc Huy,** Banking and Finance, HCM, Viet Nam
- **Dr. Engin NAS,** Duzce University, Turkey
- **Dr. A. Heidari,** California South University (CSU), Irvine, California, USA
- **Dr. Uma Choudhary,** Mody University, Lakshmangarh, India
- **Dr. Varun Gupta,** National Informatic Center, Delhi, India
- **Dr. Ahmed Kadhim Hussein,** University of Babylon, Republic of Iraq
- **Dr. Vibhash Yadav,** Rajkiya Engineering College, Banda. UP, India
- **Dr. M. Kannan,** SCSVMV University, Kanchipuram, Tamil Nadu, India
- **José G. Vargas-Hernández,** University of Guadalajara Periférico Norte 799 Edif. G201-7, Núcleo Universitario Los Belenes, Zapopan, Jalisco, 45100, México
- **Dr. Sambit Kumar Mishra,** Gandhi Institute for Education and Technology, Baniatangi, Bhubaneswar, India
- **DR. C. M. Velu,** Datta Kala Group of Institutions, Pune, India
- **Dr. Deependra Pandey,** Amity University, Uttar Pradesh, India
- **Dr. K Ashok Reddy,** MLR Institute of Technology, Dundigal, Hyderabad, India
- **Dr. S.R.Boselin Prabhu,** SVS College of Engineering, Coimbatore, India
- **N. Balakumar,** Tamilnadu College of Engineering, Karumathampatti, Coimbatore, India
- **R. Poorvadevi,** SCSVMV University, Enathur, Kanchipuram, Tamil Nadu, India
- **Dr. Subha Ganguly,** Arawali Veterinary College, Sikar, India
- **Dr. P. Murali Krishna Prasad,** GVP College of Engineering for Women, Visakhapatnam, Andhra Pradesh, India
- **Anshul Singhal,** Bio Instrumentation Lab, MIT, USA
- **Mr. Lusekelo Kibona,** Ruaha Catholic University, Iringa, Tanzania
- **Sina Mahdavi,** Urmia Graduate Institute, Urmia, Iran
- **Dr. N. S. Mohan,** Manipal Institute of Technology, Manipal, India
- **Dr. Zafer Omer Ozdemir,** University of Health Sciences,Haydarpasa, Uskudar, Istanbul, TURKIYE
- **Bingxu Wang,** 2721 Patrick Henry St Apt 510, Auburn Hills, Michigan, United States

- **Dr. Jayashree Patil-Dake,** KPB Hinduja College of Commerce, Mumbai, India
- **Dr. Neel Kamal Purohit,** S.S. Jain Subodh P.G. College, Rambagh, Jaipur, India
- **Mohd Muntjir,** Taif University, Kingdom of Saudi Arabia
- **Xian Ming Meng,** China Automotive Technology & Research Center No.68, East Xianfeng Road, Dongli District, Tianjin, China
- **Herlandi de Souza Andrade,** FATEC Guaratingueta, State Center for Technological Education Paula Souza - CEETEPS
- **Dr. Payal Chadha,** University of Maryland University College Europe, Kuwait
- **Ahmed Moustafa Abd El-hamid Elmahalawy,** Menoufia University, Al Minufya, Egypt
- **Prof. Mark H. Rummeli,** University & Head of the characterisation center, Soochow Institute for Energy Materials Innovasions (SIEMES), Suzhou, Jiangsu Province, China
- **Dr. Eman Yaser Daraghmi,** Ptuk, Tulkarm, Palestine
- **Holmes Rajagukguk,** State University of Medan, Lecturer in Sisingamangaraja University North Tapanuli, Indonesia
- **Dr. Menderes KAM,** Dr. Engin PAK Cumayeri Vocational School, DÜZCE UNIVERSITY (University in Turkey), Turkey
- **Dr. Jatin Goyal,** Punjabi University, Patiala, Punjab, India | International Collaborator of GEITEC / UNIR / CNPq, Brazil
- **Ahmet İPEKÇİ,** Dr. Engin PAK Cumayeri Vocational School, DÜZCE UNIVERSITY, Turkey
- **Baarimah Abdullah Omar,** Universiti Malaysia Pahang (UMP), Gambang, 26300, Malaysia
- **Sabri UZUNER,** Dr. Engin PAK Cumayeri Vocational School Cumayeri/Duzce/Turkey
- **Ümit AĞBULUT,** Düzce University, Turkey
- **Dr. Mustafa ÖZKAN,** Trakya University, Edirne/ TURKEY
- **Dr. Indrani Bhattacharyya,** Dr. B.C. Roy College of Pharmacy and Allied Health Sciences, Durgapur, West Bengal, India
- **Egnon Kouakouc,** Nutrition/Health at University Felix Houphouet Boigny Abidjan, Ivory Coast
- **Dr. Suat SARIDEMİR,** Düzce University, Faculty of Technology, Turkey
- **Dr. Manvinder Singh Pahwa,** Director, Alumni Relations at Manipal University Jaipur, India
- **Omid Habibzadeh Bigdarvish,** University of Texas at Arlington, Texas, USA
- **Professor Dr. Ho Soon Min,** INTI International University, Jln BBN 12/1, Bandar, Baru Nilai, 71800 Negeri Sembilan, Malaysia
- **Ahmed Mohammed Morsy Hassan,** South Egypt Cancer Institute, Assiut University, Assiut, Egypt
- **Xian Ming Meng (Ph.D),** China Automotive Technology & Research Center, No.68, East Xianfeng Road, Tianjin, China
- **Ömer Erkan,** Konuralp Campus, Düzce-Turkey
- **Dr. Yousef Daradkeh,** Prince Sattam bin Abdulaziz University) PSAU), KSA
- **Peter JO,** IPB University, Indonesia
- **Nazmi Liana Binti Azmi,** Raja Perempuan Zainab II Hospital, 15586 Kota Bharu, Kelantan, Malaysia
- **Mr. Sagar Jamle,** Oriental University, Indore, India
- **Professor Grazione de Souza,** Applied Mathematics, Rio de Janeiro State University, Brazil
- **Kim Edward S. Santos,** Nueva Ecija University of Science and Technology, Philippines.
- **Dr. Jhonas Geraldo Peixoto Flauzino,** Department of Neurosciences, Pontifical Catholic University of Rio Grande do Sul, Brazil.
- **Narender Chinthamu,** Massachusetts Institute of Technology, 7 Massachusetts Ave, Cambridge, MA 02139
- **Dr. Geeta S Nadella,** CSP-SM | Quality Assurance Specialist IEEE ENCS CS Chair
- **Dr. Karthik Meduri,** University of the Cumberlands, Kentucky, USA

Vol-13, Issue-4, April 2026

(10.22161/ijaers.134)

Detail with DOI (CrossRef)

International Journal of Advanced Engineering Research and Science (IJAERS)
Peer-Reviewed Journal
ISSN: 2349-6495(P) | 2456-1908(O)
Vol-13, Issue-4; Apr, 2026
Journal Home Page Available: https://ijaers.com/
Article DOI: https://dx.doi.org/10.22161/ijaers.134.1

Comparative Analysis of Upper Body Shape for Chinese and Bangladeshi Women Based on 3D and 2D Measurements

Israt Jahan[1], Bingfei Gu[2], Nur E Nasiba[3], Shaik Faizur Rahman[4]

[1]Master's Degree student, School of Fashion Design and Engineering, Zhejiang Sci-Tech University, Hangzhou, China
Email: jahanisrat2751@gmail.com
[2]Professor School of Fashion Design and Engineering, Zhejiang Sci-Tech University, Hangzhou, China.
Fashion Institute, Zhejiang Sci-Tech University, Hangzhou, China
Email: gubf@zstu.edu.cn
[3]Master's Degree student, School of Fashion Design and Engineering, Zhejiang Sci-Tech University, Hangzhou, China
Email: nur.dola@gmail.com
[4]Lecturer of Shanto-Mariam University of Creative Technology, Dhaka, Bangladesh.
Email: faizurboomsky@gmail.com

Received: 22 Feb 2026,

Received in revised form: 24 Mar 2026,

Accepted: 28 Mar 2026,

Available online: 03 Apr 2026

***Keywords*— Anthropometry, Body shape classification, Garment sizing, Upper body Morphology.**

***Abstract*—** *This study aims to compare the upper body morphology of young Chinese and Bangladeshi women and to evaluate whether existing garment sizing methods adequately accommodate population specific upper body shape characteristics. An integrated anthropometric approach combining three dimensional (3D) body scanning, two dimensional (2D) image based measurement, and manual anthropometry was used to obtain 16 upper body descriptors (dimensional, circumferential, thickness, and angular) from women aged 18–30 years in China (n = 189) and Bangladesh (n = 20). Descriptive statistics, principal component analysis (PCA), factor analysis, and K means clustering were applied to extract dominant morphological factors and classify upper body shape types, which were then interpreted with reference to national and international sizing criteria. In this sample of young women, Chinese participants generally exhibited broader shoulders, greater chest convexity, wider thoracic dimensions, and comparatively flatter waist–hip profiles, whereas Bangladeshi participants tended to show more sloping shoulders, thicker neck regions, reduced anterior chest projection, deeper waists, and more prominent hips. Three principal components and three upper body shape categories were identified in each population, but the key contributing variables and the distribution of individuals across clusters differed between countries. Current sizing systems cover most Chinese body types in the sample, though they do not fully address extreme proportions, while in Bangladesh, the lack of a unified national sizing standard appears to be associated with greater size–shape mismatches. This research provides a cross national, data driven comparison of female upper body morphology using combined 3D and 2D measurement techniques and a shared set of upper body descriptors. The results support the development of population adapted sizing systems and body*

shape oriented garment design strategies aimed at improving apparel fit, wearer comfort, and production efficiency.

I. INTRODUCTION

Understanding human morphology is essential in a number of fields, such as fashion design, ergonomics, and healthcare. Population disparities in body measures are influenced by a variety of factors, including genetics, environment, lifestyle, and cultural norms. Comfortable, well-fitting clothing is becoming more and more popular as the global economy expands and material living standards rise. However, human comfort is influenced by clothing and the environment in a complex and subjective way (G. Song, 2011). The relationship between a garment's size and shape and the human body is known as apparel fit (Chen, 2007). In the apparel industry, clothing fit is regarded as the most important component in assessing clothing quality and consumer happiness (Xu et al., 2023). Clothing fit is influenced by the wearer's body form and dimensions. Shape analysis is connected to style design, pattern creation, production, and virtual fitting.

It is also important for creating personalized apparel. For standardizing the size (*ISO-TR-10652-1991*, n.d.), which is followed internationally. Physical measurements are the most often used technique for obtaining body measurements (Han & Nam, 2011). There are several methods for body measurements. While current methods use 3D scanners to automatically extract exact measurements from digital data, traditional equipment like calipers and tape measures allow for manual measuring (Bartol et al., 2021). The conventional apparel sector has been replaced by automation and digitalization due to the quick development of computer information technology, which propels the expansion of online retailing and electronic commerce (Gu et al., 2020). The women's clothing industry has long struggled with fit issues (Chen, 2007). The fashion business uses 3D human body scan data for virtual fitting, tailoring, mannequin construction, and sizing surveys (Kim & Kim, 2018). Researchers have classified female body types using different techniques in recent years, for example, principal component analysis, body surface angle classification, feature index classification, side profile classification, etc. Size surveys, size group formulation, and body shape classifications are the outcomes of attempts to create sizing standards. Body shape studies are conducted in tandem with sizing difficulties (Vuruskan & Bulgun, 2011). Age is one of the most crucial variables among the many factors generating shape and postural differences that affect clothing fit. One's body shape can be influenced by the amount of activity and work choices (Bolaji et al., 2025). People's discontent with how their clothes fit tends to grow as they become older (H. K. Song et al., 2022). The female upper body has a particularly complex shape due to its many elements, including neck anteversion, shoulder slope, and the convexity of the back, bust, and hip.

Female upper-body measurements have been the subject of several studies, but the majority have been limited to single-population analyses, age ranges, or anthropometric factors. Although there are limited cross-cultural studies that employ integrated 2D and 3D measurement frameworks to systematically compare female upper-body morphology, there is significant potential for research in this area. Notably, China and Bangladesh, two of the world's leading apparel manufacturers, are at the forefront. China is a global leader in apparel technology and body measurement research, while Bangladesh is one of the largest garment manufacturing countries in the world. Despite their prominent roles in the global apparel industry, comparative anthropometric studies between these two populations are scarce. Furthermore, Chinese and Bangladeshi women belong to distinct regional and ethnic groups East Asian and South Asian—resulting in significant differences in body proportions and upper-body morphology. By comparing these two populations, researchers can gain valuable insights for developing population-specific sizing systems and improving garment fit in international apparel markets. The selection of women from China and Bangladesh as experimental subjects is supported by both industrial and anthropometric considerations. To address this critical research gap, the present study provides a comprehensive cross-national comparison of upper-body shape characteristics between young adult women from China and Bangladesh. This study provides a more comprehensive description of upper-body morphology by using a single set of sixteen upper-body descriptors that include dimensions, circumferential, thickness, and angular factors. Advanced multivariate statistical techniques, including descriptive analysis, principal component analysis (PCA), factor analysis, and K-means clustering, were applied to extract dominant morphological features and identify representative upper-body shape types. Additionally, the study's usefulness for mass customization, virtual garment fitting applications, and worldwide apparel sizing systems was increased by evaluating the generated classifications against both national and international size standards.

II. METHODS

2.1 Anthropometry Experiment

Body measurements were collected using three different methods: photographic measurement, 3D body scanning, and manual measurement. The study subjects were female college students from Bangladesh and China, aged between 18 and 30 years, with sample sizes of 189 for China and 20 for Bangladesh.

For the 2D body measurement method, digital images of the subjects were captured using a Sony A6000 camera with a resolution of 4000 × 6000 pixels(Xu et al., 2023). Three-dimensional body measurements were obtained using the American [TC]² 3D body scanner, which collected human images, three-dimensional point cloud data, and body models. During the scanning process, the temperature and relative humidity of the experimental environment were maintained at 27 ± 3 °C and 60% ± 10%, respectively. Manual measurements were conducted using a height meter and a flexible measuring tape. During the measurement process, all participants were required to stand barefoot in a designated footprint position while maintaining normal breathing. They wore skin-colored, form-fitting clothing and covered their hair with a cap to minimize measurement interference. For front-view photographs, the subjects were instructed to raise their arms and slightly bend them. For side-view photographs, their arms were positioned close to their sides to clearly reveal the front of the abdomen and the back of the waist. The standing posture of the subjects during photography is illustrated in Figure 1(a). Figure 1(b) depicts the human body's standing positions during scanning on the American [TC]² 3D body scanner. To ensure precise scanning, the 3D scanner recommends specific footprint locations and hand hangers. Three-dimensional scanning data is extracted using ImageWare software.

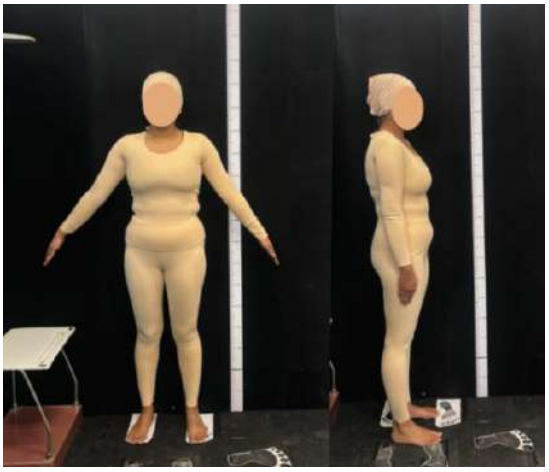

Fig.1(a): 2D images

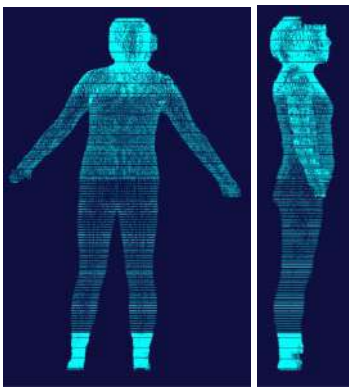

Fig.1(b) TC] ² 3D body scanning

Source(s): Author's own creation

2.2 Determination of shape descriptors

The area from the side neck line to the hip line, excluding the arms, was referred to as the upper body. The human upper body's shape variations are mainly centered in two areas for the front view, which are indicated by red lines in Figure 2. The curve that connects the armpit point (ArP), waist point (WP), and side hip point (HP) is one component; the other is the curve that forms the shoulder slope between the side neck point (SNP) and the shoulder point (SP). The bust's convexity and the back's "S" shape, which is composed of the hip convex, waist concave, and back convex, are the two primary ways the shape difference is visible from the side.

Height (H), neck width (NW), neck circumference (NC), shoulder width (SHW), back width (GW), bust thickness (BT), bust circumference (BC), waist width (WW), waist thickness (WT), waist circumference (WC), hip width (HW), hip thickness (HT), hip circumference (HC), back angle (GA), shoulder angle (SHA), and chest convex angle (BCA) are the sixteen interconnected elements which have been identified, taking into consideration both the upper body's overall and local characteristics.

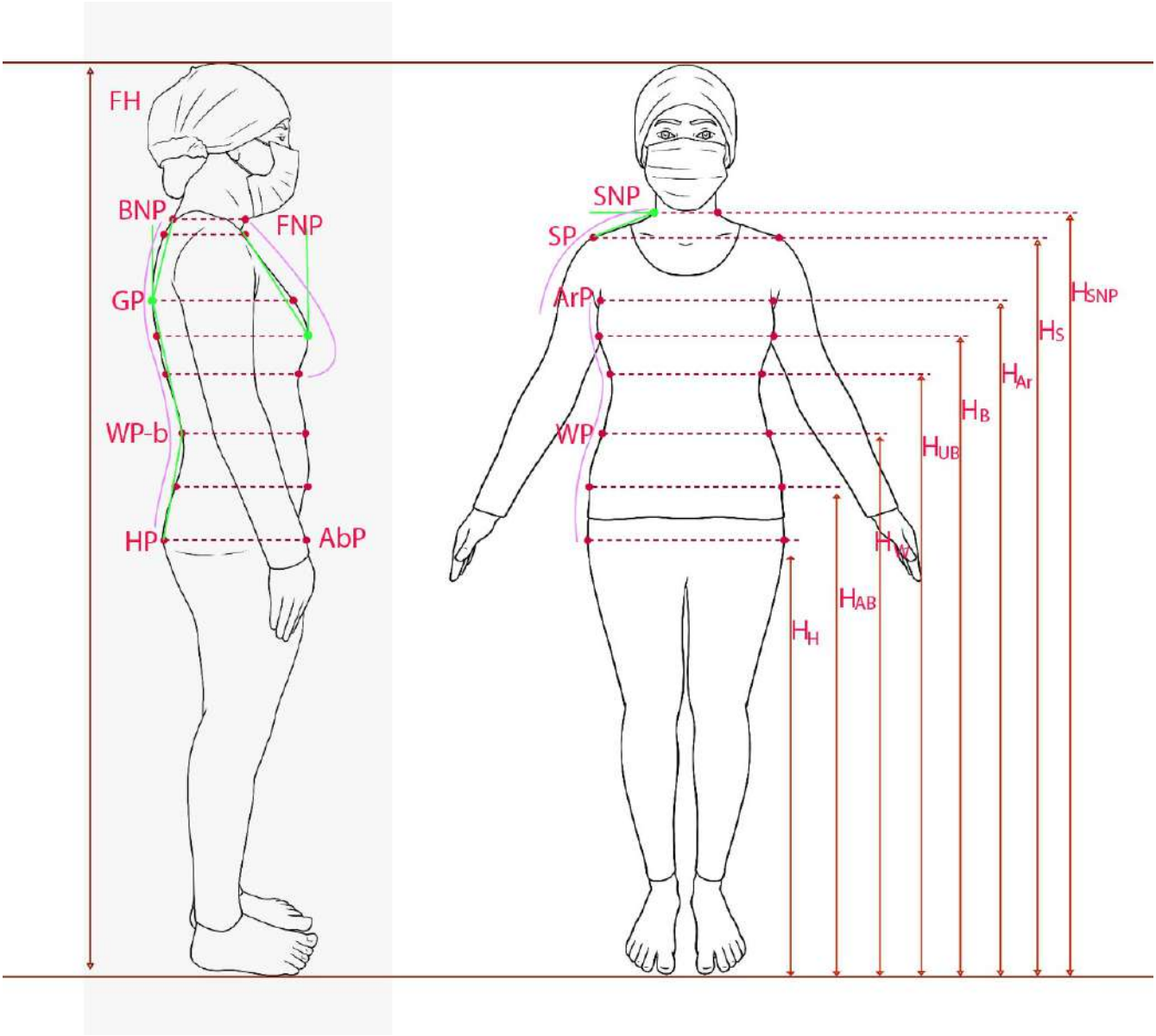

Fig.2

Source(s): Author's own creation

III. RESULTS AND DISCUSSION

3.1 Overall body type classification comparison

First, the data were assessed for normality using SPSS software to evaluate the distribution of women's upper body measurements from both China and Bangladesh.

A descriptive analysis was performed on the upper body shape data of young Chinese and Bangladeshi women. The basic descriptive statistical values of the body shapes of Bangladeshi and Chinese young women are presented in Table 1.

Table:1

Measurement point	Unit	Country	Minimum value	maximum value	mean	standard deviation	variance
Height	cm	Chinese	160.20	191.00	173.4820	5.39961	29.156
		Bangladeshi	148.00	168.00	153.1000	5.52411	30.516

Shoulder slope	cm	Chinese	19.07	36.12	26.5169	3.20371	10.264
		Bangladeshi	20.80	35.28	27.5850	3.82658	14.643
Back angle	Degree (°)	Chinese	7.49	23.66	15.6957	3.41567	11.667
		Bangladeshi	9.74	23.76	19.0125	3.41113	11.636
Bust convex angle	Degree (°)	Chinese	48.20	69.04	59.6401	4.40122	19.371
		Bangladeshi	18.07	40.83	27.0915	5.35223	28.646
Collar width	cm	Chinese	10.20	13.20	11.6571	0.475	0.226
		Bangladeshi	10.203	13.847	11.78	1.094	11.978
Collars thick	cm	Chinese	10.10	12.70	11.133	0.471	0.222
		Bangladeshi	10.124	13.782	11.657	1.1056	12.22
Collar circumference	cm	Chinese	30.20	45.10	37.2074	2.2914	5.251
		Bangladeshi	33.126	42.050	36.94551	2.5173	63.368
Shoulder width	cm	Chinese	34.60	46.20	39.4926	2.41021	5.809
		Bangladeshi	34.039	44.368	38.21291	2.6896	72.341
Curve shoulder width	cm	Chinese	29.50	56.20	48.4158	3.61364	13.058
		Bangladeshi	39.143	54.710	46.1293	4.34957	18.9188
Back width	cm	Chinese	32.40	51.00	43.9138	2.93196	8.596
		Bangladeshi	27.547	45.284	32.2808	4.00182	16.0146
Front width	cm	Chinese	28.30	43.00	35.0688	2.39595	5.741
		Bangladeshi	26.158	35.517	30.2703	2.35656	55.5340
Bust thick	cm	Chinese	16.60	34.60	24.9386	3.20919	10.299
		Bangladeshi	21.938	32.385	26.0477	2.95440	87.2851
Bust circumference	cm	Chinese	76.00	110.00	88.8476	6.30681	39.776
		Bangladeshi	82.354	113.169	93.4209	8.17756	66.8726
Waist width	cm	Chinese	21.70	39.70	27.4423	2.99027	8.942
		Bangladeshi	22.785	30.716	26.8622	2.26998	51.5283
Waist thick	cm	Chinese	15.70	30.70	20.7683	2.76254	7.632
		Bangladeshi	18.136	28.674	22.3517	2.88088	82.995
Waist circumference	cm	Chinese	56.70	106.90	74.9804	7.53752	56.814
		Bangladeshi	65.465	92.468	77.8726	7.65140	58.5440
Hip width	cm	Chinese	30.20	38.50	34.0624	2.04558	4.184
		Bangladeshi	30.679	38.993	35.3771	2.82717	79.9291
Back thick	cm	Chinese	19.70	29.80	24.5995	2.07630	4.311
		Bangladeshi	19.743	32.889	25.3013	3.43901	11.8268
Hips	cm	Chinese	81.00	115.00	94.5090	6.08642	37.045
		Bangladeshi	82.908	109.545	96.98121	8.36841	70.0303

3.2 Comparative analysis of national standard

China's standard women's sizing system follows the GB/T 1335 specification, which is a reference for the production and purchase of clothing. GB/T 1335 specification adopts a dual-indicator format based on height and bust/chest circumference (165/88A), where the first value represents body height (cm), the second indicates the key girth measurement (bust/chest, cm), and the final letter denotes the body type classification code. In this system, A corresponds to the standard body type, B represents a fuller body type, and C indicates a slimmer body type.

The body type classification codes and corresponding applicable ranges of this standard are shown in Table 2. The standard divides Chinese women's height into seven levels of 5 cm, starting from 155 cm.

Table:2

Body type classification code	Y	A	B	C
Bust-waist difference cm	17-22	12-16	7-11	2-6

According to the basic statistical analysis, the average bust-waist difference among Chinese young women is 13.86 cm, with a standard deviation of 4.8 cm. The maximum recorded value is 29.6 cm, while the minimum is -0.9 cm, indicating a wide range and a relatively dispersed distribution. This broad variability suggests significant diversity in body shapes within this demographic. The bust-waist differences have been further categorized and tallied to analyze the size distribution across various body types, as illustrated in Table 3. In summary, these findings underscore the importance of accommodating diverse body shapes when designing apparel for young Chinese women.

Table:3

Type	Chest-waist difference cm	Number of people	Type	Chest-waist difference cm	Number of people	Type	Chest-waist difference cm	Number of people
Y	17-22	42	B	7-11	47	not covered	>22	11
A	12-16	85	C	2-5	3	not covered	<2	1

According to the analysis, young Chinese women's body types fall primarily into categories A and B, with a broad range of waist circumferences and a height distribution between 150 and 160 cm. About 95.9% of young Chinese women's body types can be covered by the country's existing size standards; however, those with extremely wide chest-waist discrepancies and extremely small body types are not included in the size classification description.

Bangladesh's women's garment sizing system predominantly adopts a modified Western sizing framework, with bust/chest measurements in inch-based measurements, rather than adhering to a unified national sizing code. In industrial practice, garment manufacturers in Bangladesh commonly reference(*ISO-8559-1-2017*, n.d.), which provides standardized guidelines for anthropometric body measurements used in garment design.

The present study adopts (*ISO-TR-10652-1991*, n.d.) as the reference framework for comparative analysis of the sampled population. Under this ISO system, women's stature is categorized into five height levels, beginning at 164 cm and increasing by 6cm at each level.

Statistical analysis data showed that the mean chest–waist difference among young Bangladeshi women is 15.43 cm, with a standard deviation of 3.53 cm, indicating moderate variability in upper-torso shape. The observed values range from a minimum of 10.25 cm to a maximum of 20.79 cm, reflecting substantial diversity in body proportions within the study population.

The distribution of each body type within the ISO size framework is summarized in Table 4-5, providing a detailed representation of size prevalence and proportional characteristics among young Bangladeshi women.

Table: 4

Body shape	Chest-waist difference cm	Number of people
A	>=16	10
R	12-15	8

P	6-11	2
S	0-5	0
C	(-6) - (-1)	0

The Roche index is used to evaluate relative body fatness or thinness based on the relationship between body weight and height. It provides a preliminary assessment of overall body shape by standardizing weight against height. The Roche index is calculated as:

Roche index = 100 × weight (g) / height³ (cm³)

Higher values indicate a fuller body build, while lower values reflect a slimmer physique.

Table: 5

Body type category	Roche Index	China (number)	Bangladesh
Slender	<=1.29	126	7
Standard type	1.3-1.5	53	3
Squat type	>=1.51	10	10

3.3 Analysis of overall upper body shape characteristics

3.3.1 Analysis of Chinese women upper body shape characteristics

To identify the essential measurements that best represent overall body shape, sixteen elements were analyzed, including height, neck width and circumference, shoulder and back width, bust, waist, and hip width, thickness, and circumference, as well as back angle, shoulder angle, and chest convex angle. Factor analysis and principal component analysis (PCA) were performed using SPSS to reduce data dimensionality and to identify the principal factors influencing body shape characteristics.

The Kaiser–Meyer–Olkin (KMO) measure of sampling adequacy for young Chinese women was 0.851, with a significance level of $p < 0.001$, indicating strong correlations among the variables and confirming that the data-set was highly suitable for factor analysis. These components were therefore retained as the primary factors representing overall body shape variation.

The component matrix reveals that measurements related to body size, girth, and three-dimensional form exhibit high factor loadings, demonstrating their dominant contribution to body shape classification. The key variables associated with each principal component, along with their corresponding factor loadings and scores, are summarized in Table 6.

Factor analysis of Chinese women's upper body shape characteristics

Table: 6

Main factor	Factor	Score	Factor	Score	Factor	Score
Circumference factor	Waist circumference	0.885	Hips circumference	0.872	Neck circumference	0.844
Width & thick factor	Waist width	0.868	Waist thick	0.836	Hip width	0.753
Angle factor	Shoulder angle	0.836	Bust angle	0.748	Back angle	0.693

Based on the factor analysis results, three principal components were identified: 1. Circumference factor, 2. width & thickness factor, and 3. angle factor, which were extracted to represent the overall upper body shape characteristics of young Chinese women. Using the variables with higher factor loadings from these three principal components as clustering indicators, a K-means cluster analysis was conducted to classify upper body shape types.

Cluster analysis of Chinese women's upper body shape characteristics

Table: 7

	Category - 1	Category - 2	Category - 3
Waist circumference	83.2	75.4	68.6
Waist width	30.7	27.9	26
Shoulder angle	27.97	26.29	22.6
Number of people	57	52	80

The clustering results of the three upper body categories reflect a clear gradation in circumference, width, and structural expansion. Category -1 (Full Circumference–Wide Structure) is characterized by the largest waist dimensions and shoulder angle, indicating a fuller, laterally expanded, and robust upper body contour. Category -2 (Medium Proportion Balanced) exhibits intermediate measurements and well-proportioned relationships among circumference, width, and angular features, representing the average and most balanced upper body morphology. In contrast, Category -3 (Slim Circumference–Narrow Structure) displays the smallest waist dimensions and shoulder angle, corresponding to a slender, compact, and narrow upper body profile.

3.3.2 Analysis of Bangladeshi women's upper body shape characteristics

The same sixteen anthropometric variables were applied to examine upper body morphology among young Bangladeshi women. The KMO value of 0.649, together with a statistically significant Bartlett's test ($p < 0.001$), indicates acceptable sampling adequacy for factor analysis. According to the scree plot (Figure 4), the retention of three principal components collectively describes the major patterns of upper body shape variation.

The first principal component, designated the circumference factor, was strongly influenced by chest circumference, waist circumference, and collar circumference, emphasizing the prominence of upper torso girth in defining body shape. The second component, identified as the angle factor, was dominated by chest convex angle and shoulder angle, reflecting anterior chest projection and shoulder inclination. The third component, referred to as the width–thickness factor, was primarily associated with collar width, chest thickness, and waist thickness, capturing transverse and sagittal dimensional characteristics of the upper body.

Factor analysis of Bangladeshi women's upper body shape characteristics

Table: 8

Main factor	Factor	Score	Factor	Score	Factor	Score
Circumference factor	Bust circumference	0.94	Waist circumference	0.907	Neck circumference	0.889
Angle factor	Bust angle	0.913	Shoulder angle	0.822		
leniency factor	Neck width	0.868	Bust thick	0.867	Thick waist	0.862

Based on variables with high factor loadings, a K-means clustering analysis was conducted, resulting in three distinct upper body shape categories among young Bangladeshi women.

Cluster analysis of Bangladeshi women's upper body shape characteristics

Table: 9

	Category - 1	Category - 2	Category - 3
Bust circumference	93.3	91.44	82.82
Bust angle	29.5	25.12	20.94
Neck width	12.14	11.1	10.68
Number of people	12	3	3

The clustering results identify three distinct upper body morphology types primarily differentiated by chest circumference, anterior projection, and neckline width. Category -1 represents a large-circumference type with pronounced chest projection and a broad collar width, reflecting a strongly three-dimensional and prominent upper torso structure. Category -2 corresponds to a medium-circumference type, characterized by moderate chest projection and balanced proportions, indicating an intermediate and relatively harmonious upper body morphology. Category -3 defines a small-circumference, slim upper body type, marked by minimal chest projection and a narrow collar width, resulting in a slender and less volumetric upper torso profile.

3.4 Comparison of local body types

3.4.1 Analysis of shoulder and neck shape

The neck and shoulder region are crucial in clothing design, particularly for ensuring well-fitted garments. Variations in the anatomical structure of the neck and shoulders among different populations can affect clothing fit, especially in the upper torso and collar areas. This study examines the neck and shoulder shapes of Bangladeshi and Chinese women, using descriptive statistics and cluster analysis to better understand these variations and their impact on garment fitting.

Factors related to shoulder and neck shape characteristics include shoulder angle, shoulder width, neck width, neck thickness, and neck circumference, as detailed in Table 10.

Table10: Descriptive statistics of Shoulder and neck

China	Minimum value	Maximum value	Mean	standard deviation	Bangladesh	minimum value	maximum value	mean	standard deviation
Shoulder angle	19.07°	36.12°	26.52	3.21	Shoulder angle	20.8°	35.29°	27.59	3.83
Shoulder width	34.6	46.2	39.49	2.41	Shoulder width	34.04	44.37	38.21	2.69
Neck width	10.2	13.2	11.66	0.48	Neck width	10.2	13.85	11.78	1.09
Neck Thick	10.1	12.7	11.13	0.47	Neck Thick	10.12	13.78	11.66	1.11
Neck Circumference	30.2	45.1	37.21	2.29	Neck circumference	33.13	42.05	36.95	2.52

According to five key indices: shoulder angle, shoulder width, collar width, collar thickness, and neck circumference, Chinese subjects typically have slightly broader, visually flatter shoulders and a relatively slimmer neck, while Bangladeshi subjects show more sloping and narrower shoulders with a thicker neck, despite similar neck circumferences. Cluster analysis confirms that both populations can be categorized into three comparable shape types, ranging from broader, more sloping shoulders to narrower, more delicate shoulder-neck configurations. However, the distribution of these categories varies between countries: In China, Shape categories 1 and 3 together make up over four-fifths of the sample (42.3% and 41.3%, respectively), while in Bangladesh, Shape Type 3 is the most common (40.0%), followed by category 2 (35.0%) and category 1 (25.0%). These results indicate that although a common set of shoulder–neck shape categories apply to both populations, the dominant body types and upper-body proportional balance differ by country. For women's wear pattern development, Chinese size systems should prioritize slightly broader, less sloping shoulders and a comparatively slimmer neckline, while Bangladeshi size systems should accommodate more shoulder slope and greater neck thickness.

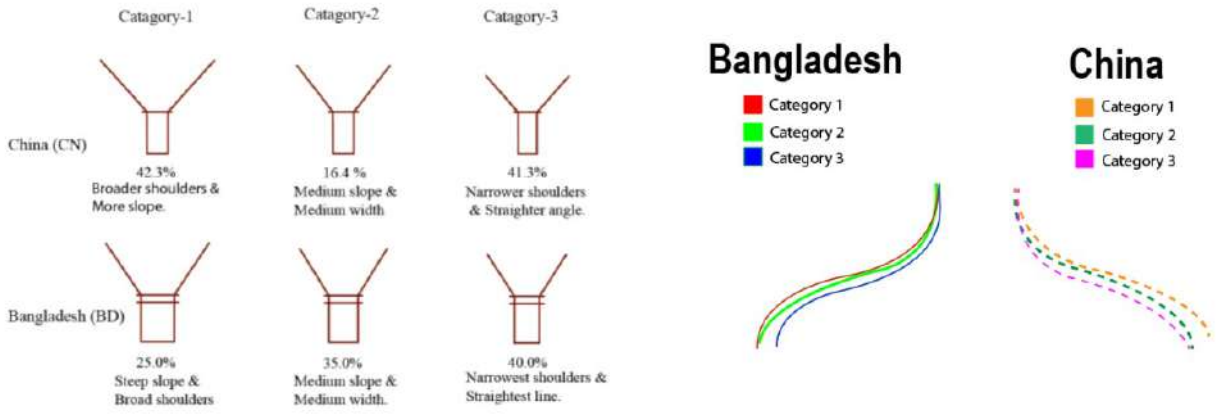

Fig.3: Shoulder & Neck shape of Chinese and Bangladeshi women

Source(s): Author's own creation

Chinese figures feature slightly broader, visually wider shoulders with slimmer necks; BD figures have more sloping, narrower shoulders with thicker necks. The outlines represent simplified visual depictions of shoulder-neck configurations based on the described shape types.

3.4.2. Bust shape analysis

It is believed that women's breasts indicate their physical attractiveness (Zhong et al., 2023). Anthropometric modeling, fit systems, and apparel design all depend on the bust. The bust morphology of Chinese and Bangladeshi women is examined in this study using descriptive statistics and cluster analysis. Four aspects of bust shape are considered, as shown in Table 11: bust convexity/angle, bust breadth, bust thickness, and bust circumference. Cluster analysis divides each population into three distinct bust-shaped groupings, each of which has a unique morphological pattern.

Table: 11

China	Minimum value	Maximum value	Mean	Standard deviation	Bangladesh	Minimum value	Maximum value	Mean	Standard deviation
Bust angle	48.2°	69.04°	59.64	4.4	Bust angle	18.07°	40.83°	27.09	5.35
Bust width	28.3	43	35.07	2.4	Bust width	26.16	35.52	30.27	2.36
Bust thick	16.6	34.6	24.94	3.21	Bust thick	21.94	32.39	26.05	2.95
Bust circumference	76	110	88.85	6.31	Bust circumference	82.35	113.17	93.42	8.18

Based on the combined descriptive statistics and cluster-analysis results, the chest/bust morphology of Bangladeshi and Chinese women exhibits clear population-level variations in convexity, width, depth, circumference balance, and distribution of shape categories.

Greater anterior convexity and wider thoracic width are the main characteristics of Chinese women's chest morphologies, resulting in a noticeably more rounded chest profile. Their clusters range from highly convex and broad to mildly convex and narrow, but all maintain considerably higher convex angles than the Bangladeshi groups. The distribution is relatively balanced across three categories, indicating a wide morphological spectrum and higher heterogeneity within the Chinese sample. The proportional increase in chest width, thickness, and circumference indicates that Chinese chest volume expands in both width and projection.

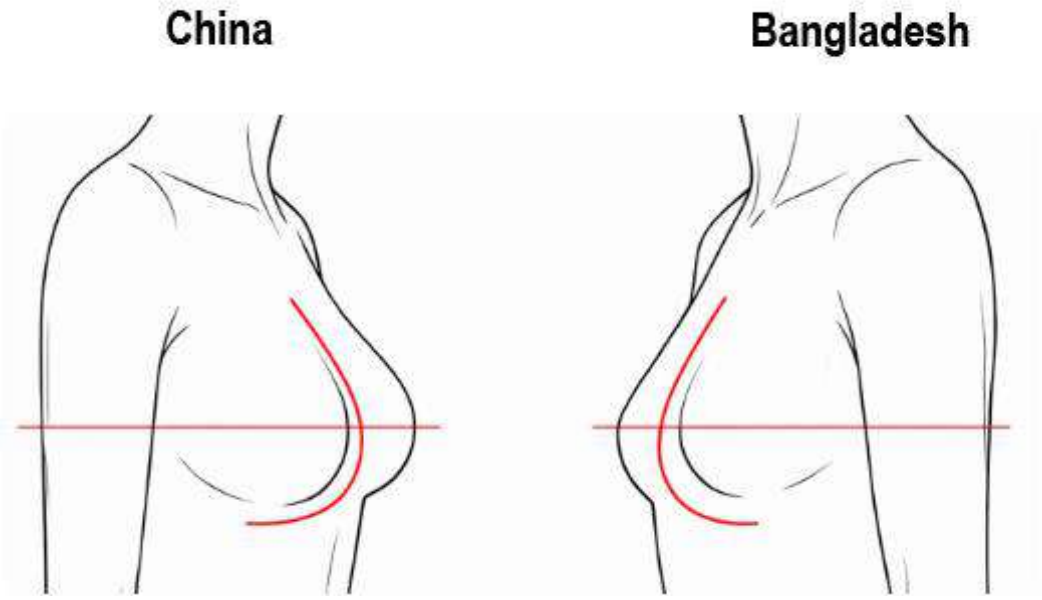

Figure 4: Bust shape of Chinese and Bangladeshi women

Source(s): Author's own creation

In contrast, Bangladeshi women have a chest morphology dominated by flat and narrow chest morphologies, with considerably lower convex angles and reduced mediolateral breadth. Despite this narrowness, many

Bangladeshi individuals demonstrate moderate chest thickness and relatively high circumference, indicating a pattern where thoracic volume is dispersed more across the ribcage rather than thrust forward. The overwhelming dominance of the flat–narrow group (75%) reveals lower shape variety among this population compared with the Chinese sample.

Overall, the two populations differ most significantly in chest convexity (high vs. low), width (wide vs. narrow), and cluster dominance (balanced three-way distribution vs. one overwhelmingly common shape). These variations point to thoracic structures that are unique to each population and may be influenced by somatic, genetic, and environmental variables.

Together, the findings underline the relevance of country-specific considerations in garment design, anthropometric modeling, and fit systems where chest volume distribution and projection play key functional roles.

3.4.3. Waist and hip body shape analysis

Anthropometric modeling, fit systems, and apparel design all depend on the shape of the waist and hips. This study uses cluster analysis and descriptive statistics to examine the hip and waist morphology of Chinese and Bangladeshi women.

Table: 12

China	Minimum value	Maximum value	Mean	Standard deviation	Bangladesh	Minimum value	Maximum value	Mean	Standard deviation
Waist width	21.7	39.7	27.44	2.99	Waist width	22.79	30.72	26.86	2.07
Waist thick	15.7	30.7	20.77	2.76	Waist thick	18.14	28.67	22.35	2.88
Waist circumference	56.7	106.9	74.98	7.54	Waist circumference	65.46	92.47	77.99	7.65
Hip width	30.2	38.5	34.06	2.05	Hip width	30.68	38.99	35.38	2..83
Back thick	19.7	29.8	24.6	2.08	Back thick	19.74	32.89	25.3	3.44
Hips	81	115	94.5	6.09	Hips	82.91	109.55	96.98	8.37

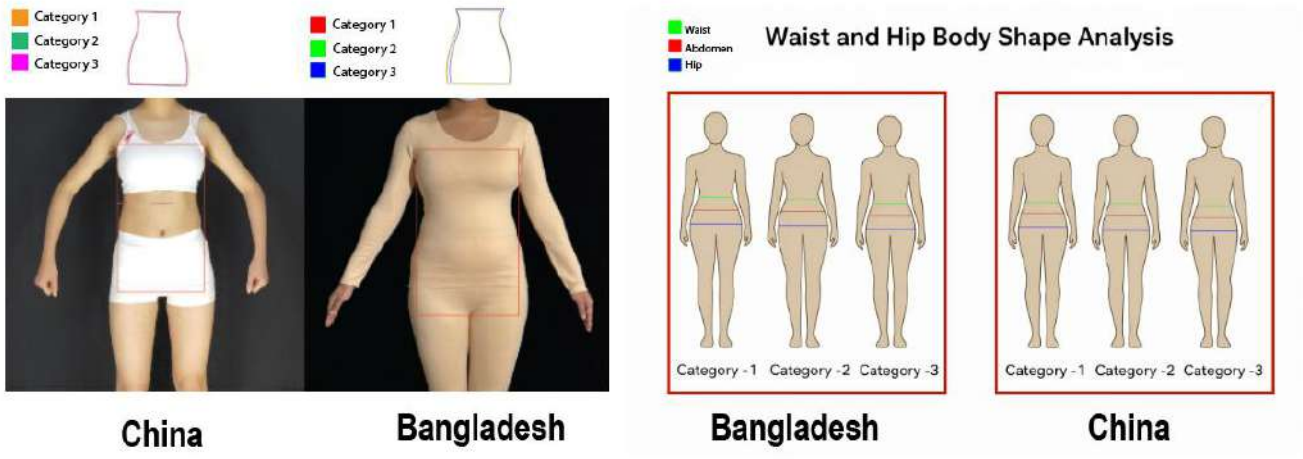

Fig.5: Waist and hip body shape of Chinese and Bangladeshi women

Source(s): Author's own creation

We looked at six anthropometric factors for both populations: hip width, hip thickness, hip circumference, waist circumference, and waist thickness. The findings indicate that Chinese women have flatter waistlines and narrower hips, while Bangladeshi women typically have deeper waists and rounder, wider hips. According to cluster analysis, each country has three different form categories, with Chinese groups exhibiting more balanced, straight-line contours and Bangladeshi groups exhibiting more lower-body prominence. The results show distinct morphological variations with implications for body-shape classification, ergonomics, and clothing design.

IV. CONCLUSION

This study used integrated 3D, 2D, and manual anthropometric measures to compare the upper body shape of young Chinese and Bangladeshi women. Through multivariate statistical analyses, key shape descriptors and structural differences between the two populations were systematically identified and classified.

The results show distinct population-specific characteristics. Chinese women are generally characterized by broader shoulders, higher chest convexity, wider upper-torso dimensions, and comparatively flatter waist–hip profiles, whereas Bangladeshi women exhibit more sloping shoulders, thicker neck regions, reduced chest projection, deeper waists, and more prominent hips. Although three principal upper body shape categories were identified in both populations, their defining variables and distribution patterns differed substantially, reflecting distinct morphological structures.

The majority of Chinese body types are sufficiently covered by current national and international sizing standards, however, people with extreme proportions are still underrepresented, according to the evaluation. In contrast, the absence of a unified national sizing system in Bangladesh results in a greater mismatch between standardized size frameworks and actual body shape characteristics.

Overall, the findings emphasize the limitations of applying uniform or imported sizing systems across diverse populations. The study supports the development of population-specific apparel sizing systems and body-shape–based garment design strategies. Such approaches can significantly improve garment fit, enhance consumer comfort, and increase industrial efficiency by relying on anthropometric standards tailored to specific populations rather than generalized sizing models.

Several limitations should be acknowledged. First, the study focused exclusively on young adult women, which limits the generalizability of the findings to other age groups. Second, some identified clusters particularly within the Bangladesh sample contained relatively small numbers of participants, which may affect statistical robustness. Additionally, the use of mixed measurement modalities may introduce methodological bias, even though consistent experimental controls were maintained.

Future research should aim to include larger and more diverse samples across different age groups. Furthermore, adopting fully standardized 3D body measurement protocols across populations would enhance methodological consistency and improve the reliability of comparative anthropometric analyses.

REFERENCES

[1] Bartol, K., Bojanic, D., Petkovic, T., & Pribanic, T. (2021). A Review of Body Measurement Using 3D Scanning. *IEEE Access*, *9*, 67281–67301. https://doi.org/10.1109/ACCESS.2021.3076595

[2] Bolaji, J., Qiu, J., McQuerry, M., & Kwon, C. (2025, January 13). A Comparative Anthropometric Analysis of Female Firefighters versus the General U.S. Female Population. *Making Waves Toward A Sustainable and Equitable Future*. Making Waves Toward A Sustainable and Equitable Future. https://doi.org/10.31274/itaa.18476

[3] Chen, C. (2007). Fit evaluation within the made-to-measure process. *International Journal of Clothing Science and Technology*, *19*(2), 131–144. https://doi.org/10.1108/09556220710725720

[4] Gu, B., Ahmed, M. K., Zhong, Z., & Jin, J. (2020). 3D female upper body modelling based on 2D images. *International Journal of Clothing Science and Technology*, *32*(4), 471–482. https://doi.org/10.1108/IJCST-03-2019-0042

[5] Han, H., & Nam, Y. (2011). Automatic body landmark identification for various body figures. *International Journal of Industrial Ergonomics*, *41*(6), 592–606. https://doi.org/10.1016/j.ergon.2011.07.002

[6] *ISO-8559-1-2017*. (n.d.).

[7] *ISO-TR-10652-1991*. (n.d.).

[8] Kim, M., & Kim, S. (2018). Development of a script-based versatile three-dimensional body measurement system. *International Journal of Clothing Science and Technology*, *30*(5), 598–609. https://doi.org/10.1108/IJCST-10-2017-0159

[9] Song, G. (Ed.). (2011). *Improving comfort in clothing*. Woodhead Pub.

[10] Song, H. K., Baytar, F., Ashdown, S. P., & Kim, S. (2022). 3D Anthropometric Analysis of Women's Aging Bodies: Upper Body Shape and Posture Changes. *Fashion Practice*, *14*(1), 26–48. https://doi.org/10.1080/17569370.2021.1879463

[11] Vuruskan, A., & Bulgun, E. (2011). Identification of female body shapes based on numerical evaluations. *International Journal of Clothing Science and Technology*, *23*(1), 46–60. https://doi.org/10.1108/09556221111096732

[12] Xu, K., Zhao, S., Zhang, J., & Gu, B. (2023). Quantifying shape similarity of female upper body silhouettes based on 2D images. *International Journal of Clothing Science and Technology*, *35*(6), 986–996. https://doi.org/10.1108/IJCST-10-2022-0137

[13] Zhong, Z., Zhang, B., Hu, Y., Zhang, L., Gu, B., & Sun, Y. (2023). Comparative Morphological Evaluation of Young Women's Breast-Bra Reshaping by Different Bra Cups. *International Journal of Environmental Research and Public Health*, *20*(5), 3856. https://doi.org/10.3390/ijerph20053856

International Journal of Advanced Engineering Research and Science (IJAERS)
Peer-Reviewed Journal
ISSN: 2349-6495(P) | 2456-1908(O)
Vol-13, Issue-4; Apr, 2026
Journal Home Page Available: https://ijaers.com/
Article DOI: https://dx.doi.org/10.22161/ijaers.134.2

Verification of High Cycle Fatigue Analyses from the Literature by using Finite Element Software

Guilherme Depentor de Souza[1] and Geraldo Creci[2,*]

[1,2]Instituto Federal de São Paulo – Campus Bragança Paulista, SP - Brazil
*Corresponding author e-mail: gcreci@ifsp.edu.br

Received: 21 Feb 2026,

Received in revised form: 25 Mar 2026,

Accepted: 30 Mar 2026,

Available online: 04 Apr 2026

***Keywords*— Mechanical Structural Fatigue, Rainflow Method, Finite Elements, Damage Accumulation.**

***Abstract*—** *This work compares fatigue analysis results presented in the literature with computational simulations performed using finite element software. To this end, two fatigue cases with distinct geometric configurations and loading conditions are analyzed. In the first case, the loading is multiaxial, with sinusoidal variation and the presence of a non-zero mean stress. In the second case, the loading presents alternating and mean stresses that vary over time, and is analyzed by counting load cycles using the Rainflow method. The results found in the literature for both cases, obtained through conventional theoretical fatigue approaches, are compared with the results of the computational simulations performed in this work using finite element software. It can be noticed that the use of numerical simulation computational tools offers great flexibility for the analysis of fatigue problems with complex geometries and loadings. Furthermore, the use of computational tools provides greater ease and speed in obtaining results, contributing to the development of more efficient designs.*

I. INTRODUCTION

Material fatigue is a process caused by alternating load amplitude, resulting in local mechanical failure, and generally occurs at a much lower value than that required for a static load to cause rupture. Mechanical failure can be characterized by the appearance of one or more cracks or the complete rupture of the material after a certain number of fluctuations. Fatigue can be described as local, progressive, and cumulative, and its progression depends on material characteristics and geometry, [1]. To obtain this information, much effort, investment, time, and extensive research with testing have been dedicated to this area, aiming to prevent and understand mechanical and structural failures caused by material fatigue, [2].

Fatigue resistance is the ability of a material to withstand a sequence of cyclic stresses without breaking, and is a determining factor in ensuring the durability and safety of structural components. Materials respond quite differently when subjected to loads that vary over time compared to static loads, [3]. Most machine designs involve the development of parts that will be exposed to variable stresses, making it essential to know the fatigue resistance of materials under these loading conditions. Fatigue resistance for a single cycle is equivalent to static tensile strength, showing a linear decrease in the log-log graph with increasing number of cycles. This trend continues until a stress level is reached, starting a horizontal line around 1E6 cycles. This fatigue resistance plateau is observed only in certain metals, especially in steels and cast irons, and is called the fatigue strength limit. In contrast, for other materials, fatigue resistance continues to decrease beyond this point, [4].

Problems that previously could only be solved through small-scale models or costly experimentation are now largely addressed in computational environments. This is partly due to limitations in physical resources and the need to optimize solutions, which often requires a complete redesign of the project. These issues become even more

critical when various engineering fields are involved in modeling, such as in the analysis of structures subjected to loads resulting from interaction with fluids or applied dynamic forces, as in the case of buildings exposed to seismic tremors or equipment that experiences thermal stresses and static and dynamic forces simultaneously.

Mechanical simulation software allows engineers and designers to analyze the performance of their designs before manufacturing, saving time and resources by identifying potential problems and testing various solutions. Achieving more efficient processes and safer products is directly linked to the software's simulation capabilities, [5].

The overall objective of this work is to analyze the difference between the results obtained in software simulations compared to the results obtained using the established mechanical structural fatigue theory found in [2,6]. For this purpose, two fatigue cases with distinct geometric configurations and loading conditions are analyzed. In the first case, the loading is multiaxial, with sinusoidal variation and the presence of a non-zero mean stress. In the second case, the loading presents alternating and mean stresses that vary over time, and is analyzed by counting load cycles using the Rainflow method, [7].

The importance of building knowledge about the tools available for calculation and their level of confidence, that is, their proximity to reality, is very high, since the applications are diverse and for numerous purposes and work areas, such as engineering structures, medical equipment, tools and installations for agriculture and industry. The improvement of equipment leads to a reduction in dimensions and even greater safety for users, [8]. It can be considered that everything is subject to stress and, during its useful life, there are variations in load, even of small amplitude, which generate everything from tolerable wear and tear to defects that render them unusable for a given application. The possibility of building a simulation close to reality brings much better results and more efficient projects. Confidence in these simulations is essential to lay the foundation for future concepts.

II. BASIC CONCEPTS

The fatigue failure process can be divided into three main stages: crack nucleation, crack propagation, and final failure. Crack nucleation generally occurs at stress concentration sites, such as discontinuities, surface imperfections, or inclusions in the material. These points are vulnerable to local stresses that can exceed the material's strength, initiating the failure process.

Furthermore, mechanical structural fatigue can be classified into different types, such as low-cycle fatigue and high-cycle fatigue, depending on the number of load cycles the material can withstand before failure. Low-cycle fatigue generally occurs in components subjected to high stresses and a reduced number of cycles (<1E3), while high-cycle fatigue refers to lower stresses and a high number of cycles (>1E3). Understanding these differences is vital for the design and analysis of components in various applications.

An important aspect of high-cycle fatigue is the influence of the material's microstructure on fatigue properties. Materials with refined microstructures, such as heat-treated steels, tend to exhibit better fatigue resistance compared to materials with coarser microstructures. The presence of inclusions, porosity, and surface discontinuities can also significantly affect fatigue resistance, as these defects can act as crack nucleation points. Figure 1(a) shows an example of fatigue fracture with the corresponding beach sand marks. Figure 1(b) shows the striations caused in the material related to the applied load.

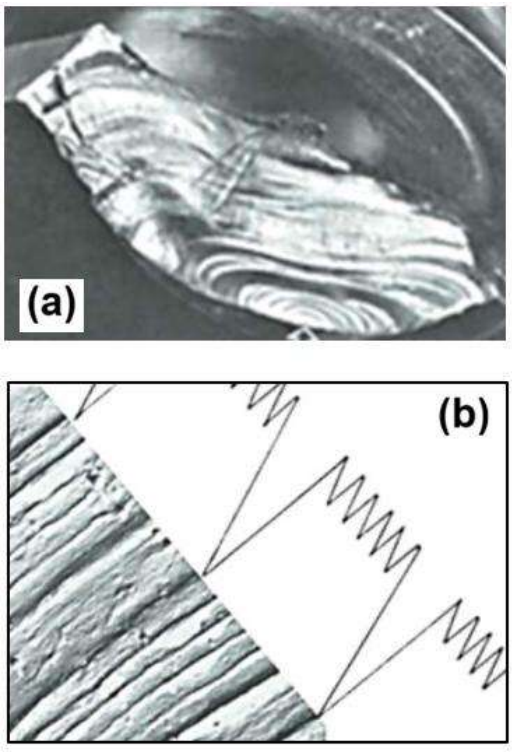

Fig.1. Adapted from [6]: (a) example of fatigue fracture; and, (b) load striations.

Furthermore, temperature and loading frequency are critical factors influencing fatigue behavior. Elevated temperature can reduce the fatigue resistance of materials, while loading frequency can affect the crack growth rate.

It is also valuable to consider the effect of the environment in which the material is operated. Factors such as humidity and corrosion can significantly influence fatigue resistance. For example, corrosion can accelerate the

crack nucleation and propagation process, reducing the component's service life. Therefore, infinite life analysis must take into account not only the material properties but also the environmental conditions in which it will be used.

Ultrasound and thermography methods have stood out as essential tools in detecting flaws in materials subject to mechanical fatigue, especially due to their ability to perform non-destructive inspections with high precision. Ultrasound, based on the propagation of high-frequency acoustic waves, allows the identification of internal discontinuities, such as cracks and delaminations, even in the early stages of formation. This technique is particularly useful in metallic and composite materials used in critical structures such as bridges, aircraft, and turbines. The application of ultrasound significantly contributes to the continuous monitoring of structural integrity, enabling preventive actions before a catastrophic failure occurs. Thermography, in turn, uses thermal images to identify temperature variations on the surface of a material, which may be associated with internal damage, excessive friction, or the onset of cracks. In components subject to fatigue, these thermal anomalies often precede visible signs of failure, making thermography an effective technique for early diagnosis.

III. THEORETICAL ASPECTS

To estimate the fatigue life of a structure, we can follow four possible paths:

A) Alternating stress tests over time with real assemblies or with prototypes of devices from a real project;

B) Fatigue tests on specimens obtained from the same material and manufacturing process as the part, such as casting, machining, forging, among others;

C) Use fatigue strength data that may be available in the literature or provided by the manufacturer or material supplier. However, these represent tests in environments different from the application and with polished specimens of a different size than the real ones. Therefore, correction factors should be applied;

D) Estimate the fatigue strength limit of the material based on available data from static tests, that is, estimate using the ultimate strength S_{ut} and the yield strength S_y.

If the actual conditions and those applied in tests are different, it is necessary to apply factors to correct the theoretical fatigue resistance values. These factors take into account the physical differences between the test specimens and the actual part, temperature differences, environmental conditions such as humidity and corrosion effects, the test conditions and the conditions to which the part will be subjected in the future after a period of operation, and also the differences in the way the load is applied. For a specific application, there are several correction factors that must be applied, according to [6]:

$$S_e = C_{load} C_{size} C_{surf} C_{temp} C_{conf} S_{e'} \quad (1)$$

$$S_f = C_{load} C_{size} C_{surf} C_{temp} C_{conf} S_{f'} \quad (2)$$

where S_f and S_e are the new corrected fatigue strength and fatigue limit values, respectively. according to test rig. C_{load} is the correction due to the loading mode, C_{size} is the correction due to the dimensions of the part, C_{surf} is the correction due to the type of surface finish, C_{temp} is the correction due to the working temperature, C_{conf} is the correction according to the desired degree of confidence, and finally, $S_{e'}$ and $S_{f'}$ are the values obtained by the theory without correction. The index e refers to a fatigue strength limit that provides infinite life, while the index f refers to a fatigue strength limit for a given number of cycles. To calculate each of the factors mentioned above, we can use the equations and tabulated values to plot the S-N diagram according to [6].

The notch sensitivity equation is a relationship that describes how the presence of a notch in a material can affect its fracture resistance. This equation is frequently used in failure analysis of materials and structures, especially in materials engineering and mechanics. The equation is expressed as:

$$K_f = 1 + q(K_t - 1) \quad (3)$$

Where K_t is the theoretical stress concentration factor for the particular geometry and K_f is the fatigue stress concentration factor. The notch sensitivity q indicates how much the presence of the notch reduces the material's resistance to fracture, and varies from 0 to 1. Finally, we can obtain the normal σ or shear stress τ by multiplying the nominal stress by the fatigue stress concentration factors related to normal and shear stresses:

$$\sigma = K_{f_\sigma} \sigma_{nom} \quad \text{or} \quad \tau = K_{f_\tau} \tau_{nom} \quad (4)$$

Due to the wide range of real-world load conditions during a structure's lifespan, a good design requires evaluating the cumulative damage. The linear cumulative damage hypothesis serves to predict the behavior of elements subjected to different loading conditions, such as, alternating and mean stresses varying with time. The total accumulation is the sum of the consumed life fraction, and when it reaches 1 (one unit), the structure's lifespan is considered complete according to Miner's Damage equation

$$D = \sum_{i=1}^{k} \frac{n_i}{N_i} \quad (5)$$

where D is the damage, malfunction, or partial loss of functionality, ranging from 0 to 1, with $D = 0$ being a virgin part and $D = 1$ being a material failure; k is the number of blocks considered; n_i is the number of cycles or time in a block, and N_i is the number of cycles or time until failure.

Alternating loads cause fatigue damage that is cumulative and irreversible. We can consider that real-world situations almost always present complex loads that vary over time, even randomly. Over time, loads tend to completely alter their amplitude and frequency; for example, in equipment such as cargo vehicles, they can assume a random nature. Due to the nature of rotating machines, fluctuating stresses often take the form of a sinusoidal pattern; however, other very irregular patterns can occur with random alternating and mean stresses. Figure 2 shows several failure curves (Gerber, Goodman and Soderberg) considering the relationship between alternating stress σ_a and mean stress σ_m. S_y is the yield stress and S_{ut} is the ultimate stress of the material.

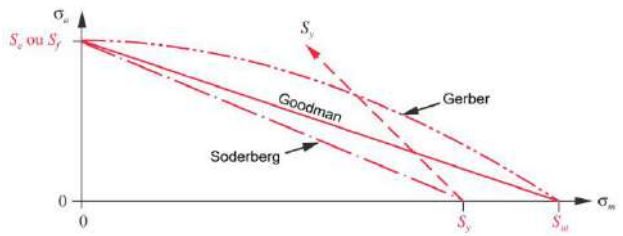

Fig. 2. Adapted from [6]: Failure curves taken into account the relationship between σ_a and σ_m.

When we have well-defined and constant σ_a and σ_m throughout the loading, it is possible to predict fatigue life in a simpler and more effective way. However, when the stress-time patterns are more complex, it is necessary to account for the damage due to the various existing stress-time modes. This could be, for example, a load with zero mean stress but with amplitude variation, or with variation in mean stress and also in the amplitude of the alternating stress. In this way, it is necessary to characterize the load in blocks of alternating stresses, and for this, cycle counting methods are used, which convert a random load into blocks of alternating stresses associated with the number of cycles. The Rainflow method is one of the most used in the industry and can represent a variable load in a very approximate way.

In the Rainflow method, the historical stress-time spectrum is plotted to scale on a coordinate system resembling a series of sloping roofs. Some rules are defined to describe the behavior of imaginary "raindrops" descending through these sloping roofs (stress) in such a way that this rainwater runoff can be used to define stress cycles. The cycle count begins with the first "raindrop" either in the most negative valley or the most positive peak, and continues numbering sequentially until all cycles of a complete block have been counted in sequence. Then, the raindrops are successively positioned on the inside of each peak or valley. Peaks and valleys are considered sources of water. Water flows according to the following rules:

1. A path starting from a valley and continuing through the sections of the "roof" until it encounters a valley more negative than the original;
2. A flow path ceases when it encounters a flow from a previous path;
3. A new path should not be started until a previous path stops;
4. There will then be half-cycles generated by the valleys all along the path;
5. The process is repeated on the other side of the time axis, with a path starting at a peak.

For sufficiently long loads, each valley generating a half-cycle will have a corresponding half-cycle generating peak, thus forming a complete cycle. At the end of the application of the Rainflow Method, a list is obtained with the values of the variations of the alternating and mean stress cycles obtained and their respective number of occurrences. These alternating and mean stresses are then transformed into equivalent alternating stresses. With this data, fatigue damage can be calculated using Miner's Damage equation.

IV. RESULTS

The first case study falls into the category of fluctuating stress in which maximum stress, minimum stress and mean stress have a value different from zero. Figure 3 shows the case studied, extracted from [6], which consists of a tubular rod fixed to the wall and an arm parallel to the support plane, made of 2024-T4 aluminum alloy which has a yield strength S_y = 47000 psi and a ultimate strength S_{ut} = 68000 psi.

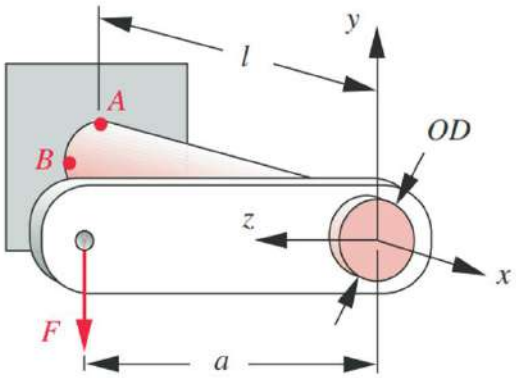

Fig.3. Adapted from [6]: Geometry and dimensions of the first case study.

The tube length is $l = 6$ in and the arm length is $a = 8$ in. The outer diameter of the tube is $OD = 2$ in and the inner diameter is $ID = 1.5$ in. The applied load varies sinusoidally from $F = 340$ lb to -200 lb. The temperature is 20°C. The notch radius in the wall is 0.25 in. The stress concentration factors are: for normal stress 1.7; and, for shear, 1.35. The desired service life is 6E7 cycles. Since aluminum does not have a fatigue limit plateau, the fatigue strength is estimated to be S_f = 19 kpsi in 5E8 cycles. Using the appropriate correction factors and calculating for the required number of cycles, S_f = 14846 psi. Since bending and torsional moments are both caused by the same force, they are synchronous and in phase, and any change in one will have a constant relationship with the other. Thus, for this situation, the safety factor at point *A* can be calculated by:

$$SF = \frac{S_f S_{ut}}{\sigma'_a S_{ut} + \sigma'_m S_f} \quad (6)$$

$$SF = \frac{14846(68000)}{6419(68000) + 1664(14846)}$$

$$SF = 2.2$$

where SF is the safety factor, σ'_a is the von Mises alternating stress and σ'_m is the von Mises mean stress.

Figures 4(a) and 4(b) show the corresponding three-dimensional analysis performed using the finite element software. As shown in the figures, the maximum stress in the most stressed region of the part is 6930.2 psi and the calculated safety factor is 2.24.

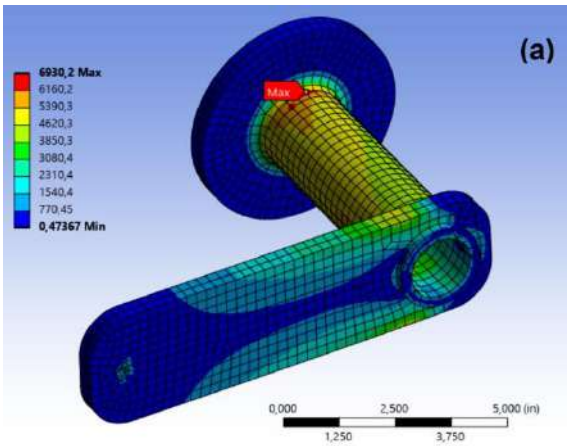

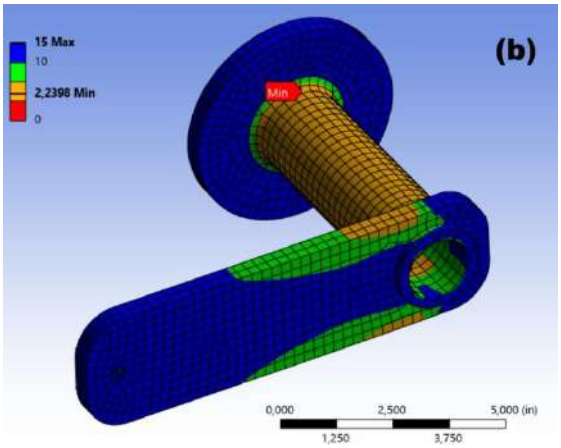

Figure 4. (a) von Mises stress analysis; and, (b) safety factor analysis.

For the second case study, the load presents both mean stresses and alternating stresses variable in time. The objective is to find how many hours the structure will withstand until failure occurs. For this, we can use the S-N curve provided for the application. The load is presented divided into blocks with a duration of 1 minute, as shown in Figure 5. The S-N curve is provided and represents the fatigue behavior with respect to fully reversible and purely alternating stresses, Figure 6.

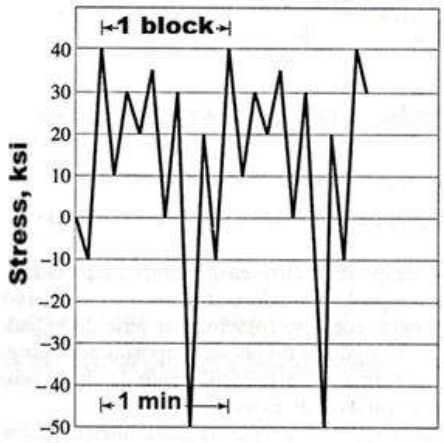

Fig.5. Adapted from [2]: History load data applied to the second case study.

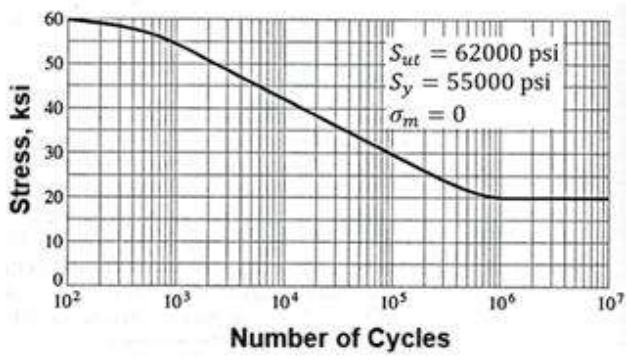

Fig.6. Adapted from [2]: S-N curve of the second case study with respect to fully reversible stresses.

Analyzing the S-N curve and grouping the raindrops, Table 1 can be obtained, where the maximum stress (σ_{max}), the minimum stress (σ_{min}), the mean stress (σ_m), the alternating stress (σ_a), the equivalent alternating stress (σ_{eq-CA}), the number of cycles of occurrence (n), and the number of cycles supported by the application according to the S-N curve (N) can be obtained:

Table 1: Raindrops data for the second case study.

σ_{max}	σ_{min}	σ_m	σ_a	σ_{eq-CA}	n	N
40	-50	-5	45	45	1	6E3
20	-10	5	15	16.3	1	∞
35	10	22.5	12.5	19.6	1	∞
30	20	25	5	8.4	1	∞
30	0	15	15	19.8	1	∞

With the non-zero mean stress cycles already converted to equivalent fully alternating cycles (σ_{eq-CA}), the damage is totaled using the Palmgren-Miner linear damage rule. z is the number of blocks and the repetition will occur 6,000 blocks before failure. Since each block lasts 1 minute, the duration will be 6,000 minutes, totaling 100 hours of operation until failure.

$$D = z\left[\sum_{i=1}^{k}\frac{n_i}{N_i}\right] \rightarrow z = 6{,}000 \text{ blocks} \rightarrow 100 \text{ h} \quad (7)$$

The problem was modeled in finite element software encompassing all the information presented in terms of loads and material data. An arbitrary simple geometry in the form of a parallelepiped was assumed to represent the problem. The software predicts the lifespan of the part as 6139 cycles equivalent to 102.5 hours, Figure 7.

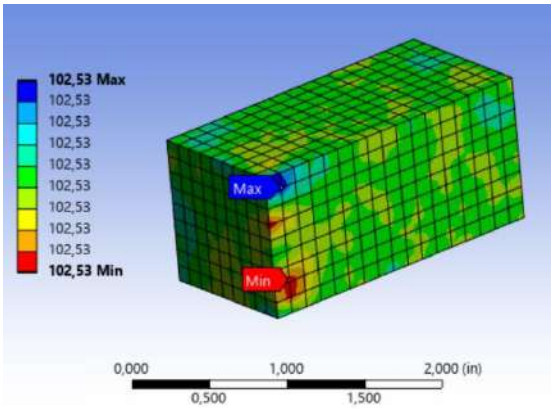

Fig.7. Computational simulation of lifespan of the second case study.

Table 2 shows the differences found for the two case studies considering the conventional theoretical approach from the literature and the computer simulations using finite element software. An excellent agreement can be observed between the calculated results.

Table 2: Summary of the results.

Case study #	Conventional theory from the literature	Numerical computational simulation (this work)	Variation %
1	SF = 2.2	SF = 2.24	1.8
2	100 h	102.5 h	2.5

V. CONCLUSIONS

Analyzing the simulation results, it is possible to conclude that the Finite Element Method using computational software can be a good tool for addressing structural fatigue problems. In the first case study, simpler with alternating and mean constant stresses over time, the difference between the values calculated by the conventional fatigue theory from the literature and the finite element software simulation is 1.8%. In the second case study, more complex because it presented alternating and mean stresses varying with time, which required cycle counting using the Rainflow method and accounting for the damage, the difference between the values calculated by the conventional fatigue theory from the literature and the finite element software simulation is 2.5%. Thus, the differences found for both cases are very low, which is quite acceptable for engineering problems of this nature that contain high statistical variations that can influence the results. Of particular importance is the fact that systems with a large amount of load information or complex geometries can, as can be realized by this work, be better modeled and handled using finite element software than by using a conventional

approach advocated in literature, reinforcing the importance of computational tools in the analysis of engineering problems.

ACKNOWLEDGEMENTS

The authors would like to thank IFSP-BRA for the opportunity to do this work.

REFERENCES

[1] Fatemi, A. and Yang, L. (1998). Cumulative fatigue damage and life prediction theories: a survey of the state of the art for homogeneous materials. *International Journal of Fatigue*, 20(1), 9-34, https://doi.org/10.1016/S0142-1123(97)00081-9

[2] Collins, J.A. (2002). Mechanical Design of Machine Elements and Machines: A Failure Prevention Perspective, Wiley, 1st edition, p. 864, ISBN-10: 0471033073, ISBN-13:978-0471033073.

[3] Fatemi, A. and Shamsaei, N. (2011). Multiaxial fatigue: An overview and some approximation models for life estimation. *International Journal of Fatigue*. 33(8), 948-958, https://doi.org/10.1016/j.ijfatigue.2011.01.003

[4] Budynas, R.G. and Nisbett, K.J. (2019). Shigley's Mechanical Engineering Design, McGraw Hill, 11th edition, p. 1120, ISBN-10: 0073398217, ISBN-13: 978-0073398211.

[5] Zienkiewicz, O.C., Taylor R.L. and Govindjee, S. (2024). The Finite Element Method: Its Basis and Fundamentals, 8th Edition, Butterworth-Heinemann, 8th edition, p. 650, ISBN-10: 0443160449, ISBN-13: 978-0443160448.

[6] Norton, R. (2019). Machine Design: An Integrated Approach, Pearson, 6th edition, p. 1120, ISBN-10: 0135184231, ISBN-13: 978-0135184233.

[7] Cui, W. (2002). A state-of-the-art review on fatigue life prediction methods for metal structures. *Journal of Marine Science and Technology*, 7, 43–56, https://doi.org/10.1007/s007730200012

[8] Grava, F. and Creci, G. (2025). Development of a Semi-Automatic Machine for Manufacturing Low-Cost Concrete Blocks for the Civil Construction Industry, *International Journal of Advanced Engineering Research and Science*, 13(2), 15-21, https://dx.doi.org/10.22161/ijaers.132.2

International Journal of Advanced Engineering Research and Science (IJAERS)
Peer-Reviewed Journal
ISSN: 2349-6495(P) | 2456-1908(O)
Vol-13, Issue-4; Apr, 2026
Journal Home Page Available: https://ijaers.com/
Article DOI: https://dx.doi.org/10.22161/ijaers.134.3

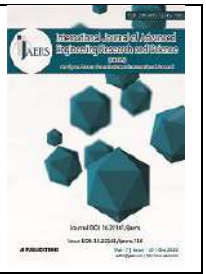

Multi-Objective Coordinated Scheduling of Virtual Power Plants for Economic, Low-Carbon, and Stability Objectives: A DOA-NSGAII Hybrid Optimization Strategy

Yu-Xuan Chen*, Yan-Zuo Chang, Yan-Xiao Jia, Kai-Ming Chen, Zi-Rui He, Wen-Min Wen, Guan-Hong Xie, Hong-Rui Yang, Jie-Zhen Yang, Yong-Qing Wang, Zheng-Kuan Deng

School of Energy and Power Engineering, Guangdong University of Petrochemical Technology, Maoming, Guangdong 525000, China
*Corresponding author : 2127951048@qq.com

Received: 24 Feb 2026,

Received in revised form: 27 Mar 2026,

Accepted: 30 Mar 2026,

Available online: 05 Apr 2026

***Keywords*— Mechanical Structural Fatigue, Rainflow Virtual Power Plant, Dream Optimization Algorithm, Multi-Objective Optimization, NSGA-II.**

***Abstract*—** *To achieve low-carbon, economical, and secure operation of power systems under the "dual carbon" goals, virtual power plants (VPPs) serve as a key technology for aggregating flexible resources such as distributed energy, storage, and demand response, making multi-objective coordinated scheduling critically important. However, the high dimensionality, multiple constraints, and conflicting objectives of this problem pose challenges for traditional optimization methods. Therefore, this paper proposes a hybrid intelligent optimization framework based on an improved Dream Optimization Algorithm (DOA) and the Non-dominated Sorting Genetic Algorithm (NSGA-II), termed DOA-NSGAII, to solve the multi-energy scheduling problem of VPPs with objectives of minimizing economic cost, carbon emissions, and peak-valley load difference. Through customized encoding, decoding, and constraint-handling mechanisms, the framework integrates DOA's global search capability with NSGA-II's multi-objective decision-making advantages. Simulation experiments on the IEEE 14-bus system with three comparative schemes show that, compared with the single-objective economic optimization scheme (S1), the proposed multi-objective coordinated optimization scheme (S3) achieves significant comprehensive benefits—reducing carbon emissions by 30.5% and improving the peak-valley load difference by 12.0%—at the cost of only a marginal 4.9% increase in economic cost. This study validates the effectiveness of the DOA-NSGAII framework in solving complex engineering optimization problems and provides a new approach for multi-objective intelligent scheduling of VPPs.*

I. INTRODUCTION

To address global environmental challenges, the global energy transition has driven the large-scale deployment of distributed energy resources (DERs). However, the instability and seasonality exhibited by DERs have hindered the pace of development **Error! Reference source not found.**. Virtual power plants (VPPs), by leveraging adjustable loads and aggregating DERs, have become a key technology for promoting DER applications and enhancing the flexibility of power systems **Error! Reference source not found.**. The grid integration planning and hosting capacity calculation of DERs have also become important prerequisites for resource aggregation in VPPs **Error! Reference source not found.**[4], as a reasonable hosting capacity assessment can effectively improve DER integration efficiency and grid operational stability **Error! Reference source not found.**[6][7].

In a VPP, it is necessary to obtain an optimal solution that meets expectations under the mutual constraints among DERs, energy storage systems, demand response, and grid interaction **Error! Reference source not found.**. To solve such optimization problems, corresponding strategies must be adopted, which serve as the key technology for addressing these issues. Compared with traditional optimization algorithms, metaheuristic algorithms do not require rigorous mathematical proof **Error! Reference source not found.**; instead, they guide the search process using heuristic information, thereby avoiding entrapment in local optima and effectively solving complex real-world problems. Consequently, they have been extensively studied and applied across various fields. The continuous emergence of novel metaheuristic algorithms also provides additional solution ideas for VPP scheduling optimization.

Metaheuristic algorithms are a class of high-level strategic frameworks for solving complex optimization problems. While they do not guarantee finding the global optimum, they can provide high-quality approximate solutions within a reasonable time. Their core concept is to mimic intelligent behaviors observed in natural or social phenomena, guiding the search process through a balance between exploration and exploitation. Among them, the Dream Optimization Algorithm (DOA) is distinguished by its strong global search capability, ability to escape local optima, dynamic balance between exploration and exploitation, and inherent diversity maintenance mechanism. It transforms the creative thinking process of human dreams into an efficient optimization search mechanism, and its core memory-forgetting-sharing framework offers new insights for solving complex optimization problems characterized by high dimensionality, nonlinearity, and multiple peaks **Error! Reference source not found.**. When addressing complex engineering optimization problems such as those encountered in VPPs—which are characterized by high dimensionality, multiple constraints, multiple objectives, and nonlinearity—DOA demonstrates potential advantages over some traditional optimization algorithms in terms of global search capability, solution set diversity, and convergence robustness.

II. VIRTUAL POWER PLANT SYSTEM MODEL

2.1 Virtual Power Plant

As a key technical form for enabling efficient utilization of distributed resources and source-grid-load-storage coordination in new-type power systems, virtual power plants (VPPs) integrate adjustable resources such as distributed energy resources, energy storage, and controllable loads within a region through advanced information communication and intelligent scheduling technologies, thereby forming a dispatchable virtual controllable unit. Centered on digital platforms and driven by market mechanisms, VPPs aggregate dispersed resources into an integrated entity with regulation capabilities equivalent to those of traditional power plants. They can participate in auxiliary services such as peak shaving and frequency regulation, as well as electricity trading, thereby enhancing renewable energy integration capability, smoothing power fluctuations, and reducing system operating costs. As such, VPPs represent an important technology for supporting the achievement of carbon peak and carbon neutrality goals. Because electricity production, transmission, and consumption occur simultaneously and cannot be stored on a large scale, the power output from distributed sources and the grid interaction power must remain balanced with the load demand at any given time within the VPP. This balance is expressed by the following constraint:

$$\mathrm{P_{WT}(t) + P_{PV}(t) + P_{GT}(t) + P_{grid}(t) + P_{BESS}(t) = L_{base}(t) + \Delta L(t)} \quad (1)$$

where $P_{WT}(t)$ is the wind power output, $P_{PV}(t)$ is the photovoltaic power output, $P_{GT}(t)$ is the gas turbine output, $P_{grid}(t)$ is the grid interaction power, $P_{BESS}(t)$ is the energy storage system power, $L_{base}(t)$ is the base load, and $\Delta L(t)$ is the load variation, i.e., the demand response amount.

If the power system fails to maintain real-time generation–consumption balance, a situation may arise where the sum of distributed generation output and grid interaction power exceeds the load demand. In this case, the surplus electrical energy, having nowhere to be absorbed, is converted into kinetic energy in the generator rotors,

causing the system frequency to increase. Conversely, when the sum of distributed generation output and grid interaction power falls short of the load demand, the resulting energy deficit slows down the generator rotors, leading to a decrease in system frequency.

2.2 Distributed Energy Resource Model

Distributed energy resources (DERs) are small-scale, decentralized energy systems developed near the consumer side. They are characterized by flexible siting, local consumption, and clean, low-carbon operation, complementing centralized energy systems and serving as an important component of new-type power systems. However, due to their small individual capacities, the intermittency of wind power constrained by wind speed variability, and the dependence of photovoltaics on solar irradiance and weather conditions, DERs exhibit nonlinear and seasonal characteristics. As a result, they need to be aggregated and managed through virtual power plants (VPPs). The DERs involved include wind power, photovoltaics, and gas turbines. Among them, gas turbines ensure supply stability at the cost of high operational expenses and carbon emissions, necessitating coordinated optimization strategies to balance the operation of the three resources to achieve economic and carbon reduction objectives. Owing to the uncontrollability, volatility, and forecasting uncertainty of wind and solar power caused by natural conditions, the actual output of wind turbines and photovoltaic systems must not exceed the predicted maximum values. This constraint is expressed as follows

$$0 \le P_{WT}(t) \le P_{WT,max}(t), 0 \le P_{PV}(t) \le P_{PV,max}(t) \quad (2)$$

where $P_{WT,max}(t)$ and $P_{PV,max}(t)$ represent the predicted maximum output of wind power and photovoltaics during period t, respectively.

2.2.1 Wind Power Generation Model INDENTATIONS AND EQUATIONS.

The output power of a wind turbine is strongly correlated with the real-time wind speed. A wind speed–power characteristic model commonly used in engineering applications is adopted:

$$P_{WT} = \begin{cases} 0, & v(t) < v_{ci} \text{或 } v(t) > v_{co} \\ P_{WT,r} \times \dfrac{v(t)^3 - v_{ci}^3}{v_r^3 - v_{ci}^3}, & v_{ci} < v(t) \le v_r \\ P_{WT,r}, & v_r \le v(t) \le v_{co} \end{cases} \quad (3)$$

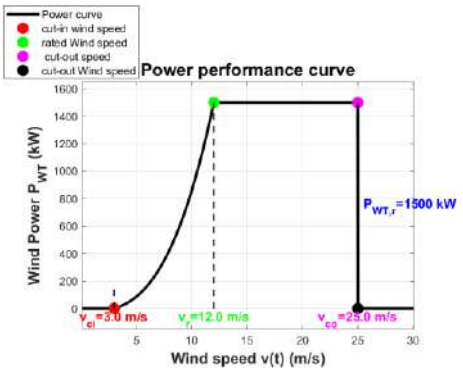

Fig. 1. Power characteristic curve of the wind turbine.

where $v(t)$ is the real-time wind speed at the hub height during period t, in m/s; v_{ci}, v_{co}, and v_r denote the cut-in wind speed, cut-out wind speed, and rated wind speed of the wind turbine, respectively. According to the figure, the values adopted in this paper are v_{ci} = 3 m/s, v_{co} = 25 m/s, and v_r = 12 m/s;$P_{WT,r}$ represents the rated power of the wind turbine, in kW. This model is suitable for system-level simulation and capacity planning, and the resulting data can be used for accurate short-term forecasting or performance evaluation.

2.2.2 Photovoltaic Power Generation Model

The output power of a photovoltaic (PV) cell is related to solar irradiance and ambient temperature. To predict the electrical power output of PV generation, the following model is constructed:

$$P_{PV}(t) = P_{Pv,r} \times \frac{G(t)}{G_{STC}} \times [1 + \alpha_T \cdot (T(t) - T_{STC})] \quad (4)$$

where $P_{PV,\ r}$ is the rated power of the PV module, in kW; G(t) is the real-time solar irradiance during period \(t\), in W/m²; GSTC is the solar irradiance under standard test conditions, taken as 1000 W/m²; α_T is the power temperature coefficient, taken as –0.43%; T(t) is the panel temperature during period t, in °C; and T_{STC} is the standard test temperature, taken as 25°C.

2.2.3 Gas Turbine Model

As a controllable and adjustable power source, the gas turbine serves to compensate for power deficits and provide peak shaving . Its output power is subject to the following constraint:

$$0 \le P_{GT}(t) \le P_{GT,max} \quad (5)$$

where $P_{GT,max}$ is the rated output of the gas turbine, taken as 800 kW in this paper.

The output variation of the gas turbine between adjacent periods is limited by the ramping rate, and this constraint is expressed as follows:

$$-\mathrm{R_{down}} \le \mathrm{P_{GT}(t)} - \mathrm{P_{GT}(t-1)} \le \mathrm{R_{up}} \quad (6)$$

where R_{down} and R_{up} are the maximum downward and upward ramping rates of the gas turbine, respectively, both taken as 200 kW/h in this paper.

2.3 Energy Storage System Model

Energy storage systems serve as core equipment for achieving spatiotemporal transfer of energy and enhancing the regulation capability of power systems, offering advantages such as fast response, high precision, and bidirectional power controllability. They can smooth fluctuations in renewable energy generation, perform peak shaving and valley filling, and improve power supply reliability. In virtual power plants (VPPs), energy storage acts as a key adjustable resource, undertaking the functions of energy buffering and power support, thereby providing flexible regulation capabilities for the VPP and serving as an important foundation for source-grid-load-storage coordination. To improve resource utilization efficiency, a lithium-ion battery energy storage model is adopted in this paper. Its core is the time-sequential recursive relationship of the state of charge (SOC), which describes the dynamic process of energy storage, expressed as follows:

$$\mathrm{SOC(t)} = \big(\mathrm{SOC(t-1)}\big) + \frac{\eta_c \cdot \max(-\mathrm{P_{BESS}(t)}.0) - \frac{\max\big((\mathrm{P_{BESS}(t)}.0)\big)}{\eta_d}}{\mathrm{E_{BESS}}} \cdot \Delta t \quad (7)$$

where SOC(t) and SOC(t-1) represent the state of charge (SOC) of the energy storage system at the end of periods t and t-1, respectively; η_c and η_d are the charging and discharging efficiencies of the energy storage system, respectively, both taken as 0.95 in this paper; E_{BESS} is the rated capacity of the energy storage system, taken as 1000 kW·h in this paper; and Δt is the time step, set to 1 h.

The operation of the energy storage system is subject to the following constraints:

$$\begin{cases} \mathrm{P_{BESS,ch,max}} \le \mathrm{P_{BESS}(t)} \le \mathrm{P_{BESS,dch,max}} \\ \mathrm{SOC_{min}} \le \mathrm{SOC(t)} \le \mathrm{SOC_{max}} \\ \mathrm{SOC(0)} = \mathrm{SOC(24)} \end{cases} \quad (8)$$

where $P_{BESS,ch,max}$ and $P_{BESS,dch,max}$ are the maximum charging and discharging power of the energy storage system, respectively, taken as −300 kW and 300 kW in this paper; SOC_{min} and SOC_{max} are the lower and upper limits of the SOC, taken as 0.2 and 0.8, respectively; and SOC(0) = SOC(24) is the equality constraint ensuring that the SOC at the beginning and end of the scheduling period are equal, thereby guaranteeing the integrity of the scheduling cycle.

2.4 Demand Response Model

Demand response (DR) is an interactive mechanism through which users actively adjust their electricity consumption in response to grid conditions, prices, or incentive signals. It can transform passive consumers into flexible regulation resources by reducing or shifting loads during peak periods or grid fluctuations, thereby alleviating grid stress, facilitating renewable energy integration, and generating benefits for users. Within the virtual power plant (VPP) framework, DR is deeply integrated with distributed energy resources (DERs) and energy storage systems, and through aggregation and coordinated control, it forms a scalable adjustable capability that serves as an important pillar for VPP participation in grid interaction and electricity market transactions. Incorporating DR into multi-energy coordinated scheduling can further enhance the economic and operational performance of VPPs. In this paper, a price-based demand response model is adopted, and the load shifting characteristics in response to electricity price variations are described using a consumer electricity consumption elasticity matrix. The model is expressed as follows:

$$\frac{\Delta \mathrm{L(t)}}{\mathrm{L_{base}(t)}} = \sum_{\tau=1}^{24} \varepsilon_{\mathrm{t,\tau}} \cdot \frac{\lambda_{\mathrm{grid}}(\tau) - \lambda_0}{\lambda_0} \quad (9)$$

where ϵ_t, τ is the price elasticity coefficient; when $\tau = t$, it represents the self-elasticity coefficient, and when $\tau = t$ it represents the cross-elasticity coefficient; λ_0 is the base electricity price, in RMB/kWh.

The load variation on the user side is limited by the maximum adjustable capacity, and this constraint is expressed as follows:

$$\Delta \mathrm{L_{min}} \le \Delta \mathrm{L(t)} \le \Delta \mathrm{L_{max}} \quad (10)$$

where $\Delta L_{\min}$ and $\Delta L_{\max}$ are the maximum load reduction and increase amounts, respectively, taken as ±200 kW in this paper.

2.5 Grid Interaction Model

Grid interaction refers to the comprehensive process of information exchange, power exchange, and dispatch coordination between power entities and the grid. It is central to ensuring system stability and enabling bidirectional energy and information flow. With the large-scale integration of consumer-side resources, the complexity of grid interaction has increased, and efficient interaction supports power balance, renewable energy integration, and ancillary services. Within the virtual power plant (VPP) framework, grid interaction serves as the link connecting distributed resources with system dispatch. By employing standardized technologies, the VPP integrates dispersed resources into a unified regulated entity, achieving standardized interaction with the grid, addressing the fluctuations and dispatch challenges associated with distributed resource grid integration, supporting the VPP's participation in various grid services, and promoting the

development of new-type power systems toward intelligence and efficiency. The power interaction between the VPP and the main grid is limited by the tie-line transmission capacity, and this constraint is expressed as follows:

$$P_{grid,min} \le P_{grid}(t) \le P_{grid,max} \quad (11)$$

where $P_{grid,min}$ and $P_{grid,max}$ are the maximum selling and purchasing power of the tie-line, respectively, taken as $P_{grid,min} = -500$ kW and $P_{grid,max} = 800$ kW in this paper.

III. DESIGN OF THE IMPROVED DREAM OPTIMIZATION ALGORITHM

3.1 Dream Optimization Algorithm

The Dream Optimization Algorithm (DOA) is a novel intelligent optimization method inspired by the cognitive mechanisms of brain sleep and dreaming. By simulating processes such as wakeful perception, dream reconstruction, memory consolidation, and state switching, it achieves a dynamic balance between global exploration and local exploitation, demonstrating strong global search capability and convergence stability. Applying DOA to the optimal scheduling problem of virtual power plants (VPPs) effectively addresses challenges such as the diversity of distributed energy resources, energy storage systems, controllable loads, and demand response resources within VPPs, along with complex operational constraints and the multi-peak nonlinear nature of the objective functions. Under constraints such as grid interaction rules, power balance, and equipment operational limits, the algorithm performs global optimization and coordinated allocation of the outputs, charging/discharging powers, and adjustable loads of various resources within the VPP, aiming to minimize operating costs, maximize profits, or maximize renewable energy integration. Compared with traditional optimization methods, DOA can rapidly escape local optima in complex high-dimensional scheduling spaces and obtain superior coordinated scheduling strategies, thereby enhancing the economic efficiency and operational performance of VPPs and strengthening their efficient, stable, and flexible interaction with the grid. This provides an efficient and reliable intelligent solution for the optimal operation of VPPs within new-type power systems.

Algorithm 1 Pseudo-code of DOA

Input: Population size(N_{max}), the lower limits of variables(X_l), the upper limits of variables(X_u), size of problem(Dim), the current number of iteration(t), the number of iteration as a demarcation(T_d), the maximum number of iterations(T_{max}), forgetting dimensions of each group and of exploitation($k_1, k_2, k_3, k_4, k_5, k_6, k_7$)
Output: the best solution X_{best} and the minimum fitness $Fitness_{best}$

```
Generate an initial population X of N individuals using Eqs. (2) and (3)
Check the bounds of the solutions
Evaluate the fitness of the solutions
Detect the best solution X_best and the minimum fitness Fitness_min
Define the current iteration t = 1
while t < T_d do
    Update the best solution X_best and the minimum fitness Fitness_min
    for q = 1 : 5 do
        Update the best solution X_bestq and the minimum fitness Fitness_minq
        Update k_q using Eq. (10)
        Update X_i^{t+1} using Eq. (4)
        (K_1, K_2, ..., K_{k_q}) = randperm(k_q, N)
        for i = (((q − 1)/5 × N) + 1) : (q/5 × N) do
            if rand < u then
                Update x_{i,j} using Eq. (5)
                Check the bounds of x_{i,j}
            else
                Update x_{i,j} using Eq. (6)
            end if
        end for
    end for
    Update the current number of iteration t by t = t + 1
end while
while t > T_d and t < T_max do
    Update k_r using Eq. (11)
    Update X_i^{t+1} using Eq. (7)
    (K_1, K_2, ..., K_{k_r}) = randperm(k_r, N)
    for i = 1 : N do
        Update x_{i,j} using Eq. (8)
        Check the bounds of x_{i,j}
    end for
    Update the current number of iteration t by t = t + 1
end while
```

Fig. 2. Pseudo-code of the dream optimization algorithm.

3.1.1 Initialization

Let the dimension of the optimization problem be D (corresponding to the total number of scheduling variables in this paper) and the population size be N. The position of the i-th individual in the g-th generation is denoted as $X_i^g = \left(x_{i,1}^g, x_{i,2}^g, \dots, x_{i,D}^g\right)$, and its fitness value is $f\left(X_i^g\right)$. Within the upper and lower bounds of the decision variables, an initial population $\{X_i^0 \mid i = 1,2,\dots,N\}$ is randomly generated, and the fitness of each initial individual is calculated.

3.1.2 Iterative Process of Dream Optimization

Based on individual fitness rankings, the population is equally divided into K groups (typically $K = 5$). Individuals within each group share the "group best position" of that group, denoted as $GBest_k^g$ (for $k = 1, \dots, K$). This constitutes the grouping and memory encoding step.

During the global exploration phase, two strategies are executed in parallel for each individual X_i^g (belonging to group k), and the better outcome is retained. Strategy A: Forgetting–Supplement Strategy – The individual randomly "forgets" a subset of dimensions according to a forgetting rate ρ_f . For each selected dimension j, the new position is explored as follows:

$$x_{I,j}^{candidate1} = GBest_{k,j}^{g} + \alpha \cdot \left(GBest_{k,j}^{g} - x_{I,j}^{g}\right) \cdot \Delta \quad (12)$$

where α is the exploration step coefficient, and Δ is a random number in $[-1,1]$. This strategy enables guided random perturbations around the group best during the search.

Strategy B: Dream Sharing Strategy – The individual also forgets a subset of dimensions. For each selected

dimension j, the new position is taken from the corresponding dimension of another randomly selected individual r in the population:

$$x_{I,j}^{g+1} = x_{I,j}^{explore} + \beta \cdot \left(Best_{global,j}^{g} - x_{I,j}^{explore}\right) \cdot \mathcal{N}(0,\ 1) \quad (13)$$

where β is the exploitation step coefficient (typically $\beta < \alpha$), and $\mathcal{N}(0,1)$ is a random number drawn from the standard normal distribution. This operation applies small-scale Gaussian perturbations around the global optimum to improve convergence accuracy.

3.1.3 Elite Retention and Iteration

Evaluate the fitness of the new population $\{X_i^{g+1}\}$ and update the global best solution $Best_{global}^{g+1}$. Return to the iterative process of the Dream Optimization Algorithm until the termination condition of reaching the maximum number of iterations $G_{\max}$ is satisfied.

3.2 Adaptation and Implementation of the Dream Optimization Algorithm in Virtual Power Plants

To address key adaptation issues such as variable encoding, constraint handling, and multi-objective integration, the Dream Optimization Algorithm (DOA) is applied to the multi-objective optimization problem of virtual power plants (VPPs) in this paper. The decision variables are defined as the power sequences of the controllable resources over the scheduling horizon ($T = 24$ hours). A complete scheduling scheme is encoded as an individual X_i, with a dimensionality of $D = 72$. The specific encoding is as follows:

$$X_i = \begin{bmatrix} P_{GT}(1), \dots, P_{GT}(24), P_{BESS}(1), \dots, \\ P_{BESS}(24), P_{grid}(1), \dots, P_{grid}(24) \end{bmatrix} \quad (14)$$

where $P_{GT}(t)$ represents the output of the gas turbine during period t, which must satisfy its upper and lower limits as well as ramping constraints; $P_{BESS}(t)$ represents the power of the energy storage system during period t, with positive values indicating discharging and negative values indicating charging, and must satisfy its charging/discharging power and SOC constraints; $P_{grid}(t)$ represents the power exchanged with the main grid during period t, with positive values indicating electricity purchase and negative values indicating electricity sale, and must satisfy the tie-line capacity constraints. The wind power output $P_{WT}(t)$ and photovoltaic output $P_{PV}(t)$ are taken as known forecast values, while the demand response load variation $\Delta L(t)$ is determined by the electricity price elasticity model, grid electricity prices, and baseline load. Neither is directly treated as an optimization variable, but both are involved in power balance calculations and objective function evaluation.

In this paper, a hybrid constraint-handling strategy is adopted to ensure efficient search within the feasible region. The power balance equality constraint is enforced as follows. Before evaluating the fitness of each individual, instead of directly using the encoded $P_{grid}(t)$, its value is calculated in real time based on other variables to satisfy the power balance equation:

$$P_{grid}^{calc}(t) = L_{base}(t) + \Delta L(t) - \left(P_{WT}(t) + P_{PV}(t) + P_{GT}(t) + P_{BESS}(t)\right) \quad (15)$$

This calculated value replaces the corresponding $P\_grid\ (t)$ in the individual encoding for subsequent evaluation. This fundamentally ensures that all solutions satisfy the power balance constraint. To ensure a high-quality product, diagrams and lettering MUST be either computer-drafted or drawn using India ink.

For inequality constraints such as equipment output limits, ramping rates, SOC limits, and tie-line capacity constraints, a static penalty function method is adopted. The total constraint violation is converted into a penalty term and added to the objective function. For example, the total penalty term $Penalty(X_i)$ is expressed as:

$$Penalty(X_i) = \lambda \sum_{t=1}^{24} \left[\max\left(0, P_{GT}(t) - P_{GT,max}\right)^2 + \cdots\right] \quad (16)$$

where λ is the penalty factor. Ultimately, the fitness function of the algorithm is formed by adding this penalty term to the original three objective function values, thereby guiding the search toward the feasible region.

In this paper, the framework of the non-dominated sorting genetic algorithm (NSGA-II) is combined with the search mechanism of the Dream Optimization Algorithm (DOA). After each generation of the DOA iteration produces a new population, the parent and offspring populations are merged. All individuals in the merged population are then subjected to non-dominated sorting based on the three objectives—economic cost, carbon emissions, and peak-valley load difference—and are divided into multiple fronts. Subsequently, the crowding distance of individuals within the same non-dominated front is calculated to measure their distribution density in the objective space. During selection, individuals with a higher non-dominated rank are prioritized; for individuals with the same rank, those with a larger crowding distance are preferred to maintain solution diversity. Finally, according to the above rules, a number of individuals equal to the initial population size are selected as the parent population for the next generation of the DOA iteration.

Given the scale (72 dimensions) and complexity of the virtual power plant (VPP) scheduling problem addressed in this paper, the parameters of the DOA algorithm were set

through preliminary experimental tuning as follows: population size $N = 100$, maximum number of iterations $G_{\max} = 300$, number of groups $K = 5$, initial forgetting rate $p_f = 0.5$ linearly decreasing to 0.1 with iterations, exploration coefficient $\alpha = 0.8$, exploitation coefficient $\beta = 0.2$, and penalty factor $\lambda = 1 \times 10^6$. This parameter set is designed to balance global search capability, convergence speed, and solution feasibility. Through the above adaptations, the Dream Optimization Algorithm has been systematically transformed into a customized intelligent optimizer capable of directly and effectively solving the multi-time-scale, multi-constraint, multi-objective coordinated scheduling problem of virtual power plants.

IV. SIMULATION

The simulation period is 24 hours, with a time resolution of $\Delta t = 1$ h. The typical daily output curves of wind power and photovoltaics, along with the base load curve, are shown in Fig. 3. The grid adopts a time-of-use electricity pricing mechanism, and the specific price signals are illustrated in Fig. 4.

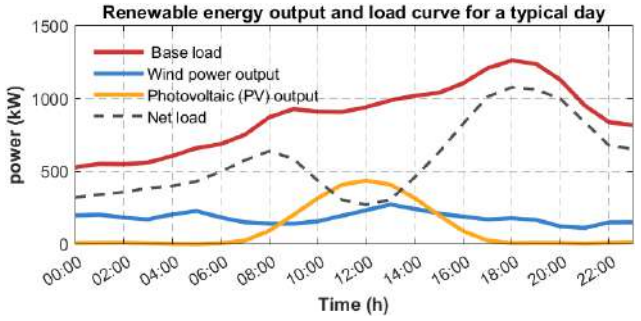

Fig. 3. Typical daily output curves of wind power and photovoltaics, and base load curve.

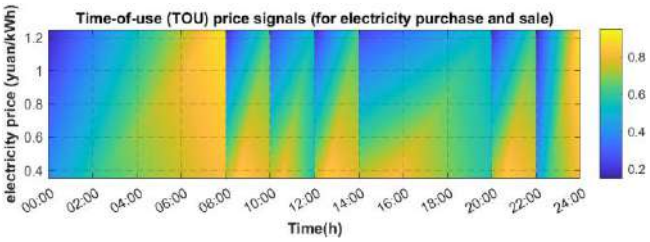

Fig. 4. Time-of-use electricity price signal.

The key parameters of each component within the virtual power plant strictly follow the models established in Chapter 2, and their specific values are summarized in Table 1 to ensure the reproducibility of the model.

Through preliminary experiments of parameter sensitivity analysis, the core parameters of the DOA-NSGAII hybrid algorithm were determined as follows: population size $N = 100$, maximum number of iterations $G_{max} = 300$, number of groups $K = 5$, exploration coefficient $\alpha = 0.8$, exploitation coefficient $\beta = 0.2$, and forgetting rate p_f linearly decreasing from 0.5 to 0.1. The crossover probability and mutation probability in the NSGA-II framework were set to 0.9 and $1/D$ (where $D = 72$ is the dimension of the decision variables), respectively.

4.2 Design of Comparative Schemes

To comprehensively evaluate the effectiveness of the proposed strategy, three comparative schemes were established as follows:

Scheme 1 (S1): Single-objective economic scheduling. The daily operational economic cost is minimized as the sole optimization objective, solved using the standard DOA. The operational strategy of the energy storage system is freely optimized by the algorithm.

Scheme 2 (S2): Fixed-strategy scheduling. The optimization objective is also to minimize economic cost, but the energy storage system adopts a fixed "charge during valley periods, discharge during peak periods" empirical strategy (i.e., charging during low-price periods and discharging during high-price periods), thereby simulating traditional scheduling modes lacking intelligent optimization.

Scheme 3 (S3): Multi-objective coordinated scheduling proposed in this paper. The DOA-NSGAII hybrid algorithm is employed to simultaneously optimize the three objectives of economic cost, carbon emissions, and peak-valley load difference. A comprehensively balanced solution is ultimately selected from the Pareto optimal solution set as the final scheduling scheme.

Table 1. Simulation parameters of the virtual power plant

Component/Parameter	Symbol	Value	Unit
gas turbine	rated power	$P_{GT,max}$	800
	ramping rate	R_{up}, R_{down}	200
lithium-ion battery energy storage	rated capacity	E_{BESS}	1000
	rated power	$P_{BESS,ch,max}/P_{BESS,dch,max}$	±300
	SOC limits	SOC_{min}/SOC_{max}	0.2/0.8
	charging/discharging efficiency	η_c/η_d	0.95/0.95
grid interaction	tie-line transmission capacity limits	$P_{grid,min}/P_{grid},max$	-500/800
demand response	maximum load adjustment capacity	$\Delta L_{min}, \Delta L_{max}$	-200/200

4.3 Results Analysis and Discussion

4.3.1 Comparative Analysis of Multi-Objective Optimization Results

The quantitative comparison of the scheduling results for the three schemes is presented in the table. Table 2. Comparison of results for different scheduling schemes.

Table 2. Comparison of scheduling results for different schemes.

Scheme	Economic Cost(10k Yuan)	Carbon Emission(ton)	Peak-Valley Diff(kW)
Scheme 1	1.44	6.88	1225.01
Scheme 2	1.76	6.65	997.12
Scheme 3	1.51	4.78	1077.67

In terms of economic performance, S1, serving as the single-objective economic benchmark, achieves the lowest cost (14,400 Yuan). After coordinating multiple objectives, S3 yields a cost of 15,100 Yuan, which is only 4.86% higher than that of S1, indicating that multi-objective optimization does not significantly compromise economic performance. S2 exhibits the poorest economic performance due to its rigid strategy, highlighting the value of intelligent optimization algorithms.

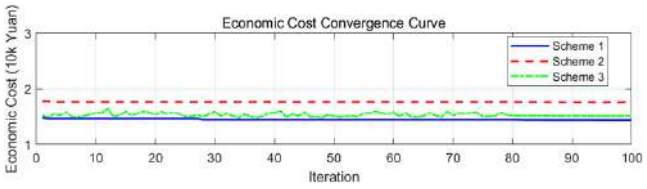

Fig. 5. Convergence curve of economic cost.

In terms of environmental performance, the carbon emissions of S3 (4.78 tons) are significantly lower than those of S1 and S2, achieving reductions of 30.52% and 28.12%, respectively. This indicates that the proposed strategy effectively promotes the integration of clean energy and reduces reliance on carbon-intensive energy sources by optimizing the output of the gas turbine and the charging/discharging schedule of the energy storage system.

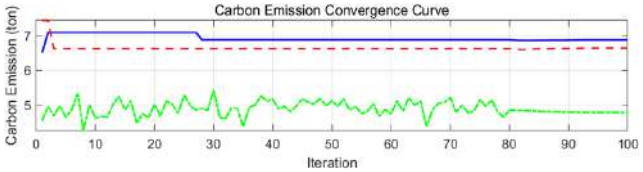

Fig. 6. Convergence curve of carbon emissions.

In terms of grid friendliness, the peak-valley load difference of S3 (1077.67 kW) is better than that of S1, which pursues economic performance alone, verifying its effectiveness in smoothing load fluctuations. Although it is slightly higher than that of S2, which adopts a fixed valley-filling strategy, this is a reasonable result of the Pareto trade-

off among the three objectives—economic performance, environmental performance, and stability—in S3.

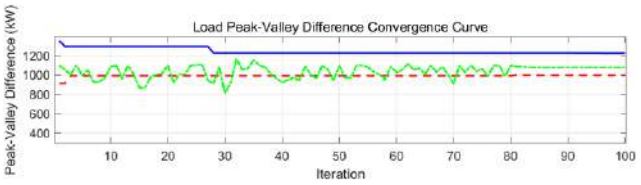

Fig. 7. Convergence curve of peak-valley load difference.

Scheme S3 simultaneously achieves a 30.52% reduction in carbon emissions and a 12.03% improvement in load curve smoothness at the cost of only a marginal 4.86% increase in economic cost, which fully demonstrates the significant advantages of the proposed multi-objective coordinated scheduling strategy in enhancing the comprehensive operational efficiency of virtual power plants.

4.3.2 Pareto Front and Scheduling Plan Analysis

Fig. 8 illustrates the three-dimensional distribution of the Pareto optimal solution set obtained by S3 in the objective space, along with its two-dimensional projections. It can be observed that the solution set is uniformly distributed, and there is a clear trade-off relationship among the three objectives (i.e., a reduction in economic cost is often accompanied by an increase in carbon emissions or load fluctuations). Decision-makers can flexibly select the final scheduling solution from this frontier based on actual policy or business preferences.

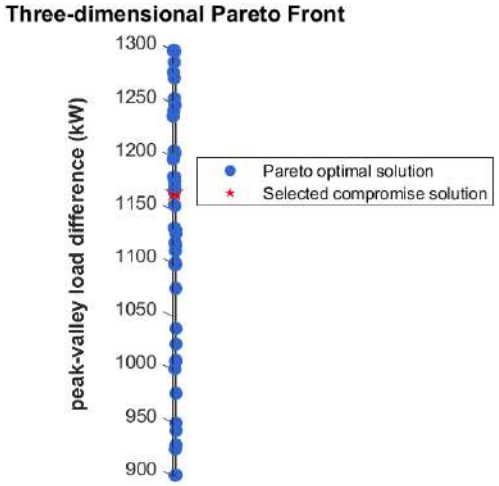

Fig. 8. Two-dimensional projections of the three-dimensional Pareto front.

In the detailed scheduling plan of Scheme S3 for a typical day, it can be observed that during the midday period when photovoltaic output is high, the energy storage system charges to absorb excess power while reducing electricity sales to the grid, thereby improving the self-consumption rate. During the evening peak load period when photovoltaic output drops to zero, the energy storage system and the gas turbine discharge in coordination, effectively supporting load demand and avoiding a sharp rise in the net load curve. Demand response mainly reduces load during peak-price periods, achieving synergy between peak shaving, valley filling, and economic incentives. This scheduling plan clearly reflects the intelligent coordinated interaction mechanism of source–storage–load–grid multiple resources driven by multi-objective optimization.

4.3.3 Algorithm Performance Comparison and Analysis

To validate the search performance of the DOA-NSGAII hybrid algorithm, it was compared with the classical multi-objective algorithms NSGA-II and MOEA/D under the same problem settings. Hypervolume (HV) and inverted generational distance (IGD) were adopted as evaluation metrics, and the statistical results after 30 independent runs are presented in Table 3.

Table 3. Performance comparison of different multi-objective algorithms (mean ± standard deviation)

Algorithm	Hypervolume (HV)	Inverted Generational Distance (IGD)	Runtime (s)
NSGA-II	0.712 ±0.021	0.085 ± 0.006	45.2
MOEA/D	0.698 ±0.025	0.091 ± 0.008	52.7
DOA-NSGAII	0.769 ±0.018	0.061 ± 0.005	58.3

The DOA-NSGAII algorithm proposed in this paper significantly outperforms the compared algorithms in terms of both HV and IGD metrics (a larger HV and a smaller IGD indicate higher solution set quality), demonstrating that the "dream exploration" and "memory consolidation" mechanisms of DOA effectively enhance the algorithm's global search capability and its ability to escape local optima, thereby enabling the discovery of Pareto solution sets with higher quality and better distribution. Although the runtime is slightly increased, the improvement in solution quality is substantial.

V. CONCLUSION

This study constructs a virtual power plant (VPP) model incorporating wind power, photovoltaics, gas turbines, energy storage systems, and price-based demand response, and proposes a hybrid intelligent solution strategy based on an improved Dream Optimization Algorithm (DOA) and the NSGA-II framework to address the multi-objective coordinated scheduling problem. Through

rigorous mathematical modeling, algorithm design, and simulation analysis, an efficient hybrid solution framework suitable for complex VPP optimization is developed. This study innovatively integrates the global search mechanism of the novel metaheuristic algorithm—the Dream Optimization Algorithm (DOA)—with the elitist selection strategy of the well-established multi-objective evolutionary algorithm NSGA-II, forming the DOA-NSGAII hybrid optimizer. This framework effectively addresses the challenges posed by the high-dimensional decision space, complex constraint coupling, and conflicting objectives in VPP scheduling. The resulting Pareto optimal solution set exhibits strong convergence and distribution performance, providing a reliable set of solutions for multi-criteria decision-making.

The validity and advantages of the Dream Optimization Algorithm in engineering optimization problems are verified. By simulating bio-inspired mechanisms such as "group-based memory," "selective forgetting," and "cross-individual information sharing," the algorithm demonstrates an excellent balance between global exploration and local exploitation when solving nonlinear, multi-peak scheduling models. Its integration with NSGA-II allows the search process to be guided by Pareto dominance, thereby systematically approaching the true Pareto front rather than becoming trapped in single-objective local optima.

The significant value of multi-objective coordinated scheduling in enhancing the comprehensive performance of VPPs is empirically demonstrated. Simulation results show that compared with the single-objective economic optimization scheme (Scheme S1), the proposed multi-objective optimization scheme (Scheme S3) achieves substantial gains-reducing carbon emissions by 30.5% and narrowing the peak-valley load difference by 12.0%—at the cost of only a marginal 4.9% increase in economic cost. This result quantitatively proves that intelligent coordinated optimization can effectively reconcile the inherent conflicts among economic efficiency, environmental performance, and system stability in VPP operation, achieving a Pareto improvement in overall operational effectiveness.

This study systematically elaborates the complete workflow for adapting the DOA algorithm to a specific engineering optimization problem, including decision variable encoding, hybrid constraint handling (equality constraint repair and penalty function method), and multi-objective integration. This provides a reproducible paradigm for the application of metaheuristic algorithms to similar complex system optimization problems.

ACKNOWLEDGEMENTS

This work was supported by the Research Funding of GDUPT, Research on Heat Transfer Enhancement of Heat Sink by Inverse Calculation Design Method (No. 2019rc074).

REFERENCES

[1] Qiu, Z., Zhang, X., Han, Z., Chen, F., Luo, Y., & Zhang, K. (2024). Power allocation optimization strategy for multiple virtual power plants with diversified distributed flexibility resources. *IET Renewable Power Generation*, 18(16), 4034–4046.

[2] Yao, L., Zhao, K., Shen, J., Xu, L., & Shen, L. (2026). Coordinated capacity configuration method for distributed resources of virtual power plants considering time-varying power coupling. *Energies*, 19(3), 614.

[3] Masiello, A., Borden, T., Buechler, N., Chassin, D., Giri, J., Hines, P., Kalsi, K., Lian, J., Liu, G., Mather, B., McJunkin, T., O'Brien, J., Palmintier, B., Pradhan, A., Rikos, E., & Vyakaranam, B. (2025). Deployment of virtual power plants for electrification enablement: Increasing hosting capacity to support electrification. *IEEE Electrification Magazine*, 13(1), 84–89.

[4] Othman, M. M., El-Khattam, W., & Hegazy, Y. G. (2023). Optimal siting and sizing of distributed generation in distribution networks considering hosting capacity. *International Journal of Electrical Power & Energy Systems*, 147, 108835.

[5] Pirouzi, A., & Aghaei, J. (2025). Risk-averse energy management of a water-heat-power virtual energy hub considering hosting capacity and Volt-VAR control of distribution network. *Energy*, 318, 134949.

[6] Ismael, S. M., Abdel Aleem, S. H. E., Abdelaziz, A. Y., & Zobaa, A. F. (2024). Review on hosting capacity of distributed energy resources: Analysis of the state of the art and future challenges. *Renewable and Sustainable Energy Reviews*, 189, 113908.

[7] Molina-Garcia, A., Mastromauro, R. A., Garcia-Sanchez, T., Pizzi, M., & Stasi, S. (2022). Distributed energy resources integration: A review of hosting capacity assessment methodologies. *IEEE Access*, 10, 124456–124481.

[8] Yang, Y., & Xu, Q. (2024). Optimal capacity allocation of energy storage in virtual power plants considering dynamic time-of-use pricing and conditional value-at-risk. *Journal of Energy Storage*, 82, 110518.

[9] Hosseini, E., Al-Ghaili, A. M., Kadir, D. H., Othman, M., & Yusof, R. (2024). Meta-heuristics and deep learning for energy applications: Review and open research challenges (2018–2023). *Energy Strategy Reviews*, 53, 101409.

[10] Lang, Y., & Gao, Y. (2025). Dream optimization algorithm (DOA): A novel metaheuristic optimization algorithm inspired by human dreams and its applications to real-world engineering problems. *Computer Methods in Applied Mechanics and Engineering*, 436, 117718.

International Journal of Advanced Engineering Research and Science (IJAERS)
Peer-Reviewed Journal
ISSN: 2349-6495(P) | 2456-1908(O)
Vol-13, Issue-4; Apr, 2026
Journal Home Page Available: https://ijaers.com/
Article DOI: https://dx.doi.org/10.22161/ijaers.134.4

Analysis of Wave Constants in the Laplace Equation Solution for Deep Water with Wave Amplitude or Wave Energy as Input

Syawaluddin Hutahaean

Ocean Engineering Program, Faculty of Civil and Environmental Engineering-Bandung Institute of Technology (ITB), Bandung 40132, Indonesia.
syawalf1@yahoo.co.id

Received: 23 Feb 2026,

Received in revised form: 25 Mar 2026,

Accepted: 02 Apr 2026,

Available online: 06 Apr 2026

***Keywords*— wave constants, wave number, wave constant G, wave period**

***Abstract*—** *In the velocity potential solution of the Laplace equation obtained using the separation of variables method, three wave constants arise: wavelength, wave period, and the wave constant G. The wave constant G represents the rate of wave energy transmission. Unlike these constants, wave amplitude is not part of the solution constants but serves as an input parameter. Therefore, the wave constants should be expressed as functions of the wave amplitude. This study derives analytical expressions for wavelength, wave constant G, and wave period in deep water with wave amplitude as the governing variable. The relationship between wavelength and wave amplitude is obtained using the Kinematic Free Surface Boundary Condition. The relationship between wave constant G and wave amplitude is derived from a modified Euler momentum conservation equation together with a wave amplitude function, which relates the three wave constants to the wave amplitude. The wave period is then determined using the equations for wave constant G and the wave amplitude function. After establishing the wave constants as functions of wave amplitude, the study further formulates wave amplitude as a function of wave energy. The resulting amplitude is then used to calculate the three wave constants. This approach can also be applied to analyze waves generated by ship motion, where the input energy corresponds to the ship's kinetic energy. The method is further extended to long waves, particularly tsunamis and sneaker waves.*

I. INTRODUCTION

The velocity potential solution of the Laplace equation obtained through the separation of variables method, as presented by Dean (1991), contains three wave constants. To apply this solution in subsequent wave analysis, the values of these constants must first be determined.

Within linear wave theory, Dean (1991) derived expressions for the wave constants using wave amplitude and wave period as input parameters. In this formulation, wave amplitude and wave period are treated as independent variables, implying that no inherent relationship exists between them.

However, several earlier studies have indicated a relationship between wave height and wave period. For instance, Robert L. Wiegel (1949, 1964) developed an empirical relationship between wave height and wave period for deep-water waves. Later, Willard J. Pierson Jr. and Lionel Moskowitz (1962) introduced the Pierson–

Moskowitz spectrum, which describes the distribution of wave energy with respect to wave period. Based on this spectrum, Robert Silvester (1974) subsequently formulated an equation relating wave period to wave height.

More recently, Hutahaean (2024) applied the kinematic free surface boundary condition to derive a wave amplitude function equation that relates wave amplitude to the three wave constants. By combining this function with the Euler equations for momentum conservation while neglecting convective acceleration, a relationship between wave period and wave amplitude was obtained.

These previous studies suggest that wave period should, in principle, be a function of wave amplitude. Accordingly, one of the primary objectives of the present study is to derive a relationship between wave period and wave amplitude based on the velocity potential equation.

Once the wave constants are expressed as functions of wave amplitude, the analysis can be extended to incorporate wave energy as the input parameter. In this framework, wave amplitude is first determined from the given wave energy, and the resulting amplitude is then used to calculate the corresponding wave constants.

II. WEIGHTED TAYLOR SERIES AND WEIGHTING COEFFICIENT.

A truncated Taylor series refers to a Taylor expansion that is retained only up to the first-order terms. This formulation constitutes the fundamental basis for the derivation of the governing equations in hydrodynamics. In this study, a weighted Taylor series is employed, which modifies the truncated Taylor series by introducing coefficients to the first-order terms to compensate for the omission of higher-order terms. Following Hutahaean (2025a), these coefficients are referred to as weighting coefficients.

For a function $f = f(x,t)$, where x denotes the horizontal coordinate and t represents time, the weighted Taylor series can be expressed as

$$f(x+\delta x, t+\delta t) = f(x,t) + \gamma_{t,2}\delta t\frac{\mathrm{d}f}{\mathrm{d}t} + \gamma_{x,2}\delta x\frac{\mathrm{d}f}{\mathrm{d}x} \quad \dots(1)$$

where $\gamma_{t,2}$ and $\gamma_{x,2}$ are weighting coefficients. Their baseline values are $\gamma_{t,2} = 2.0$ and $\gamma_{x,2} = 1.0$. In this study, the values $\gamma_{t,2} = 1.998933$ and $\gamma_{x,2} = 0.998933$ are adopted.

For a function $f = f(x,z,t)$, where x denotes the horizontal coordinate, z the vertical coordinate, and t time, the weighted Taylor series becomes

$$f(x+\delta x, z+\delta z, t+\delta t) = f(x,z,t) + \gamma_{t,3}\delta t\frac{\mathrm{d}f}{\mathrm{d}t} + \gamma_{x,3}\delta x\frac{\mathrm{d}f}{\mathrm{d}x} + \gamma_{z,3}\delta z\frac{\mathrm{d}f}{\mathrm{d}z} \quad \dots(2)$$

$\gamma_{t,3}$, $\gamma_{x,3}$and $\gamma_{z,3}$ are weighting coefficients. Their baseline values are $\gamma_{t,3} = 3.0$, $\gamma_{x,3} = 2.0$ and $\gamma_{z,3} = 2.0$. In the present study, the values $\gamma_{t,3} = 3.098667$ and $\gamma_{x,3} = \gamma_{z,3} = 2.098667$.

The procedure for calculating these weighting coefficients is described in Hutahaean (2025a).

III. VELOCITY POTENTIAL EQUATION.

The velocity potential equation, obtained as a solution of the Laplace's Equation using the separation of variables method, as presented by Robert G. Dean (1991) is

$$\phi(x,z,t) = G\,(\cos kx + \sin kx)\cosh k(h+z)\sin\sigma t \quad \dots(3)$$

At the characteristic point, where $\cos kx = \sin kx$, this equation reduces to,

$$\phi(x,z,t) = 2G\cos kx\cosh k(h+z)\sin\sigma t \quad \dots(4)$$

In equations (3) and (4), $\phi(x,z,t)$ denotes the velocity potential, G, k and σ are wave constants. G represents the rate of energy transmission, k is the wave number defined as $k = \frac{2\pi}{L}$, L is the wavelength, σ is angular frequency, $\sigma = \frac{2\pi}{T}$, T is wave period, h is water depth.

Along the axis-x, the complete velocity potential in Eq. (3) consists of two functions $\cos kx$ *and* $\sin kx$. These functions attain equal values when $\cos kx = \sin kx = \frac{1}{2}\sqrt{2}$ (see Figure 1). The calculation of wave constants, such as the wave number k is performed at this point, where the equality holds for both functions. This point is therefore referred to as the characteristic point.

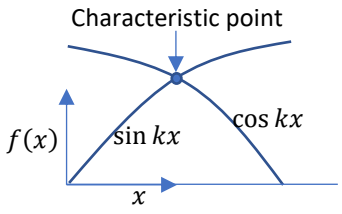

Fig (1). Characteristic point.

Along the time axis-t, Equation (3) contains the term $\sin\sigma t$. In subsequent derivations, expressions may involve both $\sin\sigma t$ and $\cos\sigma t$, or require the evaluation of one or both of these functions. For this reason, the calculations are

carried out at the temporal characteristic point where $\sin \sigma t = \cos \sigma t = \frac{1}{2}\sqrt{2}$.

IV. RELATIONSHIP BETWEEN WAVE NUMBER AND WAVE AMPLITUDE

4.1. Review of the Wave Energy Equation

The total energy contained within one wavelength, according to Robert G. Dean (1991), is expressed as,

$$E = \frac{1}{8}\rho g H^2 L \qquad \dots (5)$$

ρ is the water density, g is the gravitational acceleration, H is the wave height. For a sinusoidal wave $H = 2A$, A is wave amplitude, $L = \frac{2\pi}{k}$ is wavelength and k is wave number.

Equation (5) is written as,

$$E = \rho g \pi \left(\frac{A^2}{k}\right)$$

From the equation, for a given total energy E,

$$\frac{A^2}{k} = constant$$

This relation indicates an interdependence between the wave number k and A. A larger wave amplitude corresponds to a larger wave number k and therefore a shorter wavelength. Conversely, a smaller wave number (i.e., a longer wavelength) corresponds to a smaller wave amplitude.

Consequently, for a given input wave amplitude A, multiple wave configurations may arise. For example, waves W-I, W-II or W-III. Where η_{max} denotes the crest elevation; then $\eta_{max-I} > \eta_{max-II} > \eta_{max-III}$, and $L_I < L_{II} < L_{III}$, (See Figure 2).

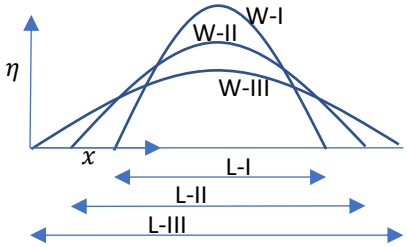

Fig (2). Possible wave profiles from wave input amplitude A.

4.2. Formulation of the Relationship Between k and A Using the Kinematic Free Surface Boundary Condition

Hutahaean (2023) formulated an equation relating the wave amplitude to the three wave constants. This equation is referred to as the wave amplitude function.

The formulation of the wave amplitude function employs the kinematic free surface boundary condition. By applying the weighted Taylor series formulation in Eq. (1), the Kinematic Free Surface Boundary Condition can be written as

$$w_\eta = \gamma_{t,2}\frac{\partial \eta}{\partial t} + \gamma_{x,2} u_\eta \frac{\partial \eta}{\partial x}$$

w is the vertical water particle velocity along the vertical axis-z, u s the horizontal water particle velocity along the horizontal x axis, w_η is the surface vertical water particle velocity and u_η is surface horizontal water particle velocity, $\eta = \eta(x,t)$ is water surface elevation.

Rearranging the equation yields the water surface elevation equation,

$$\gamma_{t,2}\frac{\partial \eta}{\partial t} = w_\eta - \gamma_{x,2} u_\eta \frac{\partial \eta}{\partial x} \qquad \dots (6)$$

a. Wave Amplitude Function Type I

Using equation (3),

$$u(x,z,t) = -\frac{\partial \phi}{\partial x} = -Gk(-\sin kx + \cos kx) \cosh k(h+z) \sin \sigma t$$

$$u(x,\eta,t) = u_\eta(x,t) = -Gk(-\sin kx + \cos kx) \cosh k(h+\eta) \sin \sigma t \qquad \dots (7)$$

$$w(x,z,t) = -\frac{\partial \phi}{\partial z} = -Gk(\cos kx + \sin kx) \sinh k(h+z) \sin \sigma t$$

$$w(x,\eta,t) = w_\eta(x,t) = -Gk(\cos kx + \sin kx) \sinh k(h+\eta) \sin \sigma t \qquad \dots (8)$$

Substituting (7) and (8) to (6), to be integrated to time t,

$$\eta(x,t) = -\frac{2Gk}{\gamma_{t,2}}(\cos kx + \sin kx) \int \sinh k(h+\eta) \sin \sigma t \, dt + \frac{\gamma_{x,2} 2Gk}{\gamma_{t,2}}(-\sin kx + \cos kx) \int \cosh k(h+\eta) \sin \sigma t \frac{\partial \eta}{\partial x} dt$$

$k(h+\eta) = kh\left(1 + \frac{\eta}{h}\right)$, at deep water where $\frac{\eta}{h} \ll 1$, thus the fluctuation of $\frac{\eta}{h}$ towards time t is very small, that value $\frac{\eta}{h}$ is considered constant. Hence, $\sinh k(h+\eta)$ can be exempted from the integral. Meanwhile, the fluctuation

$\cosh kh\left(1+\frac{\eta}{h}\right)\frac{\partial\eta}{\partial x}$ towards time t becomes significantly smaller and it can be exempted from the integral. Under these approximations, the integration reduces to the time integration of $\sin\sigma t$ alone.

$$\eta(x,t)=\frac{Gk}{\gamma_{t,2}\sigma}(\cos kx+\sin kx)\sinh k(h+\eta)\cos\sigma t-\frac{\gamma_{x,2}Gk}{\gamma_{t,2}\sigma}(-\sin kx+\cos kx)\cosh k(h+\eta)\cos\sigma t\frac{\partial\eta}{\partial x} \quad \dots(9)$$

η reaches the maximum value if $\frac{\partial\eta}{\partial x}=0$ and $\cos\sigma t=1$.

$$\eta_{max}=\frac{Gk}{\gamma_{t,2}\sigma}(\cos kx+\sin kx)\sinh k(h+\eta_{max})$$

$(\cos kx+\sin kx)$ reaches the maximum value if $\cos kx=\sin kx=\frac{1}{2}\sqrt{2}$.

$$\eta_{max}=\frac{\sqrt{2}Gk}{\gamma_{t,2}\sigma}\sinh k(h+\eta_{max}) \quad \dots(10)$$

At this stage, the value of η_{max} still depends on the term $\sinh k(h+\eta_{max})$ and, in particular, on the wave number k. Depending on the wavelength formed, for a given input wave amplitude A, a wave may be generated with

$\eta_{max}=\alpha_\eta A$, where $0<\alpha_\eta<1$.

$$\alpha_\eta A=\frac{\sqrt{2}Gk}{\gamma_{t,2}\sigma}\sinh k\left(h+\alpha_\eta A\right)$$

Or

$$A=\frac{\sqrt{2}Gk}{\alpha_\eta\gamma_{t,2}\sigma}\sinh k\left(h+\alpha_\eta A\right) \quad \dots(11)$$

Equation (11) is referred to as the wave amplitude function Type I.

b. Wave Amplitude Function Type II.

In this section, the formulation is performed at the characteristic point, where $\cos kx=\sin kx$ .Using the velocity potential in equation (4).

$$u(x,z,t)=-\frac{\partial\phi}{\partial x}=2Gk\sin kx\cosh k(h+z)\sin\sigma t$$

$$u(x,\eta,t)=u_\eta(x,t)=2Gk\sin kx\cosh k(h+\eta)\sin\sigma t \quad \dots(12)$$

$$w(x,z,t)=-\frac{\partial\phi}{\partial z}=-2Gk\cos kx\sinh k(h+z)\sin\sigma t$$

$$w(x,\eta,t)=w_\eta(x,t)-2Gk\cos kx\sinh k(h+\eta)\sin\sigma t \quad \dots(13)$$

Substituting Equations (12) and (13) into Eq. (6), and integrating with respect to time t using the same procedure as in the previous section, while evaluating the expression at the characteristic point, yields

$$\eta(x,t)=\frac{2Gk}{\gamma_{t,2}\sigma}\cosh k(h+\eta)\left(\tanh k(h+\eta)+\gamma_{x,2}\frac{\partial\eta}{\partial x}\right)\cos kx\cos\sigma t$$

Since this expression represents a periodic wave, hence

$$\frac{2Gk}{\gamma_{t,2}\sigma}\cosh k(h+\eta)\left(\tanh k(h+\eta)+\gamma_{x,2}\frac{\partial\eta}{\partial x}\right)=constant$$

For a given input wave amplitude A, a periodic wave profile can be written as

$$\eta(x,t)=\alpha_\eta A\cos kx\cos\sigma t \quad \dots(14)$$

$$\frac{\partial\eta}{\partial x}=-\alpha_\eta kA\sin kx\cos\sigma t$$

At the characteristic point,

$$\frac{\partial\eta}{\partial x}=-\frac{\alpha_\eta kA}{2}$$

Thus

$$A=\frac{2Gk}{\alpha_\eta\gamma_{t,2}\sigma}\cosh k\left(h+\alpha_\eta A\right)\left(\tanh k\left(h+\alpha_\eta A\right)-\frac{\gamma_{x,2}\alpha_\eta kA}{2}\right) \quad \dots(15)$$

Equation (15) is referred to as the wave amplitude function Type II. A breaking-wave condition emerges from this equation when

$$\tanh k\left(h+\alpha_\eta A\right)-\frac{\gamma_{x,2}\alpha_\eta kA}{2}=0$$

Or,

$$\frac{H_b}{L_b}=\frac{2\tanh k\left(h+\alpha_\eta A\right)}{\gamma_{x,2}\alpha_\eta\pi}$$

or

$$\frac{H_b}{L_b}=\frac{2\tanh\theta\pi}{\gamma_{x,2}\alpha_\eta\pi} \quad \dots(16)$$

The relationship between $k\left(h+\alpha_\eta A\right)$ and $\theta\pi$ is expressed in the following section.

c. Wave number equations

Wave amplitude at equation (11) should be the same as the wave amplitude at equation (15).

$$\frac{\sqrt{2}Gk}{\alpha_\eta\gamma_{t,2}\sigma}\sinh k\left(h+\alpha_\eta A\right)=\frac{2Gk}{\alpha_\eta\gamma_{t,2}\sigma}$$

$$\cosh k(h+\alpha_\eta A)\left(\tanh k(h+\alpha_\eta A)-\frac{\gamma_{x,2}\alpha_\eta kA}{2}\right)$$

$$k=\frac{(2-\sqrt{2})}{\gamma_{x,2}\alpha_\eta A}\tanh k(h+\alpha_\eta A) \quad \dots(17)$$

At deep water, $\tanh k(h+\alpha_\eta A)\approx 1.0$. Where (Hutahaean (2023)),

$$k(h+\alpha_\eta A)=\theta\pi \quad \dots(18)$$

This (17) becomes

$$k_0=\frac{(2-\sqrt{2})}{\gamma_{x,2}\alpha_\eta A_0}\tanh\theta\pi \quad \dots(19)$$

The subscript 0 in k_0 and A_0 indicates that these quantities correspond to deep-water conditions. The parameter θ is referred to as the deep-water coefficient. For short waves, the approximation $\tanh\theta\pi\approx 1.0$ is commonly used.

As long as $\tanh\theta\pi\approx 1.0$, the calculated wave number is not highly sensitive to the value of θ. For example, the wave number obtained using $\theta=1.5$, for which $\tanh 1.5\pi=0.999839$ is very close to the value obtained using $\theta=3.0$, where $\tanh 3\pi=1.0$.

V. THE RELATIONSHIP BETWEEN WAVE CONSTANT *G* AND WAVE PERIOD AND WAVE AMPLITUDE.

The relationship between the wave constant G and the wave amplitude is formulated using the modified two-dimensional Euler momentum conservation equations proposed by Hutahaean (2025b), neglecting energy dissipation. The formulation consists of two governing equations.

The force balance in the horizontal $\boldsymbol{x}$ direction is

$$\gamma_{t,3}\frac{\partial u}{\partial t}-\frac{\gamma_{x,3}}{2}\frac{\partial uu}{\partial x}=-\frac{1}{\rho}\frac{\partial p}{\partial x} \quad \dots(20)$$

The force balance in the vertical-z is

$$\gamma_{t,3}\frac{\partial w}{\partial t}-\frac{\gamma_{z,3}}{2}\frac{\partial ww}{\partial z}=-\frac{1}{\rho}\frac{\partial p}{\partial z}-g \quad \dots(21)$$

u is horizontal water particle velocity, w is vertical water particle velocity, p is pressure to water particles, ρ is water mass density, and $\gamma_{t,3}$, $\gamma_{x,3}$ and $\gamma_{z,3}$ are weighting coefficients.

Equation (21) is first rearranged to obtain an expression for the pressure p. The resulting equation is then integrated along the vertical z axis while applying the dynamic free surface boundary condition, $p_\eta=0$. Subsequently, the resulting expression is differentiated with respect to the horizontal coordinate x,

$$\frac{1}{\rho}\frac{\partial p}{\partial x}=\gamma_{t,3}\frac{\partial}{\partial x}\int_z^\eta\frac{\partial w}{\partial t}dz-\frac{\gamma_{z,3}}{2}\frac{\partial}{\partial x}(w_\eta w_\eta-ww)+g\frac{\partial\eta}{\partial x}$$

The integration of the first term on the right-hand side is performed using the velocity potential formulation. From the velocity potential, the vertical velocity derivative with respect to time is,

$$\frac{\partial w}{\partial t}=-2Gk\sigma\cos kx\sinh k(h+z)\cos\sigma t$$

$$\int_z^\eta\frac{\partial w}{\partial t}\,dz=-2G\sigma\cos kx\,(\cosh k(h+\eta)-\cosh k(h+z))\cos\sigma t$$

$$\frac{\partial}{\partial x}\int_z^\eta\frac{\partial w}{\partial t}\,dz=2Gk\sigma\sin kx\,(\cosh k(h+\eta)-\cosh k(h+z))\cos\sigma t$$

Since,

$$u=2Gk\sin kx\cosh k(h+z)\sin\sigma t \quad \dots(22)$$

$$\frac{\partial u}{\partial t}=2Gk\sigma\sin kx\cosh k(h+z)\cos\sigma t \quad \dots(23)$$

Thus,

$$\frac{\partial}{\partial x}\int_z^\eta\frac{\partial w}{\partial t}\,dz=\left(\frac{\partial u_\eta}{\partial t}-\frac{\partial u}{\partial t}\right)$$

Thus

$$\frac{1}{\rho}\frac{\partial p}{\partial x}=\gamma_{t,3}\left(\frac{\partial u_\eta}{\partial t}-\frac{\partial u}{\partial t}\right)-\frac{\gamma_{z,3}}{2}\frac{\partial}{\partial x}(w_\eta w_\eta-ww)+g\frac{\partial\eta}{\partial x}$$

Substituted to (20), yields

$$\gamma_{t,3}\frac{\partial u}{\partial t}-\frac{\gamma_{x,3}}{2}\frac{\partial uu}{\partial x}=-\gamma_{t,3}\left(\frac{\partial u_\eta}{\partial t}-\frac{\partial u}{\partial t}\right)+\frac{\gamma_{z,3}}{2}\frac{\partial}{\partial x}(w_\eta w_\eta-ww)-g\frac{\partial\eta}{\partial x}$$

Identical terms cancel, yielding,

$$\gamma_{t,3}\frac{\partial u_\eta}{\partial t}-\frac{\gamma_{x,3}}{2}\frac{\partial uu}{\partial x}=\frac{\gamma_{z,3}}{2}\frac{\partial}{\partial x}(w_\eta w_\eta-ww)-g\frac{\partial\eta}{\partial x}$$

With $z=\eta$,

$$\gamma_{t,3}\frac{\partial u_\eta}{\partial t}-\frac{\gamma_{x,3}}{2}\frac{\partial u_\eta u_\eta}{\partial x}=-g\frac{\partial\eta}{\partial x} \quad \dots(24)$$

Equations (22) and (23) are then evaluated at $z=\eta$. Using the free-surface elevation given by Eq. (14), and substituting these expressions into Eq. (24), the relation evaluated at the characteristic point becomes

$$\gamma_{t,3}2G\sigma\cosh\theta\pi-2\gamma_{x,3}G^2k^2\cosh^2\theta\pi=g\alpha_\eta A$$

Equation (11) can be rewritten as,

$$\sigma=\frac{\sqrt{2}Gk}{\alpha_\eta\gamma_{t,2}A}\sinh\theta\pi \quad \dots(25)$$

Substituting it to equation (24)

$$\gamma_{t,3} 2G \frac{\sqrt{2}Gk}{\alpha_c \gamma_{t,2} A} \sinh \theta\pi \cosh \theta\pi - 2\gamma_{x,3} G^2 k^2 \cosh^2 \theta\pi = g\alpha_\eta A$$

$$\left(\gamma_{t,3} \frac{\sqrt{2}k_0}{\alpha_c \gamma_{t,2} A_0} \sinh \theta\pi \cosh \theta\pi - \gamma_{x,3} k_0^2 \cosh^2 \theta\pi\right) G_0^2 = \frac{g\alpha_\eta A_0}{2} \quad \ldots (26)$$

Substituting equation (19) to k,

$$\left(\frac{\gamma_{t,3}\sqrt{2}}{\gamma_{t,2}\gamma_{x,2}} - \frac{\gamma_{x,3}(2-\sqrt{2})}{\gamma_{x,2}^2}\right) G_0^2 = \frac{g\alpha_\eta^3 A_0^3}{2(2-\sqrt{2}) \sinh^2 \theta\pi} \quad \ldots (27)$$

Index 0 shows the variable at deep water,This equation calculates G_0, and σ is calculated using equation (25).

VI. DETERMINING THE α_η VALUE

The analysis is performed using the water surface elevation equation (9) by computing the maximum elevation η_{max} and minimum elevation η_{min}. The appropriate value of α_η is obtained when $\eta_{max} - \eta_{min} = 2\,A_0$.

α_η value is obtained through the following steps.

a. Setting $\theta = 2.0$, or greater, where $\tanh \theta\pi \approx 1.0$, and $\cos \sigma t = 1$.

b. Setting $\alpha_\eta = 1.0$

c. Using the input wave amplitude A_0, k_0 is calculated using equation (19), G_0 is calculated using equation (27) and σ is calculated using equation (25).

d. Calculating the water depth $h = \frac{\theta\pi}{k_0} - \alpha_\eta A_0$

e. For $x = 0.625L - 2.0L$, η is calculated, and η_{max} and η_{min} are determined

$$\eta_0 = \alpha_\eta A_0 (\cos k_0 x + \sin k_0 x)$$

$$\frac{\partial \eta}{\partial x} = \alpha_\eta k_0 A_0 (-\sin k_0 x + \cos k_0 x)$$

$$\eta(x,t) = \frac{G_0 k_0}{\gamma_{t,2}\sigma} (\cos k_0 x + \sin k_0 x) \sinh k_0 (h + \eta_0) \cos \sigma t - \frac{\gamma_{x,2} G_0 k_0}{\gamma_{t,2}\sigma} (-\sin k_0 x + \cos k_0 x) \cosh k_0 (h + \eta_0) \cos \sigma t \frac{\partial \eta}{\partial x} \quad \ldots (9)$$

f. Checking, $\eta_{max} - \eta_{min}$,

- If $(\eta_{max} - \eta_{min}) < 2\,A_0$, α_η increases, repeat step c.
- If $(\eta_{max} - \eta_{min}) > 2\,A_0$, α_η decreases repeat step c.
- If $(\eta_{max} - \eta_{min}) \approx 2\,A_0$, the last α_η value is the α_η value being calculated.

This method yields $\alpha_\eta = 1.145011$. Figure (3) shows the results of the wave profile $\frac{\eta_{max}}{2A_0} = 0.7299$, where $A_0 = 1.20\,m$. In reference to Wilson's criteria (1963), this profile is cnoidal profile.

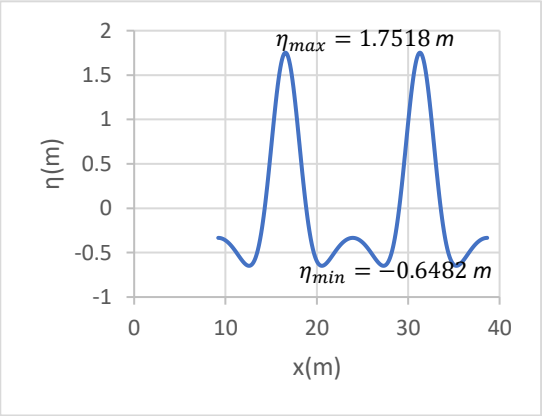

Fig (3) Resulting wave profile.

The corresponding wavelengths and wave periods for several wave amplitudes are presented in Table (1).

Table (1) Wavelength and Wave period for several wave amplitudes

$H = 2A$ (m)	L (m)	T (sec.)	$\frac{H}{L}$
1.2	7.367	4.247	0.163
1.6	9.823	4.904	0.163
2	12.278	5.482	0.163
2.4	14.734	6.006	0.163
2.8	17.19	6.487	0.163
3.2	19.646	6.935	0.163
3.6	22.101	7.355	0.163

Wave steepness obtained exceeds the critical wave steepness criteria proposed by Michell (1893), $\left(\frac{H}{L}\right)_{crit} = 0.142$, yet it is still smaller than the critical wave steepness criteria by Toffoli (2010), $\left(\frac{H}{L}\right)_{crit} = 0.170$.

Wiegel (1949, 1964) formulated the relationship between wave period and wave height as follows,

$$T_{Wieg} = 15.6\sqrt{\frac{H}{g}}\sec \quad \ldots(28)$$

Where wave height $H = 2A$ (in meter).

Using the Pierson–Moskowitz spectrum, Silvester (1974) formulated a relationship between the wave period and the wave height as

$$T_{Silv} = 2.43\sqrt{\frac{H}{0.3048}}\ sec. \quad \ldots(29)$$

Wave height H in meter.

A comparison with the formulations of Robert L. Wiegel and Silvester is presented in Table (2), Fig. (4), and Table (3). As shown in Table (2), the largest wave period corresponds to T_{Wieg}, followed by T_{silv}, while the smallest values correspond to the wave period T obtained from the equation developed in the present study. Nevertheless, all three formulations exhibit a similar distribution pattern with respect to wave height, as illustrated in Fig. (3). The difference relative to T_{Wieg} reaches 22.167%, while the difference relative to T_{Silv} reaches 11.925% (Table 3). It should be noted, however, that both T_{Wieg} and T_{Silv} represent maximum possible values. Consequently, the wave period that typically occurs in practice is likely to be smaller than these maximum estimates.

Table (2). The comparison to Wiegel and Silvester's Equations.

H (m)	T (sec.)	T_{Wieg} (sec)	T_{Silv} (sec)
1.2	4.247	5.456	4.822
1.6	4.904	6.3	5.567
2	5.482	7.044	6.225
2.4	6.006	7.716	6.819
2.8	6.487	8.334	7.365
3.2	6.935	8.91	7.874
3.6	7.355	9.45	8.351

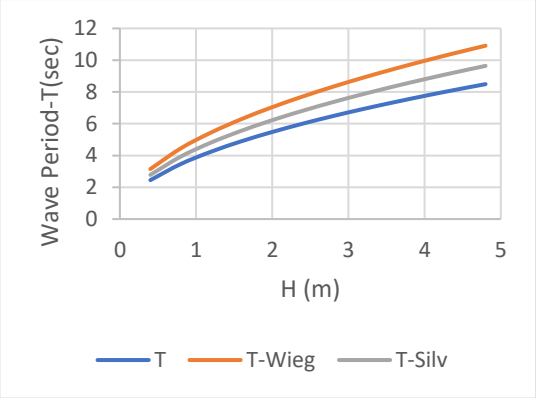

Fig (4) Wave period-T towards wave height H.

Table (3). Relative Differences from Wiegel and Silvester's Equations

H (m)	$\left\|\frac{T-T_{Wieg}}{T_{Wieg}}\right\| x100\%$	$\left\|\frac{T-T_{Silv}}{T_{Silv}}\right\| x100\%$
1.2	22.167	11.925
1.6	22.167	11.925
2	22.167	11.925
2.4	22.167	11.925
2.8	22.167	11.925
3.2	22.167	11.925
3.6	22.167	11.925

When adjustment is needed, for instance to T_{Wieg}, equation (19) is multiplied by $\alpha_k = 0.776163$, yielding equation (19) as,

$$k_0 = \frac{\alpha_k\left(2-\sqrt{2}\right)}{\gamma_{x,2}\alpha_\eta A_0}\tanh\theta\pi \quad \ldots(30)$$

The adjustment does not modify either α_η or wave profile. The results of the adjustments are presented in Table (4).

Table (4). Adjustment Using Wiegel's Equation.

H (m)	T (sec.)	T_{Wieg} (sec)	$\left\|\frac{T-T_{Wieg}}{T_{Wieg}}\right\| x100\%$
1.2	5.456	5.456	0
1.6	6.3	6.3	0
2	7.044	7.044	0
2.4	7.716	7.716	0
2.8	8.334	8.334	0
3.2	8.91	8.91	0
3.6	9.45	9.45	0

The adjustment increases the wavelength (Table 5).

Table (5). Wavelength at the adjusted wave period

$H = 2A$ (m)	L (m)	T (sec.)	$\frac{H}{L}$
1.2	9.492	5.456	0.126
1.6	12.656	6.3	0.126
2	15.819	7.044	0.126
2.4	18.983	7.716	0.126
2.8	22.147	8.334	0.126
3.2	25.311	8.91	0.126
3.6	28.475	9.45	0.126

With the revised wavelength, the resulting wave steepness becomes smaller than the critical wave steepness proposed by John Michell (1893).

Based on this result, the selection of the coefficient α_k can be determined by first specifying the most probable value of the wave steepness $\frac{H}{L}$. Once this representative steepness is established, the corresponding relationship between wave period and wave height can subsequently be derived.

VII. RELATIONSHIP BETWEEN WAVE AMPLITUDE AND WAVE ENERGY

6.1. Relationship between Wave Amplitude and Wave Energy.

The equation for wave energy over one wavelength (5) can be written as,

$$E = \rho g A^2 \frac{\pi}{k} \quad \ldots . (31)$$

Substituting k to (19),

$$k = \frac{(2-\sqrt{2})}{\gamma_{x,2}\alpha_\eta A}\tanh\theta\pi$$

$$E = \rho g \frac{\pi\gamma_{x,2}\alpha_\eta}{(2-\sqrt{2})\tanh\theta\pi}A^3$$

$$A_0 = \left(\frac{(2-\sqrt{2})\tanh\theta\pi\, E_0}{\rho g\pi\gamma_{x,2}\alpha_\eta}\right)^{1/3} \quad \ldots (32)$$

Once the wave amplitude A_0 is obtained, the wave number k_0 can be calculated using Equation (19), the wave constant G_0 can be determined using Equation (27), and the angular wave frequency σ can be obtained from Equation (25). An example of the calculation results is presented in Table (6).

Table (6). The results of A_0, L_0 and T calculations and input energy.

E_0 (m)	$H_0 = 2A_0$ (m)	L_0 (m)	T (sec)
10000	1.099	6.749	4.064
20000	1.385	8.503	4.562
30000	1.585	9.733	4.881
40000	1.745	10.713	5.121
50000	1.88	11.54	5.315
60000	1.997	12.263	5.479
70000	2.103	12.91	5.621
80000	2.199	13.497	5.748
90000	2.287	14.038	5.862
100000	2.368	14.54	5.966

This method allows for the extension of the wave height, wave number, and wave period calculations to waves generated by ship motion, where the wave energy is assumed to originate from the ship's kinetic energy. Assuming a no-slip condition between the water and the ship hull, the wave energy can be approximated by

$$E = \rho\frac{V^2}{2g}D$$

V is the ship velocity and D is the ship draft.

VIII. APPLICATION TO LONG WAVES.

In this context, long waves refer to tsunamis and sneaker waves, which are sometimes also referred to as mini-tsunamis.

In deep water, the influence of wave amplitude on wavelength is very small, while the dominant parameter is the water depth. In this case, deep water refers to the water depth at which the calculation begins or the depth at which the wave is initially generated.

The relationship between deep-water wavelength and deep-water depth for long waves can be expressed using the wave number conservation equation (18):

$$k_0(h_0 + \alpha_\eta A_0) = \theta\pi \quad \ldots (18)$$

k_0 is deep water wave number, h_0 is deep water depth, A_0 is deep water wave amplitude, θ is deep water coefficient at short wave, $\tanh\theta\pi \approx 1$ is used at the long wave. Whereas, $\tanh\theta\pi \approx \theta\pi$ at 5 % margin of error applies at $\theta = 0.124$. From (17), yielding

$$k_0 = \frac{\theta\pi}{h_0 + \alpha_\eta A_0} \quad \ldots (33)$$

Since $A_0 \ll h_0$, the final equation can be approached using the following equation

$$k_0 = \frac{\theta\pi}{h_0} \quad \ldots (34)$$

The deep-water wave number can therefore be calculated using either Equation (33) or Equation (34), while the constant G is determined using Equation (26). It should not be calculated using Equation (27), since the influence of θ becomes significant in the case of long waves. Subsequently, the wave period is calculated using Equation (25).

An example of calculation results using a deep-water wave amplitude of $A_0 = 0.50\ m$ for several values of deep-water depth h_0 is presented in Table (7).

For long waves, the coefficient $\alpha_\eta = 1.000399$ is used, resulting in a sinusoidal wave profile. Figure (5) illustrates the long-wave profile for $h_0 = 100.0\ m,\ A_0 = 0.50\ m$.

Table (7). Deep water wavelength to the corresponding wave period

h_0 (m)	L_0 (m)	T (sec.)
50	109.303	810.484
100	154.771	1616.94
150	189.634	2423.39
200	219.016	3229.84
250	244.898	4036.29
300	268.294	4842.74

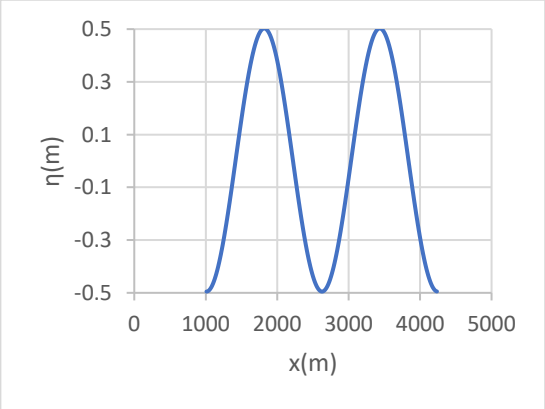

Fig (5). Longwave profile $A_0 = 0.50\ m, h_0 = 100.0\ m$

7.1. Calculation Using Input Energy.

Equation (28) can be rewritten as an expression for the wave amplitude:

$$A_0^2 = \frac{k_0}{\rho g \pi} E \quad \ldots (35)$$

where k_0 is calculated using Equation (34).

If a more accurate calculation is required, once A_0 has been obtained, the value of k_0 can be recalculated using Equation (33). Using this updated value of k_0, A_0 can then be recalculated accordingly. Subsequently, the wave period is determined using Equations (26) and (25).

Table (8) presents the calculation results for $E = 500000\ m$ at several values of deep-water depth h_0.

Table (8) Wave period and deep-water wave amplitude and wave length

h_0 (m)	A_0 (m)	T (sec)	L_0 (m)
100	0.502	154.867	1614.93
150	0.41	189.727	2421.01
200	0.355	219.104	3227.24
250	0.318	244.981	4033.54
300	0.29	268.373	4839.88
350	0.269	289.884	5646.25
400	0.251	309.904	6452.63
450	0.237	328.707	7259.02
500	0.225	346.491	8065.42

Table (9) presents the calculated deep-water wave amplitude, wavelength, and wave period at a deep-water depth of $h_0 = 100\ m$ for several values of input energy.

It can be observed that the wave period and wavelength remain nearly constant. This occurs because the resulting wave amplitude is very small compared with the water depth.

Table (9). Wave amplitude, wave period, and wavelength at $h_0 = 100\ m$.

E (m)	A_0 (m)	T (sec)	L_0 (m)
10000	0.071	154.95	1613.19
20000	0.101	154.945	1613.31
30000	0.123	154.94	1613.40
40000	0.142	154.937	1613.48
50000	0.159	154.933	1613.54
60000	0.174	154.93	1613.61
70000	0.188	154.928	1613.66
80000	0.201	154.925	1613.71
90000	0.213	154.923	1613.76
100000	0.225	154.921	1613.81

IX. CONCLUSION

The wave constant equations in this study were formulated analytically using conservation equations. Therefore, the resulting wave constants satisfy the fundamental conservation laws of hydrodynamics.

Some differences exist compared with empirical formulations, particularly in the relationship between wave amplitude (or wave height) and wave period. However, it should also be noted that the results obtained from empirical equations generally represent the maximum possible values that may occur.

In general, the wave constants obtained in this study provide reasonably good results and are sufficiently reliable for use in both wave dynamics analysis and engineering design of hydraulic or coastal structures.

REFERENCES

[1] Dean, R.G., Dalrymple, R.A. (1991). Water wave mechanics for engineers and scientists. Advance Series on Ocean Engineering.2. Singapore: World Scientific. ISBN 978-981-02-0420-4. OCLC 22907242.

[2] Wiegel,R.L. (1949). An Analysisis of Data from Wave Recorders on the Pacific Coast of tht United States, Trans.Am. Geophys. Union, Vol.30, pp.700-704.

[3] Wiegel,R.L. (1964). Oceanographical Engineering, Prentice-Hall, Englewoods Cliffs, N.J.

[4] Pierson, W.J. & Moskowitz, L. (1964). A Proposed Spectral Form for Fully Developed Wind Seas Based on the Similarity Theory of S.A. Kitaigorodskil. J. Geophys Res.69:5181-5190.

[5] Silvester, R. (1974). Coastal Engineering 1. Generation, propagation and Influence of Waves. Developments in Geotechnical Engineering Vol 4B. Department of Civil Engineering, University of Western Australia, Nedlands, W.A., Australia. Elsevier Scientific Publishing Company. Amsterdam London New York 1974.

[6] Hutahaean, S. (2024). The Relationshio between Wave Period, Deep Water Wave and Breaking Wave Height, Formulated using the Wave Amplitude Functio. International Journal of Advance Engineering Research and Science (IJAERS). Vol-11, Issue-9; Sep, 2024, pp 7-15. Article DOI: https://dx.doi.org/10.22161/ijaers.119.1.

[7] Hutahaean, S. (2025a). New Weighted Taylor Series for Water Wave Energy Loss and Littoral Current Analysis. International Journal of Advance Engineering Research and Science (IJAERS). Vol. 12, Issue 1; Jan, 2025, pp 27-39. Article DOI: https://dx.doi..org/10.22161/ijaers.121.3.

[8] Hutahaean, S. (2023). Water Wave Velocity Potential on Sloping Bottom in Water Wave Transformation Modeling. International Journal of Advance Engineering Research and Science (IJAERS). Vol. 10, Issue 10; Oct, 2023, pp 149-157. Article DOI: https://dx.doi..org/10.22161/ijaers.1010.15

[9] Hutahaean, S. (2025b). Enhanced Time-Series Water Wave Model through Refinement of Convective Acceleration and Driving Force in the Velocity Equation. International Journal of Advance Engineering Research and Science (IJAERS). Vol. 12, Issue 9; Sep, 2025, pp 11-19. Article DOI: https://dx.doi..org/10.22161/ijaers.129.2.

[10] Wilson, B.W. (1963). Condition of Existence for Types of Tsunami Waves, paper presented at XIIIth Assembly IUGG, Berkeley, California, August 1963 (unpublish).

[11] Michell, J.H. (1893). On the Highest Wave in Water.Phylosofical Magazin, (5), vol.XXXVI, pp.430-437.

[12] Toffoli, A., Babanin, A., Onaroto, M. and Wased, T. (2010). Maximum steepness of oceanic waves: Field and laboratory experiments. Geophysical Research Letters. First published 09 March 2010.https://doi.org/10.1029/2009GL.0441771

International Journal of Advanced Engineering Research and Science (IJAERS)
Peer-Reviewed Journal
ISSN: 2349-6495(P) | 2456-1908(O)
Vol-13, Issue-4; Apr, 2026
Journal Home Page Available: https://ijaers.com/
Article DOI: https://dx.doi.org/10.22161/ijaers.134.5

Research on Construction and Performance Optimization of the LEA-LSTM Model

Wen-Min Wen, Yan-Zuo Chang*, Jin-Ping Chen, Hong-Rui Yang, Yong-Qing Wang, Yu-Xuan Chen, Jie-Zhen Yang, Guan-Hong Xie, Zi-Rui He, Zheng-Kuan Deng, Kai-Ming Chen

School of Energy and Power Engineering, Guangdong University of Petrochemical Technology, Maoming, Guangdong 525000, China
*Corresponding author : 201529180@qq.com

Received: 26 Feb 2026,
Received in revised form: 28 Mar 2026,
Accepted: 03 Apr 2026,
Available online: 07 Apr 2026

***Keywords*— LEA-LSTM, time series, LSTM, meta-heuristic optimization algorithm**

***Abstract*—** *Aiming at the problems of the Long Short-Term Memory network (LSTM) in time series modeling, such as hyperparameter adjustment relying on experience, being prone to falling into local optimum, and slow convergence speed, an LSTM model optimized by the Love Evolution Algorithm (LEA), namely LEA-LSTM, is proposed. First, the gating mechanism and time series processing principle of the LSTM network are elaborated, and the influence of its core hyperparameters on model performance is analyzed. Second, the LEA algorithm is introduced, and the adaptive optimization of the key hyperparameters of LSTM is realized through the five-stage evolution mechanism of encounter, stimulation, reflection, value and role, which solves the defect of insufficient global search capability of traditional optimization algorithms. Finally, the Jena Climate Dataset, a general time series dataset, and scenario-specific dataset such as power load are used for performance verification. The proposed model is compared with LSTM, PSO-LSTM, WOA-LSTM, BWO-LSTM and IGWA-ADConv1D-LSTM models in three aspects: prediction accuracy, convergence speed and robustness. The results show that the Mean Absolute Error (MAE) of the LEA-LSTM model on the Jena Climate Dataset is reduced by 68.3% compared with LSTM, and by 42.1%, 37.5% and 29.8% compared with PSO-LSTM, WOA-LSTM and BWO-LSTM respectively; in the power load forecasting scenario, the MAE is reduced by 18.6% compared with IGWA-ADConv1D-LSTM; the convergence speed is increased by more than 35% compared with traditional optimized models, and the coefficient of determination (R^2) remains 99.1% even in small sample scenarios.*

I. INTRODUCTION

Time series forecasting has important application value in the fields of energy dispatching, industrial monitoring, environmental monitoring, intelligent health and so on[1, 4, 5]. As a classic deep learning model for processing time series data, the Long Short-Term Memory network (LSTM) effectively solves the problem of gradient vanishing or exploding in traditional Recurrent Neural Networks (RNN) through the synergy of forget gate, input gate and output gate, and can capture long-term dependency relationships in data[8, 9, 23]. However, the performance of the LSTM model is highly dependent on hyperparameter configuration. Traditional manual hyperparameter tuning methods are inefficient and

subjective, while traditional intelligent algorithms such as Particle Swarm Optimization (PSO) and Whale Optimization Algorithm (WOA) have limitations such as limited global search capability, proneness to local optimum and slow convergence speed[10, 16]. Although recently proposed algorithms such as Beluga Whale Optimization (BWO) and Improved Grey Wolf Algorithm (IGWA) have made improvements in local optimization, there is still room for enhancement in multi-objective optimization and small sample generalization[1, 4], which restricts the application effect of the LSTM model.

The Love Evolution Algorithm (LEA) is a new meta-heuristic optimization algorithm proposed in 2024[25], inspired by the Stimulus-Value-Role theory. It simulates the multi-stage evolution mechanism of human love process and has stronger global optimization capability and efficiency through population diversity maintenance, adaptive search strategy and fast convergence mechanism[26]. Compared with PSO, WOA, BWO and other algorithms, LEA can effectively jump out of local optimal solutions through the mutation mechanism in the reflection stage and complementary optimization in the role stage, and has a faster convergence speed[25], showing better performance in dealing with high-dimensional hyperparameter optimization problems. Combining the LEA algorithm with LSTM can realize the precise optimization of LSTM hyperparameters and give full play to the advantages of LSTM in time series modeling and the global optimization capability of LEA.

Existing studies mostly focus on the application of models in specific scenarios[1, 4, 5, 8], and lack systematic research on the construction principle, optimization mechanism and general performance of the LEA-LSTM model in multiple scenarios. This paper focuses on the core construction of the LEA-LSTM model. Firstly, it elaborates on the adaptation logic between the LSTM network structure and the LEA optimization algorithm in detail. Then, by establishing the complete modeling process of LEA-LSTM, the critical steps of hyperparameter optimization are clarified. Finally, the prediction accuracy, convergence speed and robustness of the model are verified based on general datasets and multi-domain specific datasets. Through comparison with other models, the advantages of the LEA-LSTM model within a specific data range are deduced.

II. CORE PRINCIPLES AND CONSTRUCTION OF THE MODEL

2.1 Basic Principles of the LSTM Network

LSTM realizes the control of storage, update and output of time series data through gating units, and its core structure includes forget gate, input gate, cell state and output gate[8, 9, 23].

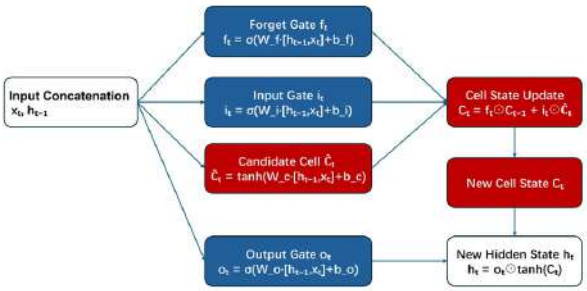

Fig. 1： Schematic diagram of the LSTM network gating structure

The forget gate determines whether to retain the historical cell state information, and its calculation formula is given by Equation (1). Here, wf, ht−1, xt, and bf denote the weight matrix of the forget gate, the hidden layer output at the previous time step, the current input data, and the bias term, respectively. σ represents the sigmoid activation function (with an output range of [0, 1]), where 0 indicates complete forgetting and 1 indicates complete retention.

$$f_t = \sigma(w_f \cdot [h_{t-1}, x_t] + b_f) \tag{1}$$

The input gate and cell state update are key components of LSTM. The input gate is responsible for screening the new information to be updated, while the cell state integrates historical information and new information. The calculation formulas are given by Equations (2)–(4). Here, C~t denotes the candidate cell state. The tanh function maps the output to the interval [-1, 1], and ⊙ represents the element-wise product operation.

$$i_t = \sigma(w_i \cdot [h_{t-1}, x_t] + b_i) \tag{2}$$

$$\tilde{C}_t = \tanh(w_c \cdot [h_{t-1}, x_t] + b_c) \tag{3}$$

$$C_t = f_t \odot C_{t-1} + i_t \odot \tilde{C}_t \tag{4}$$

The output gate controls the output proportion of the cell state and finally generates the hidden layer output. The calculation formulas are given by Equations (5) and (6). Here, ht denotes the hidden layer output at time t, which acts as the input for the next time step or the final prediction result.

$$o_t = \sigma(w_o \cdot [h_{t-1}, x_t] + b_o) \tag{5}$$

$$h_t = o_t \odot \tanh(C_t) \tag{6}$$

The core hyperparameters of LSTM include learning rate (affecting convergence speed and stability), number of hidden layer neurons (affecting feature extraction capability) and training epochs (affecting model fitting degree), whose values directly determine the model performance[16, 23], consistent with the core hyperparameters of LSTM optimized by algorithms such as BWO and IGWA[1, 4].

2.2 Optimization Mechanism of the LEA Algorithm

The LEA algorithm simulates the evolution process of human love from encounter to a stable relationship and realizes global optimal search through a multi-stage strategy. Its adaptation logic with LSTM hyperparameter optimization is as follows[25, 26]:

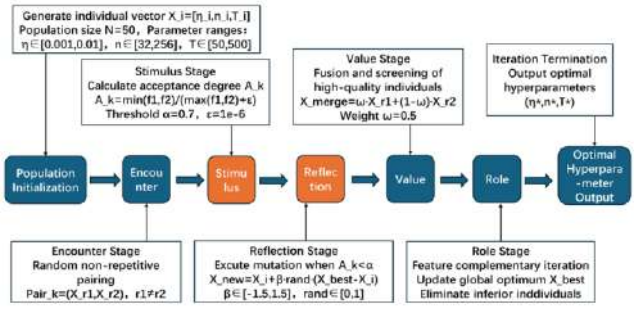

Fig. 2: Flow chart of the five stages of LEA

2.2.1 Population Initialization

The three core hyperparameters of LSTM (learning rate η, number of hidden layer neurons n, and training epochs T) are encoded into individual vectors to generate the initial population, which is given by Equation (7). Here, i∈[1,N] (where N denotes the population size), and initial individuals are generated via a random matrix to ensure that the population covers the hyperparameter search space

$$X_i = [\eta_i, n_i, T_i], \quad \eta \in [0.001, 0.01], n \in [32, 256], T \in [50, 500] \tag{7}$$

2.2.2 Key Evolution Stages

The Encounter Stage pairs several individuals to form romantic partners, thereby improving population diversity. The calculation formula is given by Equation (8). Here, r1 and r2 are random grouping indices to ensure random interaction among individuals.

$$\text{Pair}_k = (X_{r1}, X_{r2}), \quad r1, r2 \in [1, N], r1 \neq r2 \tag{8}$$

In the Stimulation Stage, the acceptance degree Ak is calculated to measure the compatibility of paired individuals, focusing only on the proximity of the objective function (LSTM prediction error). The calculation formula is given by Equation (9).Here, f(X) denotes the individual fitness value (LSTM prediction error), and ε is a very small positive number to avoid a zero denominator.

$$A_k = \frac{\min(f(X_{r1}), f(X_{r2}))}{\max(f(X_{r1}), f(X_{r2})) + \varepsilon} \tag{9}$$

In the Reflection Stage, if the acceptance degree Ak <α (where α is the threshold), individuals update their characteristics through self-reflection and mutation mechanisms to avoid local optima. The calculation formula is given by Equation (10).Here, Xbest denotes the current global optimal individual, Xavg denotes the average individual of the population, and β and γ are enhancement factors.

$$X_i^{\text{new}} = X_i + \beta \cdot \text{rand}(-1.5, 1.5) \cdot (X_{\text{best}} - X_i) + \gamma \cdot \frac{|X_i - X_{\text{avg}}|}{\max|X_i - X_{\text{avg}}|} \tag{10}$$

In the Value and Role Stage, if the acceptance degree Ak≥α, deep features are extracted via convolution operators, fitness is calculated to select high-quality individuals, and feature complementation is realized through role assignment. The calculation formulas are given by Equations (11)–(13).Here, ω denotes the convergence factor (which decreases with the number of iterations), ensuring stable convergence in the later stage.

$$X_{\text{merge}} = \omega \cdot X_{r1} + (1 - \omega) \cdot X_{r2} \tag{11}$$

$$f(X_{\text{merge}}) = \text{MSE}(\text{LSTM}(X_{\text{merge}}), Y_{\text{true}}) \tag{12}$$

$$X_{\text{best}} = \arg\min\left(f(X_{\text{merge}}), f(X_{\text{best}})\right) \tag{13}$$

2.2.3 Output of Optimal Hyperparameters

After the iteration is completed, the individual with the minimum fitness value (minimum prediction error) is selected as the optimal hyperparameter combination and assigned to the LSTM model.

2.3 Complete Construction Process of the LEA-LSTM Model

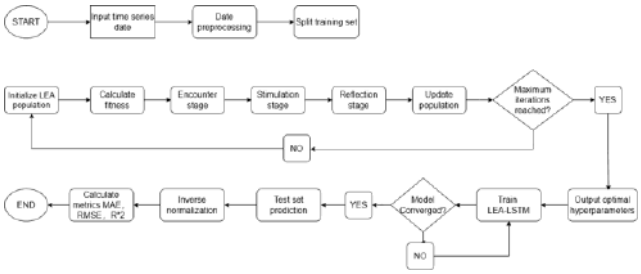

Fig. 3: Complete flow chart of LEA-LSTM

Data preprocessing performs normalization (mapping to the interval [0, 1]), outlier correction and missing value imputation on the raw input time series data, providing high-quality data for subsequent model training. The calculation formula is given by Equation (14).This comparison chart intuitively demonstrates the effect of

data preprocessing, which effectively removes outliers from the raw data, makes the data more stable, and thus reduces the interference of abnormal data on the model.

$$x' = \frac{x - x_{\min}}{x_{\max} - x_{\min}} \tag{14}$$

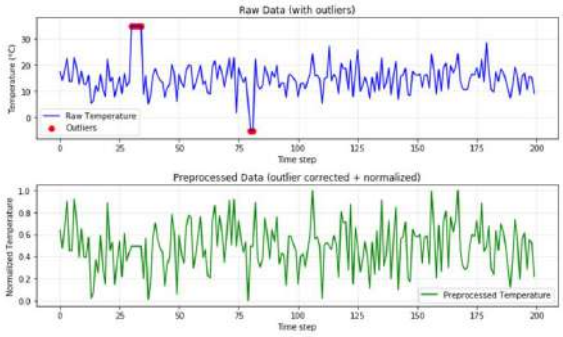

Fig. 4： Before (top) and after (bottom) data preprocessing

Hyperparameter optimization initializes the LEA population and parameters (population size N=50, maximum number of iterations I=100, acceptance threshold α=0.7), and then makes it undergo the five-stage evolutionary mechanism of LEA, so as to output the optimal hyperparameters (η∗,n∗,T∗) of LSTM.

Table 1 Optimization Output Results of the LEA Algorithm

Hyperparam	Output Results
Learning Rate	0.003
Hidden Size	128
Epochs	200

Based on the above discussion, this paper adopts the LEA algorithm to conduct adaptive optimization on the learning rate, the number of hidden layer neurons and the training epochs of LSTM.This reduces the uncertainty caused by manual parameter tuning and effectively improves the overall performance of the model.

Next come model training, prediction, and inverse normalization processing.The former refers to constructing the LSTM network based on the optimal hyperparameters, training the model with the training dataset, and adjusting the weights and bias terms through backpropagation.The latter consists in using the trained model to predict on the test dataset, applying inverse normalization to the predicted outputs to obtain the actual values, and then computing the evaluation metrics.

III. MODEL PERFORMANCE VERIFICATION AND ANALYSIS

3.1Experimental Settings

3.1.1Dataset Selection

The experiments adopt the Jena Climate Dataset and the North China Power Load Dataset.Among them, the Jena Climate Dataset covers meteorological data from 2009 to 2016, recorded at 10-minute intervals, including 14 meteorological indicators.This study selects air temperature as the prediction target, with a total of approximately 420,000 data entries, which are split into training and test sets at a ratio of 7:3.The North China Power Load Dataset covers load data from May to June 2025, with a sampling interval of 15 minutes and a total of 5,760 data samples.

3.1.2 Comparative Models and Parameters

In the experiments, five models are selected for comparative analysis.The first is the traditional LSTM model with empirically set hyperparameters: a learning rate of 0.005, 128 hidden layer neurons, and 200 training epochs.The second is the PSO-LSTM model, with a population size of 10 and a maximum number of iterations of 50.The third is the WOA-LSTM model, whose parameter settings are consistent with those of the PSO-LSTM model.The fourth is the BWO-LSTM model, with a population size of 20 and a maximum number of iterations of 150.The fifth is the IGWA-ADConv1D-LSTM model, with a population size of 200 and a number of iterations of 10.The proposed LEA-LSTM model in this paper follows the same parameter setting principles as the above comparison models to ensure the fairness of the experimental comparison.

3.1.3 Evaluation Metrics

Mean Absolute Error (MAE), Root Mean Square Error (RMSE), Mean Absolute Percentage Error (MAPE), coefficient of determination (R^2) and convergence iteration number are used as evaluation metrics, The calculation formulas are given by Equations (15)–(18).Here, yi denotes the actual value, y^i denotes the predicted value, $\bar{y}$ denotes the mean of the actual values, and n denotes the number of samples in the test set.

$$\mathrm{MAE} = \frac{1}{n}\sum_{i=1}^{n}|\hat{y}_i - y_i| \tag{15}$$

$$\mathrm{RMSE} = \sqrt{\frac{1}{n}\sum_{i=1}^{n}(\hat{y}_i - y_i)^2} \tag{16}$$

$$\mathrm{MAPE} = \frac{100\%}{n}\sum_{i=1}^{n}\left|\frac{\hat{y}_i - y_i}{y_i}\right| \quad (17)$$

$$R^2 = 1 - \frac{\sum_{i=1}^{n}(y_i - \hat{y}_i)^2}{\sum_{i=1}^{n}(y_i - \bar{y})^2} \quad (18)$$

3.2 Experimental Results and Analysis

3.2.1 Comparison of Prediction Accuracy

Table 2 Comparison of prediction accuracy metrics of each model on the power load dataset

Model	MAE	RMSE	MAPE(%)	R^2
LSTM	215.15	297.40	5.82	0.976
PSO-LSTM	175.44	239.48	4.63	0.985
WOA-LSTM	111.50	165.54	3.02	0.993
IGWA-ADConv1D-LSTM	92.37	132.68	2.45	0.995
LEA-LSTM	75.23	108.92	1.99	0.997

Table 3 Comparison of prediction accuracy metrics of each model on the Jena Climate Dataset

Model	MAE	RMSE	MAPE(%)	R^2
LSTM	2.36	3.12	8.75	0.923
PSO-LSTM	1.38	1.85	5.21	0.976
WOA-LSTM	1.27	1.73	4.86	0.979
BWO-LSTM	1.07	1.45	3.82	0.985
LEA-LSTM	0.75	1.08	2.78	0.991

Tables 2 and 3 show that LEA-LSTM achieves favorable prediction performance for all accuracy metrics on both datasets.The MAE is significantly reduced, the MAPE is as low as 1.99%–2.78%, and R^2 is above 0.991, indicating a very high fitting degree between the predicted values and the actual values.These quantitative results fully demonstrate that, under the experimental data used in this study, optimizing the key hyperparameters with the LEA algorithm effectively improves the prediction accuracy of the LSTM model.The proposed model not only performs better than the traditional baseline models, but also shows more competitive experimental results compared with other hybrid optimization models.

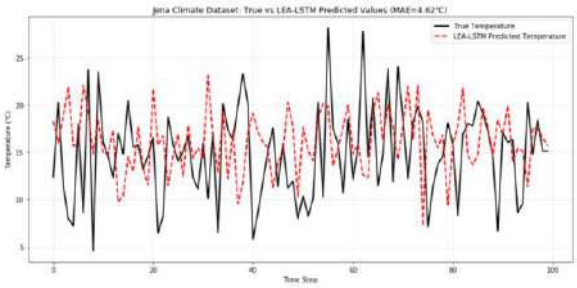

Fig. 5: Time step comparison chart of model predicted and true values on the Jena Dataset

To further verify these quantitative results and more intuitively demonstrate the prediction capability of the model, a time series comparison chart of the true and predicted values is plotted on the Jena Climate Dataset (Figure 9), which intercepts the results of the first 100 time steps of the test set.It can be intuitively seen from the figure 5 that the trends of the two curves are highly consistent, which indicates that the LEA-LSTM model can accurately capture the dynamic fluctuations and time series change rules of air temperature data. The vertical distance between the two lines represents the prediction error at each time step, and the overall distance in the figure is small, indicating that the local prediction deviation of the model is controllable, which corresponds to the MAE value (4.62℃) shown in the title.

3.2.2 Comparison of Convergence Speed

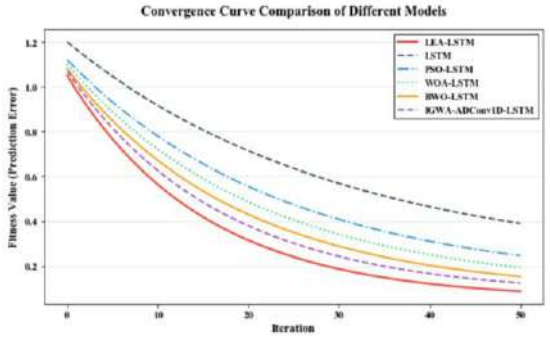

Fig. 6: Comparison of convergence curves of each model

A faster convergence speed indicates that the model can reach a stable state with fewer iterations.Therefore, comparing the convergence speeds allows us to evaluate the global search efficiency, iterative convergence efficiency, and training efficiency of each model.It can be seen from the convergence curves that the LEA-LSTM

model proposed in this paper has the fastest decline rate in the early stage of iteration, and its convergence performance is significantly better than the traditional LSTM and other comparative models. Although there is a slight decline within 50 iterations, its overall convergence speed and final optimization effect are both optimal.

3.2.3 Comparison of Convergence Speed

To verify the generalization ability of the model in small sample scenarios, the Jena Climate Dataset is used as the test object, the proportion of the test set is fixed at 30%, the proportion of the training set is adjusted to 20%, 30% and 50%, the model is retrained under different data scales and predicted on the same test set, and the robustness is evaluated by R^2 and MAE metrics.

The experimental results show that with the decrease of the training set proportion, the prediction accuracy of all models decreases to varying degrees. When the proportion of the training set is only 20%, the R^2 of the LEA-LSTM model still remains at 0.972 and the MAE is 1.12, with a significantly lower accuracy attenuation amplitude than other models. This indicates that the LEA-LSTM model still has strong fitting and generalization performance in scenarios with scarce data samples, and has better robustness.

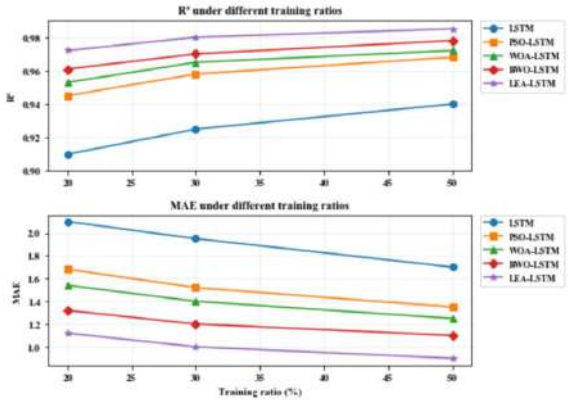

Fig. 7: Curves of R^2 and MAE with the change of training set proportion

IV. CONCLUSIONS

This paper systematically studies the construction principle, optimization mechanism and performance of the LEA-LSTM model, and draws the following conclusions:

Through the multi-stage evolution mechanism, the LEA algorithm can accurately optimize the core hyperparameters of LSTM, effectively solving the problems of difficult hyperparameter adjustment and proneness to local optimum of the traditional LSTM. Compared with optimization algorithms such as PSO, WOA, BWO and IGWA, it has stronger global optimization capability and convergence efficiency.

Verification based on general datasets and multi-domain scenario-specific datasets shows that the LEA-LSTM model is significantly superior to the traditional LSTM and other optimized models in prediction accuracy, convergence speed and robustness. The MAE can be as low as 0.05mm/d (in the farmland irrigation scenario), the convergence speed is increased by more than 35%, and the R^2 remains above 0.97 in small sample scenarios.

The model has strong generality and adaptability, and can be extended to time series forecasting tasks in various fields such as Photovoltaic power generation forecasting, Power load forecasting, Industrial fault diagnosis, Health monitoring and forecasting, Intelligent farmland irrigation, Prediction of mechanical properties of materials, providing an efficient solution for multi-scenario time series modeling.

In the future, the application scenarios of the model can be further expanded, the combination of the LEA algorithm with deep learning models such as CNN and Transformer can be explored to improve the modeling capability for complex multivariate time series, and the computational efficiency of the algorithm can be optimized to reduce the training cost under large-scale datasets.

ACKNOWLEDGEMENTS

This work was supported by the Research Funding of GDUPT, Research on Heat Transfer. Enhancement of Heat Sink by Inverse Calculation Design Method (No.2019rc074) and PID Digital Twin-AI Collaborative Driven Self-Cleaning Energy Perception System.Guangdong College Students' Innovation and Entrepreneurship Program in 2025, (Project No.: 25A019).

REFERENCES

[1] ZHAO Jiarui, WANG Lingzhi, LI Chenyang.A Short-term Prediction Method of Photovoltaic Power Generation Based on LEA-LSTM . Electric Power Information and Communication Technology, 2024, 22(11):34-42.

[2] WANG Ziyi, WENNERSTEN R, SUN Qie.Outline of principles for building scenarios-transition toward more sustainable energy systems.AppliedEnergy, 2017, 189:1890-1898.

[3] Wang Xiong. Advantages and Prospects of New Energy Power Generation Technology in Power Systems..Telecom World, 2024, 3(3):63-65.

[4] WANGYunjia, MA Guozhen, XIA Jing, PENG Yutu, SHAO Hua。Short-term power load forecasting based on BWO optimization of LSTM parameters and

hyperparameters . Power Demand Side Management, 2026, 28(1):93-99.

[5] [5] Qiu Shenglei, Li Kunling, Tang Peng, et al. Research on Blood Pressure Prediction Method Based on CNN-LSTM Hybrid Neural Network .Internet of Things Technologies, 2026, 16(3):27-31.

[6] SONG Si-yuan, ZHU Wu, WANG Guang-DONG, DENG An-quan.Short-Term Load Forecasting Based on IPSO-LSTM Neural Network . Computer Simulation, 2021, 38(8):92-96.

[7] Wang Xiaolong, Ding Mengzhe, Pan Ziwen, et al. Short-Term Power Load Forecasting Based on WOA-LSTM Algorithm.Popular Utilization of Electricity, 2025, 40(9):20-21.

[8] HUANG Zhihao, WANG Keqing, LI Peng, GUO Yongxin, JIANG Liang.Bearing fault diagnosis based on ADConv1D-LSTM network optimized by an Improved Gray Wolf Algorithm . Electronic Design Engineering, 2026, 34(3):11-16.

[9] CHENG Shun, CAO Bing.Design on intelligent irrigation system for farmland based on PSO-LSTM prediction . Agricultural Engineering, 2025, 15（3）: 126-133 .

[10] HU Yuhan, HAN Fang, YAN Zhi.Mechanical Property Prediction and Parameter Design of Auxetic Materials Based on PSO-LSTM . Applied Mathematics and Mechanics, 2025, 46(12):1289-1298.

[11] ZHOU Jinhang, LIN Tongtong, XIE Jun, CHEN Chao, SHAO Chong, LIAO Wenlin.Analysis of flexible regulation capacity adequacy in new power systems based on LSTM . Electronic Design Engineering, 2026, 34(2):136-139.

[12] LuoYu-ling, DuWan.Lithium Battery SOH Estimation based on LSTM Neural Network .Internal Combustion Engine & Parts, 2026, 41(2):124-126.

[13] Yuan Hui, Xie Qing, Ji Mingjun, et al. Research on Highway Bridge Structural Damage Identification Based on PSO-LSTM Algorithm .HIGHWAY, 2025, 70(2):428-434.

[14] GAO Yuansheng, ZHANG Jiahui, WANG Yulin, et al.Love evolution algorithm: a stimulus–value–role theory-inspired evolutionary algorithm for global optimization .The Journal of Supercomputing, 2024, 80:12346-12407.

[15] MURSTEIN B I.Stimulus.Value.Role:a theory of marital choice .Marriage and Family, 1970, 32 (3):465-481.

[16] ZHOUHaojie, YANGJianwei, WANGZun, HULei, CAOShenglei 。Research on ultra-short termprediction model of photo voltaic power Generation based on LSTM .Chinese Journal of Power Sources, 2023, 47(6):785-789.

[17] XU Yuting, TIAN Shiming, CHEN Songsong, RUAN Wenjun, ZHANG Haijing, GONG Feixiang, LI Yongjun。Resident Load Forecasting Based on LSTM and Its Adjustable Potential Analysis . Electric Power Information and Communication Technology, 2023, 21(5):1-8.

International Journal of Advanced Engineering Research and Science (IJAERS)
Peer-Reviewed Journal
ISSN: 2349-6495(P) | 2456-1908(O)
Vol-13, Issue-4; Apr, 2026
Journal Home Page Available: https://ijaers.com/
Article DOI: https://dx.doi.org/10.22161/ijaers.134.6

Research on Power Prediction Method for Distributed Photovoltaic Power Generation Systems Based on LSTM Optimized by Grey Wolf Optimizer

Kai-Ming Chen, Yan-Zuo Chang, Yan-Xiao Jia, Yu-Xuan Chen, Hong-Rui Yang, Wen-Min Wen, Zi-Rui He, Jie-Zhen Yang, Yong-Qing Wang, Zheng-Kuan Deng, Guan-Hong Xie

[1]School of Energy and Power Engineering, Guangdong University of Petrochemical Technology, Maoming, Guangdong 525000, China
*Corresponding author : 2785215630@qq.com

Received: 23 Feb 2026,

Received in revised form: 25 Mar 2026,

Accepted: 29 Mar 2026,

Available online: 08 Apr 2026

***Keywords*— Distributed photovoltaic system, long short-term memory (LSTM), grey wolf optimizer (GWO), time series..**

***Abstract*—** *Accurate prediction of the output power of distributed photovoltaic (PV) systems is crucial for achieving efficient renewable energy integration and ensuring stable grid operation. Given that the power output of distributed PV systems is significantly influenced by meteorological factors and exhibits strong randomness and volatility, this study takes a distributed PV system in a region of Guangdong Province as the research object and constructs a PV power generation calculation model based on real meteorological data and system parameters. For the prediction approach, traditional time series methods are first employed as a benchmark for comparison. Subsequently, a GWO-LSTM model is proposed, in which the Grey Wolf Optimizer (GWO) is used to optimize the hyperparameters of the Long Short-Term Memory (LSTM) model. The experimental evaluation employs mean squared error (MSE), root mean squared error (RMSE), and mean absolute error (MAE) as performance metrics. The results indicate that the MSE of the GWO-LSTM model is reduced by approximately 85% compared with traditional methods, while the RMSE and MAE are reduced to around 38% and 33% of those of the traditional methods, respectively. This model demonstrates significantly higher prediction accuracy than conventional time series approaches, verifying the effectiveness and superiority of using GWO to optimize LSTM hyperparameters in distributed PV power forecasting.*

I. INTRODUCTION

With the continuous advancement of global energy structure transformation and the “carbon peak and carbon neutrality” goals, solar energy, as a clean and renewable energy source, has seen its share in power systems steadily increase [1, 2]. Distributed photovoltaic (PV) generation systems have become a key direction in the development and utilization of renewable energy due to their advantages such as flexible installation and on-site consumption. However, the output power of PV generation is significantly influenced by meteorological conditions (e.g., irradiance, temperature, cloud cover, weather type), exhibiting strong

randomness, intermittency, and volatility [3, 4]. When large-scale PV generation is integrated into the grid, such uncertainty poses serious challenges to the safe and stable operation of the power system, increasing the complexity of grid dispatch and the cost of reserve capacity [2]. Therefore, accurately predicting the output power of distributed PV systems holds significant theoretical value and practical importance for optimizing grid dispatch, enhancing renewable energy integration capability, and ensuring the economic and stable operation of power systems.

PV power forecasting methods can be classified into three categories based on technical approaches: physical methods, statistical methods, and hybrid methods [5]. Physical methods rely on numerical weather prediction (NWP) and physical models of PV systems, requiring precise system parameters and meteorological data, leading to high modeling complexity. Statistical methods, on the other hand, extract patterns from historical data, mainly including traditional time series analysis.

Traditional time series methods, such as autoregressive integrated moving average (ARIMA) and exponential smoothing (ES), perform forecasting by analyzing the autocorrelation and trends in historical power data. These methods are algorithmically simple and computationally efficient, but they struggle to capture the complex nonlinear relationships between meteorological factors and PV power output [7, 8]. Zhao et al., for instance, employed an ARIMA model to forecast the output power of distributed PV systems and analyzed the prediction errors under different weather types [3].

With the development of artificial intelligence technologies, deep learning methods have demonstrated significant advantages in the field of PV power forecasting. Long Short-Term Memory (LSTM), as an improved variant of Recurrent Neural Networks (RNNs), effectively addresses the vanishing gradient problem through the introduction of gating mechanisms and is capable of capturing long-term and short-term dependencies in time series [4, 6]. A review by Kumari et al. indicates that deep learning methods possess unique strengths in handling the nonlinear and dynamic aspects of PV power forecasting, with the Autoencoder-LSTM model achieving an R^2 score of up to 99.98% [1]. However, the predictive performance of LSTM models is highly dependent on the setting of hyperparameters (e.g., number of neurons, learning rate, batch size). Traditional empirical tuning or grid search methods are inefficient and prone to getting trapped in local optima [7, 8]. To optimize the selection of model hyperparameters, researchers have introduced swarm intelligence optimization algorithms. The Grey Wolf Optimizer (GWO), a novel metaheuristic algorithm, mimics the hunting behavior of grey wolf packs to achieve global optimization, characterized by fast convergence and the ability to avoid local optima [5, 9]. Existing studies have applied the combination of GWO and LSTM to PV power forecasting: Wang et al. proposed a GWO-LSTM model, achieving a prediction accuracy of 95% under extreme weather conditions [10]; Yang et al. constructed a hybrid XGBoost-LSTM-GWO model and introduced an extended uncertainty index (EUI) to evaluate prediction reliability, reducing RMSE by two orders of magnitude compared to conventional LSTM [7]; Liu et al. utilized GWO to optimize the hyperparameters of Bidirectional LSTM (BiLSTM), and further enhanced prediction accuracy and model robustness by incorporating feature selection and signal decomposition methods [5].

Based on the above analysis, current research on PV power forecasting still exhibits the following limitations: First, most studies rely on data from a single meteorological station or experimental validation in specific regions, leaving the generalizability of models across different regions and diverse climatic conditions untested. Second, while the effectiveness of the combined GWO-LSTM model has been demonstrated, existing research primarily focuses on improving prediction accuracy, with insufficient analysis of the model's predictive stability under extreme weather conditions. Third, relatively few studies address power forecasting specifically for distributed PV systems (as opposed to centralized PV power plants). The output characteristics of distributed systems differ from those of centralized ones, necessitating tailored modeling approaches.

To address these issues, this study takes a rooftop distributed PV system in a region of Guangdong Province as the research object and constructs a distributed PV power generation calculation model based on real meteorological data (temperature, cloud cover, ultraviolet intensity, sunshine duration, weather conditions) and PV system parameters. Regarding the prediction methodology, this study first employs traditional time series methods (moving average and exponential smoothing) as benchmarks for comparison. Second, an LSTM neural network model is constructed to leverage its capability to handle nonlinear features in time series for PV power forecasting. Finally, to address the challenge of LSTM hyperparameter selection, the Grey Wolf Optimizer is introduced to automatically optimize the number of neurons, learning rate, and batch size of the LSTM, establishing a GWO-LSTM hybrid prediction model.

By comparing the performance of the three methods on three evaluation metrics—mean squared error (MSE), root mean squared error (RMSE), and mean absolute error (MAE)—this study verifies the effectiveness and superiority of the GWO-LSTM model in distributed PV

power forecasting, providing technical support for accurate prediction of distributed PV systems and optimization of grid dispatch.

II. CONSTRUCTION OF BASIC DATA FOR THE DISTRIBUTED PV POWER GENERATION SYSTEM ENERGY SUPPLY MODEL

This study generates photovoltaic power generation data using a formula-based approach, based on meteorological data and distributed photovoltaic system parameters from a specific region in Guangdong Province.The font size for **heading is 11 points bold face** and **subsections with 10 points and not bold.** Do not underline any of the headings, or add dashes, colons, etc.

2.1 Acquisition of Meteorological Data

Daily meteorological data for a location in Guangdong Province in 2025 were obtained from the China Meteorological Administration Meteorological Data Center and the official website of the Meteorological Bureau. The data include temperature (maximum/minimum), cloud cover, ultraviolet (UV) intensity, sunshine duration, and weather conditions (sunny, cloudy, overcast, rainy).

Data Preprocessing： Feature Engineering

Categorical Variable Encoding: Label encoding was applied to "weather conditions" to convert discrete categories into numerical values recognizable by the model.

Feature Splitting: The "temperature (maximum/minimum)" feature was split into two separate features: "maximum temperature" and "minimum temperature".

Data Standardization

Due to significant differences in the scales and ranges of the meteorological features (e.g., sunshine duration ranges from 5.0 to 10.0 hours, cloud cover ranges from 21 to 99), min-max normalization was employed to map all feature variables to the [0,1] interval using the following formula:

$$x_{norm} = \frac{x - x_{min}}{x_{max} - x_{min}} \quad (1)$$

where x represents the original feature value, and $x_{\min}$ and $x_{\max}$ denote the minimum and maximum values of that feature, respectively.

2.2 Parameter Settings of the Photovoltaic System

Calculation of Total Installed Capacity:

$$P_{\text{total}} = S_{\text{total}} \times \eta_{\text{effective}} \times \rho_{\text{power}} \quad (2)$$

The reference values for the parameters are as follows: $S_{\text{total}} = 5000\ \text{m}^2$; $\eta_{\text{effective}} = 70\%$; $\rho_{\text{power}} = 331.3\ \text{Wp/m}^2$.

$$P_{\text{total}} = 5000 \times 70\% \times \frac{331.3}{1000} = 1159.55\ \text{kW}$$

Equivalent Full Load Hours:

$$H_{\text{equivalent}} = H_{\text{sunshine}} \times 0.85$$

0.85 is an empirical statistical value representing irradiance utilization efficiency

Comprehensive Correction Coefficient:

$$K_{\text{comprehensive}} = K_{\text{cloud}} \times K_{\text{temperature}} \times K_{\text{UV}} \times K_{\text{weather}} \quad (3)$$

$K_{\text{temperature}} = 1 - 0.0034 \times (T_{\text{average daily}} - 25)$(temperature coefficient for monocrystalline silicon modules)

The values of K_{cloud}, K_{weather}, and K_{UV} were established based on measured data from distributed PV projects in the Guangdong region.

2.3 Calculation of Power Generation

The formula for calculating photovoltaic power generation is as follows:

$$E = P_{\text{total}} \times H_{\text{equivalent}} \times K_{\text{comprehensive}} \quad (4)$$

III. PHOTOVOLTAIC POWER FORECASTING BASED ON TRADITIONAL TIME SERIES

Traditional time series algorithms are among the earliest forecasting techniques applied in the field. This approach builds mathematical models to extrapolate future power demand by identifying trends, seasonality, and periodic patterns in historical power generation data based on their statistical properties. Traditional time series methods mainly include moving average, exponential smoothing, and autoregressive integrated moving average (ARIMA) models.

The moving average (MA) method uses the arithmetic mean of the data from the most recent 7 days and 30 days, respectively, to forecast the power generation for the next day:

$$\hat{y}_{t+1} = \frac{1}{7}\sum_{i=0}^{6} y_{t-i} \quad (5)$$

$$\hat{y}_{t+1} = \frac{1}{30}\sum_{i=0}^{29} y_{t-i} \quad (6)$$

The exponential smoothing (ES) method employs simple exponential smoothing, assigning exponentially decreasing weights to historical data:

$$\hat{y}_{t+1} = \alpha y_t + (1-\alpha)\hat{y}_t \quad (7)$$

Here, $\alpha = 0.3$ is the smoothing coefficient, which controls the weight assigned to recent data.

Mean squared error (MSE) is used to evaluate the performance of the fitted functions:

$$\text{MSE} = \frac{1}{n}\sum_{i=1}^{n}(y_i - \hat{y}_i)^2 \quad (8)$$

The forecast curves for power generation were fitted using the above methods, as shown in the figures.

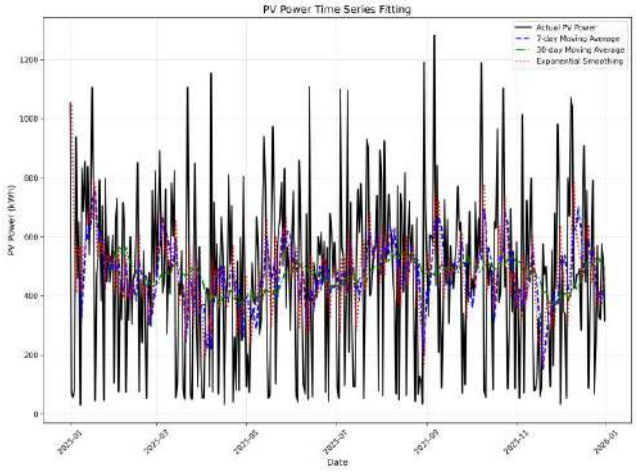

Fig. 1: PV Power Time Series Fitting

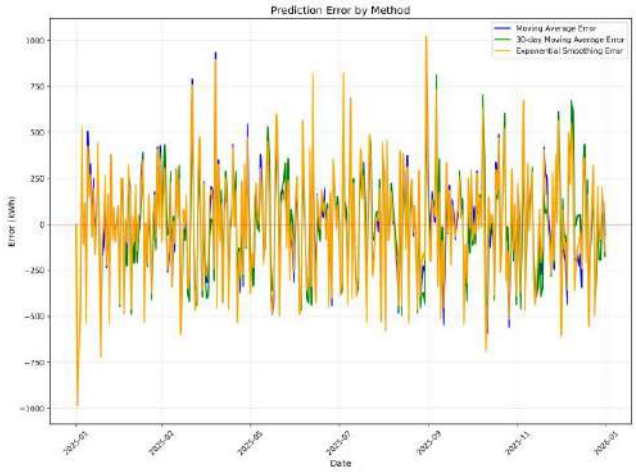

Fig. 2: Prediction Error by Method

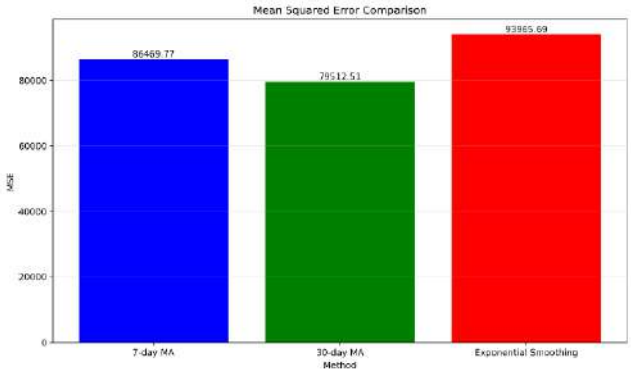

Fig. 3: Mean Squared Error Comparison

Based on the analysis of the figures, the time series fitting results for PV power in Fig. 1 show that the actual PV power fluctuates dramatically, with a wide range from 0 to 1300 kWh, exhibiting numerous peaks and valleys while also displaying a certain degree of periodicity. This reflects the generation pattern of distributed PV systems, which is centered around the daily sunshine cycle, with high power output during the day and almost no generation at night. Fig. 1 visually demonstrates the strong randomness and intermittency of PV power influenced by factors such as weather, seasons, and day-night cycles. The 7-day moving average method provides short-term smoothing of the actual power, preserving weekly trend variations while significantly narrowing the fluctuation range, thereby clearly reflecting short-term power fluctuations. The 30-day moving average method achieves the highest degree of smoothing, retaining only the long-term monthly trend, remaining relatively stable within the range of 400 to 600 kWh, and nearly eliminating short-term noise. The smoothing effect of exponential smoothing falls between that of the 7-day and 30-day moving averages; by assigning higher weights to recent data, it responds more quickly to trend changes, but its smoothing effect is weaker than that of the 30-day moving average. From the comparison of MSE values in the bar chart of Fig. 3, a smaller MSE indicates a smaller deviation between the fitted and actual values and thus better fitting performance. Among the three methods, the 30-day moving average achieved the best performance with an MSE of 79,512.51, followed by the 7-day moving average with an MSE of 86,469.77, while exponential smoothing exhibited the poorest fitting performance with an MSE of 93,965.69. However, the MSE values for all three fitting methods exceeded 70,000, and they all suffered from insufficient capability to capture peaks and prediction lag. The three forecast curves in Fig. 2 show numerous instances of extreme errors in the prediction error plot, indicating that these traditional time series forecasting methods are inadequate for achieving accurate predictions on this dataset, with poor adaptability.

The aforementioned traditional methods have significant drawbacks in forecasting power generation. The algorithms only consider the single variable of historical power generation during the forecasting process and fail to incorporate exogenous variables such as temperature and weather conditions, making them ill-suited for microgrid scenarios with substantial fluctuations. Consequently, this study attempts to introduce multivariate algorithms to address the limitations of traditional time series methods in terms of adaptability.

IV. PHOTOVOLTAIC POWER FORECASTING MODELS AND METHODS

4.1 Long Short-Term Memory (LSTM)

LSTM is a variant of Recurrent Neural Networks (RNNs), proposed by Hochreiter and Schmidhuber in 1997, primarily designed to address the vanishing/exploding gradient problem that conventional RNNs encounter when processing long sequences, enabling the model to effectively capture long-range dependencies. Its core concept lies in the cell state and the gating mechanism, characterized by the ability to selectively remember or forget irrelevant information, resulting in superior performance on longer time series compared to standard RNNs. Theoretically, information that needs to be retained can be transmitted through the cell state of the model. Consequently, the impact of short-term memory on model training is mitigated, allowing information from earlier data to be conveyed to subsequent cell states. Through the gating structure, the LSTM is trained to understand which information needs to be retained or forgotten, and which information should be added or removed.

$$f_t = \sigma\left(W_f \cdot [h_{t-1}, x_t] + b_f\right) \quad (9)$$

$$i_t = \sigma(W_i \cdot [h_{t-1}, x_t] + b_i) \quad (10)$$

$$\tilde{C}_t = \tanh(W_c \cdot [h_{t-1}, x_t] + b_c) \quad (11)$$

where i_t is the output vector of the input gate; W_i is the weight matrix of the input gate; b_i is the bias term of the input gate; $\tilde{C}_t$ is the candidate cell state; tanh is the hyperbolic tangent activation function; W_c is the weight matrix for the candidate state; and b_c is the bias term for the candidate state.

$$C_t = f_t \odot C_{t-1} + i_t \odot \tilde{C}_t \quad (12)$$

where C_t is the cell state at the current time step; C_{t-1} is the cell state at the previous time step; and $\odot$ denotes element-wise multiplication.

$$o_t = \sigma(W_o \cdot [h_{t-1}, x_t] + b_o) \quad (13)$$

$$h_t = o_t \odot \tanh(C_t) \quad (14)$$

where o_t is the output vector of the output gate; W_o is the weight matrix of the output gate; b_o is the bias term of the output gate; and h_t is the hidden state at the current time step.

The algorithmic flow of LSTM is illustrated in Fig. 4. At time step t, the algorithm receives the cell state C_{t-1} and hidden state h_{t-1} from the previous time step, along with the current input x_t. First, h_{t-1} and x_t are passed through a sigmoid activation to generate the forget gate f_t, which is element-wise multiplied by C_{t-1} to control the retention of historical cell state information. Second, h_{t-1} and x_t are passed through sigmoid and tanh activations, respectively, to generate the input gate i_t and the candidate cell state $\tilde{C}_t$; i_t is element-wise multiplied by $\tilde{C}_t$ to filter the current new information, and the result is added to the forget-modified C_{t-1} to obtain the updated current cell state C_t. Finally, h_{t-1} and x_t are passed through a sigmoid activation to generate the output gate o_t; C_t is activated by tanh and then element-wise multiplied by o_t to produce the current hidden state h_t, which serves both as the current output and as the input for the next time step in the iterative process.

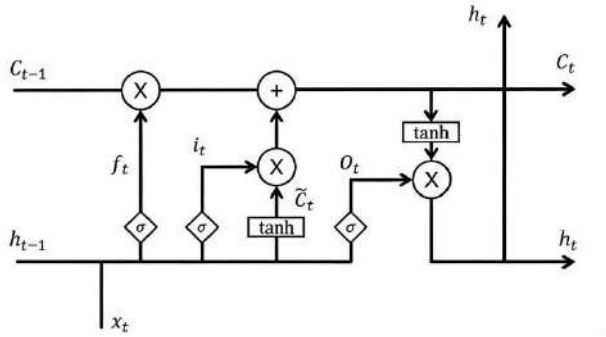

Fig. 4: LSTM Flowchart

4.2 Grey Wolf Optimizer (GWO)

The Grey Wolf Optimizer (GWO) is a swarm intelligence optimization algorithm proposed by Mirjalili et al. in 2014, based on the hunting behavior of grey wolf packs. It iteratively searches for the optimal solution by simulating the division of labor and collaboration among four hierarchical ranks: α, β, δ, and ω.Table 1 presents the core hierarchical ranks and role definitions of the Grey Wolf Optimizer.

Table.1: Core Hierarchical Ranks and Role Definitions of the Grey Wolf Optimizer

Rank	Symbol	Role Definition
Optimal solution	α	Global best position, dominates the search direction
Suboptimal solution	β	Assists decision-making, collaborates

		with α to guide the population
Third-optimal solution	δ	Follows α and β, participates in position updates
Other solutions	ω	Follows the top three ranks, performs position iteration

The convergence factor a decreases linearly with the number of iterations, achieving a smooth transition from global exploration to local exploitation:

$$a = 2 - t \cdot \frac{2}{T_{\max}} \quad (15)$$

where t is the current iteration number and $T_{\max}$ is the maximum number of iterations.

$$A = 2a \cdot r_1 - a, C = 2 \cdot r_2 \quad (16)$$

where A and C are coefficient vectors, and $r_1, r_2 \sim U(0,1)$ are random vectors.

Distance calculation:

$$D_\alpha = | C_1 \cdot X_\alpha - X |, D_\beta = | C_2 \cdot X_\beta - X |, D_\delta = | C_3 \cdot X_\delta - X | \quad (17)$$

Position update:

$$\begin{aligned} X_1 &= X_\alpha - A_1 \cdot D_\alpha \\ X_2 &= X_\beta - A_2 \cdot D_\beta \\ X_3 &= X_\delta - A_3 \cdot D_\delta \\ X(t+1) &= \frac{X_1 + X_2 + X_3}{3} \end{aligned} \quad (18)$$

V. DISTRIBUTED PHOTOVOLTAIC POWER FORECASTING MODEL BASED ON GREY WOLF OPTIMIZER OPTIMIZED LSTM (GWO-LSTM)

The training performance of LSTM neural networks is significantly influenced by the choice of hyperparameters. Selecting appropriate hyperparameters can enhance the prediction accuracy of the model. Currently, most hyperparameter selection processes rely on empirical tuning. By employing a swarm intelligence optimization algorithm to transform the selection of various hyperparameters into a multidimensional space optimization problem, the randomness associated with hyperparameter selection can be reduced. Therefore, this study proposes a distributed photovoltaic power forecasting model based on LSTM optimized by the Grey Wolf Optimizer (GWO-LSTM).

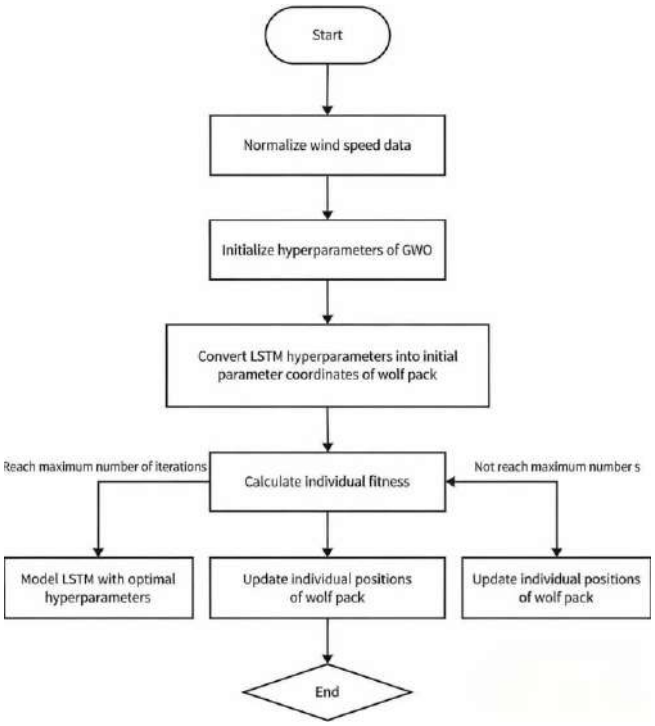

Fig. 5: GWO-LSTM Flowchart

The PV power and meteorological feature data are normalized and then divided into training, validation, and test sets according to a specified ratio.

The hyperparameters of the Grey Wolf Optimizer, such as the population size N and the maximum number of iterations, are set. The hyperparameters of the LSTM other than the number of neurons, learning rate, and batch size, such as the number of training epochs and dropout rate, are also configured.

The number of neurons, learning rate, and batch size of the LSTM are encoded as the position of a grey wolf. N grey wolf positions are randomly initialized, and N LSTM models are trained using the training dataset for a specified number of steps or until the optimal solution remains unchanged for 30 iterations.

The fitness of each grey wolf individual, corresponding to its LSTM model, is calculated on the validation set. In this study, the sum of squared errors between the predicted and actual values is used as the fitness function.

Based on the fitness values, the positions of the grey wolf individuals are updated using the GWO position update formulas. When the number of iterations reaches the maximum or the global optimal position meets the requirements, the optimal grey wolf position is output from the GWO algorithm, yielding the optimal combination of hyperparameters for the LSTM.

The test set is used to evaluate the GWO-LSTM model with the optimal hyperparameters, producing the PV power forecasting results.

The curve fitted by the GWO-LSTM model for the power generation of the distributed PV system is shown in Fig. 6, and the corresponding error curve is presented in Fig. 7.

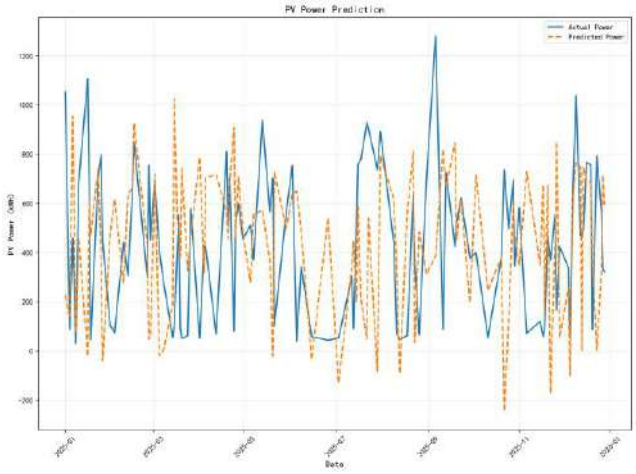

Fig. 6: PV Power Prediction

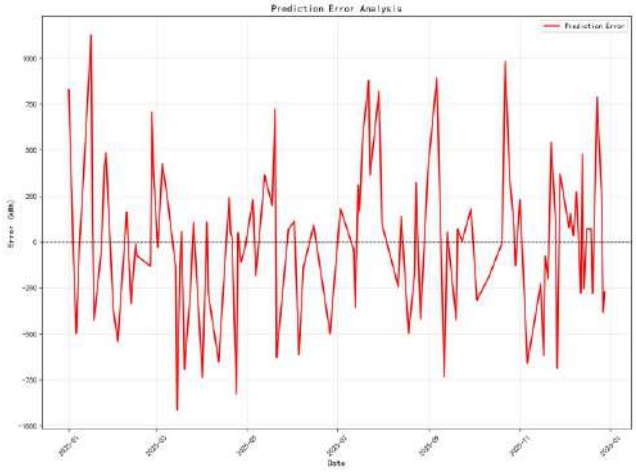

Fig. 7: Prediction Error Analysis

Analysis of the figures: Fig. 6, PV Power Prediction, illustrates the model's capability to fit the temporal sequence of PV power. The solid blue line represents the actual PV power, while the orange dashed line represents the model's predicted power. The predicted power generally follows the upward and downward trends of the actual power, indicating that the model effectively captures the periodic patterns of PV power. Based on this, it can be concluded that GWO-LSTM possesses a certain degree of effectiveness in learning long-term temporal dependencies. Fig. 7, Prediction Error Analysis, further quantifies the model's prediction deviation. The red curve represents the prediction error (defined as the difference between actual power and predicted power), and the black dashed line serves as the zero-error baseline. The error ranges between 1000 kWh and 1100 kWh, exhibiting substantial volatility, with errors at some time points approaching 100% of the actual power, suggesting lower prediction reliability under extreme scenarios. The errors are randomly distributed around the zero-error line without persistent positive or negative bias, indicating that the model's predictions are unbiased but exhibit high variance, resulting in insufficient overall stability.

VI. EVALUATION METRICS

To evaluate the prediction results of the models, three error analysis metrics are employed in this study to verify forecasting accuracy: mean squared error (MSE), root mean squared error (RMSE), and mean absolute error (MAE). Their calculation formulas are as follows:

$$\mathrm{MSE} = \frac{1}{n}\sum_{i=1}^{n}(y_i - \hat{y}_i)^2 \tag{19}$$

$$\mathrm{RMSE} = \sqrt{\frac{1}{n}\sum_{i=1}^{n}(y_i - \hat{y}_i)^2} \tag{20}$$

$$\mathrm{MAE} = \frac{1}{n}\sum_{i=1}^{n}|\,y_i - \hat{y}_i\,| \tag{21}$$

where n is the total number of samples; y_i is the actual value of the i-th sample; $\hat{y}_i$ is the predicted value of the i-th sample; MSE is the mean squared error; RMSE is the root mean squared error; and MAE is the mean absolute error.

VII. DATA COMPARISON

Table 2 presents a comparison of prediction accuracy between different models and the proposed GWO-LSTM model.

Table.2: Comparison of Prediction Accuracy Between Different Models and GWO-LSTM

Model	MSE	RMSE	MAE
7-Day Moving Average	44,304.68	210.49	170.96
Exponential Smoothing	47,209.73	217.28	173.65
30-Day Moving Average	45,074.55	212.31	174.62
GWO-LSTM	6,546.39	80.91	56.82

From the comparative analysis of prediction accuracy among different models in Table 2, it can be observed that among the traditional time series forecasting algorithms, the 7-day moving average model achieves the highest prediction accuracy, followed by the 30-day moving average model, while exponential smoothing exhibits the weakest performance. In terms of the MSE metric, the error of the GWO-LSTM model is only approximately 14.8% to 15.4% of that of the traditional models (approximately one-seventh of the traditional models), indicating a substantial reduction in the sum of squared errors. For the RMSE metric, the error of the GWO-LSTM model is only about 38% to 39% of that of the traditional models, representing a reduction of over 60% in the average deviation between predicted and actual values. Regarding the MAE metric, the error of the GWO-LSTM model is only about 32% to 33% of that of the traditional models, roughly one-third of the traditional models. In summary, the GWO-LSTM model outperforms traditional time series methods in terms of prediction accuracy. This result fully demonstrates that the model combining the Grey Wolf Optimizer (GWO) with Long Short-Term Memory (LSTM) networks possesses stronger fitting capability and lower prediction error when handling such time series forecasting tasks, exhibiting superior performance advantages.

VIII. CONCLUSION

This study addresses the core characteristics of distributed photovoltaic (PV) power generation systems—namely, the significant influence of meteorological factors and the presence of strong randomness and volatility—by proposing a hybrid forecasting model that integrates the Grey Wolf Optimizer (GWO) with Long Short-Term Memory (LSTM) networks, referred to as GWO-LSTM. A systematic empirical analysis is conducted using a distributed PV system in a region of Guangdong Province as the research object.

In terms of research contributions, this study constructs a comprehensive PV power generation dataset based on daily meteorological data for a location in Guangdong Province in 2025, obtained from the China Meteorological Administration Meteorological Data Center, combined with the parameters of the distributed PV system itself. The Min-Max normalization method is employed for data preprocessing, effectively eliminating dimensional differences among the various feature variables. Additionally, the study systematically compares the predictive performance of three traditional time series forecasting methods against the proposed GWO-LSTM hybrid model, using mean squared error (MSE), root mean squared error (RMSE), and mean absolute error (MAE) as unified model evaluation metrics. Furthermore, by leveraging the Grey Wolf Optimizer to automatically optimize the key hyperparameters of the LSTM model, the hyperparameter selection problem is transformed into a global optimization problem in a multidimensional space, effectively overcoming the limitations of traditional empirical tuning and grid search methods, such as low efficiency and susceptibility to local optima.

Regarding the main findings, the experimental results demonstrate that the GWO-LSTM model significantly outperforms the traditional forecasting methods across all evaluation metrics. Specifically, the MSE is reduced by approximately 85% compared to the traditional methods, the RMSE is reduced to about 38% of that of the traditional methods, and the MAE is only one-third of that of the traditional methods. The average deviation between predicted and actual values is reduced by over 60%. These results fully validate the effectiveness and superiority of the proposed hybrid model in the task of PV power forecasting.

In terms of model advantages, the GWO-LSTM model possesses four core strengths. First, through its unique gating mechanism, LSTM effectively captures long-term and short-term dependencies in time series, enabling accurate learning of the complex nonlinear mapping relationship between PV power and meteorological factors. Second, the GWO algorithm, by simulating the hunting behavior of grey wolf packs, achieves a smooth transition from global exploration to local exploitation, characterized by fast convergence and the ability to effectively avoid local optima. Third, in contrast to traditional time series methods that rely solely on historical power data, the proposed model can incorporate multidimensional meteorological features such as temperature, weather conditions, and sunshine duration, significantly enhancing its adaptability in microgrid scenarios with substantial fluctuations. Fourth, the error analysis indicates that the prediction errors are randomly distributed around the zero-error line without persistent positive or negative bias, demonstrating the model's favorable unbiasedness.

Regarding limitations and shortcomings, although the GWO-LSTM model achieves significantly higher prediction accuracy than traditional methods, this study still has certain limitations. The prediction errors at some time points approach 100% of the actual power, indicating that there remains room for improvement in the model's prediction stability under extreme weather conditions. This study only utilizes meteorological data from a specific region in Guangdong Province for empirical analysis, and the model's generalizability across different regions and diverse climatic conditions has yet to be fully validated. The current model only incorporates basic meteorological

features and does not account for more detailed meteorological variables such as cloud movement trajectories or aerosol concentrations, leaving room for further expansion of the feature dimensions. During the GWO optimization process, the LSTM model must be trained multiple times, and each fitness evaluation requires a complete training process, resulting in relatively high computational time.

In terms of future research directions, subsequent studies can be further explored in the following areas. First, explore the integration of GWO with other optimization algorithms, or introduce attention mechanisms and Transformer architectures to further enhance model prediction performance. Second, combine signal decomposition methods such as empirical mode decomposition (EMD) or variational mode decomposition (VMD) to decompose the original power sequence into multiple subsequences for separate prediction, thereby reducing the impact of sequence non-stationarity on model prediction effectiveness. Third, establish specialized prediction sub-models for extreme weather conditions such as typhoons, heavy rainfall, and prolonged cloudy weather, or introduce uncertainty quantification metrics to evaluate prediction reliability. Fourth, collect PV data from different climatic regions to validate the model's cross-regional generalizability and adaptability. Fifth, deploy the model proposed in this study in actual grid dispatch systems to achieve real-time online prediction updates, providing robust technical support for the accurate integration of distributed PV power and stable grid operation.

In summary, the GWO-LSTM hybrid forecasting model proposed in this study demonstrates significant performance advantages in the task of distributed PV power forecasting, effectively validating the feasibility and effectiveness of integrating swarm intelligence optimization algorithms with deep learning models. Although there remains room for further improvement, this study provides a feasible technical pathway and methodological reference for accurate forecasting of distributed PV systems and optimization of grid dispatch, holding both theoretical value and practical significance for promoting efficient renewable energy integration and ensuring stable power system operation.

ACKNOWLEDGEMENTS

This work was supported by the Research Funding of GDUPT, Research on Heat Transfer Enhancement of Heat Sink by Inverse Calculation Design Method (No. 2019rc074).

REFERENCES

[1]. Ahmed, R., Sreeram, V., Mishra, Y., & Arif, M. D. (2020). A review and evaluation of the state-of-the-art in PV solar power forecasting: Techniques and optimization. Renewable and Sustainable Energy Reviews, 124, 109792.

[2]. Ozdemir, A., & Polat, K. (2025). Optimized CNN-LSTM with hybrid metaheuristic approaches for solar radiation forecasting. Heliyon, *11*(10), e42161.

[3]. Zhao, B. B., Wang, Y., Wang, B., Xuan, W. B., Lei, Z., Ge, L. J., & Xu, X. M. (2019). Research on output power prediction method of distributed photovoltaic system based on ARIMA time series. Renewable Energy, *37*(6), 820-823.

[4]. Kumari, S., & Singh, S. K. (2025). Exploring deep learning methods for solar photovoltaic power output forecasting: A review. Renewable Energy Focus, *53*, 100682.

[5]. Liu, Y., & Zhang, H. (2025). Short-term photovoltaic power prediction based on RF-SGMD-GWO-BiLSTM hybrid models. Energy, *316*, 134545.

[6]. Short-term photovoltaic power prediction based on GWO-CNN-LSTM-MATT hybrid model. (2025). In 2025 3rd International Conference on Power Electronics and Electrical Engineering (PEEE) (pp. 1-6). IEEE.

[7]. Wang, D., Zhang, H., Lin, X., Yu, Y., Zheng, J., & Zhu, J. (2025). A GWO-LSTM based approach for photovoltaic power generation prediction under extreme climate conditions. Journal of Physics: Conference Series, *3163*, 012009.

[8]. Research on photovoltaic power prediction method based on variational mode decomposition and LSTM optimization. (2025). In 2024 IEEE International Conference on Advances in Electrical Engineering and Computer Applications (AEECA) (pp. 1-5). IEEE.

[9]. Yang, Y., Ding, S., & Wu, X. (2025). Optimization of solar power generation prediction based on the XGBoost-LSTM model and the grey wolf optimization algorithm. In 2025 4th International Conference on Power System and Energy Technology (ICPSET) (pp. 1–6). IEEE.

[10]. Dong, M., Li, X. F., Yang, Z., Chang, Y., Ren, M., Zhang, C. X., & Jiao, Z. B. (2024). Research progress of data-driven distributed photovoltaic power prediction methods. Power System and Clean Energy, *40*(1), 8-17+28.

International Journal of Advanced Engineering Research and Science (IJAERS)
Peer-Reviewed Journal
ISSN: 2349-6495(P) | 2456-1908(O)
Vol-13, Issue-4; Apr, 2026
Journal Home Page Available: https://ijaers.com/
Article DOI: https://dx.doi.org/10.22161/ijaers.134.7

Research and Testing Results on the Ability of Certain Compounds to Reduce CS Gas Skin Irritation in Rabbits

Le Đuc Thien*, Ho Minh Trung, Nguyen Manh Hieu, Nguyen Thi Phuong, Tran Van Cong, Le Thi Ha Trang

Institute of Military Environmental Chemistry, Chemical Command, Ha Noi, Viet Nam.

Received: 05 Mar 2026,

Received in revised form: 08 Apr 2026,

Accepted: 11 Apr 2026,

Available online: 14 Apr 2026

***Keywords*— CS gas, Dermal irritation, GHS 2025, In vivo testing.**

***Abstract*—** *This study employs in vivo testing on rabbit skin to evaluate the toxicity and detoxification efficacy of CS gas (o-chlorobenzylidene malononitrile) based on the GHS 2025 standards (Globally Harmonized System of Classification and Labelling of Chemicals, Eleventh revised edition). Test samples were applied via direct dermal permeation to monitor the progression of erythema and edema at fixed intervals of 24, 48, and 72 hours. The research combines experimental tear gas irritation models with simple irritation tests to accurately determine safety profiles and injury recovery capabilities. Results were determined through a standardized scoring system, allowing for the classification of chemical hazard levels according to international categories. The test samples demonstrated significant effectiveness in reducing acute irritation symptoms caused by CS gas in rabbit skin models. By monitoring erythema and edema indices, the irritation-reducing active ingredients significantly shortened epithelial recovery time compared to the control group. Observations at 24, 48, and 72 hours evidenced the ability to soothe the skin, prevent widespread inflammation, and limit deep lesions such as hyperkeratosis or alopecia. Comparison with GHS 2025 scales confirmed that these test samples could lower irritation levels from Category 2 to Category 3 or to a non-irritating status. This provides an important scientific basis for confirming the practical application of these compounds in the safe and effective treatment of lachrymatory agents. The research offers high practical value by establishing a scientific and objective evaluation process for irritation reduction in animal models. Strict application of the latest international standards from GHS 2025 not only ensures accuracy in irritation classification but also enhances the legal validity and reliability of testing results in Vietnam. The efficacy of the test samples was clearly proven through the rapid reduction of inflammatory reactions, erythema, and edema, opening great prospects for developing specialized medical support products. This serves as an important prerequisite for practical applications aimed at protecting human health against potent irritants.*

I. INTRODUCTION

CS gas was first synthesized in 1928 and saw extensive use by the U.S. military during the conflict in Vietnam, with volumes reaching approximately 9,000 tons [2]. Currently, in addition to environmental residues from buried munitions in various regions, CS is utilized by

public security forces in the form of tear gas sprays for maintaining security and order. However, it is an extremely potent irritant capable of causing skin burns, corneal damage, and respiratory issues, with high concentrations posing severe health risks. The dermal impact of CS often results in congestion and blistering [1]. Consequently, researching solutions and detoxification compounds is necessary to protect health from these toxic effects.

The substance causes intense irritation through direct chemical interaction with TRPA1 sensory nerve receptors. Upon contact, CS forms stable covalent bonds with the thiol groups of proteins, causing ion channels to open and inducing membrane depolarization. This process transmits acute burning pain signals to the brain and activates TRPV1 receptors, which are sensitive to heat and capsaicin, prolonging the sensation [3]. This dual impact on the pain receptor system necessitates specialized measures to interrupt the chemical reaction chain.

Current detoxification research focuses on multi-layered mechanisms. Amphoteric properties play a role in neutralizing irritation, while chelating capabilities help prevent the formation of covalent bonds with nerve receptors. Hypertonic characteristics assist in drawing chemical molecules from the epithelium to the surface, and lipid membrane solubility helps remove adhering particles. Combining these mechanisms aims to soothe immediate sensations and prevent inflammatory complications.

This study investigates specific chemicals capable of neutralizing skin irritation caused by CS. A comprehensive evaluation of safety and epithelial recovery is conducted on experimental models to ensure practical applicability. These results provide a scientific basis for selecting optimal components for health protection compounds.

II. RESEARCH CONTENT

2.1. Materials and Equipment

2.1.1. Equipment

- Biomedical digital camera (high resolution, standardized lighting)
- Skinfold thickness gauge (or mini ultrasound device)
- Corneometer (for skin hydration measurement)
- Skin surface pH meter
- Handheld dermatoscope (dermatological microscope)

2.1.2. Chemicals

- CS agent (USA)
- Ammonia; Ethanol; PEG - 400; $NaHCO_3$ (Sodium bicarbonate)

2.1.3. Experimental Models

Tests were conducted on three healthy rabbits in accordance with OECD 404 guidelines and GHS 2025 classification. The skin on both flanks was shaved 24 hours prior to the procedure. Five specific sites were marked: a control site, a site for the irritant spray (CS), and three sites for the irritant spray combined with different irritation-reducing samples. The samples were applied in their original form, sprayed from a distance of 10 cm in three 1-second bursts. Immediately following the irritant application, the reduction samples were applied to their respective sites. After 4 hours, the skin areas were gently cleaned. Dermal reactions were monitored at 1, 24, 48, and 72 hours. The degree of irritation was scored based on erythema and edema (on a scale of 0 to 4) to calculate the mean score and classify the irritation level [4,5].

Table 1. Evaluation Scores of Dermal Irritation in Rabbits

No.	Dermal Reaction	Score
Erythema and Eschar Formation		
1	No erythema	0
2	Very slight erythema (barely perceptible)	1
3	Well-defined erythema	2
4	Moderate to severe erythema	3
5	Severe erythema (beet redness) to eschar formation preventing grading of erythema	4
Edema Formation		
1	No edema	0
2	Very slight edema (barely perceptible)	1
3	Slight edema (edges of area well defined by definite raising)	2
4	Moderate edema (raised approximately 1 mm)	3
5	Severe edema (raised more than 1 mm and extending beyond area of exposure)	4

Table 2. Classification Scale for Dermal Irritation Severity in Rabbits

Reaction Category	Mean Irritation Score (MIS)
Non-irritating	0
Negligible irritant	> 0 - 0,4
Slight irritan	0,5 - 1,9
Moderate irritant	2,0 - 4,9
Severe irritant	5,0 - 8,0

III. RESULTS AND DISCUSSION

3.1. Dermal Irritation Test Results for CS Agent

In the group exposed to the CS agent, erythema appeared 1 hour after skin cleansing. Two subjects showed well-defined reactions, while one showed only very slight effects, indicating individual biological variation within the slight-to-moderate irritation range. After 24 hours, erythema persisted and became more uniform across all three subjects, reflecting an acute transient inflammatory response. By 48 hours, erythema significantly subsided to very slight levels, with no signs of severe damage such as edema, excoriation, or necrosis. After 72 hours, the skin of all subjects returned to normal. These results demonstrate that the CS agent causes temporary dermal irritation, primarily characterized by erythema typical of lachrymatory agents, without causing long-term injury.

3.2. Irritation Reduction Results for Test Sample 1 (Containing Ammonia)

Ammonia (NH_3) reduces the irritant effects of CS by creating a mildly alkaline environment that promotes CS decomposition and diminishes sensory receptor activation. Additionally, NH3 helps mitigate local inflammation and increases fluid secretion, aiding in the rinsing of CS from the contact surface. Results showed that in the Ammonia-treated group, erythema was very slight immediately after cleansing and subsided rapidly. By 24 hours, irritation remained only at a slight level with no strong inflammatory response. Most subjects recovered by 48 hours, and all achieved full recovery by 72 hours. Compared to the control group, Sample 1 significantly reduced both the intensity and duration of the CS-induced reaction.

3.3. Irritation Reduction Results for Test Sample 2 (Containing Sodium Bicarbonate)

Sodium bicarbonate ($NaHCO_3$) mitigates CS irritation by providing a mild alkaline buffer that accelerates decomposition and reduces the stimulatory activity of CS on the skin surface. Simultaneously, $NaHCO_3$ neutralizes local inflammatory responses and assists in dissolving and washing away CS, rapidly alleviating burning sensations. Results for Sample 2 showed very slight to nearly no irritation immediately after cleansing. Within 1 hour, most subjects returned to a normal skin state; by 24 hours, only one subject exhibited very slight erythema. At 48 and 72 hours, all subjects were completely normal with no delayed inflammation or residual irritation. Sample 2 demonstrated superior efficacy and high safety compared to the control group.

3.4. Irritation Reduction Results for Test Sample 3 (Containing Sodium Bicarbonate and Polyethylene Glycol)

The combination of Sodium bicarbonate ($NaHCO_3$) and Polyethylene glycol (PEG) reduces CS irritation through a synergy of chemical and physical mechanisms. While $NaHCO_3$ neutralizes the agent and local inflammation, PEG acts as a solvent and carrier, effectively dissolving and lifting CS from the skin while forming a moisturizing barrier to prevent secondary irritation. Testing showed that immediately after cleansing (approximately 4 hours), the skin of all three subjects was completely normal with no recorded erythema or irritation, whereas the control group still showed well-defined erythema. At the 1, 24, 48, and 72-hour marks, the skin remained stable with no signs of delayed inflammatory reactions or residual irritation.

3.5. Dermal Scoring Results According to OECD Guidelines

Table 3. Mean Skin Reaction Score in Rabbits

Sample	Rabbit		Mean Skin Reaction Score	
	No.	Sex	Erythema score	Edema score
CS toxicant sample	1	♂	1,0	0,0
	2	♂	1,0	0,0
	3	♀	1,0	0,0
Sample 1	1	♂	0,3	0,0
	2	♂	0,7	0,0
	3	♀	0,7	0,0
Sample 2	1	♂	0,0	0,0
	2	♂	0,0	0,0
	3	♀	0,3	0,0
Sample 3	1	♂	0,0	0,0
	2	♂	0,0	0,0
	3	♀	0,0	0,0

Compared to the control group and other test samples, sample No. 3 demonstrated superior anti-irritant efficacy, not only reducing but completely eliminating the symptoms of irritation caused by the CS agent. These results prove that the NaHCO3/PEG mixture possesses high anti-irritant effectiveness, safety, and good skin tolerance, providing an important scientific basis for further research and practical application.

IV. CONCLUSION

The research results initially identified several compounds capable of reducing skin irritation caused by the CS agent on rabbit models, among which Sodium bicarbonate and the Sodium bicarbonate/Polyethylene glycol mixture showed significant efficacy. Tests conducted on rabbit skin models following OECD guidelines demonstrated that the test samples could rapidly reduce erythema levels, shorten the duration of inflammatory responses, and prevent prolonged skin damage. Notably, the $NaHCO_3$/PEG mixture exhibited the highest anti-irritant effect with a mean irritation score of 0, proving excellent tolerance and high safety. These findings help clarify the scientific basis for selecting CS irritant neutralizers while providing critical experimental data for the development of skin decontamination compounds. Furthermore, the study opens up potential applications in chemical safety and the management of tear gas-related incidents in practice.

REFERENCES

[1] S.Franke, Cao Hung Thai "*Chemistry of Military Toxic Agents*", (1984).

[2] "*Chemical Warfare*". The Gale Encyclopedia of Science, năm 2018.

[3] Bert Brone, PieterJ. Peeters, Roger Marrannes, Marc Mercken, Ronny Nuydens, Theo Meert, Harrie J.M. Gijsen "*Tear gasses CN, CR, and CS are potent activators of the human TRPA1 receptor*", (2008).

[4] United Nations "*Globally Harmonized System Of Classification And Labelling Of Chemicals (GHS)*", Geneva, (2025).

[5] *OECD Guideline for the Testing of Chemicals 404 - Acute Dermal Irritation/Corrosion,* (2015).

International Journal of Advanced Engineering Research and Science (IJAERS)
Peer-Reviewed Journal
ISSN: 2349-6495(P) | 2456-1908(O)
Vol-13, Issue-4; Apr, 2026
Journal Home Page Available: https://ijaers.com/
Article DOI: https://dx.doi.org/10.22161/ijaers.134.8

Study of a small-scale system for water desalination and filtration: Reverse osmosis using renewable energy and physicochemical analysis of samples

Estudo de um sistema de pequeno porte para dessalinização e filtragem de água: Osmose reversa com uso de energia renovável e análise físico-quimica de amostras

M. de O. Santos[1], R. A. Menezes Junior[2], M. M. da S. Sá[3], M. G. Nascimento[4], A. C. G. Fernandes[5], L. S. Gomes[6], M. da F. Santana[7], H. da S. Oliveira[8], L. C. M. Nascimento Júnior[9], P. C. de O. Queiroz[10]

[1]Instituto Federal de Sergipe, Lagarto, Sergipe, Brasil.
E-mail: marcos.oliveira@ifs.edu.br; Orcid: https://orcid.org/0009-0007-7659-756X

[2]Universidade Federal da Paraíba, João Pessoa, Paraíba, Brasil.
E-mail: jrmenezes@cear.ufpb.br; Orcid: https://orcid.org/0000-0002-2311-1278

[3]Universidade Federal da Paraíba, João Pessoa, Paraíba, Brasil.
E-mail: marianamirelly2@gmail.com; Orcid: https://orcid.org/0000-0001-5574-4515

[4]Corpo de Bombeiros Militar da Paraíba, Campina Grande, Paraíba, Brasil.
E-mail: fisiconascimento@hotmail.com; Orcid: https://orcid.org/0000-0003-4551-8463

[5]Universidade Federal da Paraíba, João Pessoa, Paraíba, Brasil.
E-mail: amandafernandestt@gmail.com; Orcid: https://orcid.org/0000-0001-8462-6171

[6]Universidade Federal da Paraíba, João Pessoa, Paraíba, Brasil.
E-mail: luciano.silva.gomes@aluno.uepb.edu.br; Orcid: https://orcid.org/0009-0002-2230-9116

[7]Universidade Federal da Paraíba, João Pessoa, Paraíba, Brasil.
E-mail: marfonsecas@hotmail.com; Orcid: https://orcid.org/0000-0002-5497-0147

[8]Universidade Federal da Paraíba, João Pessoa, Paraíba, Brasil.
E-mail: humberto.ufpb@gmail.com; Orcid: https://orcid.org/0009-0003-5633-6347

[9]Universidade Federal da Paraíba, João Pessoa, Paraíba, Brasil.
E-mail: luizcarlospb@yahoo.com.br;
Orcid: https://orcid.org/0009-0009-4622-234X

[10]Universidade Federal do Maranhão, São Luis, Maranhão, Brasil.
E-mail: pc.ufma@gmail.com
Orcid: https://orcid.org/0000-0002-8905-1757

Received: 04 Mar 2026,

Received in revised form: 06 Apr 2026,

Accepted: 12 Apr 2026,

Available online: 16 Apr 2026

Keywords*— *CS gas, Dermal irritation, GHS 2025, In vivo testing.

Keywords* — *Reverse Osmosis, Renewable Energy, Water Treatment, Physicochemical Analysis, Small-Scale System, Water Sustainability, Water Filtration, Drinking Water, Energy Efficiency

Palavras-chave*— *Osmose Reversa, Energia Renovável, Tratamento de Água, Análise Físico-Química, Sistema de Pequeno Porte, Sustentabilidade Hídrica, Filtragem de Água, Água Potável, Eficiência Energética

***Abstract*— *This article addresses the study, development, and evaluation of a small-scale system for water desalination and filtration, using reverse osmosis integrated with a renewable hybrid energy system. The main objective of the research is to propose an efficient and sustainable system for water treatment in areas facing water scarcity, with a specific focus on the interior of the State of Sergipe, Brazil. The methodology employed combines bibliographic research with experimental research. Water samples were collected and analyzed from an artesian well located in the municipality of Estância, between 2020 and 2022. Water quality analyses were performed in a laboratory environment, before and after the desalination process. The desalination system used employed a small-scale reverse osmosis filter with a flow rate of 16 liters per hour. This water processing system was integrated into a Hybrid Energy System (HES) that uses photovoltaic solar and wind energy to operate the water pump, the cooling system, and the reverse osmosis filter. Furthermore, the study included modeling the energy production for the hydroelectric power plant, based on historical wind speed and solar irradiance data from 1990 to 2020 in regions of the State of Sergipe. The results of the water quality analyses demonstrated the effectiveness of the desalination process. There was a considerable reduction in chloride concentrations (from 50.13 mg/L to 3.71 mg/L) and sodium (from 43.27 mg/L to 3.42 mg/L). The concentration of total dissolved solids also decreased significantly (from 395.1 mg/L to 30.46 mg/L). Physicochemical parameters such as total hardness (from 300 mg/L to 29.74 mg/L) and apparent color (from 31.9 mg/L to 5.4 mg/L) showed drastic reductions and significant improvement, respectively. The process did not alter the concentration of most of the analyzed metals, sulfates, nitrites, and total selenium, with the exception of manganese, which had its concentration reduced. The pH of the water varied slightly from 7.84 to 6.00, but remained within the acceptable limit for potability according to Brazilian legislation. Regarding the system's energy demand, estimated at 57.6 kWh/month, the modeling demonstrated that the average monthly photovoltaic energy production was sufficient to meet this need. Wind energy production in the region was considered less viable due to low production and high cost. In conclusion, the study validated the viability of the desalination system under study, powered by renewable energy, as a promising alternative to guarantee access to potable water in a sustainable way in regions with water scarcity. The results in improving water quality and the adequacy of renewable energy supply support the proposal.*

Resumo*— *O presente artigo aborda o estudo, desenvolvimento e avaliação de um sistema de pequeno porte para dessalinização e filtragem de água, utilizando a técnica de osmose reversa integrado a um sistema de energia híbrida renovável. O objetivo principal da pesquisa é propor um sistema eficiente e sustentável para o tratamento de água em áreas que enfrentam escassez hídrica, com foco específico no interior do Estado de Sergipe-Brasil. A metodologia empregada combina pesquisa bibliográfica com pesquisa experimental. Amostras de água foram coletadas e analisadas de um poço artesiano localizado no município de Estância, entre os anos de 2020 e 2022. As análises da qualidade da água

foram realizadas em ambiente laboratorial, antes e após o processo de dessalinização. O sistema de dessalinização utilizado empregou um filtro de osmose reversa de pequeno porte, com vazão de 16 litros por hora. Este sistema de processamento de água foi integrado a um Sistema de Energia Híbrida (SHE) que utiliza energia solar fotovoltaica e eólica para operar a bomba d'água, o sistema de refrigeração e o filtro de osmose reversa. Além disso, o estudo incluiu a modelagem da produção de energia para o SHE, baseada em dados históricos de velocidade do vento e irradiação solar de 1990 a 2020 em regiões do Estado de Sergipe. Os resultados das análises de qualidade da água demonstraram a eficácia do processo de dessalinização. Houve uma redução considerável nas concentrações de cloretos (de 50,13 mg/L para 3,71 mg/L) e sódio (de 43,27 mg/L para 3,42 mg/L). A concentração de sólidos dissolvidos totais também diminuiu significativamente (de 395,1 mg/L para 30,46 mg/L). Parâmetros físico-químicos como dureza total (de 300 mg/L para 29,74 mg/L) e cor aparente (de 31,9 mg/L para 5,4 mg/L) apresentaram reduções drásticas e expressiva melhora, respectivamente. O processo não alterou a concentração da maioria dos metais analisados, sulfatos, nitritos e selênio total, com exceção do manganês, que teve sua concentração reduzida. O pH da água variou ligeiramente de 7,84 para 6,00, mas permaneceu dentro do limite aceitável para potabilidade segundo a legislação brasileira. Em relação à demanda energética do sistema, estimada em 57,6 KWh/mês, a modelagem demonstrou que a produção média mensal de energia fotovoltaica foi suficiente para atender essa necessidade. A produção de energia eólica na região foi considerada menos viável devido à baixa produção e alto custo. Em conclusão, o estudo validou a viabilidade do sistema de dessalinização estudo, alimentado por energia renovável como alternativa promissora para garantir o acesso à água potável de forma sustentável em regiões com escassez hídrica. Os resultados na melhoria da qualidade da água e na adequação da oferta energética renovável sustentam a proposta.

I. INTRODUÇÃO

Segundo dados da Agência Nacional de Águas – ANA, órgão do governo brasileiro, 97,5% da água existente no mundo é salgada, e portanto, não adequada ao consumo direto, nem à irrigação. Além disto, dos 2,5% de água doce, 69% estão nas geleiras e 30% são águas subterrâneas, sendo só 1% de fácil acesso, em rios e lagos. O Brasil possui 12% da água doce, mas a distribuição natural deste recurso não é equilibrada. A região Norte, por exemplo, concentra cerca de 80% desta água, mas representa apenas 5% da população brasileira; já as regiões centrais e as próximas ao litoral, possuem mais de 45% da população, e menos de 3% dos recursos hídricos do país (ANA, 2020).

A perfuração de poços artesianos é uma das técnicas de obtenção de água mais antigas do mundo, muito comum em todo mundo, havendo registros de mais de 10.000 anos atrás que comprovam a busca do homem por águas subterrâneas (Kavand et al., 2023). Dos programas desenvolvidos pelo governo brasileiro para fornecer água às comunidades residentes em áreas que sofrem com a seca e a estiagem, como o "Polígono das Secas", na região nordeste do Brasil, destacam-se aqueles voltados à instalação de cisternas e perfuração de poços (Oliveira et al., 2021).

Um fator importante para classificação da água de um poço ou de uma cisterna como utilizável para o seu uso é a verificação da qualidade da mesma. Tal verificação se dá por meio da análise de características físico-químicas, pois a água obtida dessa forma pode conter parâmetros com valores indesejados, tornando inviável sua utilização para determinados fins. A salinidade é outro parâmetro a ser observado, pois a água salobra pode fazer mal à saúde animal e vegetal e, a longo prazo, acarretar em alterações dos parâmetros do solo quando usada na irrigação (Dias, Melo & Oliveira, 2020).

Neste contexto, o presente artigo tem por objetivo o estudo de um sistema protótipo de dessalinização, filtragem, refrigeração e bombeamento da água de forma eficiente,

com uso de energia híbrida renovável a ser utilizado em poços localizados no interior do estado de Sergipe.

II. METODOLOGIA

2.1 Tipo de pesquisa, onde e quando foi realizada

Este artigo traz uma pesquisa de carater bibliográfico, pois baseia-se em dados contidos em textos científicos e bases de dados provenientes de satélite. Também apresenta um perfil de uma pesquisa experimental, pois nesta foram realizados testes para levantamento de informações, tanto em campo, quanto em ambiente laboratorial. Quanto ao poço artesiano analisado, o mesmo está localizado no municipio de Estância, no Estado de Sergipe, situado no Nordeste brasileiro.

As amostras de água foram coletadas e analisadas em um poço no Estado de Sergipe, de 2020 a 2022, cuja água vem à superfície através de bombeamento. A coleta e testes foram realizados no munícipio de Estância (vide Figura 1), no mês de Novembro de 2020. O experimento foi feito sazonalmente, com objetivo de verificar possíveis variações nos resultados dos parâmetros.

Fig.1: Localidades do estudo no estado de Sergipe

2.2 Sistema de dessalinização

Para tratamento da água com a finalidade de remoção de contaminação por particulados, a fim de torná-la potável, foi empregado um filtro de osmose reversa de pequeno porte, com uma vazão de 16 litros por hora (Figura 2).

Fig.2: Filtro de osmose reversa pequeno porte

2.3 Sistema Híbrido de Energia (SHE)

O sistema consistirá em quatro componentes principais, organizados da seguinte maneira: os painéis fotovoltaicos e o aerogerador montados em uma estrutura de suporte, com cabeamento para transporte de tensão e corrente ao sistema de monitoramento e controle.

O painel solar utilizado tem dimensões 200 cm x 100 cm x 4 cm, do tipo policristalino, com uma potência de pico de 350 W. O aerogerador, por sua vez, tem 4 hélices do tipo vertical, com 600 W de potência de pico. Tanto o painel solar, quanto o aerogerador, encontram-se representados na figura 3.

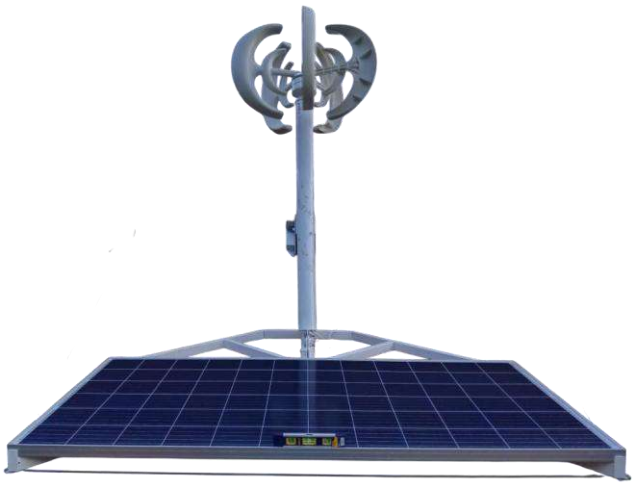

Fig.3: Sistema de Energia Híbrida Renovável

2.4 Integração do Sistema de Dessalinização com o Sistema Híbrido de Energia

O sistema de processamento da água foi integrado ao sistema híbrido de energia apresentado, a fim de bombear, resfriar e filtrar. Para seleção correta do equipamento, levou-se em consideração diversos critérios, a saber: (i) vazão de produção de água dessalinizada em determinado período; (ii) tipo de membrana a ser utilizada no processo de osmose reversa; e (iii) demanda de água da localidade.

Devido a tais dessalinizadores terem custo elevado, esta pesquisa visa constituir um sistema de baixo custo que seja adequado para atender uma demanda menor, pelo uso do SHE da Figura 3. Acredita-se que a partir destes processos, seja possível obter água potável de água salobra de poço.

2.5 Análise da qualidade da água

Para analisar a qualidade da água, fizeram-se coletas da mesma, antes e após o processo de dessalinização, e depois disto, levou-se cada coleta para ser analisada em ambiente laboratorial para estudo da concentração de determinados elementos químicos e observação de certas propriedades físico-químicas, listadas no quadro da figura 4.

Parametros Analisados		
Ensaio	Padrão	Unidade
Antimônio	0,01	mg Sb/L
Arsênio	0,01	mg As/L
Cádmio Total	0,00	mg Cd/L
Chumbo Total	0,01	mg Pb/L
Cromo Total	0,05	mg Cr/L
Cobre Total	2,00	mg Cu/L
Ferro Total	0,30	mg Fe/L
Manganês Total	0,10	mg Mn/L
Alumínio Total	0,20	mg Al/L
Níquel Total	0,07	mg Ni/L
Zinco Total	5,00	mg Zn/L
Bário Total	0,70	mg Ba/L
pH	4-10	6,0 a 9,0
Cor Aparente	15,00	uT
Sólidos Dissolvidos Totais	500,00	mg/L
Dureza Total (mg CaCO3/L)	300,00	mg CaCO3/L
Sódio	200,00	mg Na/L
Cloretos RBLE	250,00	mg Cl/L

Fig.4: Propriedades físico-químicas analisadas

Para uma melhor compreensão da análise da qualidade da água, ela foi dividida em duas etapas: (I) verificação de concentração e propriedades da água do poço sem passagem pelo processo de dessalinização (Figura 5); e (II) verificação de propriedades da água de poço processada por meio do sistema proposto (Figura 6).

Nesta primeira etapa, a água do poço é bombeada até o conjunto filtro-refrigerador. A bomba funcionará a partir da energia elétrica proveniente de baterias, que armazenam a energia híbrida renovável captada no SHE proposto neste trabalho. Parte desta energia será usada para refrigeração da água (Figura 5).

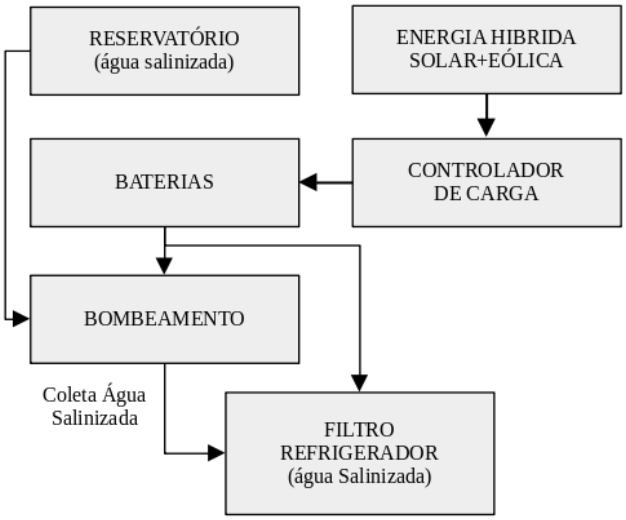

Fig.5: Coleta de água salinizada para análise

Já na segunda etapa, apesar da água do poço também ser bombeada, ela passa pelo dessalinizador (Figura 2) antes de ser levada ao filtro refrigerador. Semelhantemente a etapa anterior, tanto o bombeamento, quanto a refrigeração e a filtragem da água serão realizadas a partir da energia elétrica advinda da energia híbrida renovável captada no SHE proposto (Figura 6).

Fig.6: Coleta de água dessalinizada para análise

Para etapa da análise da água salinizada, foram feitos três gráficos de barra, sendo dada a cor vermelha às barras. O primeiro gráfico contem o nome dos elementos químicos nas ordenadas, enquanto que nas abscissas foram inseridas as concentrações em mg/L (Figura 7).

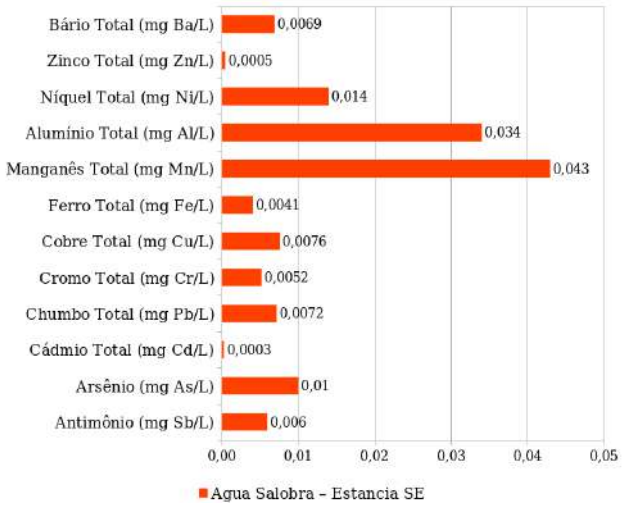

Fig.7: Gráficos de concentração de elementos químicos em mg/L – análise de água salinizada

No segundo e no terceiro gráfico, por conseguinte, foi dado destaque a propriedades físico-químicas comumente observadas nas análises da qualidade da água em geral, tais como dureza total, cor aparente e pH, dentre outras, todas expressas nos gráficos da figura 8.

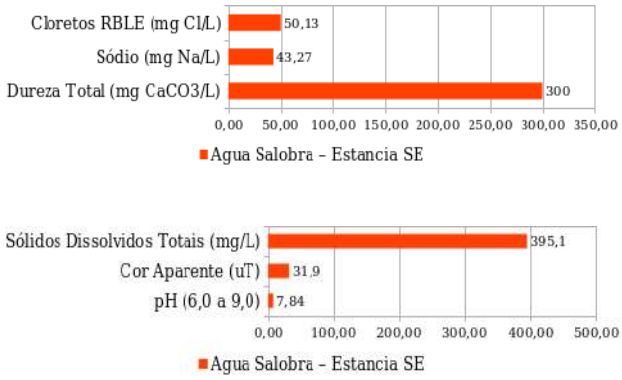

Fig.8: Gráficos de propriedades físico químicas – análise de água salinizada

Na etapa da análise da qualidade da água dessalinizada, foram feitos três gráficos idênticos aos contruídos na etapa anterior, inclusive envolvendo dados das mesmas grandezas e unidades, contudo foi dada a cor azul a cada barra. O primeiro gráfico também apresenta os elementos químicos no eixo das ordenadas e as concentrações de cada um deles nas abscissas (figuras 9).

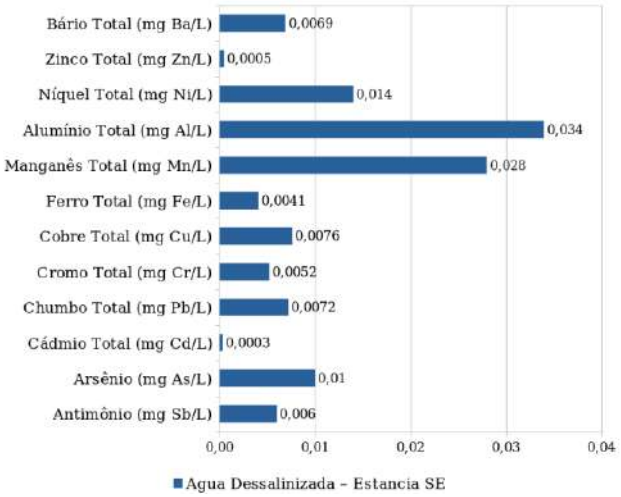

Fig.9: Gráficos de concentração de elementos químicos em mg/L – análise de água dessalinizada

Nos dois últimos gráficos foram destacados as mesmas propriedades físico-químicas observadas na etapa da análise da água salinizada, como pode ser observado na figura 10.

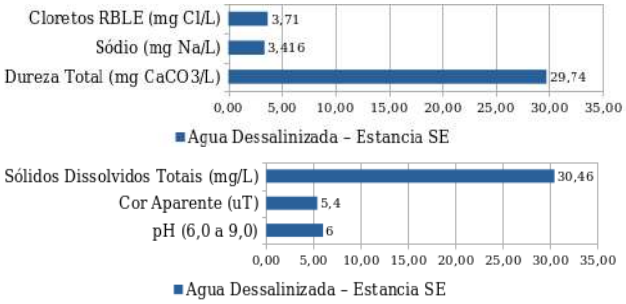

Fig.10: Gráficos de propriedades físico químicas – análise de água dessalinizada

Os gráficos das figuras 7 e 9 comparam as concentrações dos vários elementos químicos (em mg/L) numa amostra de água antes e após a dessalinização. Por sua vez, os gráficos das figuras 8 e 10 apresentam concentrações dos principais indicadores de salinidade e qualidade organoléptica (Cor Aparente e pH) da amostra. Esta análise é essencial para quantificar a remoção de sais e avaliar se a dessalinização fez com quer a água atingisse os padrões de consumo.

2.6 Demanda energética do sistema

Para o levantamento da demanda de energia do sistema, considerou-se 01 bomba de dessalinização e 01 bomba para extrair água do reservatório para superfície, ambas de 48W (0,065 CV), funcionando em torno de 8 horas por dia; além disso, 01 sistema de refrigeração composto por 04 condensadores de 24W funcionando por 12 horas diárias.

A tabela da figura 11 traz a descrição de cada item que utiliza energia elétrica em seu funcionamento, bem como, o tempo de funcionamento diário e o consumo médio mensal

de cada um deles. Nas condições postas, a potência total demandada pelo sistema de processamento da água gira em torno de 57,6 KWh/mês.

Calculo de Demanda do Sistema de Dessalinizaçao, Tratamento e Refrigeraçao					
Elemento	Bombas	Tensão (Volts)	Corrente (Amper)	Tempo Funcionamento (h/dia)	Potencia Demanda (Kwh/mês)
Bomba Dessalinizador	1,0	24,0	2,0	8,0	11,5
Bomba Reservatorio	1,0	24,0	2,0	8,0	11,5
Sistema de Refrigeração	4,0	12,0	2,0	12,0	34,6
Demanda Total Instalada					57,6

Fig.11: Levantamento da potência de demanda do sistema

2.7 Modelagem da produção energética

No modelo de previsão de potência energética fotovoltaica, foi usada a média da irradiância (*short wave*) em W/m^2 para cada mês do ano, desde janeiro de 1990 a dezembro de 2020. Para prognóstico da potência energética eólica, foi usada a média das velocidades do vento em *m/s* para cada mês do ano do mesmo período.

Processamento de dados e Modelo de previsão de potência do sistema fotovoltaico

No que diz respeito à previsão de potência do sistema solar, a análise foi feita com base em dados de radiação solar nas coordenadas geográficas de latitude de 11º23'54"S e longitude de 37º18'55"W (Cidade de Estância – SE), a uma elevação média de 53 metros em relação ao nível do mar. Esses dados foram adquiridos e processados usando imagens de satélite armazenados na base de dados *Terraclimate* pelo uso de programação *JavaScript*, no período que vai de janeiro de 1990 a dezembro de 2020 (Figura 12).

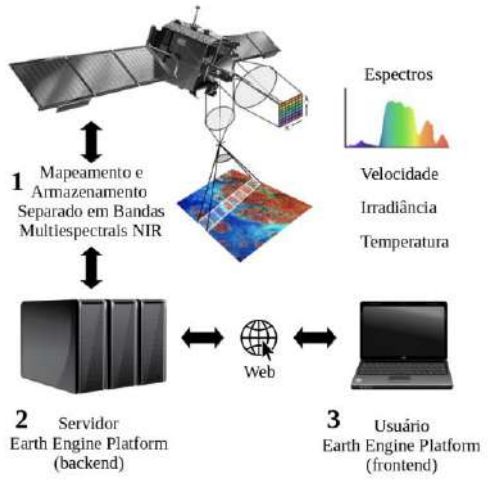

Fig.12: Mapeamento, armazenamento e processamento de dados

O estudo da previsão da potência solar envolveu a consideração do modelo de comportamento elétrico do painel fotovoltaico, representado por um circuito que combina uma fonte de corrente em paralelo com um diodo (modelo de diodo).

Foram adicionadas duas resistências para representar a resistência elétrica entre os contatos da célula e a corrente de fuga do diodo. É importante notar que a corrente fotoelétrica varia linearmente com a temperatura e mantém uma relação diretamente proporcional com a irradiância. Em geral, essa corrente é determinada com base em condições padronizadas (G_n = 1000 W/m^2 e T_n = 25ºC).

Processamento de dados e Modelo de previsão de potência do sistema eólico

Partindo-se do princípio de que o vento possui energia cinética mensurável em função da velocidade, a previsão de potência do sistema eólico foi feita com base nos dados de velocidade do vento obtidos nas coordenadas de latitude e longitude do município de Estância. Os dados relativos ao período de início do ano de 1990 ao final do ano de 2020 foram extraídos e processados a partir do mesmo conjunto de imagens de satélite usados no modelo de previsão de potência do sistema fotovoltaico, a partir da linguagem de programação *JavaScript* (Figura 12). Contudo, deve-se explicitar que não é possível converter em potência efetiva toda potência presente na velocidade do vento que passa através das pás que fazem girar o gerador eólico. Assim, adotou-se o modelo de Betz, quanto à limitação na conversão de potência total em potência efetiva (~ 59,3%) (Freitas, Oliveira & Santos, 2023).

Predições do sistema híbrido fotovoltaico e eólico

Na construção dos gráficos de potência energética fotovoltaica, eólica e total do Sistema, foi realizado um tratamento estatístico a partir dos dados adquiridos, os quais foram expostos por espectros, de maneira que a combinação deles levou à obtenção das variáveis analisadas (Figura 13).

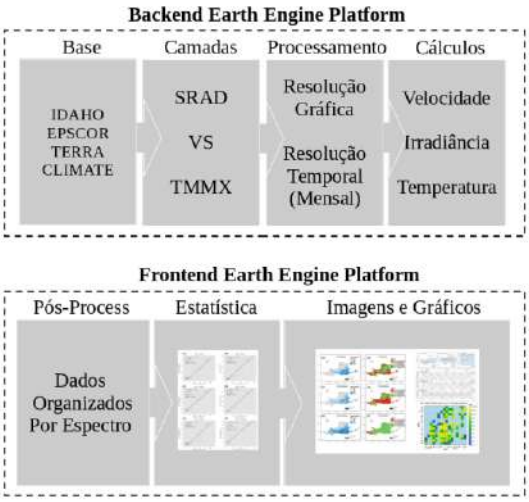

Fig.13: Esquema de tratamento estatístico

Para estudo da capacidade da produção energética, fotovoltaica e eólica no município em estudo, foram construídos dois gráficos para cada fonte de energia. No primeiro gráfico foram expressos no eixo das abscissas os meses do ano, enquanto que no eixo das ordenadas, foram destacadas uma curva para cada ano, de 1990 até 2020, concernente à irradiância média mensal, no gráfico da potência fotovoltaica, e à velocidade média mensal do vento, no gráfico da potência eólica, totalizando 31 curvas.

No segundo gráfico, por sua vez, foram postos no eixo das abscissas os meses do ano, já no eixo das ordenadas, foi destacada uma única curva referente a potência mensal média de Janeiro a dezembro, sendo este valor da média composto pelos valores das potências dos meses entre Janeiro de 1990 a dezembro de 2020.

Finalmente, para expressar a potência total possível de ser gerada pelo SHE em questão, foi feito um gráfico, no qual no eixo das abscissas apareceram os meses do ano, já no eixo das ordenadas, foram expressas a potência. No gráfico, foram constituído três curvas: duas tracajadas e uma contínua. Dentre as curvas tracejadas, a de cor azul representa a potência mensal média eólica, enquanto que a de cor verde representa a potência mensal média fotovoltaica. A curva contínua, por sua vez, representa a potência mensal média total do Sistema Híbrido, expressa na cor vermelha.

III. RESULTADOS

3.1 Qualidade da água

Os dados comparativos apresentados nas Figuras 7 e 9, detalham as concentrações de doze elementos químicos em miligramas por litro (mg/L) em uma amostra de Água Salobra (Figura 7) e Água Dessalinizada (Figura 9), ambas provenientes da cidade de Estância – SE. A principal observação é a redução seletiva na concentração do Manganês Total (Mn), que diminuiu de 0,043 mg/L na água salobra para 0,028 mg/L na água dessalinizada, redução esta percebida com clareza na figura 14, o qual apresenta os dados das Figuras 7 e 9 em um único gráfico. Tal redução de aproximadamente 34,9% sugere que o Manganês, que é frequentemente um contaminante que causa problemas estéticos a água (cor e sabor) e incrustações, foi parcialmente removido pelo sistema de dessalinização ou por uma etapa de pré-tratamento específica (como oxidação seguida de filtração).

(metais)

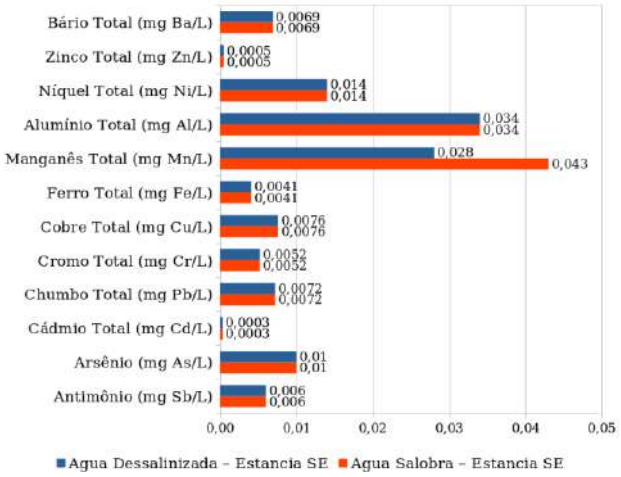

Fig.14: Comparação antes e após a dessalinização

Também foram observados concentrações de cloretos e de sódio, além da concentração de sólidos dissolvidos totais. Tanto o cloreto, quanto o sódio, mostraram uma considerável redução de suas concentrações.

Conforme se observa nas figuras 15 e 17, os cloretos passaram de 50,13 mg/L a 3,71 mg/L, uma redução de mais de 92,6%. O sódio, por sua vez, passou de 43,27 mg/L para 3,42 mg/L, aproximadamente, obtendo-se uma redução em sua concentração de mais de 92,1%. Não diferente dos cloretos e do sódio, a filtragem fez com que houvesse uma grande diminuição também na concentração dos sólidos dissolvidos, que passaram de uma concentração de 395,1 mg/L para 30,46 mg/L.

Figura 15: Comparação antes e após dessalinização (cloretos, sódio e sólidos dissolvidos)

Outrossim, foram vistas ainda propriedades físico-químicas mais destacadas em caso de tratamento de água, tais como dureza total, cor aparente e pH, também expressas nos gráficos das figuras 15 e 17.

A dureza total sofreu uma redução drástica, em razão da diminuição de partículas sólidas no fluido, passando de 300 mg/L para 29,74 mg/L. Já a cor aparente apresentou uma expressiva melhora, passando de 31,9 mg/L para 5,4 mg/L, deixando de ter uma coloração escura para assumir um aspecto límpido e tranparente (Figura 16).

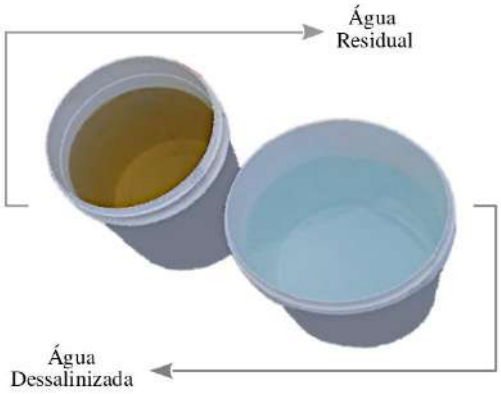

Fig.16: Cor aparente antes e após o processo de dessalinização

A taxa de recuperação é calculada pela razão entre a quantidade de água convertida em água purificada e a quantidade de água processada. Em geral, os valores de taxa de recuperação ficam em torno de 50% (Khare & Bhuiyan, 2022):

$$r(\%) = \left(\frac{Q_p}{Q_a}\right) \cdot 100 \qquad \text{(Equação 1)}$$

Onde:

r — Nível de recuperação do sistema (%)
Q_p — Vazão recuperada (m³/h)
Q_a — Vazão processada (m³/h)

Finalmente, notou-se que o pH sofreu uma variação, contudo pequena, indo de uma condição um pouco básica (7,84) para um pouco ácida (6).

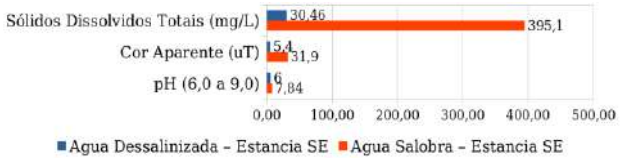

Fig.17: Comparação de Propriedades Físico-químicas (Dureza total, Cor aparente e pH)

3.2 Capacidade de produção de energia fotovoltaica e eólica

O gráfico da figura 18 demonstra a potência energética fotovoltaica mensal média entre 1990 e 2020, e nele está evidenciado que os meses de menor produção energética está em junho e julho de cada ano, com média entre 125W e 130W. Já os picos de produção ocorrem nos meses de novembro, dezembro, janeiro e fevereiro, com média de produção acima dos 180W.

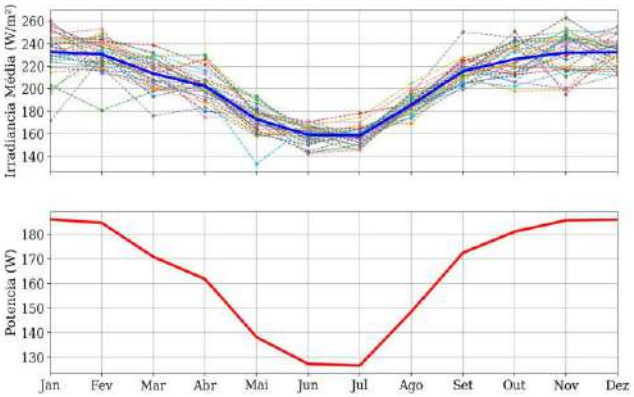

Fig.18: Potência média de 1990 a 2020 (Energia fotovoltaica)

Com relação a potência energética eólica mensal média de 1990 a 2020, o gráfico da figura 19 revela que os meses de valores produtivos menores são novembro e dezembro, com apenas 10W de produção, já os meses de junho e julho apresentam maior nível de produção, com média entre 30W e 35W de potência.

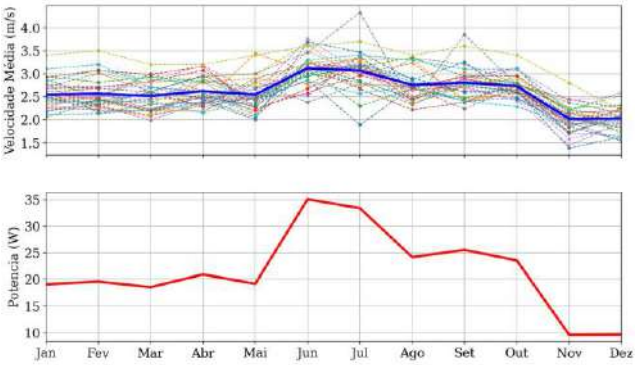

Fig.19: Potência média de 1990 a 2020 (Energia eólica)

Quando se faz uma análise de produção energética associada com geração eólica e fotovoltaica, obtém-se o gráfico da figura 20. Neste, nota-se que somadas, estas formas de energia são capazes de produzir entre 150W e 205W de potência energética mensal média, sendo os meses de maio, junho e julho aqueles com menor índice de produção, enquanto que os meses de janeiro, fevereiro, setembro, outubro, novembro e dezembro são aqueles com maior nível de produção, ficando em torno dos 200W de potência produzida.

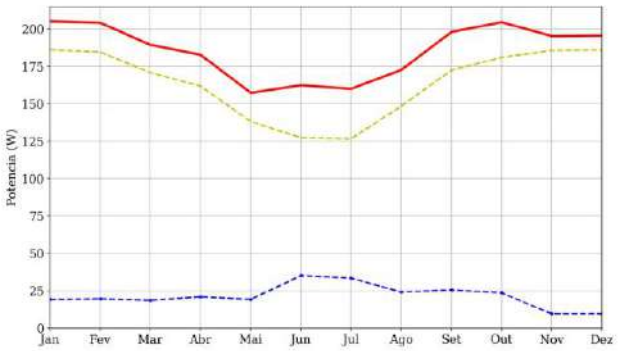

Fig.20: Potência média de 1990 a 2020 (Energia eólica-fotovoltaica)

IV. DISCUSSÃO

A partir dos resultados obtidos, nota-se que com relação a proposta de dessalinização de água salobra, o filtro selecionado e o processo adotado se mostrou satisfatório para tornar a água livre de maior parte dos cloretos e sais, além de propiciar enorme redução de partículas sólidas presentes nas amostras.

Destaca-se a estabilidade da concentração de outros elementos analisados, incluindo os cátions alumínio total (0,034 mg/L), níquel total (0,014 mg/L) e bário total (0,0069 mg/L), e os ânions do Arsênio (0,010 mg/L). Tal inalteração na maioria dos elementos pode ser pela: (i) baixa concentração inicial (Fe, Cu, Cr, Pb, Cd, Sb e Zn) (≤0,01 mg/L), podendo a precisão de metodologia analítica ser insuficiente para detectar variações significativas em níveis tão residuais; (ii) forma química do elemento, pois a eficiência da remoção em processos de dessalinização depende do tamanho e da carga iônica; e (iii) seletividade do processo em si, podendo ter feito o sistema de tratamento ser otimizado para o Manganes, que, em geral, é um elemento problemático

O processo mostrou elevadíssima eficácia na remoção de sais e íons responsáveis pela salinidade e dureza, atingindo eficiências superiores a 90% para SDT, Dureza Total, Cloretos e Sódio. A concentração de SDT foi reduzida de 395,1 mg/L para 30,46 mg/L. O valor final de 30,46 mg/L está bem abaixo do Valor Máximo Permitido (VMP) para SDT em água potável (500 mg/L segundo a legislação brasileira), confirmando o sucesso da dessalinização.

A dureza total passou de 300 mg/L (CaCO3) ("água dura") para 29,74 mg/L ("água mole"), indicando excelente rejeição de íons divalentes como Cálcio (Ca2+) e Magnésio (Mg2+), responsáveis pela incrustação e pelos problemas associados à dureza. A remoção de Cloretos e Sódio em mais de 92% demonstra a capacidade do sistema em rejeitar os principais íons que caracterizam a água salobra. O valor final de 3,71 mg/L de Cloretos também está muito abaixo do VMP organoléptico (250 mg/L).

Em relação a cor aparente, houve uma redução significativa de 31,9 uT para 5,4 uT. O valor de 5,4 uT é muito próximo do padrão ideal de potabilidade, que é ter uma cor inferior a 5 uT (Unidade Hazen, ou uH). O pré-tratamento ou a filtração do sistema foi eficiente na remoção de matéria orgânica ou coloidal responsável pela cor.

Quanto ao pH, ele passou de 7,84 (levemente alcalino) para 6,0 (levemente ácido), tal variação não torna a água imprópria ao consumo, já que segundo o Ministério da Saúde do governo brasileiro, este pH está dentro do patamar aceitável para que a água seja considerada potável (Dias, Melo & Oliveira, 2020).

Para se definir a potência energética necessária para se realizar o bombeamento, refrigeração e filtragem da água foi considerado a potência individual de cada elemento que compõe o sistema de dessalinização, sendo observado que para realização deste trabalho, é preciso, no mínimo, uma potência de 57,6 KWh/mês (figura 11).

A fim de se reduzir o risco de ocorrência de déficit de energia durante o fornecimento da mesma ao sistema, admitiu-se neste estudo, um fator de segurança de pelo menos 25% quanto a potência gerada para atender a demanda.

Considerando-se a produção energética do SHE adotado, é possível dizer que a mínima quantidade de energia para bombear, resfriar e filtrar a água conforme proposto, de modo que o suprimento energético seja satisfatório e sem risco de déficit energético, é de cerca de 72,0 KWh/mês.

Contudo, avaliando-se o valor médio mensal de energia fotovoltaica produzidos por m² de área de placa solar, chegou-se a quantidade de 4 m² de área como sendo o mínimo necessário para atender a toda a demanda do sistema. O valor médio de potência produzida por mês através da energia eólica por m² de área varrida pelas hélices do aerogerador, mostra-se baixo quando comparado à potência produzida pela área do sistema solar. A quantidade de energia disponibilizada pelo SHE através das placas solares é superior e mais que suficiente para atender as demandas de energia e o fator de segurança adotado.

Além do mais, em razão da baixa produção de energia por meio do aerogerador e do elevado valor de compra e manutenção do mesmo, a relação custo-benefício torna pouco viável o uso desta forma de energia, já que 4 m² de placa solar são capazes de proporcionar uma produção entre 91,4 KWh/mês e 130,3 KWh/mês, bem além do valor mínimo necessário, conforme se observa na tabela da figura 21 e no gráfico da figura 22.

Calculo da Geração de Energia Solar Médio					
				Area de Paineis Solares (m²)	4,0
Mês	Potencial de Geracao (Kw/m²)	Tempo Geracao (h/dia)	Potencia Gerada (Kwh/dia/m²)	Potencia Gerada (Kwh/mês/m²)	Potencia Gerada Total (Kwh/mês)
Jan	0,181	6,0	1,1	32,6	130,3
Fev	0,178	6,0	1,1	32,0	128,2
Mar	0,173	6,0	1,0	31,1	124,6
Abr	0,168	6,0	1,0	30,2	121,0
Mai	0,135	6,0	0,8	24,3	97,2
Jun	0,127	6,0	0,8	22,9	91,4
Jul	0,127	6,0	0,8	22,9	91,4
Ago	0,150	6,0	0,9	27,0	108,0
Set	0,175	6,0	1,1	31,5	126,0
Out	0,178	6,0	1,1	32,0	128,2
Nov	0,179	6,0	1,1	32,2	128,9
Dez	0,179	6,0	1,1	32,2	128,9

Fig.21: Potência média gerada (Energia fotovoltaica)

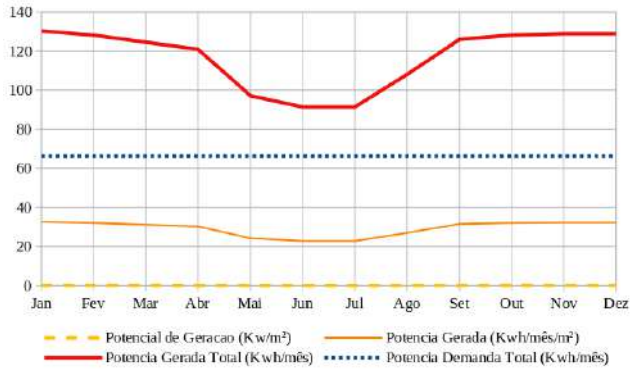

Fig.22: Grafico de Potência média gerada e demandada (Energia fotovoltaica)

O mesmo estudo de capacidade energética realizado para a cidade de Estancia, também foi realizado para as cidades de Lagarto, Carmopolis e Poço Redondo obtendo se os resultados mostrados na Figura 22.

Fig.22: Potência média energia eólica-fotovoltaica

V. CONCLUSÃO

Os gráficos indicam que o processo de dessalinização aplicado na amostra do municipio de Estância – SE demonstrou eficácia parcial e seletiva na remoção de elementos traço. A principal melhoria na qualidade da água, no que tange a estes contaminantes específicos, foi a redução do Manganês Total em cerca de 35%.

A estabilidade de outros elementos, notadamente o Alumínio e o Níquel, em concentrações idênticas entre a água salobra e a dessalinizada, levanta questões sobre a forma química em que esses elementos estão presentes e a capacidade da tecnologia empregada em removê-los efetivamente.

Os resultados alcançados na análise da qualidade da água demonstraram eficácia na melhoria da potabilidade, tanto pela remoção dos sais primários (Sódio, Cloreto, Dureza), quanto pela redução da SDT e da Cor Aparente, resultando em uma água de alta pureza química.

O pH da água, por sua vez, sofreu uma alteração, deixando de ter um teor pouco básico para pouco ácido. A queda no pH e a consequente acidificação da água pós-dessalinização é um fenômeno típico em sistemas de osmose reversa, onde a desmineralização e a remoção da alcalinidade (bicarbonatos) facilitam a dissolução de CO_2 na água, formando ácido carbônico. Esta água ácida pode ser corrosiva às redes de distribuição e, portanto, haveria necessidade de uma etapa final de remineralização e ajuste

de pH (pós-tratamento) para se adequar plenamente aos padrões de potabilidade.

Em relação ao suprimento energético em resposta a demanda (57,6 KWh/mês), a modelagem da produção de energia do Sistema de Energia Híbrida (SHE) possui uma previsibilidade mais que suficiente para atendê-la, isto já considerando um fator de segurança **de 25%**. O estudo indicou que a energia gerada pelas placas solares possui quantidade superior e satisfatória ao funcionamento do sistema. Já, a produção de energia eólica foi considerada baixa, tornando esta fonte menos viável do ponto de vista energetico.

A partir do que fora exposto, conclui-se que os resultados obtidos na melhoria da qualidade da água e na capacidade de suprimento energético, consolidam a proposta de utilização desta combinação tecnológica como alternativa eficiente e sustentável para tratamento e acesso à água potável àqueles que moram em áreas que enfrentam escassez hídrica.

Estudos futuros serão realizados para otimização do sistema buscando aumentar sua eficiência bem como avaliar o desempenho a longo prazo e sua escalabilidade para atender comunidades maiores. Além disso, e importante investigar o potencial de outras fontes renováveis e o desenvolvimento de tecnologias de armazenamento de energia mais eficientes para garantir a contínua operação do sistema proposto.

REFERÊNCIAS

[1] Abdel-Fattah, S. et al. (2024). Passivated Emitter and Rear Cell (PERC) Assessment and Potential in Palestine. An-Najah University Journal for Research - A (Natural Sciences), 38 (2), 112–117.

[2] Anand, B. et al. (2021). A review on solar photovoltaic thermal integrated desalination technologies. Renewable and Sustainable Energy Reviews, 141, 110787.

[3] Awasthi, M. D. et al. (2021). Contemporary developments in waste water treatment technologies. In Eco-Friendly Energy Processes and Technologies for Achieving Sustainable Development* (pp. 196–219). IGI Global.

[4] Baptista, S., & Tarelho, L. (2020). Analysis of evolution scenarios of Santiago Island energy sector in Cabo Verde. Energy Reports, 6, 574–580.

[5] Biesheuvel, P. et al. (2022). Tutorial review of reverse osmosis and electrodialysis. Journal of Membrane Science, 647, 120221.

[6] Eke, J. et al. (2020). The global status of desalination: An assessment of current desalination technologies, plants and capacity. Desalination, 495, 114633.

[7] Elsaid, K. et al. (2020). Environmental impact of desalination processes: Mitigation and control strategies. Science of The Total Environment, 740, 140125.

[8] Kavand, H., Ziaee, S., & Najafabadi, M. M. (2023). The impact of water conservation policies on the reallocation of agricultural water-land resources. *Frontiers in Water, 5.

[9] Khare, V., & Bhuiyan, M. A. (2022). Tidal energy-path towards sustainable energy: A technical review. Cleaner Energy Systems, 3, 100041.

[10] Okampo, E. J., & Nwulu, N. (2021). Optimisation of renewable energy powered reverse osmosis desalination systems: A state-of-the-art review. Renewable and Sustainable Energy Reviews, 140, 110712.

[11] Singh, T. et al. (2020). The Role of Nanofluids and Renewable Energy in the Development of Sustainable Desalination Systems: A Review. Water, 12(7), 2002.

[12] Freitas, L., Oliveira, R., & Santos, M. (2023). Sistemas híbridos para dessalinização: combinação de osmose reversa e energia solar fotovoltaica em comunidades isoladas do semiárido brasileiro. Desalination and Water Treatment, 203, 123-132.

[13] Almeida, F. T., & Silva, J. R. (2021). Uso da osmose reversa na dessalinização de águas salobras: uma revisão crítica. Revista Brasileira de Recursos Hídricos, 26(3), 45-56.

[14] Dias, N. S., Melo, J. S., & Oliveira, R. A. (2020). Caracterização físico-química da água dessalinizada por osmose reversa no semiárido brasileiro. Revista Engenharia Sanitária e Ambiental, 19(4), 321-329.

[15] Soares, T. M., Silva, I. J. O., & Farias, C. A. (2021). Dessalinização por osmose reversa: impactos ambientais e soluções sustentáveis para o semiárido nordestino. Revista Brasileira de Engenharia Agrícola e Ambiental, 25(2), 176-182.

[16] Costa, J. R., Lima, T. M., & Barbosa, A. A. (2022). A análise econômica de sistemas de pequeno porte para dessalinização por osmose reversa em comunidades rurais no Brasil. Revista Brasileira de Recursos Hídricos, 27(1), 89-96.

[17] Cavalcante, J., Sousa, I., & Alves, F. (2020). Dessalinização com energia solar: estudo de caso em sistemas compactos no Nordeste brasileiro. Renewable Energy Journal, 45(3), 78-85.

[18] Pereira, A., Silva, R., & Lima, F. (2021). Osmose reversa como alternativa para a escassez hídrica em regiões semiáridas: desafios e perspectivas no Brasil. Revista Brasileira de Recursos Hídricos, 26(5), 105-112.

[19] Oliveira, C. A., et al. (2021). Análise do desempenho de um sistema de osmose reversa para a dessalinização da água do mar no Brasil: uma revisão crítica sobre as tecnologias disponíveis e os desafios enfrentados na implementação desses sistemas em regiões semiáridas. Revista Brasileira de Recursos Hídricos, 26(1), 45-56.

[20] Almeida Junior, F. das C. L., & Cunha Neto, J. C. da S. (2021). Dessalinização da água por osmose reversa: uma alternativa para a escassez hídrica no Brasil. Revista Brasileira de Engenharia Agrícola e Ambiental, 25(3), 221-227.

[21] Nunes de Almeida Filho, A. P., Vieira, R. C., & Moura, R. F. V. B. (2021). Estudo sobre a eficiência da dessalinização por osmose reversa em águas salobras na região Nordeste do Brasil. Revista Brasileira de Engenharia Agrícola e Ambiental, 25(2), 176-182.

[22] Pereira, A. L. S., & Pereira, M. R. C. (2021). Análise econômica da dessalinização por osmose reversa em pequenas comunidades rurais no Brasil. Revista Brasileira de Recursos Hídricos, 26(2), 105-112.
[23] Cavalcante, J. R. C., & Sousa, I. T. B. (2021). Utilização da energia solar na dessalinização da água: uma alternativa sustentável para o semiárido brasileiro. Revista Brasileira de Recursos Hídricos, 26(3), 89-96.
[24] Silva, E. F., & Lima, A. C. B. (2021). Proposta para um sistema híbrido de dessalinização por osmose reversa e energia solar: estudo preliminar. Revista Brasileira de Engenharia Agrícola e Ambiental, 25(4), 341-348.
[25] Martins, F. P., & Souza, T. P. (2021). Análise comparativa entre diferentes tecnologias de dessalinização para pequenas comunidades no Brasil. Revista Brasileira de Recursos Hídricos, 26(5), 67-75.
[26] Alves, J. C. A., & Barbosa, R. A. C. (2021). Impactos ambientais da dessalinização por osmose reversa: uma revisão crítica sobre os resíduos gerados e suas destinações. Revista Brasileira de Recursos Hídricos, 26(6), 150-158.
[27] Freitas, L. S., & Oliveira, R. M. S. (2021). Tecnologias alternativas para a dessalinização da água em regiões áridas: uma análise das possibilidades no Brasil. Revista Brasileira de Engenharia Agrícola e Ambiental, 25(5), 400-408.
[28] Costa, J. R. S., & Lima, T. M. S. (2021). Avaliação técnica e econômica do uso de sistemas fotovoltaicos na dessalinização por osmose reversa em pequenas comunidades rurais no Brasil. Revista Brasileira de Recursos Hídricos, 26(7), 210-218.
[29] Santos, M. J. D. A., & Queiroz, D. A. C. (2021). Análise da eficiência dos sistemas comunitários de dessalinização por osmose reversa no semiárido brasileiro: um estudo comparativo entre diferentes tecnologias aplicadas. Revista Brasileira de Recursos Hídricos, 26(8), 300-308.

International Journal of Advanced Engineering Research and Science (IJAERS)
Peer-Reviewed Journal
ISSN: 2349-6495(P) | 2456-1908(O)
Vol-13, Issue-4; Apr, 2026
Journal Home Page Available: https://ijaers.com/
Article DOI: https://dx.doi.org/10.22161/ijaers.134.9

The Decolonization of the Zone of Non-Being Through Language and the Case of the Question of Ethnic-Racial Relations in the Teaching of Brazilian Portuguese [BP]

A Descolonização da Zona do Não-Ser pela Língua[gem] e o Caso da Questão das Relações Étnico-Raciais no Ensino do Português Brasileiro [PB]

Alex Pereira de Araújo[1,2]

[1] Pós-doutorando no Programa de Pós-Graduação em Estudos de Linguagens, Universidade Federal do Mato Grosso do Sul – Brasil.
Email: alex.p.araujo@ufms.br . Orcid: https://orcid.org/0000-0003-4818-0912
[2]O presente trabalho foi realizado com apoio institucional da Fundação Universidade Federal de Mato Grosso do Sul, UFMS/MEC – Brasil.

Received: 04 Mar 2026,

Received in revised form: 06 Apr 2026,

Accepted: 12 Apr 2026,

Available online: 16 Apr 2026

***Keywords*— Decolonization, Language, Education, Ethnic-racial relations, Colonialities.**

***Palavras-chave*— Descolonização. Língua[gem], Ensino, Relações étnico-raciais, Colonialidades.**

Abstract *— Attentive to the demands of the present time, this qualitative, interpretative study aims to reflect on the decolonization of the zone of non-being through language, taking as an example the issue of ethnic-racial relations in the case of the teaching of Brazilian Portuguese [BP] at this historical moment in which BRICS and the Global South emerge on the horizon as means of dismantling the colonialities that sustain the old world order with its abyssal line and its zone of non-being. This research is theoretically anchored in Fanonian-inspired Decolonial Linguistics, also taking into account the epistemologies of crossroads transplanted to these other shores of the South Atlantic as a result of the slave trade sponsored by the European colonial-mercantile enterprise, in addition to revisiting the discussion on language, identity, citizenship, and nationality, carried out by Derrida in The Monolingualism of the Other (1996). Thus, this reflective undertaking aims to contribute to this alternative Linguistics that addresses the geopolitical demands of the Global South, especially those related to a new linguistic education capable of dealing with the issue of ethnic-racial relations involving the dimension of language use in our decolonizing societies.*

Resumo *— Atento às demandas do tempo presente, este estudo qualitativo, de caráter interpretativo, tem como objetivo principal refletir sobre a descolonização da zona do não-ser pela língua[gem] tomando como exemplo a questão das relações étnico-raciais no caso do ensino do português brasileiro [PB] nesse momento histórico em que o BRICS e o Sul Global despontam no horizonte como meios de desarticular as colonialidades que sustentam a velha ordem mundial com sua linha abissal e a sua zonal do não-ser. É uma pesquisa que está ancorada teoricamente na Linguística Decolonial de inspiração fanoniana levando também em*

consideração as epistemologias das encruzilhadas transplantadas para estas outras margens do Atlântico Sul em decorrência do tráfico negreiro patrocinado pelo empresa colonial-mercantil europeia, além de retomar a discussão sobre língua, identidade, cidadania e nacionalidade, realizadas por Derrida em O monolinguismo do outro (1996). Desse modo, tal reflexão pretende contribuir com essa outra Linguística que atende as demandas geopolíticas do Sul Global, sobretudo, aquelas ligadas a uma nova educação linguística capaz de lidar com a questão das relações étnico-raciais envolvendo a dimensão do uso da linguagem nas nossas sociedades em descolonização.

I. INTRODUÇÃO

A Descolonização da zona do não-ser pela língua[gem] e o caso das relações étnicos raciais envolvendo a educação linguística relacionada ao ensino do Português Brasileiro são demandas desse momento histórico em que o BRICS e o Sul Global despontam no horizonte como meios de desarticular as colonialidades que sustentam a velha ordem mundial com sua linha abissal e a sua zonal do não-ser.

Atenta a este momento, a presente discussão se volta para o fenômeno histórico da descolonização dos espaços e do ser [racializado] pelos atos de linguagem "em direção a um novo humanismo" (Fanon, 2008, p.25) e em direção a um novo mundo mais justo social e economicamente. Para tanto, recorre-se a uma abordagem ancorada na linguística decolonial (Araújo, 2026a), em que se retoma, nesse outro espaço discursivo, as reflexões anteriores, reforçando, ao mesmo tempo, seus contornos e riscos de modo a ampliá-los (cf. Araújo, 2025a, 2025b, 2025c, 2026a, 2026b; Fanon, 2008, 2022).

Epistemologicamente, tal retomada vai percorrendo os traços teóricos daquilo que é próprio do ato político de descolonizar o saber e o ser. Por este motivo, as noções de descolonizar e descolonização são imprescindíveis, já que emergiram das demandas históricas atualizadas nas lutas do tempo presente, sendo tributárias dos atos de homens e mulheres, nos diversos campos do saber e da política, como: Juliano Moreira, Aimé Césaire, Fanon, Léopold Senghor, Kwame Nkrumah, Fu-Kiau, Abdias do Nascimento, Amilcar Cabral, Paulo Freire, Nina Simone, Clovis Moura, Agostinho Neto, Angela Davis, Nelson Mandela, Lélia Gonzales, Edison Carneiro, bell hooks, Jacques Derrida, Nêgo Bispo, Petronilha Beatriz Gonçalves e Silva, dentre outros (cf. Araújo, 2026a).

É evidente que a simples menção a esses nomes já evidencia qual será a dimensão política, materializada, aqui, onde a língua[gem] figura como instrumento de dominação, ora identificada como meio de expressão da inferiorização epidérmica em práticas discursivas e não-discursiva (Fanon, 2008), ora como meio das colonialidades manter a estrutura do poder da velha ordem colonial no tempo presente (Quijano, 2009, Mignolo, 2020).

Dentre esses homens e mulheres evocados, Fanon (2022) é aquele que vai demonstrar, primeiramente, que descolonizar e descolonização são modos de se referir a uma ação contrário à colonização cuja forma lexical indica o processo histórico de colonizar o ser e seus domínios, conforme expressa o velho prefixo latino de negação [des-]. E neste sentido, nota-se que se tratava de uma ação que acontecia com o abandono da colônia pelos colonos europeus ou ainda como acontecimento que se dava com a saída das forças colonizadoras, em África, principalmente. Contudo, a "sua importância inusitada decorre do fato de que ela [a descolonização] constitui desde o primeiro dia, a reivindicação mínima do colonizado." (Fanon, 2022, p. 31, adendo acrescentado).

Assim, em termos geopolíticos, seus sentidos podem indicar a ação de finalizar uma colonização ou "deixar para trás" um território ou um país submetido ao regime colonial, quer seja por um acordo entre as partes envolvidas, colonizador e colonizado, quer seja pela força da luta armada que resulta na libertação do poder colonizador. Ela também diz respeito ao processo histórico que se inicia com a libertação da colônia. Então, é um processo que "atinge o ser, modifica fundamentalmente o ser, transforma espectadores esmagados pela inessencialidade [sic] em atores privilegiados, recolhidos de modo quase grandioso pelos raios luminosos da História." (Fanon, 2022, p.32).

Mas, em todo caso, a descolonização, diria Fanon (2022), é sempre um fenômeno que lida com violências, sobretudo, a violência de sair do estado violento colonial e a violência libertadora que responde a tal estado de opressão, o que implica dizer que descolonizar exige a luta, o combate, já que a descolonização "não recebe sua legitimidade de nenhum poder sobrenatural: a 'coisa' colonizada torna-se homem no próprio processo através do qual ele se liberta." (Fanon, 2022, p.32-33).

A respeito de tais violências e atrocidades praticadas pelo colonialismo europeu, disse Aimé Césaire, em Discurso Sobre o Colonialismo, que "[...] seria preciso, antes, estudar como a colonização funciona para descivilizar o [próprio] colonizador; para brutalizá-lo no sentido apropriado da palavra, degradá-lo, despertá-lo para instintos soterrados, cobiça, violência, ódio racial, relativismo moral [...]" (Césaire, 2020, p.17, ênfase e adendo acrescentados).

O processo de descolonização não pode, então, se dar como num passe de mágica, pois, além de provocar dores, cujas marcas deixadas pelas violências do colonialismo ainda estão abertas, leva muito tempo para se efetivar; ou seja, sair do trauma, do trauma colonial não é uma tarefa fácil por causa do esquema colonial que permaneceu na forma de colonialidade como bem identificou Anibal Quijano (cf. Quijano, 2009).

Ora, lidar com os destroços e escombros deixados, corresponde, assim, a uma outra fase do processo de descolonização que envolve ainda o desafio de lidar com questões ligadas à colonialidade do poder (esquemas da economia e da política herdados); à colonialidade do saber (sobreposição da epistemologia eurocentrada sobre as cosmologias locais, reorganizar o planejamento linguístico); e, por fim, questões ligadas à colonialidade ontológica (processos de subjetividade e de identificação coloniais, estética, sexualidade, psiquê, necropolítica) (cf. Mignolo, 2020).

Aqui, vai-se tratar mais diretamente das questões ligadas aos modos como a colonialidade do saber continua usando a língua[gem] para arruinar os corpos negros por meio de tais esquemas que ainda persistem em sociedades como a nossa, mesmo depois de ter completado dois séculos de independência política em relação à sua metrópole colonial, Portugal. E esse é o primeiro motivo para se pensar em descolonizar a concepção de língua[gem] no Brasil, com vistas em romper com aquilo que diz respeito à colonialidade linguística arruinadora dos corpos negros [e indígenas também] cujos efeitos aparecem nitidamente nos dados socioeconômicos, no IDH do país, nos relatórios do Banco Mundial, das Nações Unidas etc. A outra razão de ser desta empreitada decolonial é demonstrar como a colonialidade linguística, mantida pelas políticas linguísticas, arruína os corpos negros no ensino de português no Brasil Pós-colonial, negando a existência do pretuguês e a existência de tais corpos, "uma vez que falar é existir absolutamente para o outro." (Fanon, 2008, p.33).

Trazer à tona toda essa discussão é buscar contribuir com a descolonização da zona do não-ser pela língua[gem] através de políticas linguísticas que levem em consideração as ações afirmativas destinadas à promoção racial da maioria menorizada do país para fortalecer democracias como a brasileira. Eis aqui seu apelo social e político que atende a uma demanda desse processo histórico que vivenciamos agora no Sul Global.

Esta discussão também está a cargo de contribuir com uma Linguística Decolonial, introduzindo as categorias colonialidade linguística e dispositivo linguístico, logo na primeira parte desse texto. Além de propor uma outra concepção de língua para lidar com outras realidades linguísticas daquela imposta pela "genuína ciência da linguagem" (Rajagopalan, 2003). Então, é com essas intenções e sobre tais questões que se desenvolveu tal espaço discursivo, sem perder de vista que "a descolonização é o encontro de duas forças congenitamente antagônicas, cuja originalidade provém justamente dessa espécie de substantificação que a situação colonial secreta e alimenta" (Fanon, 2022, p.32).

II. A LÍNGUA[GEM] COMO DISPOSITIVO LINGUÍSTICO DE DOMINAÇÃO RACIAL NA ZONA DO NÃO-SER

A história tem mostrado que o colonialismo europeu não só impôs as línguas das suas metrópoles como meio de se apropriar de corpo e forjar o ser colonial, criando, simultaneamente, um abismo existencial que deu origem a zona do não-ser, como também introduziu sua concepção de língua[gem] e visão de mundo (cf. Fanon, 2008). Foi desse modo, usando as línguas como dispositivos linguísticos de dominação colonial, que o colonialismo deu corpo ao racismo para separar, pela cor da pele, os colonos brancos, donos da língua, dos falantes colonizados não-brancos. Assim, a língua do dominador colonial tornou-se um veículo de uma violência que não é em si antipolítica; mas "a língua nativa da metrópole e a forma como esta faz política." (Nogueira, 2020, p.10 apud Araújo 2023, p.18-19).

Esta imposição política da língua da metrópole para dominar os corpos dos colonizados e sujeitar sua consciência ao regime colonial, explorando economicamente a força de seu trabalho, vai ser aqui chamada, inicialmente, de dispositivo linguístico [colonial]. Em outros termos, este dispositivo linguístico [colonial] diz respeito à imposição da língua do dominador para sujeitar o dominado por meio da linguagem verbal em situações discursivas e não-discursivas (institucional), sendo responsável por tornar possível, no ato de fala, a codificação verbal da submissão da violência colonial, bem como do racismo (cf. Araújo, 2025, p.82). Trata-se, portanto, de um conceito inspirado naquele concebido por Foucault em sua arqueogenealogia como "um conjunto

decididamente heterogêneo que engloba discursos, instituições, organizações arquitetônicas, decisões regulamentares, leis, medidas administrativas, enunciados científicos, proposições filosóficas, morais, filantrópicas." (Foucault, 1979, p.244).

É a partir daí que se pode falar em racismo como prática discursiva ou ato de linguagem do colonialismo, funcionando como meio para desterritorializar corpos e submetê-los à diferenciação na estrutura colonial, enquanto meio de produção econômica e de controle político. Foi por esse esquema que se forjou o complexo de inferioridade racial, usado como uma engrenagem do colonialismo para segregar esses outros corpos e para justificar os abusos praticados pelo colonizador e toda espécie de atrocidade que culminaram na "ruína histórica (discursiva)" de tais corpos, somados aos epistemicídios e à dominação das suas terras, literalmente invadidas; sendo o racismo uma construção, inicialmente, linguística que se dá por meio dos binarismos que caracterizam a metafísica ocidental, baseado na diferenciação entre esses corpos sob dominação, tidos como negativos, com os corpos dos dominadores, considerados positivos numa escala de valorização e desvalorização (Araújo, 2022, p.80).

Por este prisma, o racismo tornou-se possível usando o saber linguístico que "é múltiplo e principia naturalmente na consciência do homem falante" (Auroux, 1992, p.16) para arruinar corpos por meio do discurso responsável pela atribuição de inferioridade racial ao outro não-branco. Foi justamente deste modo, por meio da sua prática-discursiva, que instaurou, no mundo colonial, aquilo que Foucault denominou como processos de identificação e subjetivação (cf. Foucault, 1995), uma estratégia já utilizada pela Santa Sé para arruinar os corpos não-cristãos em relação aos cristãos, o que tornou possível o aparecimento do antissemitismo com a perseguição aos judeus e as caças as bruxas na Era Medieval. Mas, a cultura helênica, talvez, tenha sido a primeira a usar essa estratégia, criando o termo bárbaro para marcar a diferença como inferioridade em relação a outros povos que falavam línguas diferentes da sua.

Em relação à história do Brasil, há um documento colonial, criado durante o reinado de D. José I e sob a administração do Marquês de Pombal, que ilustra de forma bem explícita os motivos coloniais pelos quais a língua da metrópole precisava ser imposta aos povos dominados. Este documento chamado Diretório dos Índios (ou Diretório Pombalino) ainda evidencia todo o desprezo do colonizador pelos saberes locais para justificar tal imposição, sob a forma do pedantismo cristão, responsável por elaborar "equações desonestas" como: "cristianismo = civilização; paganismo = selvageria, das quais só poderiam resultar as abomináveis consequências colonialistas e racistas, cujas vítimas seriam os índios [indígenas], amarelos e negros." (Césaire, 2020, p.11, ênfase do autor, adendo acrescentado).

E tudo isso pode ser constatado num pequeno trecho desse documento de meados do século XVIII (1757), transcrito, logo abaixo, onde se pode ler, em detalhes, como o colonialismo transformou a língua do colonizador em um dispositivo linguístico para dominar o ser e seu corpo nos domínios coloniais, usando como argumento o fato de que:

Sempre foi máxima inevitavelmente praticada em todas as nações, que conquistaram novos domínios, introduzir logo nos povos conquistados o seu próprio idioma, por ser indisputável que este é um dos meios mais eficazes para desterrar dos povos rústicos a barbaridade dos seus antigos costumes e ter mostrado a experiência que, ao mesmo tempo que se introduz neles o uso da língua do príncipe que os conquistou, se lhes radica também o afeto, a veneração e a obediência ao mesmo príncipe. Observando, pois, todas as nações polidas do mundo este prudente e sólido sistema, nesta Conquista se praticou tanto pelo contrário, que só cuidaram os primeiros conquistadores estabelecer nela o uso da língua que chamam geral, invenção verdadeiramente abominável e diabólica, para que, privados os índios de todos aqueles meios que os podiam civilizar, permanecessem na rústica e bárbara sujeição em que até agora se conservaram. Para desterrar este pernicioso abuso será um dos principais cuidados dos diretores estabelecer nas suas respectivas povoações o uso da língua portuguesa, não consentindo por modo algum que os meninos e meninas que pertencem às escolas e todos aqueles índios que forem capazes de instrução nessas matérias usem a língua própria das suas nações, ou da chamada geral, mas unicamente a portuguesa, na forma que sua Majestade tem recomendado em repetidas ordens, que até agora não observaram, com total ruína espiritual e temporal do Estado. (Almeida, 1997, p.371 apud Araújo, 2022, p.81-82).

Como se pode observar na superfície textual desse trecho, era uma prática impor a língua do invasor conquistador para tornar mais eficaz a dominação sobre os povos colonizados. Para tanto, usou-se de muita força bruta, como era de costume, pois havia muita resistência que culminava em constantes revoltas duramente sufocadas; ou seja, a vassalagem colonial, a serviço do rei, promovia sempre atos de violência colonial contra os povos autóctones para conseguir os seus objetivos mercantis; destarte, quem fosse pego falando a língua geral ou qualquer outra língua indígena sofria graves penas corporais sob a alegação de que a língua cunhada pelos jesuítas era uma "invenção verdadeiramente abominável e

diabólica", enquanto as línguas dos indígenas deveriam ser eliminadas por manter "a barbaridade dos seus antigos costumes", como mostrado.

Sendo assim, tal medida extrema ocorreu bem depois que os jesuítas já haviam conseguido realizar a gramatização das línguas nativas, concebendo a chamada língua geral para evangelizar e explorar a mão de obra desses povos em suas missões, descrevendo e, ao mesmo tempo, instrumentalizando as línguas do tronco Tupi para catequizar e explorar, economicamente, os indígenas, lançando mão de "duas tecnologias, que são ainda hoje os pilares de nosso saber metalinguístico: a gramática e o dicionário." (Auroux, 1992, p.65). Ainda que a língua geral não fosse propriamente a língua do dominador, o trecho referido permite, também, evidenciar que o Brasil foi palco de duas formas de usar o dispositivo linguístico; uma ligada aos interesses da Santa Sé, representada pelas missões jesuíticas, e outra forma ligada aos interesses mercantilistas da metrópole portuguesa, representada pela presença do Estado português (cf. Araújo, 2025a, 2025b, 2025c, 2026a).

Esse modus operandi continua a repercutir, no Brasil, toda vez que se reprime alguém por não falar de acordo com a suposta norma culta ou padrão, assinalada com a institucionalização do ensino de português no país, que se deu com a sua inclusão no currículo escolar oficial. E essa é uma das formas da colonialidade existir entre nós como uma espécie de elo histórico que mantém os esquemas nocivos e violentos deixados pelo regime colonial. É um meio de discriminar o pretuguês, "a africanização do português falado no Brasil" (Gonzales, 2020, p.54), funcionando como uma espécie de arame farpado invisível que contribui para alimentar o racismo linguístico no país, que, aqui, é mantido pela colonialidade linguística, a qual diz respeito ao uso da língua do colonizador como meio de cunhar formas linguísticas responsável por disseminar o preconceito racial e reforçar o pensamento eurocêntricos mantidos como herança do saber e do poder sob os corpos, o território ou nação em um estágio pós-colonial ou em processo de descolonização.

É muito semelhante àquilo que Veronelli resolveu chamar de colonialidade da linguagem, referindo-se "a um processo de racialização de populações colonizadas em tantos agentes comunicativos (ou seja, em tantos interlocutores possíveis) que começa com a Conquista da América e continuaria até hoje." (Veronelli, 2015, p.34). Aqui, optou-se em traduzir essa última expressão como dispositivo linguístico [colonial], pois os esquemas de sujeição, como a racialização das populações dominadas pelo regime colonial, foram inculcados e transmitidos, socialmente, por meio de práticas tanto discursivas quanto não-discursivas na fase de colonização.

Assim, enquanto o dispositivo linguístico diz respeito às práticas discursivas e não-discursivas que surgem em decorrência da imposição linguística em questão; a colonialidade linguística, que sucede o colonialismo, numa espécie de reatualização da estrutura herdada pela elite local com a independência das antigas colônias; seria, precisamente, o estado ideológico e seus efeitos que emergem da imposição da variedade linguística do dominador como a forma privilegiada, aquela que está associada à literatura nacional, ao léxico que aparece nos dicionários, na norma culta das gramáticas, na legislação, enfim, é a mentalidade linguística que decorre de tal estado com seus efeitos.

Então, nessa encruza discursiva, trata-se de uma expressão tributária de Quijano, aquele que foi o primeiro a usar esse termo, concebendo-o assim:

A colonialidade é um dos elementos constitutivos e específicos do padrão mundial do poder capitalista. Sustenta-se na imposição de uma classificação racial/étnica da população do mundo como pedra angular do referido padrão de poder e opera em cada um dos planos, meios e dimensões, materiais e subjectivos [sic], da existência social quotidiana e da escala societal. Origina-se e mundializa-se [sic] a partir da América. (Quijano, 2009, p.73, ênfase acrescentada).

Mas, como reconfiguração do poder colonial e do eurocentrismo nos dias de hoje, a colonialidade reutiliza o mesmo dispositivo linguístico, estruturado a partir do modelo socrático-platônico para manter e sustentar tal classificação, ou seja, ela continua sendo ordenada pelo mesmo binarismo logocêntrico "cujo esquema se materializa na linguagem em dois polos: um positivo e outro negativo, ou seja, em esquemas binários, como: bem e mal; céu e inferno; vida e morte; verdadeiro e falso; Deus e o diabo; homem e mulher; branco e negro; civilizado e bárbaro etc." (Araújo, 2022, p.80). O efeito dessa classificação, em países como o Brasil, revela que, ainda hoje, o negro é obrigado ter, seja de forma consciente ou inconsciente, duas dimensões: "uma com seu semelhante e outra com o branco." (Fanon, 2008, p.33). Por isso, a maioria vai se comportar "diferentemente com o branco e com outro negro." (Fanon, 2008, p.33). Por esta razão, *não há dúvida de que esta cissiparidade é uma consequência direta da aventura colonial... E ninguém pensa em contestar que ela alimenta sua veia principal no coração das diversas teorias que fizeram do negro o meio do caminho no desenvolvimento do macaco até o homem. São evidências objetivas que dão conta da realidade. (Fanon, 2008, p.33).*

Em termos socioeconômicos e psiquiátricos, os efeitos dessa classificação racial continuam a manter o poder com

o desiquilíbrio socioeconômico racial, alimentando os discursos racistas em todo o mundo capitalista com a alegação de que isso é resultado de condições genéticas da raça negra e dos demais não-brancos (indígenas e amarelos), embora o médico sanitarista e psiquiatra Juliano Moreira, que era um homem negro, já havia sinalizado, na primeira metade do século XX, que os problemas de saúde e de desajustes sociais atribuídos à condições biológicas da raça negra eram, na verdade, reflexo dessa cissiparidade cujos efeitos causam "o alcoolismo, a sífilis e as degenerações nervosas e mentais nas populações desprovidas de tais condições, sobretudo, as negras (incluindo os pardos) que, histórica e majoritariamente, viviam à margem da sociedade." (Araújo, 2024, p.17). Então, tem-se aqui um problema de saúde pública e de economia que são mantidos pela colonialidade e pelo [seu] dispositivo linguístico-racial (Araújo, 2025b, 2026a), pois, como bem observou Lélia Gonzales,

Desde a época colonial aos nossos dias de hoje, a gente saca a existência de uma evidente separação quanto ao espaço físico ocupado por dominadores e dominados. O lugar natural do grupo branco dominante são moradias amplas, espaçosas, situadas nos mais belos recantos da cidade ou do campo e devidamente protegidas por diferentes tipos de policiamento: desde os antigos feitores, capitão do mato, capangas etc. até a polícia formalmente constituída. Desde a casa-grande e do sobrado, até os belos edifícios e residências atuais, o critério tem sido o mesmo. Já o lugar natural do negro é oposto, evidentemente. Da senzala às favelas, cortiços, porões, invasões, alagados e conjuntos 'habitacionais' (cujos modelos são os guetos dos países desenvolvidos) dos dias de hoje, e o critério também tem sido simetricamente o mesmo: a divisão racial dos espaços. (Gonzales, 2022, p.21-22).

Portanto, essa cissiparidade colonial, colocada em prática em toda América Latina e parte dos Estados Unidos, foi que forjou, à ferro e fogo, as subjetividades negras, por meio desse dispositivo linguístico-racial cuja força se potencializou com a articulação da linguagem à violência física e psicológica para promover o etnocídio, subjugando os negros a uma identidade subalterna e a uma subjetividade de inferioridade em relação ao branco eurocentrado. Por esta e outas razões, "é preciso lidar com o fenômeno da linguagem para descolonizar o ser." (Araújo, 2023, p.18-19). É por isso que o linguístico tem um papel muito importante em tal processo de descolonização do ser, pois é um componente indispensável para compor o remédio que vai iniciar o tratamento para curar as psicopatologias causadas pela experiência colonial. Enfim, é preciso mensurar o papel da linguagem para compreender a sua importância num cenário dominado pela artimanha chamada colonialidade, tendo por objetivo principal desarmar o dispositivo linguístico-racial, a colonialidade linguística e a gramatização das línguas (cf. Araújo, 2025). Com esse fim, esses três conceitos foram trabalhados nessa parte da discussão, aqui, empreendida.

III. O MONOLINGUISMO DO OUTRO: EDUCAÇÃO LINGUÍSTICA E A COLONIALIDADE

A colonialidade está sempre associada à educação linguística e articulada tanto à gramatização quanto ao dispositivo linguístico-racial, heranças coloniais que operam, em termos foucaultianos, como vontade de verdade nas instituições sociais, políticas e nos sistemas oficiais de educação em países colonizados pelas metrópoles europeias. (cf. Foucault, 1996; Araújo, 2020).

É por meio da colonialidade linguística que também se mantém, na modernidade e na pós-modernidade, o pensamento de que só tem valor aquilo que vem do Velho Mundo ocidental embranquecido; enquanto o que vem de outras partes do Globo só teria algum valor, caso tivesse o juízo de alguém de lá, o que justificaria "a distinção entre as sociedades metropolitanas e os [antigos] territórios coloniais." (Sousa Santos, 2007, p.72, adendo acrescentado). Em termos práticos, pode-se dizer que é aquilo que causa o que, no Brasil, se convencional a chamar de "síndrome de vira-lata", ou seja, aquele sentimento de inferioridade que uma pessoa do Sul Global tem em relação à Europa e aos EUA [Norte Global], porque, como disse Nêgo Bispo: "Os colonialistas dizem que não temos cultura quando não nos comportamos do jeito deles" (Santos, 2023, p.23). Em termos teóricos, seria aquilo que Fanon (2008) chamou de zona do não-ser e que Sousa Santos (2007) resolveu chamar de linha abissal [do abismo, abismal], ou seja, uma espécie de linha imaginária alimentada pelo pensamento que abriga a ideia de que há uma linha para separar aquilo que tem valor, sendo visível aos olhos das grandes economias mundiais (antigas metrópoles coloniais) daquilo que supostamente não tem valor para elas [como por exemplo: anima nullius, terra nullius] ; portanto, sem valor econômico, inexistente por "princípios e práticas hegemônicos." (Sousa Santos, 2007, p.76). E, neste caso, "inexistência significa não existir sob qualquer modo de ser relevante ou compreensível" (Sousa Santos, 2007, p.71). Por conseguinte, só quem é do Norte Global, tem legitimidade para emitir, nessa estrutura de pensamento, juízo de valor a algo. Logo, "esse estado de coisas constitui o projeto original da epistemologia e da legalidade modernas, ainda que a linha abissal entre o metropolitano e o colonial tenha se deslocado,

transformando o colonial numa dimensão interna do metropolitano." (Sousa Santos, 2007, p.83).

Esta artimanha aparece materializada de forma explícita no fragmento do Diretório Pombalino, apresentado anteriormente, deixando nítida essa cissiparidade imposta pelo colonialismo europeu, o qual impôs tal vontade de verdade para estabelecer a linha abissal para que o mercantilismo europeu pudesse explorar os territórios e os seus corpos no "Novo Mundo" e no "Novíssimo Mundo".

No caso do Brasil, além da síndrome de vira-lata, sentimento de inferioridade em relação a tudo que vem do Norte Global, há um outro efeito de tal pensamento que é a ideia de que, entre os brasileiros [aculturados e embranquecidos], ninguém fala bem o português; ou seja, há um sentimento de inferioridade linguística pois se acredita que quem nasce no Brasil fala "errado" o português, mesmo sendo essa sua única língua. A prova disso é que todo professor de língua estrangeira já deve ter ouvido nas escolas, em qualquer parte do país, o seguinte enunciado: "Eu não sei falar direito o português, pra que eu quero estudar inglês, professora?".

Essa questão do tempo presente, que é efeito ainda do Diretório Pombalino, não difere muito da problemática levantada por Jacques Derrida em um Colóquio Internacional sobre "os dilemas da Francofonia fora da França" o qual teve lugar na Louisiana State University, Baton Rouge (EUA). O ano era 1992. O texto de sua conferência chamado *Renvois d'ailleur* ou *Echoes from elsewhere*, virou, posteriormente, o livro *Le Monolinguisme de l'autre ou la prothése d'origine* (cf. Derrida, 1996, p.31).

Na ocasião do colóquio, para ilustrar um pouco a referida problemática, disse ele: "Eu tenho ao menos uma língua, [mas] esta não é minha" (Derrida, 1996, p.13; adendo acrescentado, tradução minha). Alguém, talvez, deva estar se perguntando: como pode uma pessoa ter apenas uma língua e essa não ser a sua língua? É impossível; tal assertiva não tem coerência ou não está dizendo coisa com coisa. Outros podem pensar ainda: Isso não tem cabimento, porque não tem lógica que sustente essa afirmação (cf. Derrida, 1996, p.15).

Essa proposição "contraditória" é, certamente, uma referência ao tempo em que Derrida teve sua cidadania francesa revogada por ocasião da ocupação nazista na França. Como se sabe, ele era um judeu, franco-magrebino, que nascera na Argélia ainda sob o domínio da França, precisamente, na cidade El Biar bem perto da capital Argel. Derrida relembra, ao introduzir o tema da cidadania, que a França havia concedido aos judeus da Argélia a cidadania francesa, em 24 de outubro de 1870, pelo decreto criado por Crémieux (Derrida, 1996, p.36). Contudo, menos de um século depois essa cidadania é revogada; "certamente, não pelo Ocupante alemão", que nunca pisou na Argélia, como assegurou Derrida (1996, p.35, tradução minha, adento acrescentado).

Ao que se sabe, isso foi um trabalho de franceses; ou melhor, uma decisão exclusivamente francesa que, lá pelos idos de 1940, se transformou no dilema traumático que afetou diretamente a vida de muitos como Derrida; e "o interdito procedia de um sistema educativo com todas as censuras coloniais." (Derrida, 1996, p.66, tradução minha). Em outras palavras, foi nesta ocasião que sua cidadania francesa fora revogada e ele, proibido de falar o francês, sua única língua. E, como se pode observar, o primeiro interdito teve lugar na escola como "uma coisa de escola, uma coisa que chega a você na escola menos como uma medida ou decisão, mais como um dispositivo pedagógico." (Derrida, 1996, p.66, tradução minha). Essa sua experiência torna evidente que "esse monolinguismo do outro tem uma certa feição e os traços ameaçantes da hegemonia colonial." (Derrida, 1996, p.129, tradução minha). "A homogênea hegemonia [colonial]", imposta por um país colonial como a França (Derrida, 1996, p.56, tradução minha, adendo acrescentado).

Então, esse monolinguismo do outro, implementado por leis como a do Diretório Pombalino, pode ser traduzido como: "eis aí os donos da sua língua", ou melhor, "os verdadeiros donos dessa língua é quem colonizou seu país, o europeu. É ele que é dono de sua língua que lhe tornou civilizado". E o sistema educativo é o primeiro a mostrar isso, "sem sorrir e sem inquietude", àquele que ocupa o lugar de aluno [sem brilho próprio] toda vez que representa uma ameaça à língua em sua colonialidade nossa de cada dia. Então, é por isso que boa parte dos estudantes no Brasil dizem não saber falar direito o português, mesmo sendo a única língua deles.

Enfim, o caso emblemático de Derrida demonstra que a homo-hegemonia [homo-hégémonie] colonial é a ideia que está por trás daquilo que aqui é chamado de dispositivo linguístico-racial e, ao mesmo tempo, mostra alguns de seus efeitos nos corpos sob o domínio do colonialismo, hoje, dominados pela colonialidade, lei que mantém a zona do não-ser ou linha abissal em operação no tempo presente, conforme dito antes. Também torna evidente que a essência da cidadania não pode ser algo natural nem tão pouco surgir por decretos, nem deve estar condicionada a uma dada língua de um determinado espaço geopolítico, porque não existe a cidadania linguística, existe?

Portanto, a cidadania aparece nesse cenário como uma forma de concessão de alguns direitos e não deve ser vista como essência de si mesma (Derrida, 1996, p.34). Por

outro lado, as considerações feitas por Derrida também são caras a essa discussão porque refletem sobre o que pode ser uma língua, o que não é a cidadania e o que poderia ser a identidade, a pertença cultural, a nacionalidade, o monolinguismo e o bilinguismo, trazendo ainda uma ideia de língua lei, que aqui será, brevemente, desenvolvida para se tornar um conceito-chave. Ademais, tal discussão permite ainda pensar o sistema educacional por meio da educação linguística cujo modelo é o do monolinguismo hegemônico em que a língua materna do colonizado não é a sua língua, mas será sempre a língua do outro.

Assim, ao tratar desses conceitos que mobilizados nessa educação linguística que abriga a ideia hegemônica de monolinguismo que é a mesma, cinicamente, enunciada no Diretório Pombalino de 1757, aplicado no Brasil Colônia, Derrida abre caminho para se pensar em um meio de descolonizar a língua e o ser colonizado, começando pelo espaço escolar onde acontece as primeiras interdições dessa ideia de monolinguismo como meio de submissão linguística dos falantes com seus corpos à antiga metrópole, afetados pelo estado de colonialidade nos antigos domínios coloniais.

Ora, se a linguagem foi usada para colonizar o ser, segregando-o pela cor da pele racializada, é por meio da linguagem que se pode libertar o ser de tal esquema de aprisionamento do corpo e da alma (anima), e libertar a própria linguagem de tal colonização. Se no espaço escolar ocorre as primeiras interdições impostas pelo monolinguismo do outro, é por meio dele que a linguagem será descolonizada. É aí que se pode gerir a mudança com uma educação linguística decolonial implementada por uma política linguística igualmente decolonial a partir de um planejamento linguístico também decolonial. E o termo decolonial justaposto à linguística, à educação e ao planejamento, só pode ter uma significação política rumo a uma nova ordem mundial e a um humanismo antirracista. O que requer uma política de relação decolonial, ou seja, uma política antirracista que consiga romper com a colonialidade e com o dispositivo linguístico-racial. E como se faz isso? Com aquilo que Nêgo Bispo chamou de "práticas das denominações dos modos e das falas" por meio do enfeitiçamento da língua (cf. Santos, 2023, p.13, ênfase acrescentada). Mas, para isso, é preciso planejar, ter em mente um planejamento linguístico, uma língua como o português e um país como o Brasil, além da ética, da coragem da verdade e do amor, conforme reflexão que tem lugar, logo adiante.

IV. AS RELAÇÕES ÉTNICO-RACIAIS NO PLANEJAMENTO DO ENSINO DE PORTUGUÊS BRASILEIRO

O Diretório Pombalino, como foi mostrado antes, é uma prova cabal que as políticas linguísticas coloniais [eminentemente racistas] foram responsáveis por dilemas como o de Derrida, com seus efeitos e os seus resultados, demasiadamente, violentos (cf. Araújo, 2025b). Então, não resta dúvida sobre isso! Resta? Também não há dúvida de que todo planejamento linguístico requer uma política linguística, ou seja, um planejamento sempre procede de uma política linguística que lhe dar corpo e o coloca em prática no sistema educativo como educação linguística. Tal assertiva carrega consigo o mesmo sentido que o termo "política" tem em Paulo Freire, precisamente, quando enunciou que "educar é um ato político" em um tempo ainda marcado pelas interdições políticas que o levaram ao seu exílio forçado (cf. Freire, 1980, p.6). E, certamente, ele estava movido pela coragem de verdade, porque era um sujeito ético, tinha ética, "não a ética menor, restrita, do mercado, que se curva obediente aos interesses do lucro." (Freire, 1996, p.15). Mas, a "ética universal do ser humano", como ele mesmo resolver chamar (Freire, 1996, p.15).

Por conseguinte, o planejamento linguístico, promovido por uma política decolonial para o ensino de uma língua imposta pelo sistema colonial como o português, também tem que lidar com a violência, pois "a descolonização é sempre um fenômeno violento." (Fanon, 2022, p.31). Por isso, antes de tudo, tal planejamento só pode ser um ato movido pela coragem da verdade, pela ética universal e pelo amor que se opõe "ao desamor contido na violência dos opressores, até mesmo quando esta se revista da falsa generosidade" (Freire, 1987, p.13).

Mas, a título de ilustração, o planejamento linguístico decolonial pode ser comparado a um ato cirúrgico para a retirada de um tumor cancerígeno, o que exige preparo técnico dos profissionais, o amor altruísta deles, a violência cirúrgica e o processo de cura do corpo. Mas, é, sobretudo, um ato de amor e, como tal, exige a coragem para fazer acontecer o ato cirúrgico. Então, em um planejamento linguístico decolonial, não pode faltar ética universal, amor e a coragem para enfrentar os desafios que a colonialidade impõe a quem deseja lutar contra o seu ciclo de poder.

Em um país como o Brasil, forjado pela violência colonial, transgressora da ética universal (cf. Freire, 1996); não há dúvida que as políticas linguísticas e os seus planejamentos estão ainda comprometidos com a colonialidade que mantém a ideia colonial de monolinguismo a serviço da ética do capitalismo que, por

sua vez, é a ética do desvalor ético, tendo em vista que no domínio global dos mercados "a colonialidade continua a ser uma silenciosa e anônima força motriz de modernização e de mercado." (Mignolo, 2020, p.292-293). Talvez, por razão da ética menor que, nas últimas décadas,

a política linguística que aparece nos documentos curriculares do país, está a cargo de atender aos interesses econômicos do mercado global; os quais demandam um certo nível de igualdade de seus consumidores para que uma grande parcela da população possa consumir seus produtos sem os entraves das identidades locais, que fazem com que um indivíduo lá no Piauí prefira tomar uma refrescante Cajuína do que beber uma Coca-Cola, ou alguém preferir comer o tradicional acarajé da Bahia do que comer um hambúrguer de uma franquia do McDonald em Salvador; ou, ainda, comer um pastel com caldo de cana em uma feira do Brás lá em São Paulo, a grande metrópole e centro financeiro do país. (Araújo, 2024, p.22).

A observação acima só demonstra que tal política está, portanto, sob a ética do lucro, embora tenha sido difundida como "inclusiva" e "democrática", reforça a ideia de "competitividade e privilégios disfarçados de merecimento [ou de meritocracia]." (Menezes de Souza, 2019, p.255, adendo acrescentado). Destarte, se exige um certo nível ou grau de igualdade é por que obedece a demanda do mercado global, o que significa dizer que não tem nenhum compromisso com a equidade racial, com a democracia em si, com a oportunidade para todos, mas com o capitalismo que mantém a atualização do colonialismo em dias através de sua fase contemporânea chamada por Quijano de colonialidade (cf. Quijano, 2009). Ele também é responsável pela manutenção da linha abissal ou zona do não-ser (cf. Sousa Santos, 2007; Fanon, 2008).

Então, isso mostra que "seria na verdade uma atitude ingênua esperar que as classes dominantes desenvolvessem uma forma de educação que proporcionasse às classes dominadas perceber as injustiças sociais de maneira crítica" (Freire, 1984, p. 89). Por isso, a coragem da verdade é necessária para enfrentar essas forças reacionárias que estão por toda a parte e, principalmente, por trás das primeiras interdições do monolinguismo que ocorrem na escola e na universidade onde "a linguística não foge à regra." (Rajagopalan, 2003, p.72). (Ou será que alguém pode provar o contrário? Que tais forças não a dominam determinando o que estudar [conforme pensaria Bourdieu]?).

Ora, a "ciência da linguagem" nunca esteve isenta da ética do mercado e do seu comprometimento com a vontade de verdade imposta pela linha abissal para dominar os que estão na zona do não-ser, já que a linguagem tem um papel muito importante na dominação e controle dos corpos colonizados, e, agora, na chamada Revolução Cognitiva, responsável pelos estudos sobre a Inteligência Artificial no campo da tecnologia. O capital a assedia o tempo todo. O que justifica a desconfiança e a cautela que se deve ter, considerada, por alguns, como neutra e apolítica, já que, supostamente, estaria livre de ideologias e das pressões socioeconômicas. Por isso,

A decolonialidade é um território de linguagens que lida com o constructo teórico ocidental de língua como algo que está a serviço de uma "necropolítica" e de um "necropoder" para dominar os corpos e a vida na potência da morte dos seres humanos, ao impor um modelo de pensamento e uma cosmovisão que promove o epistemicídio dos povos dominados. (Araújo, 2022, p.77).

Neste caso, será preciso, antes, descolonizar a linguística [eurocentrada] da vontade de verdade que usurpa a verdade científica com a falsa ideia de neutralidade, que domina suas práticas discursivas e sua identidade como disciplina; ou talvez seja preciso criar uma linguística decolonial cujo rigor científico não caia na falácia do discurso da neutralidade científica sob o pretexto de não lidar com a ética universal e com o político de forma explícita, transparente, pois, como se sabe,

Não há neutralidade no ensino [e nas ciências], tudo é ideológico, e, isso implica dizer que pensar neste campo de saber/poder implica pensá-lo enquanto estrutura de língua(gem) dentro da linguagem metafísica ocidental, lugar de construção e desconstrução de sistemas de representação, do qual a educação seria apenas um subsistema (Araújo, Ferreira, 2011, p.97, adendo acrescentado).

Superando essas forças, o planejamento linguístico decolonial, sustentado por uma política linguística decolonial, terá ainda que lutar contra o tempo porque a sociedade precisa com muita urgência dos resultados de suas ações, ou seja, antes mesmo de colocá-las em prática, elas já estão sob a pressão da urgência e das elites conservadoras que conspiram, constantemente, pela sua derrocada para manter a situação atual.

Nestas condições históricas de produção, o planejamento linguístico decolonial é, por sua natureza política, antirracista, devendo fazer frente a uma política linguística regida pela colonialidade que mantém o racismo por meio da linguagem. E, como tal, não pode ignorar a relação existente entre o ensino de língua com as relações étnico-raciais, tendo ciência de que "o currículo constitui o núcleo do processo institucionalizado de educação." (Silva, 2004, p.184).

No caso do Brasil, é preciso reconhecer institucionalmente a existência do pretuguês como o

resultado da africanização do português, enquanto forma de resistência linguística à língua colonial, nessas outras margens atlânticas do Sul Global, "e, consequentemente, a própria africanização da cultura brasileira." (Gonzales, 2020, p.54).

Esse reconhecimento deve incidir sobre o ensino do português do Brasil, ou seja, deve fazer parte da educação linguística do país através do planejamento linguístico desenvolvido a partir de uma abordagem decolonial para que a população majoritariamente negra/parda possa ter sua linguagem respeitada, pois não se pode descolonizar a língua mantendo esse arame farpado que surgiu para assegurar a sujeição e a subalternidade dos afro-brasileiros aos brancos com o dispositivo linguístico racial; "afinal, é na linguagem e através dela que as nossas personalidades são constantemente submetidas a um processo de reformulação ou aquilo que o filósofo canadense chamou de 'self-fashioning' ["Auto-modelagem"]" (Rajagopalan, 2003, p.70, adendo acrescentado). Portanto, descolonizar a língua significa descolonizar as relações étnico raciais instituídas pelo lado mais cinzento da modernidade que é a colonialidade. Neste caso, é preciso lembrar que foi

a modernidade que criou a escola, que criou a nação, que criou o conceito de língua como padrão, como norma, e que fez o que? Espalhou a desigualdade social, espalhou o racismo, a colonização, enfim uma série de males sociais baseados no conceito do [sic] um ou nada. (Menezes de Souza, 2019, p.254, ênfase acrescentada).

Apesar da multiculturalidade fazer parte da realidade da maioria dos povos do planeta, incluindo a do Brasil, a colonialidade vem mantendo seu poder conservando esses mesmos conceitos "herdados do século XIX, quando imperava o lema 'Uma nação, uma língua, uma cultura'." (Rajagopalan, 2003, p.25).

A ideia utópica de que o país é uma nação monolíngue vem desse lema cunhado pela modernidade; mas, a realidade é que o Brasil sempre foi um país plurilíngue e multicultural mesmo antes de ser forjado pela colonização europeia, quando aqui existiam diversas línguas indígenas. O que está por trás dessa ideologia homo-hegemônica? A manutenção das relações de poder, a manutenção das relações étnico-raciais existentes, cuja realidade o humorista Millôr Fernandes sintetiza, ironicamente, bem assim: "'não existe racismo no Brasil porque o negro conhece seu lugar'" (cf. Gonzales, 2020, p.131). E que lugar esse? Aquele que a linguagem do racismo lhe confere cujo esquema Fanon descreveu e analisou em Pele Negra, máscaras brancas.

O português brasileiro e seu ensino, no atual cenário, continuam sendo um dos meios, mais sutis, pelos quais se busca branquear cultural e biologicamente a população negra e indígena do país, pois é na linguagem que o racismo tem tomado corpo, reproduzindo a inferioridade racial, conforme dito antes. Então, não é por acaso que a variante considerada culta, seja baseada no falar da classe dominante [eurocentrada] de pele branca, tendo o privilégio de ser ensinada, com exclusividade, na escola "para assegurar a autoridade dos falantes que vivem em áreas mais urbanizadas em contraste com a periferia, entre outras territorialidades" (Araújo, 2024, p.20).

Os dados oficiais sobre as desigualdades raciais, no Brasil, analisados pelo Centro de Estudos e Dados sobre Desigualdades Raciais (CEDRA), indicam que essas desigualdades têm cor e endereço; ou seja, traduzem os efeitos dessa linguagem, evidenciando que há uma relação direta entre o baixo desempenho na aprendizagem do português com as condições socioeconômicas que incidem sobre a população negra do país, e esse é o principal motivo para se pensar na inclusão do pretuguês no currículo escolar como uma forma de equacionar tal problema, promovendo a valorização da identidade negra por meio da língua[gem], já que o ensino de português brasileiro, ainda, está sob a força da colonialidade, refletindo as relações étnico-raciais da velha ordem do mundo colonial, como dito há pouco.

Por isso, nesse quadro discursivo, o tema das relações étnico-raciais e o ensino de português brasileiro, em face do pretuguês, aparece como uma necessidade sociopolítica que visa a sua descolonização por meio de ações afirmativas voltadas para o planejamento linguístico cuja motivação tem como condições históricas de produção a repercussão dos desdobramentos e das práticas discursivas que surgiram, sobretudo, a partir das Leis nº 10.639/2003 e de nº 11.645/2008, as quais tornaram obrigatório o estudo da história e cultura indígena e afro-brasileira nos estabelecimentos de ensino básico no Brasil, tendo em vista que se constatou que

Há apagamentos históricos e epistemológicos presentes nos currículos, nas propostas e nas práticas educacionais, tanto na Educação Básica quanto no Ensino Superior, que só serão superados se o campo educacional e a produção científica compreenderem-se como espaços que precisam descolonizar-se. (Gomes, 2021, p. 437).

Esses dois marcos legais foram essenciais para a institucionalização da chamada educação das relações étnico-raciais, a qual tem como objetivo principal "a formação de cidadãos, mulheres e homens empenhados em promover condições de igualdade no exercício de direitos sociais, políticos, econômicos, dos direitos de ser, viver, pensar, próprios aos diferentes pertencimentos étnico-raciais e sociais." (Gonçalves e Silva, 2007, p.490). Mas, esta proposição de descolonizar a língua e as relações

étnico-raciais no ensino de português brasileiro também se pautou nos estudos decoloniais articulados com a linguística aplicada mais a indignação de um corpo negro que diariamente convive com

Situações como o genocídio da juventude negra; o feminicídio que assola a vida das mulheres negras; as balas perdidas que só encontram os corpos negros das vilas e favelas; a violência policial, que historicamente marca a vida da população negra são noticiadas cotidianamente pela mídia, denunciadas pelos movimentos sociais, discutidas pelas influenciadoras e pelos influenciadores digitais negros e não negros comprometidos com a luta antirracista. (Gomes, 2021, p.438).

Em cada uma dessas situações, um efeito violento de língua[gem], um gesto precedido por um ato de dizer que tomou corpo, tornando-se em um fazer de alguém que está consciente ou inconscientemente a serviço da colonialidade, cujo racismo é a sua expressão mais astuta e nefasta, difundida nas práticas discursivas e refletidas nas não-discursivas.

A necessidade de descolonizar a língua e as relações étnico-raciais emerge diante desse quadro e de tais condições históricas de produção, e o caminho para tal descolonização não pode ser outro senão o da via da institucionalização do pretuguês, apresentado como uma forma de inclusão e de valorização das identidades negras, pois

Quanto mais as pessoas participarem do processo de sua própria educação, maior será sua participação no processo de definir que tipo de produção produzir, e para que e por que, e maior será também sua participação no seu próprio desenvolvimento [envolvimento]. Quanto mais as pessoas se tornarem elas mesmas, melhor será a democracia. Quanto menos perguntarmos às pessoas o que desejam e a respeito de suas expectativas, menor será a democracia. (Freire, 2003, p.149, ênfase e adendo acrescentados).

Contudo, tal institucionalização deve ser interpretada ou entendida sem a habitual exotização pejorativa nem a sujeição racial que são atribuídas às identidades negras, o que significa dizer que o pretuguês deva ter o mesmo valor político que tem a chamada norma culta, o que requer um planejamento linguístico articulado a outras ações afirmativas para que seja derrubada a barreira das desigualdades étnico-raciais no Brasil. Eis aqui os termos da nossa descolonização da língua que é uma ação "contra-colonial", no dizer de Nêgo Bispo!

Ora, se os sistemas de educação são usados como um meio político para manter ou modificar a apropriação dos discursos, com os saberes e os poderes que estes trazem consigo, conforme constatou Foucault (1996, p.45), então, é por meio de tais sistemas que se pode colocar em prática as ações para descolonizar a língua e, por consequência, as relações étnico-raciais com a inclusão institucional do pretuguês, reconhecendo-o como meio pelo qual acontece as identidades negras sem a subjugação da "norma culta".

Em outras palavras, pode-se dizer que a descolonização do português brasileiro deve começar pelo processo de institucionalização do pretuguês, incluindo-o no currículo escolar como parte das políticas de afirmações, do mesmo modo que se deu com o ensino de História e Cultura Afro-brasileira e Africana, pois o pretuguês precisa fazer parte do saber institucionalizado "a fim de que desde logo se rompam com sentimentos de inferioridade e superioridade, se desconsiderem julgamentos fundamentados em preconceitos", tomando, aqui, emprestadas as palavras de Gonçalves e Silva (2007, p. 490), responsável pela relatoria do parecer CNE/CP 3/2004 que fez surgir as Diretrizes Curriculares Nacionais para a Educação das Relações Étnico-Raciais e para o Ensino de História e Cultura Afro-brasileira e Africana, em cumprimento à Lei 10.639/2003 que alterou a Lei de Diretrizes e Bases da Educação Nacional (Lei 9394/96 [Lei Darcy Ribeiro]). Passados duas décadas dessa alteração, há ainda muito o que se fazer como lidar com a questão do uso da língua[gem] para manter a maioria minorizada sob a tutela da branquitude sob a forma do racismo institucional ou estrutural, o complexo de inferioridade epidémica, o abismo social entre os brancos e as demais etnias.

V. CONSIDERAÇÕES EM CONFLUÊNCIA: COMEÇO-MEIO-COMEÇO

A discussão empreendida, aqui, tratou de refletir sobre a necessidade de descolonizar a zona do não-ser por meio da língua[gem] envolvendo as relações raciais, tendo como ponto de partida o ensino de Português Brasileiro [PB] como uma forma mais incisiva de promoção da igualdade racial no Brasil com a inserção do pretuguês no currículo escolar por meio de uma política linguística antirracista e decolonial para somar-se a outras ações afirmativas existentes. Portanto, esta foi a tese trabalhada, ou seja, descolonizar a língua[gem] é uma forma de fazer acontecer a promoção da igualdade racial no Brasil, pois foi por meio da língua[gem] que o racismo se estruturou, na medida que ela foi usada como dispositivo linguístico-racial para explorar os povos dominados e seus territórios, forjando um sistema de inferioridade com base na racialização de tais populações dominadas pelo colonialismo; ou seja, utilizando as línguas do dominador para se materializar em práticas discursivas e não-discursivas por meio de tal dispositivo[de dominação]

linguístico-racial, tese, enunciada nessa discussão decolonial.

Destarte, não resta nenhuma dúvida que foi o uso do signo linguístico, articulado ao esquema binário metafísico, que tornou possível o surgimento da linha abissal, uma das formas mais astutas e desumanas da história, responsável pela violência simbólica, segregação e controle sobre as populações subjugadas.

Neste esquema, a língua colonizadora foi usada como açoite verbal para reprimir o corpo físico à medida que todo dizer é um fazer e foi assim que as línguas das metrópoles criaram o racismo ao impor a inferioridade desconcertante que ainda açoita os seres sob o estado de colonialidade na zona estabelecida do não-ser. Por isso, em muitas partes do mundo a língua do antigo colonizador continua sendo a língua do outro, mesmo passado décadas ou séculos do rompimento com a antiga metrópole, como aconteceu no caso do Brasil.

O dilema de Derrida, nascido em África, foi evocado nessa encruza textual para ilustrar as contradições desencadeadas pelo monolinguismo do outro, o meio pelo qual se tem colocado, em prática, a ideia moderna expressa no lema: "Uma nação, uma língua, uma cultura", tanto nas antigas colônias quando nas velhas metrópoles, onde ele foi testado primeiramente, conforme mencionado antes. E, tal monolinguismo do outro só poderia estar sob o domínio da Lei como língua ou da língua da Lei, como disse Derrida (1996, p.69); ou seja, o monolinguismo estaria sob a força de lei, o que significa dizer que uma coisa é a língua, entidade linguística imaterial, outra coisa é o direito enquanto lógica política usada para dominar uma língua, seus falantes, a própria política em si e criar barreiras como a linha abissal ou zona do não-ser.

Embora, a língua não esteja no domínio das coisas que possam ser possuídas, a vontade de verdade, usurpadora da verdade, acaba criando a ilusão de que "a própria língua da Lei" e "a Lei como língua" são uma coisa só, portanto, algo que pode ser possuído, controlável, vindo de outro lugar, de alhures (cf. Derrida, 1996), ou seja, a língua é um instrumento de dominação e controle, tal qual o sistema jurídico que a utiliza como meio de expressão do seu dizer-fazer.

Então, o dispositivo linguístico-racial, que, aqui aparece como um conceito decolonial, está associado a tal monolinguismo à medida que servia para impor a língua do antigo colonizador aos indígenas e à população negra no Brasil, como um meio de submissão "civilizatória" e como meio de promover a unificação linguística. Ele foi essencial ao discurso que deu corpo ao novo projeto de nação pretendido pelos intelectuais brasileiros, a partir da virada do século XIX para o XX, no qual, a língua portuguesa continuaria com o seu papel "civilizador" na qualidade de língua nacional para difundir a ideia de unidade com a mestiçagem tanto cultural quanto racial contra a "uma ameaça ao futuro da raça e da civilização brancas no país" (Munanga, 2008, p.103). Esse projeto eugênico de branqueamento da população consistia em se valer da linguagem para continuar difundindo uma avaliação negativa de qualquer diferença e justificar "a destruição da identidade racial e étnica dos grupos dominados, ou seja, o etnocídio." (Munanga, 2008, p.103).

Mas, engana-se quem pensa que tal projeto deixou de existir. Ele permanece vivo, sobretudo, nas aulas de português e nos cursos de formação de professores de língua. A prova de sua existência utópica é que ainda se defende, com toda a veemência, que o papel da escola é ensinar a norma culta da língua portuguesa. E qual seria a posição da linguística diante de situações como essa?

Ora, a "genuína ciência da linguagem" enquanto disciplina que surge como expressão da modernidade, estaria, neste quadro, totalmente comprometida com a colonialidade, uma vez que sempre esteve do outro lado da linha abissal, acima da zona do não-ser (Araújo, 2025a, 2025b, 2026). Talvez, isso possa explicar os motivos pelos quais tenha se mostrado durante muito tempo como apolítica e acima da ética, sob o pretexto da falsa neutralidade, mesmo estando a serviço dos interesses por trás da inteligência artificial, da indústria bélica, do imperialismo europeu e do imperialismo anglo-americano.

Foi por tal razão que, aqui, se defendeu a ideia da criação de uma linguística decolonial que pudesse dar conta das questões enunciadas ao longo dessa encruza textual (cf. Araújo, 2025a, 2025b, 2026a, 2026b), cujo desfecho final não poderia ser outro, senão voltar ao início de Pele Negra: máscaras brancas, para ouvir a potência da voz de Fanon ecoar na leitura do enunciado: "a explosão não vai acontecer hoje. Ainda é muito cedo... ou tarde demais." (cf. Fanon, 2008, p.25). Eis aqui uma encruza desse agora que é o nosso tempo presente, cuja geração tem por missão avançar na descolonização do ser e da língua por meio da justiça epistemológica, sem a qual as democracias permanecem ameaçadas e com elas as maiorias menorizadas permanecem sob o regime das colonialidades que mantém o quadro de injustiça social.

REFERENCES

[1] ARAÚJO, Alex Pereira de. A linguística decolonial: de Fanon aos fenômenos linguísticos ligados à transformação histórica da zona do não-ser em Sul Global. International Journal of Advanced Engineering Research and Science, vol. 13, nº2, fev., 2026a. DOI: https://doi.org/10.22161/ijaers.132.7 . Disponível em:

https://ijaers.com/issue-detail/vol-13-issue-2/. Acesso em: fev., 2026.

[2] ARAÚJO, Alex Pereira de. Decolonizing language and ethnic-racial relationships in Brazilian Portuguese teaching. International Journal of Language, Linguistics, Literature and Culture (IJLLLC), vol. 5, nº 1, jan., 2026b, p.55-71. DOI: https://doi.org/10.59009/ijlllc.2026.0179. Disponível em: https://ijlllc.org/decolonizing-language-and-ethnic-racial-relationships-in-brazilian-portuguese-teaching/ . Acesso em 13 jan., 2026.

[3] ARAÚJO, Alex Pereira de. The emergence of decolonial linguistics: a demand from the global south in the [ancestral] post-future. International Journal of Language, Linguistics, Literature and Culture (IJLLLC), vol. 4, nº 6, dez., 2025a, p.128-135. DOI: https://doi.org/10.59009/ijlllc.2025.0164 . Disponível em: https://ijlllc.org/volume-4-issue-6-nov-dec-2025/. Acesso em 30 dez., 2025a.

[4] ARAÚJO, Alex P. de. A variação linguística entre o político e o decolonial. In: ROCHA, Patrícia Graciela da; LEAL ORDENEZ, Linoel; NINK SOUZA, Ivonete (org.). Linguagem: poder e ensino: debates sobre políticas e práticas educacionais. São Paulo: Pimenta Cultural, 2025b, p.61-89.

[5] ARAÚJO, Alex P. de. O ensino de Português Brasileiro como encruzilhada e as implicações da política linguística para a questão racial e educacional no Brasil decolonial. 2024. Projeto de estágio pós-doutoral. 16f. Universidade Federal do Mato Grosso do Sul, 2025c. DOI: https://doi.org/10.13140/RG.2.2.21540.33927. Acesso em 12 jan. 2026.

[6] ARAÚJO, Alex P. de. BNCC e o ensino de Português: uma normativa curricular para a língua [em face do pretuguês] ou a linguagem [dos falantes] sob força de lei? Tabuleiro de Letras, [S. l.], v. 18, n. 1, p. 11–28, 2024. DOI: https://doi.org/10.35499/tl.v18i1.19967. Disponível em: https://www.revistas.uneb.br/index.php/tabuleirodeletras/article/view/19967. Acesso em: 10 jun. 2026.

[7] ARAÚJO, Alex P. de. Exu diaspórico: um conceito decolonial forjado para compreender o princípio exúlico de comunicação e a pedagogia das encruzilhadas. Revista Calundu, [S. l.], v. 7, n. 2, p. 4–24, 2023. DOI: https://doi.org/10.26512/revistacalundu.v7i2.50906. Disponível em: https://periodicos.unb.br/index.php/revistacalundu/article/view/50906. Acesso em: 21 mar. 2026.

[8] ARAÚJO, Alex P. de. A língua-linguagem como encruzilhada: desafios e implicações tradutórias de um conceito decolonial em elaboração. Língu@ Nostr@, [S. l.], v. 9, n. 2, p. 76 - 99, 2022. DOI: https://doi.org/10.29327/232521.8.2-6 . Disponível em: https://periodicos2.uesb.br/index.php/lnostra/article/view/13091. Acesso em: 10 mar. 2026.

[9] ARAÚJO, Alex P. de. A ordem do discurso de Michel Foucault: 50 anos de uma obra que revelou o jogo da rarefação dos sujeitos e a microfísica dos discursos. Unidad Sociológica, Buenos Aires, v. 19, n. 5, p. 14-23, jun./-set., 2020. Disponível em: https://philarchive.org/archive/PERAOD-7. Acesso em 10 mar., 2026.

[10] ARAÚJO, Alex P. de. A desconstrução da política linguística educacional: em foco a identidade do professor de português. Revista Ibero-Americana de Estudos em Educação, Araraquara, v. 11, n. 3, p. 1259–1280, 2016. DOI: https://doi.org/10.21723/riaee.v11.n3.2827. Disponível em: https://periodicos.fclar.unesp.br/iberoamericana/article/view/2827. Acesso em: 9 mar. 2026.

[11] ARAÚJO, Alex P. de. A desconstrução da ordem do discurso e a violência simbólica nas Orientações Curriculares Nacionais: em questão a identidade do sujeito-professor. Revista Horizontes de Linguística Aplicada, [S. l.], v. 11, n. 2, 2013. DOI: https://doi.org/10.26512/rhla.v11i2.1211. Disponível em: http://periodicos.unb.br/index.php/horizontesla. Acesso em: 9 mar. 2024.

[12] ARAÚJO, Alex P. de; FERREIRA, Élida Paulina (2011). A identidade em parâmetros curriculares: em questão a subjetividade do professor de português. Revista Eletrônica de Educação. São Carlos, SP: UFSCar, v. 5, n. 2, p.96-123, nov. 2011. DOI: https://doi.org/10.14244/19827199226 . Disponível em: http://www.reveduc.ufscar.br. Acesso em: 9 mar. 2024.

[13] AUROUX, Sylvain A revolução tecnológica da gramatização. Tradução de Eni Puccinelli Orlandi. – Campinas-SP: Editora da Unicamp, 1992. (Coleção Repertórios).

[14] CALVET, Louis-Jean. As políticas linguísticas. Tradução de Isabel de Oliveira Duarte, Jonas Tenfen e Marcos Bagno de Araújo. Prefácio Gilvan Mülher de Oliveira. – São Paulo: Parábola Editorial: IPOL, 2007. (col. Na Ponta da Língua).

[15] CÉSAIRE, Aimé. Discurso sobre o colonialismo. Tradução Claudio Willer; Ilustração Marcelo D'Salete. – São Paulo: Veneta, 2020.

[16] DERRIDA, Jacques. Le monolinguisme de l'autre ou la prothése d'origine. Paris: Éditions Galilée, 1996.

[17] FANON, Frantz. Os condenados da terra. Tradução de Lígia Fonseca Ferreira e de Regina Salgado Campos. 1ª edição. – Rio de Janeiro: Zahar, 2022.

[18] FANON, Frantz. Alienação e liberdade: escritos psiquiátricos. Tradução de Sebastião Nascimento; prefácio de Renato Nogueira; introdução e notas de Jean Khalfa. – São Paulo: Ubu Editora, 2020.

[19] FANON, Frantz. Pele negra, máscaras brancas. Tradução de Renato da Silveira. – Salvador: EDUFBA, 2008.

[20] FREIRE, Paulo. Pedagogia da Autonomia: saberes necessários à prática educativa. 28ª edição – São Paulo: Paz e Terra, 1996.

[21] FREIRE, Paulo. A importância do ato de ler: em três artigos que se completam. 23ª edição – São Paulo: Autores Associados: Cortez, 1989.

[22] FREIRE, Paulo. Pedagogia do Oprimido. Rio de Janeiro: Paz e Terra,1987.

[23] FREIRE, Paulo. Ação cultural para a liberdade. Rio de Janeiro: Paz e Terra, 1984.

[24] FREIRE, Paulo. Educação como prática da Liberdade. 14ª edição. – Rio de Janeiro: Paz e Terra, 1983.
[25] FREIRE, Paulo. Freire: Educar é um ato político. Diário do Povo, p.6, 14 ago.1980. Disponível em: https://acervo.paulofreire.org/handle/7891/3041 Acesso em: 12 mar. 2024.
[26] FREIRE, Paulo.; HORTON, Myles. O caminho se faz caminhando: conversas sobre educação e mudança social. – Petrópolis-RJ: Vozes, 2003.
[27] FOUCAULT, Michel. Microfísica do poder. Organização e tradução de Roberto Machado. Rio de Janeiro: Edições Graal, 1979.
[28] FOUCAULT, Michel. A ordem do discurso: aula inaugural no Collège de France, pronunciada em 2 de dezembro de 1970. Tradução de Laura Fraga de Almeida Sampaio. São Paulo: Loyola, 1996. (coleção Leituras Filosóficas).
[29] FOUCAULT, Michel. O sujeito e o poder. In: DREYFUS, Hubert; RABINOW, Paul. Michel Foucault, uma trajetória filosófica: para além do estruturalismo e da hermenêutica. Tradução de Vera Porto Carrero. Rio de Janeiro: Forense Universitária, 1995.p. 231-249.
[30] FU-KIAU, Kimbwandènde Bunseki. O livro africano sem título:cosmologia dos Bantu-Kongo. Tradução e notas à edição brasileira; Tiganá Santana. – 1 ª edição. – Rio de Janeiro: Cobogó, 2024 (col. Encruzilhada).
[31] GERALDI, João W. A ambiguidade dos letrados e o ensino da língua materna no Brasil. Revista Eletrônica de Estudos Integrados em Discurso e Argumentação, v. 5, n. 1, p. 108-121, 17 abr. 2015. Disponível em: <https://periodicos.uesc.br/index.php/eidea/article/view/435>. Acesso em 9 mar. 2024.
[32] GOMES, Nilma L. O combate ao racismo e a descolonização das práticas educativas e acadêmicas. Revista de Filosofia Aurora, [S. l.], v. 33, n. 59, 2021. DOI: 10.7213/1980-5934.33.059.DS06. Disponível em: https://periodicos.pucpr.br/aurora/article/view/27991 . Acesso em: 3 jul. 2024.
[33] GONÇALVES e SILVA, Petronilha Beatriz. Aprender, ensinar e relações étnico-raciais no Brasil. Educação, 30(3). Recuperado de https://revistaseletronicas.pucrs.br/faced/article/view/2745
[34] GONZALES, Lélia. O golpe de 1964: o novo modelo econômico e a população negra. In.: GONZAKES, Lélia; HASENBALG, Carlos. Lugar de negro. – Rio de Janeiro: Zahar, 2022.
[35] GONZALES, Lélia. A categoria político-cultural de amefricanidade. In: GONZALES, Lélia. Por um feminismo afro-latino-americano: ensaios, intervenções e diálogos. – 1ª edição. – Rio de Janeiro: Zahar, 2020.
[36] GNERRE, Maurizio. Linguagem, escrita e poder. – São Paulo: Martins Fontes, 1994.
[37] MENEZES DE SOUZA, Lynn Mario Trindade. Educação linguística: repensando os conceitos de língua e linguagem. In: FERRAZ, Daniel de Mello; KAWACHI-FURLAN, Claudia Jotto (org.). Bate-papo com educadores linguísticos: letramentos, formação docente e criticidade. São Paulo: Pimenta Cultural, 2019.
[38] MIGNOLO, Walter. Histórias Locais / Projetos Globais: Colonialidade, Saberes Subalternos e Pensamento Liminar. Tradução de Solange Ribeiro de Oliveira. 1ª ed. rev. – Belo Horizonte: Editora da UFMG, 2020.
[39] QUIJANO, Anibal. Colonialidade do Poder e Classificação Social. In.: SOUSA SANTOS, Boaventura de.; Meneses, Maria Paula. Epistemologias do Sul. – Coimbra: Edições Almedina, (CES), 2009.
[40] RAJAGOPALAN, Kanavillil. Por uma linguística crítica: linguagem, identidade e a questão ética. – São Paulo: Parábola Editorial, 2003.
[41] SANTOS, Antônio Bispo dos. A terra dá, a terra quer. Imagens de Santídio Pereira – São Paulo: Ubu Editora/PISEAGRAMA, 2023.
[42] SILVA, Tomaz Tadeu da. Os novos mapas culturais e o lugar do currículo numa paisagem pós-moderna. In.: SILVA, Tomaz Tadeu da; MOREIRA, Antonio Flávio (org.). Territórios contestados: o currículo e os novos mapas políticos e culturais. – 6ª edição – Petrópolis-RJ: Vozes, 2004.
[43] SOARES, Magda. B. Linguagem e escola: uma perspectiva social. São Paulo: Ática, 1986.
[44] SOUSA SANTOS, Boaventura de. et al. As Epistemologias do Sul num mundo fora do mapa. Sociologias, Porto Alegre, ano 18, n. 43, set/dez 2016, p. 14-23. https://doi.org/10.1590/15174522-01800430. Disponível em:
[45] https://www.scielo.br/j/soc/a/Y3Fh6D3ywMCFym4wMFVdzsq/?format=pdf&lang=. Acesso 10 maio.2025.
[46] SOUSA SANTOS, Boaventura de. Para além do pensamento abissal: das linhas globais a uma ecologia de saberes. Novos estud. CEBRAP (79), nov. 2007. p. 71-94. https://doi.org/10.1590/S0101-33002007000300004. Disponível em: <https://www.scielo.br/j/nec/a/ytPjkXXYbTRxnJ7THFDBrgc/?format=pdf&lang=pt>. Acesso em 10 maio.2024.
[47] SOUZA, Neusa Santos. Tornar-se negro ou as vicissitudes da identidade do negro brasileiro em ascensão social. Prefácio de Maria Lúcia da Silva e Jurandir Freire Costa. Rio de Janeiro: Zahar, 2021.
[48] VERONELLI, Gabriela Alejandra. Sobre la colonialidad del lenguaje y el decir. Universitas Humanística, [S. l.], v. 81, n. 81, 2015. DOI: https://doi.org/10.11144/Javeriana.uh81.scdl. Disponível em: <https://revistas.javeriana.edu.co/index.php/univhumanistica/article/view/11432>. Acesso em: 6 março, 2026.

International Journal of Advanced Engineering Research and Science (IJAERS)
Peer-Reviewed Journal
ISSN: 2349-6495(P) | 2456-1908(O)
Vol-13, Issue-4; Apr, 2026
Journal Home Page Available: https://ijaers.com/
Article DOI: https://dx.doi.org/10.22161/ijaers.134.10

Effect of Natural Dyes on Jute and Jute-Cotton Blended Fabrics: An Approach of Screen Printing

Mir Akmam Noor Rashid[1*], Shuranjan Sarkar[1], M. M. Alamgir Sayeed[1], Moslem Uddin[2], Ayesha Khatton[3]

[1]Dyeing and Printing Division, Bangladesh Jute Research Institute, Dhaka-1207
[2]Technolgy Wing, Bangladesh Jute Research Institute, Dhaka-1207
[3]Chemistry Division, Bangladesh Jute Research Institute, Dhaka-1207
*Email: noorakmam@gmail.com

Received: 18 Mar 2026,

Received in revised form: 18 Apr 2026,

Accepted: 22 Apr 2026,

Available online: 27 Apr 2026

***Keywords*— Jute fabric, Screen printing, Thickener, Natural dyes, GSM,**

Abstract *— The increasing demand for sustainable and non-toxic textile production has revived interest in natural dyes and biodegradable thickeners as eco-friendly alternatives to synthetic chemicals. This study presents the screen printing on jute-cotton blended fabric using three natural dyes such as turmeric (Curcuma longa), catechu (Acacia catechu), and manjistha (Rubia cordifolia) combined with natural thickener starch. The preliminary results reveal that catechu color performed well based on light fastness (grading 4 out of 5) properties compared to turmeric and manjistha. The rubbing fastness properties were found good in the Manjistha and catechu color applied printed fabric (grading 2-3) compared to turmeric. The GSM study of the catechu printed fabric shows the 35% dye uptake compared to raw jute-cotton blended fabric, 12.7 gm/m^2 was found in the without printed fabric rather than printed fabric it was 19.0 gm/m^2. The bursting strength of the raw jute-cotton blended fabric shows the average time frame 19.1 sec and within the average 400 Kpa pressure which is good enough according to international standard value of bursting strength. The FTIR results were found that the reaction of color with the raw fabric was extreme level. The most intense and complex spectrum was observed for the DP2 means catechu sample (e), indicating the highest level of dye-fiber interaction. This is evident from the significant absorbance in the fingerprint region (900–600 cm^{-1}), where bending vibrations of aromatic and heterocyclic rings in the dye are usually recorded. The use of natural thickener (starch) maintained favorable properties, ensuring smooth screen printability and acceptable print definition.*

I. INTRODUCTION

Printing jute-cotton blended fabric with natural dyes and natural thickeners after environmentally friendly chemical processing results in printed jute fabric that may be applied to a range of diverse and high-value applications. Because textiles come into intimate touch with human tissue, they have an immediate impact on people's safety and health (El-Sayed et al., 2021). The textile industry has made significant investments in the development of novel raw materials and printing techniques in response to technological improvements, with the goal of producing high-quality, reasonably priced textiles in large quantities (Kumelachew et al., 2023). However, a number of environmental issues have been brought about by new technology, such as water contamination from the printing and textile processing industries.

These issues have a significant global impact on both climate change and biological ecosystems. People are becoming more conscious of environmental protection, and as a result, they are paying more attention to the pollution that the textile industry causes in the environment (Bhatia & Devraj, 2017). To safeguard the environment and natural resources, governments have developed a number of rules. "The return to a more natural life has been demonstrated in the emergence of organic agriculture and the popularization of natural food," claims a report on the American textile business. Furthermore, it has permeated the textile industry, as seen by the revival of natural dyes and fibers (Reganold & Wachter, 2016).

Natural coloring and dyes have been used for as long as textiles. Textile coloring has always been a human endeavor; the technique dates back thousands of years, and many of the dyes are ancient. It was used in Europe during the Bronze Age (Gupta and V. K. (2020; Pizzicato et al., 2023). Since the introduction of more affordable and generally accessible synthetic dyes with moderate to exceptional fastness capabilities in 1856, the use of natural dyes with poor to moderate fastness has significantly decreased.

However, the use of natural dyes for textile coloring has primarily been limited to small-scale exporters and producers dealing with high-end eco-friendly textile production and sales, as well as craftsmen, small-scale dyers, and printers (Repon et al., 2024; Bechtold T & Mussak 2009; Vankar 2007). In an effort to combat the environmental damage that synthetic dyes do, several commercial dye companies and small-scale export houses are now investigating the possibility of regularly employing natural dyes for textile printing and dyeing (Ahmed et al., 2024). When it comes to coloring, natural colors are much more unique, calming, and delicate than synthetic ones. The number of businesses that are now known to manufacture natural dyes on a commercial scale is modest, but it is growing every day. Adopting suitable and standardized dyeing and printing procedures is necessary for the commercial utilization of natural dyes without compromising the necessary quality of colored textile products. In order to control each treatment, that is, the variables related to the printing and preparation processes, and produce various hues with balanced color fastness, it has also been thought necessary to reexamine and reconstruct the traditional coloration method.

There has been a great deal of work done on natural dye-based textile dying, but relatively little has been done on printing. Rekaby et al. (2009) investigated the use of pigment printing technology to print natural colors from rhubarb and alkanet on natural materials (wool, silk, cotton, and flax). Karolia and Buch [2008] investigated the Ajarkh textiles with resist printing and natural dyes. Reactive cyclodextrin was assessed by Hebeish et al. (2006) for use in cotton printing with henna as a natural color. Hakeim et al. (2005) investigated the pretreatment cotton fabric printed with curcumin, a natural coloring substance, using chitosan. It was discovered that raising the molecular weight of chitosan increased the color yield. In their 2023 study, Hassabo et al. (2023) examined various printing techniques for cotton fabric printing.

Combining jute with cotton fibre could be a viable strategy for diversifying jute and creating value-added products. Jute fibres provide many benefits, including good qualities, a beautiful golden appearance, and great toughness. Therefore, the methods of printing and dyeing could be used to improve the quality of jute and create a new class of jute-based fabrics with a growing market both domestically and abroad. A lot of properties of printed blended jute and cotton fabrics will be assessed in this work. It is assumed that the printing of jute fabric can be tried using natural dyes and suitable printing additives to produce printed fabric with reasonable fastness to washing, rubbing, and light. Therefore, in the present work, blended jute fabric will be subjected to scouring, eco-friendly bleaching, and mordanting, and subsequently printed with natural dyes extracted from indigo, turmeric and catechu and a natural thickener will be utilized for preparing the print paste. Previously, not much research has been associated to find out the Optimization of Eco-Friendly Screen Printing of Jute-Cotton Blended Fabric with Natural Dyes and Thickener Using Central Composite Design**,** besides physical, mechanical, and structural analysis of natural colour printed jute-cotton blended fabric.

II. MATERIALS AND METHODS

Jute cotton blended fabric was prepared following the scouring and bleaching process to take the treatment of mordanting the blended fabric. The scouring and bleaching process make the fabric white soft and lucrative to do screen printing. On this fabric printing colour looks glossy and increases the fabric value.

Jute-cotton blended fabric has been collected from Narayanganj to run this experiment (Fig. 1). This fabric was cut in GSM cutter machine to know its weight in gram per square meter. It was found that 12.7 gm/m^2

Fig.1: Jute-cotton blended fabric

Natural Dyes: Natural color like turmeric, indigo, catechu, and manjistha were selected based on their eco-friendliness and availability shown in Figure 2. This natural color was collected from the Siddik Bazar, old Dhaka. After collecting this color as a raw form, it was blended by using blundering machine to make it powder form. This powder form natural color was used in the printing paste directly to make a colorful printing paste preparation

Fig.2: Turmeric, Catechu, Manjistha and Indigo dye

Thickeners: Natural thickeners like guar gum, xanthan gum, or starch were used as a thickener. In my printing paste the starch gum was used to make printing paste.

Figure 3 shows the starch gum and table gum. This gum plays important role to make reaction with the binder and natural dyes to form a required printing paste preparation.

Fig.3: Starch gum

Screen Printing Equipment: The screen-printing frame with different designs were made from Nilkhet printing shop. It was 5 different types of frames and printing book was collected to run the modelling part.

Key Process Parameters:

1. Thickener concentration (%)
2. Screen mesh size (threads per inch)

3. Binder (NK)

4. Fixer

Natural color (3 types: Turmeric, Catechu, Manjistha)

III. EXPERIMENTAL PROCEDURE

Preparation for Printing Paste

Prepare the printing pastes using natural dyes and eco-friendly thickeners according to the Table 1. Ensure homogeneous mixing to achieve consistent paste properties.

Table 1: Printing paste preparation recipe

Chemicals	Amount(gm/liter)
Water	700
Binder	200
Fixer	10
Thickener	15
Softener	10
NK Binder	30
Natural color	35

Screen Printing

Print the jute-cotton blended fabric using the prepared pastes. Maintain consistent printing conditions except for the variables under study. Figure 4 shows the printing frame which has been used for the screen printing

Drying and Curing

Dry and cure the printed fabrics as per the specified conditions in the design matrix.

Evaluation of Printed Fabrics

1) Measure color strength using a crock meter

2) Measuring the GSM after printed sample

3) Light fastness test

4) Evaluate wash fastness according to standard washing protocols.

5) Assess fabric hand feel subjectively and/or through tactile testing methods.

GSM measurement

GSM is an important indicator of fabric compactness, yarn linear density, and end-use suitability. Jute-cotton blended fabrics are widely used in packaging, furnishings, agro-textiles, geotextiles, and eco-friendly apparel. Therefore, accurate measurement of catechu printed fabrics GSM is essential for quality control, product classification, and performance evaluation of jute-based textiles. Equation 1 is followed to measure the GSM of the raw fabric and printed fabric. Figure

$$GSM = \frac{m\ (g)}{A\ (m^2)}\ g/m^2 \quad \text{(Equation 1)}$$

Fig.4: GSM measurement

Bursting Strength Test

Bursting strength is a key mechanical property of textile fabrics that indicates their resistance to rupture when subjected to multi-directional stress. Unlike tensile strength, which applies force in one direction, bursting strength simulates real service conditions where fabrics experience pressure from all directions simultaneously. Figure 5 shows the bursting strength test applied sample.

Fig.5: Bursting strength test

Color Fastness

Wash Fastness of all the natural printed samples were determined as per ISO standards ISO

105-C05:2010. Wash fastness rating was measured by the computer color matching system

(Spectra scan 5100).

Light Fastness

Light fastness of all the natural printed samples were determined as per ISO standard ISO 105-

B02:2014.

Crock Fastness

Crock fastness (dry and wet) of the printed sample samples were determined as per ISO standard ISO 105-X12:2016.

Whiteness and Brightness:

Whiteness and Brightness (%) of grey and jute-cotton blended fabrics were determined by

Photo voltmeter using green and blue filters. An average of 10 readings were taken for each

fabric samples.

Tensile Properties:

A Testometric Materials Testing Machine was used for evaluation of tensile properties 6 of grey,

and bleached jute fabric samples using the two-inch raveled Strip Test Method (ASTM D5035), i.e., fabric specimen was gripped between two pneumatic jaws of the tensile tester (gauge length

of 20 cm). A continually increasing load was applied longitudinally to the fabric specimen by

moving the upper jaw at an x-head speed of 5 cm/min until the fabric specimen broke. Breaking

load and elongation were determined. Tenacity and extension (%) at break were then

calculated.

$$\text{Tenacity (cN/tex)} = \frac{(L \times 100)}{W \times GSM} \quad \text{(Equation 2)}$$

L is the breaking load (N), W is the test width (mm), and gsm is the areal density of fabric (g/m^2).

$$\text{Extension (\%)} = \frac{\text{Elongation (mm)}}{\text{Original length (mm)} \times 100} \quad \text{(Equation 3)}$$

An average of 5 readings, in both warp and weft directions, was taken to represent the tensile

properties of the jute fabric.

Fig.6: Screen printing frame

IV. RESULTS AND DISCUSSIONS

Study on Catechu Color Printing

Three different weight percentages of catechu, turmeric, manjistha color was measured in the Sartorius balance with a scale of 20 gm, 40gm and 60 gm. The coloring powder was mixed with the printing paste to the designated paste preparation recipe and paste was finally applied on the jute-cotton blended fabric.

Study on GSM

GSM (Grams per Square Meter) is a critical physical property used to express the mass or weight of a fabric. In jute fabrics, GSM reflects the bulk, strength, and durability, which are essential for industrial, packaging, and fashion applications (e.g., bags, home décor, blended textiles). In this study, before printing the jute-cotton blended fabric the gram per square meter of the fabric was measured (12.7 & 12.3 gm/m^2). After printing with catechu color, the GSM increased 35% of the fabric (19.0 & 19.7 gm/m^2) (Fig.6).

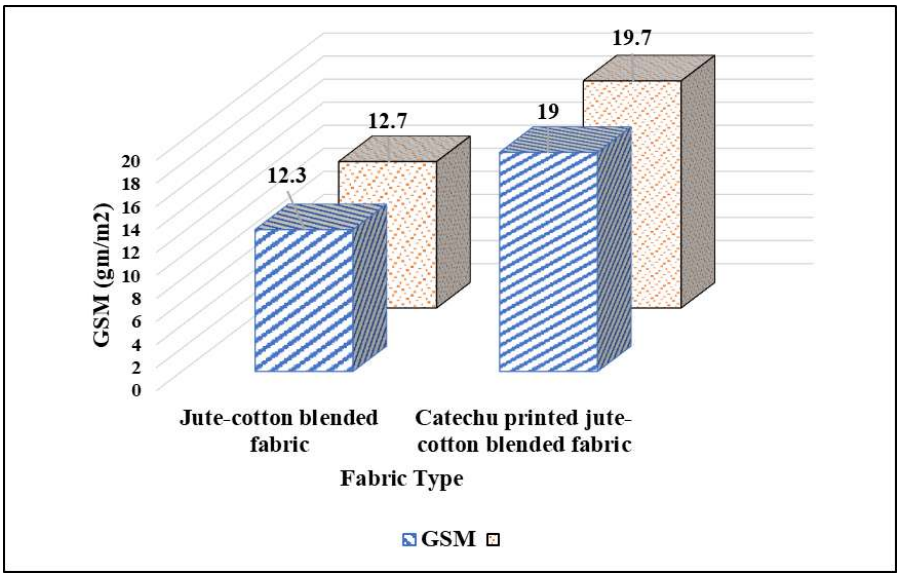

Fig.6: GSM measurement

Study on Bursting Strength Test

Bursting strength refers to the ability of a fabric to withstand pressure applied perpendicular to its surface until rupture. It is particularly important for fabrics used in applications that experience multi-directional stress, such as sacks, bags, and upholstery. In the context of jute fabric, bursting strength is a key mechanical property, given jute's coarse texture and use in load-bearing textiles.. It reveals that the catechu printed sample shows the highest bursting strength test results (428.6 Kpa) within 20.6 seconds. Figure 7 shows the bursting strength test results on 2 types of fabric.

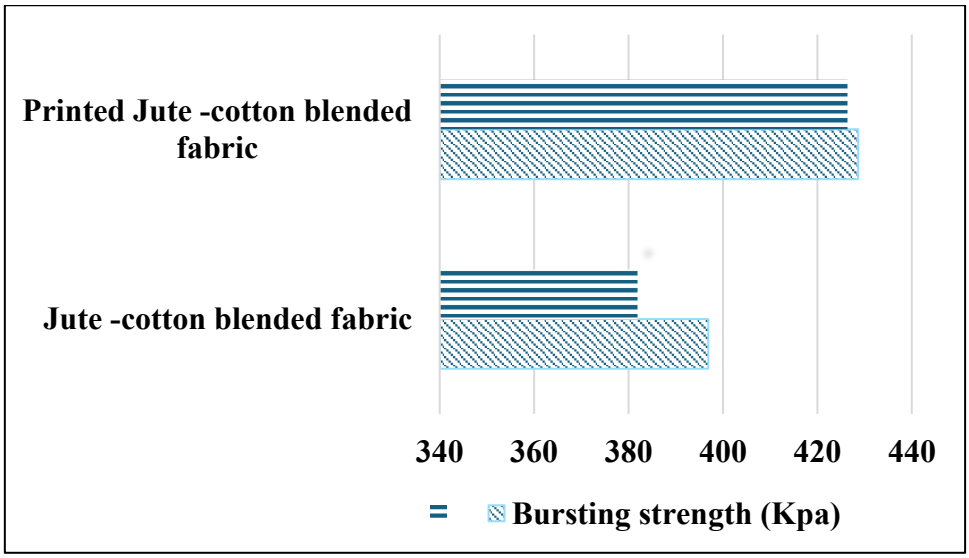

Fig.7: Bursting strength test

Study of Wash Fastness

Wash fastness refers to the resistance of dyed or printed fabrics to washing or laundering. It is an essential quality parameter, especially for jute-cotton blended fabrics printed with natural dyes, as these fabrics are expected to retain color after repeated washes in sustainable textile applications. Table 2 shows the wash fastness on catechu printed blended fabric. It shows that the natural color printed fabric rated 2-3 wash fastness which is internationally acceptable because of natural color application.

Table 2: Wash Fastness on different color percentage of catechu printed blended fabric

No.	Wash Fastness on Catechu printed fabric		
	Loss of depth of shade	Staining	Cross Staining
01.	2	3	3
02.	2	3	3
03	2	4	3
04	2-3	3	3

Study of Color Fastness

Color fastness is a key performance criterion in evaluating the durability and applicability of dyed textiles. In this study, the jute-cotton blended fabrics were printed using three natural dyes are Catechu, Turmeric, and Manjistha were tested for their light fastness and crocking (rubbing) fastness properties. The results are summarized in Table 4.3.

Light Fastness

Light fastness refers to the resistance of printed or dyed fabric colors to fading or degradation upon exposure to sunlight or artificial light (UV radiation). For jute-cotton blended fabric printed with natural dyes, light fastness is a crucial parameter, especially for home textiles, fashion, or outdoor applications where exposure to light is common. In this study 3 different color Turmeric, Catechu and Manjistha was used to observe the light fastness properties. The results demonstrate that Catechu-dyed samples exhibit relatively good light fastness ratings of 4, showing strong resistance to photo-degradation. Manjistha-dyed samples exhibited moderate light fastness values ranging between 3 and 4, while Turmeric-dyed fabrics performed the worst, with values between 2 and 3, reflecting poor resistance to fading under light exposure.

Rubbing Fastness

Rubbing fastness (also called crocking fastness) refers to the resistance of dyed or printed fabric to color transfer when rubbed against another surface. This is especially significant for jute-cotton blended fabrics printed with natural dyes such as turmeric, catechu, and manjistha, which often exhibit variable rubbing resistance due to their poor fixation on cellulose fibers. Dry crocking fastness values were consistently high across most samples, ranging from 4 to 4–5, indicating very good resistance to dry rubbing. Wet crocking, however, showed significantly lower fastness. Catechu and Turmeric samples generally recorded values of 1–2, indicating a tendency for color bleeding when wet. In comparison, Manjistha showed slightly better wet fastness, scoring 2–3, which suggests moderate resistance. These results highlight the limitations of certain natural dyes, particularly in moisture-exposed conditions, despite their ecological benefits.

As shown in Table 3, the natural dye Catechu exhibited the best overall performance, particularly in light and dry crock fastness, although its wet fastness remains low. Manjistha provides a balanced performance with moderate ratings in all categories. In contrast, Turmeric, despite its vibrant color, shows poor light and wet rubbing fastness, limiting its applicability without further treatment or mordanting.

Table 3: Light Fastness and rubbing fastness on different color (turmeric, catechu & manjistha) printed blended fabric

No.	Fastness properties		
	Light fastness	Crock Fastness	
		Dry	Wet
01.	4 (catechu)	4	1-2
02.	4 (catechu)	4-5	2
03	4 (catechu)	4-5	1-2
04	4 (catechu)	4	1-2
05	2-3 (turmeric)	4	1-2
06	2 (turmeric)	4-5	1-2
07	3-4 (manjistha)	4-5	2-3

Fourier Transform Infrared (FTIR) Spectroscopic Analysis

FTIR spectroscopy was employed to investigate the chemical interactions and structural modifications of the jute-cotton blended fabrics before and after dyeing with Indigo DP at different dyeing penetration levels (DP2 catechu, DP32 turmeric, DP40 manjistha). The FTIR spectra of the raw and dyed fabrics are shown in Figure 8, with spectral bands ranging from 4000 to 500 cm^{-1}.

Raw Fabric (a)

The spectrum of the untreated (raw) fabric exhibits characteristic absorption bands associated with cellulose, the main component of jute and cotton fibers. A broad peak observed around 3300 cm^{-1} corresponds to O–H stretching vibrations, indicative of hydroxyl groups in cellulose. The C–H stretching bands at approximately 2900 cm^{-1} also confirm the presence of alkyl groups in the cellulose structure. Additionally, peaks observed in the region of 1000–1200 cm^{-1} are attributed to C–O–C and C–C stretching vibrations, which are typical of polysaccharide backbones.

Dyed Fabrics – Indigo DP and DP Treatments (b to e)

Noticeable changes in the FTIR spectra of the dyed fabrics (b to e) confirm the successful interaction of the natural dye with the fabric structure. The spectrum labelled as (b), representing the Indigo DP treated sample, exhibits new peaks or increased intensity in regions associated with carbonyl (C=O) and aromatic (C=C) groups, particularly around 1650–1600 cm^{-1}. These peaks are attributed to the aromatic structures and conjugated systems present in the Indigo dye molecules.

As the dye penetration level increases from DP40 (c) represents Manjistha to DP2 (e) represents Catechu, the intensity of the characteristic peaks becomes more pronounced. The broadening and shifting of the O–H stretching band near 3300 cm^{-1} in the dyed samples suggest potential hydrogen bonding between the hydroxyl groups of cellulose and the functional groups of the dye. Additionally, enhanced peaks around 1000–1300 cm^{-1} reflect the presence of C–N and C–O stretching, likely resulting from the interaction of dye molecules with the fibre matrix.

The most intense and complex spectrum was observed for the DP2 means catechu sample (e), indicating the highest level of dye-fibre interaction. This is evident from the significant absorbance in the fingerprint region (900–600 cm^{-1}), where bending vibrations of aromatic and heterocyclic rings in the dye are usually recorded.

The progressive increase in band intensity and the emergence of new peaks in the dyed fabrics compared to the raw fabric confirm the successful deposition and chemical bonding of the Indigo DP dye onto the jute-cotton substrate. The FTIR results support the effectiveness of the dyeing process and the strong interaction between the dye and the fibre, especially at higher dye penetration levels such as DP2 (catechu).

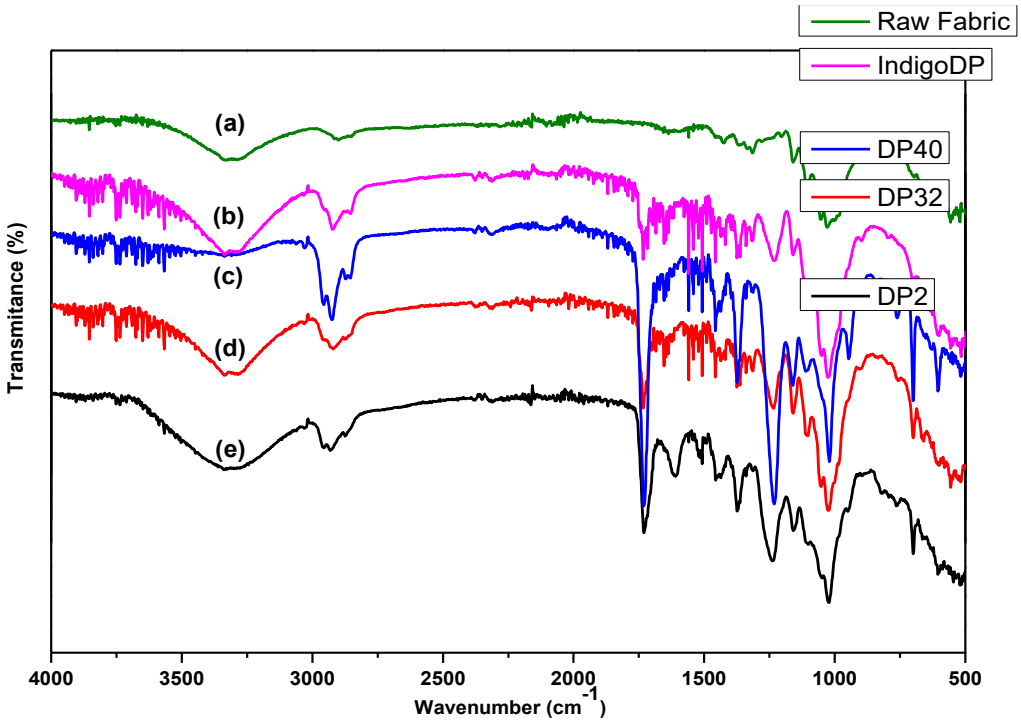

Fig.8: FTIR analysis on Turmeric, Catechu, Manjistha, Indigo color printed fabric with jute-cotton blended fabric

V. CONCLUSION

The preliminary experiment result shows that the rubbing fastness properties was found good in the Manjistha and catechu color applied printed fabric (grading 2-3) compared to turmeric. The GSM study of the catechu printed fabric shows the 35% dye uptake compared to raw jute-cotton blended fabric, 127 gm/m^2 was found in the without printed fabric rather on printed fabric it was 190 gm/m^2. The

bursting strength of the raw jute-cotton blended fabric shows the average time frame 19.1 sec and within the average 400 Kpa pressure which is good enough according to international standard value of bursting strength. The FTIR results were found that the reaction of color with the raw fabric was extreme level. The most intense and complex spectrum was observed for the DP_2 means catechu sample (e), indicating the highest level of dye-fiber interaction. This is evident from the significant absorbance in the fingerprint region (900–600 cm^{-1}), where bending vibrations of aromatic and heterocyclic rings in the dye are usually recorded. The use of natural thickener (starch) maintained favorable properties, ensuring smooth screen printability and acceptable print definition.

ACKNOWLEDGEMENT

First, we express our gratitude to Allah (SWT) for giving us the ability to complete this research. We also acknowledge the support of the Bangladesh Jute Research Institute, Manik Mia Avenue, Dhaka. In addition, we sincerely thank the Ministry of Science and Technology (MOST) for providing financial support for this work.

AUTHOR CONTRIBUTION

Mir Akmam Noor Rashid served as the Project Investigator (PI) and conducted experiments, characterization, data collection, and analysis. He also played the main role in writing the manuscript and developing research ideas. Shuranjan Sarkar and MM Alamgir Sayeed provided technical assistance in achieving the research outcomes. Ayesha Khatton, as Co-PI, and Moslem Uddin helped to manage official documentation and provided logistical support.

FUNDING

This research was funded by a grant from the Ministry of Science and Technology (MOST) (SRG-244387). Mir Akmam Noor Rashid was appointed as the Project Investigator (PI), and Ayesha Khatton served as the Co-PI for this project.

DECLARATION

Not applicable, as this study did not involve human participants or animals.

REFERENCES

[1] El-Sayed, G. A., Othman, H., & Hassabo, A. G. (2021). An overview on the eco-friendly printing of jute fabrics using natural dyes. *Journal of Textiles, Coloration and Polymer Science*, *18*(2), 239-245.

[2] Kumelachew, D. M., Wagaye, B. T., & Adamu, B. F. (2023). Digital textile printing innovations and the future. In *Digital Textile Printing* (pp. 241-259). Woodhead Publishing.

[3] Bhatia, S. C., & Devraj, S. (2017). *Pollution control in textile industry*. WPI publishing.

[4] Reganold, J. P., & Wachter, J. M. (2016). Organic agriculture in the twenty-first century. *Nature plants*, *2*(2), 1-8.

[5] Gupta, V. K. (2020). Fundamentals of Natural Dyes and Its Application on Textile. *Chemistry and technology of natural and synthetic dyes and pigments*, 43.

[6] Pizzicato, B., Pacifico, S., Cayuela, D., Mijas, G., & Riba-Moliner, M. (2023). Advancements in sustainable natural dyes for textile applications: a review. *Molecules*, *28*(16), 5954.

[7] Repon, M. R., Islam, T., Paul, T. K., Jurkonienė, S., Haji, A., Shukhratov, S., & Toki, G. F. I. (2024). Natural dyes in textile printing: parameters, methods, and performance. *Environmental Science and Pollution Research*, *31*(35), 47552-47583.

[8] Bechtold T & Mussak R, *Handbook of Natural Colorants* (John Wiley & Sons, West Sussex), 2009.

[9] Vankar P S, *Handbook on Natural Dyes for Industrial Applications* (National Institute of Industrial Research (2007).

[10] Ahmed, T., Toki, G. F. I., Mia, R., Islam, S. R., Al Fahad, M. A., Adeel, S., & Alpár, T. (2024). New trends in printing applications of natural dyes and pigments. In *Renewable dyes and pigments* (pp. 139-163). Elsevier.

[11] Rekaby, M., Salem, A. A., & Nassar, S. H. (2009). Eco-friendly printing of natural fabrics using natural dyes from alkanet and rhubarb. *The Journal of The Textile Institute*, *100*(6), 486-495.

[12] Karolia, A., & Buch, H. (2008). Ajarkh, the resist printed fabric of Gujarat. *Indian Journal of Traditional Knowledge*, *7*(1), 93-97.

[13] Hebeish A A, Ragheb A A, Nassar S H, Allam E E & EI Thalouth, J I A, *Appl Polym Sci*, 102(1) (2006) 338.

[14] Hakeim O A, Abou-Okeil A, Abdob L A W & Waly A, *Appl Polym Sci*, 97(2) (2005) 559

[15] Hassabo, A. G., Elmorsy, H. M., Gamal, N., Sediek, A., Saad, F., Hegazy, B. M., & Othman, H. (2023). Evaluation of various printing techniques for cotton fabrics. *Journal of Textiles, Coloration and Polymer Science*, *20*(2), 243-253.

International Journal of Advanced Engineering Research and Science (IJAERS)
Peer-Reviewed Journal
ISSN: 2349-6495(P) | 2456-1908(O)
Vol-13, Issue-4; Apr, 2026
Journal Home Page Available: https://ijaers.com/
Article DOI: https://dx.doi.org/10.22161/ijaers.134.11

Some Properties of Max-Min Composition

Kshetrimayum Mangijaobi Devi[1], T. Loidang Chanu[2]

[1]Department of Mathematics, Waikhom Mani Girls' College, Thoubal-795138, Manipur, India
Email: mangijaobiksh@gmail.com
[2]Department of Basic Engineering and Applied Sciences, College of Agricultural Engineering and Post Harvest Technology, Central Agricultural University, Imphal, Ranipool, Sikkim, India
Email : loidangtt@gmail.com

Received: 20 Mar 2026,

Received in revised form: 21 Apr 2026,

Accepted: 25 Apr 2026,

Available online: 28 Apr 2026

***Keywords*—Fuzzy relations, fuzzy sets, max-min composition, max-min transitivity, symmetry.**

Abstract*—*This paper discusses several properties of max-min composition, with particular emphasis on symmetry, max-min transitivity, and inverse composition. Furthermore, the paper presents mathematical proofs of these properties and verifies them through numerical examples using a* 3×3 *order of matrix.

I. INTRODUCTION

In classical set theory, relations define the connections between elements of two or more sets, typically as a subset of the Cartesian product of the sets. However, in fuzzy set theory, fuzzy relations generalize this concept by introducing degrees of membership. This allows partial or uncertain relationships between elements, making fuzzy relations more flexible for modeling real-world scenarios involving uncertainty and vagueness. A fuzzy relation is a mapping that assigns each pair of elements from two sets a value between 0 and 1, representing the strength or degree of relation between those elements.

Whereas, the composition of fuzzy relations is a method to combine two or more fuzzy relations to derive a new relationship. This concept extends the idea of relational composition from classical set theory to fuzzy set theory, allowing for modeling of complex, uncertain and imprecise systems. In real-world scenarios, relationships between elements are often indirect. For example, if there is a fuzzy relation between sets P and Q and another between Q and R, then the composition helps to establish a fuzzy relation between P and R. Fuzzy relation composition plays a crucial role in systems where indirect, uncertain, or gradual relationships need to be effective.

The concept of fuzzy relations is an extension of the fuzzy set theory introduced by Zadeh [1]. In 2012, Dorugade Namdev et al. [2] presented a simple approach to predict life of a component indirectly from imprecise information by exploring the compositional rule of inference of fuzzy relations. They also developed a MATLAB program to compute the degree of success of the outcome.

Gowrishankar et al. [3] presented a systematic exposition of fundamental operations on fuzzy relations, with particular emphasis on max-min and max-product compositions supported by illustrative examples. The authors further analyze key algebraic properties—including zero, identity, equality, inequality, subset, associativity, union, intersection, and distributivity and substantiate these properties through numerical verification using 2×2 matrix representations, supplemented by exercise problems with detailed solutions. Shakhatreh and Qawasmeh [4] presented some concepts and definitions related to the max-min composition of fuzzy relations. They also proved max-min

composition of three fuzzy relations using associativity. Mangijaobi [5] introduced associative properties in max-product composition of three binary fuzzy relations and also presented the reversal law of two binary fuzzy relations holds under max-product composition. Further, an example is also provided by using a 3×3 order of matrix. Bezdek and Harris [6] explored some connections between fuzzy partitions and similarity relations. Also finally they showed that every fuzzy c-partition can induce pseudo-metrics on finite data sets, providing a theoretical basis for fuzzy clustering. Related work can be found in the references [7,8,9,10,11,12,13].

This paper discusses several properties of max-min composition. It presents formal mathematical proofs of these properties and verifies them through numerical examples using a 3×3 order fuzzy relation matrix.

II. PRELIMINARIES

First, we will discuss some definitions and preliminaries concepts related to fuzzy sets, fuzzy relations and max-min composition.

Definition 2.1 [10]. If U is a universe of discourse and u be any particular element of U, then a fuzzy set $\tilde{P}$ defined on U may be written as a collection of ordered pairs $\tilde{P}=\{(u,\mu_{\tilde{P}}(u)):u\in U\}$ where, each pair $(u,\mu_{\tilde{P}}(u))$ is called a singleton.

Definition 2.2 [4]. Let U and V be nonempty sets. Then $\tilde{P}=\{((u,v),\mu_{\tilde{P}}(u,v)):(u,v)\in U\times V\}$ is called a fuzzy relations in $U\times V$.

Definition 2.3 [4]. Let U, V and W be nonempty sets, $\tilde{P}_1$ be a fuzzy relation in $U\times V$, and $\tilde{P}_2$ be a fuzzy relation in $V\times W$. Then $\tilde{P}_1\circ\tilde{P}_2=\{(u,\mathrm{w}),\ \max_{v\in V}\{\min\{\mu_{\tilde{P}_1}(u,v),\mu_{\tilde{P}_2}(v,w)\}:u\in U,v\in V,w\in W\}$ is called max-min composition of $\tilde{P}_1$ and $\tilde{P}_2$.

III. RESULTS

Now we prove the following theorems

Theorem 3.1. If $\tilde{P}_1$ and $\tilde{P}_2$ are symmetric, then $\tilde{P}_1\circ\tilde{P}_2$ is symmetric if $\tilde{P}_1\circ\tilde{P}_2=\tilde{P}_2\circ\tilde{P}_1$.

Proof: Here we need to prove that

$\mu_{\tilde{P}_1\circ\tilde{P}_2}(u,w)=\mu_{\tilde{P}_2\circ\tilde{P}_1}(w,u)$ for all $u,w\in U$.

We have,

$\tilde{P}_1(u,v)=\tilde{P}_1(v,u)[\because \tilde{P}_1$ is symmetric]

Similarly, $\tilde{P}_2(v,w)=\tilde{P}_2(w,v)[\because \tilde{P}_2$ is symmetric]

We have

$$\mu_{\tilde{P}_1\circ\tilde{P}_2}(u,w)=\max_{v\in U}\{\min\{\mu_{\tilde{P}_1}(u,v),\mu_{\tilde{P}_2}(v,w)\}\} \text{ for all } u,w\in U. \quad (1)$$

$$\mu_{\tilde{P}_2\circ\tilde{P}_1}(w,u)=\max_{v\in U}\{\min\{\mu_{\tilde{P}_2}(w,v),\mu_{\tilde{P}_1}(v,u)\}\}$$

$$=\max_{v\in U}\{\min\{\mu_{\tilde{P}_2}(v,w),\mu_{\tilde{P}_1}(u,v)\}\} \quad (2)$$

$[\because \tilde{P}_2$ and $\tilde{P}_1$ are both symmetric]

From (1) and (2)

$\mu_{\tilde{P}_1\circ\tilde{P}_2}(u,w)=\mu_{\tilde{P}_2\circ\tilde{P}_1}(w,u)$

$\therefore \tilde{P}_1\circ\tilde{P}_2=\tilde{P}_2\circ\tilde{P}_1$

$\therefore$ It is obviously $\tilde{P}_1\circ\tilde{P}_2$ is symmetric.

Example3.1.1.

If $\tilde{P}_1=\begin{bmatrix}.8&.5&.3\\.5&.7&.6\\.3&.6&.9\end{bmatrix}$, and $\tilde{P}_2=\begin{bmatrix}.6&.4&.5\\.4&.9&.7\\.5&.7&.8\end{bmatrix}$ are symmetric,

then $\tilde{P}_1\circ\tilde{P}_2$ is symmetric if $\tilde{P}_1\circ\tilde{P}_2=\tilde{P}_2\circ\tilde{P}_1$.

Proof: We have to prove that $\tilde{P}_1\circ\tilde{P}_2=\tilde{P}_2\circ\tilde{P}_1$.

Then by using max-min composition of fuzzy relation, we have,

$$\tilde{P}_1\circ\tilde{P}_2=\begin{bmatrix}.8&.5&.3\\.5&.7&.6\\.3&.6&.9\end{bmatrix}\circ\begin{bmatrix}.6&.4&.5\\.4&.9&.7\\.5&.7&.8\end{bmatrix}$$

$$=\begin{bmatrix}.6&.5&.5\\.5&.7&.7\\.5&.7&.8\end{bmatrix} \quad (3)$$

Here, we see that $\tilde{P}_1\circ\tilde{P}_2$ is symmetric.

Again,

$$\tilde{P}_2\circ\tilde{P}_1=\begin{bmatrix}.6&.4&.5\\.4&.9&.7\\.5&.7&.8\end{bmatrix}\circ\begin{bmatrix}.8&.5&.3\\.5&.7&.6\\.3&.6&.9\end{bmatrix}$$

$$=\begin{bmatrix}.6&.5&.5\\.5&.7&.7\\.5&.7&.8\end{bmatrix} \quad (4)$$

Hence, From equation (3) and (4) we get,

$$\tilde{P}_1 o \tilde{P}_2 = \tilde{P}_2 o \tilde{P}_1.$$

Theorem 3. 2. If $\tilde{P}$ is symmetric, then show that each power of $\tilde{P}$ is symmetric.

Proof: We have

$\mu_{\tilde{P}(u,v)} = \mu_{\tilde{P}(v,u)}$[$\because \tilde{P}(u,v)$ is symmetric for all $u, v \in U$.

$$\tilde{P}^2 = \tilde{P} \circ \tilde{P}$$
$$= \tilde{P}(u,v) \circ \tilde{P}(u,v)$$
$$= \tilde{P}(u,v) \circ \tilde{P}(v,u)[\because \tilde{P}(u,v) \text{ is symmetric}]$$
$$\mu_{(\tilde{P}\circ\tilde{P})\circ\tilde{P}}(u,v) = \max_{u\in U}\{\min\{\mu_{\tilde{P}\circ\tilde{P}}(u,u), \mu_p(u,v)\}\}$$
$$= \max_{u\in U}\{\min\{\max_{v\in U}\{\min\{\mu_{\tilde{P}}(u,v), \mu_{\tilde{P}}(v,u)\}\}, \mu_{\tilde{P}}(u,v)\}\}$$

Hence, each power of $\tilde{P}$ is symmetric.

Example 3.2.1. If $\tilde{P}$ is symmetric, then show that each power of $\tilde{P}$ is symmetric.

Proof:

Let $\tilde{P} = \begin{bmatrix} .7 & .5 & .3 \\ .5 & .6 & .4 \\ .3 & .4 & .8 \end{bmatrix}$ be a symmetric.

Now, we have to show that each power of power of $\tilde{P}$ is also symmetric.

$$\tilde{P} \circ \tilde{P} = \begin{bmatrix} .7 & .5 & .3 \\ .5 & .6 & .4 \\ .3 & .4 & .8 \end{bmatrix} \circ \begin{bmatrix} .7 & .5 & .3 \\ .5 & .6 & .4 \\ .3 & .4 & .8 \end{bmatrix}$$

$$= \begin{bmatrix} .7 & .5 & .4 \\ .5 & .6 & .4 \\ .4 & .4 & .8 \end{bmatrix}$$

Here, we see that $\tilde{P} \circ \tilde{P}$ is symmetric.

Now,

$$(\tilde{P} \circ \tilde{P}) \circ \tilde{P} = \begin{bmatrix} .7 & .5 & .4 \\ .5 & .6 & .4 \\ .4 & .4 & .8 \end{bmatrix} \circ \begin{bmatrix} .7 & .5 & .3 \\ .5 & .6 & .4 \\ .3 & .4 & .8 \end{bmatrix}$$

$$= \begin{bmatrix} .7 & .5 & .4 \\ .5 & .6 & .4 \\ .4 & .4 & .8 \end{bmatrix}$$

Thus, we observe that $(\tilde{P} \circ \tilde{P}) \circ \tilde{P}$ is symmetric.

Hence, if $\tilde{P}$ is symmetric, then each power of $\tilde{P}$ is symmetric.

Theorem 3. 3. A fuzzy relation $\tilde{P}(U,U)$ is called max-min transitive if $\tilde{P} \circ \tilde{P} \subseteq \tilde{P}$.

Proof: A fuzzy relation $\tilde{P}(U,U)$ is called max-min transitive if

$\mu_{\tilde{P}}(u,w) \geq \max_{v\in U}\{\min \mu_{\tilde{P}}(u,v), \mu_{\tilde{P}}(v,w)\}$, for each pair $(u,w) \in U \times U$.

By the definition of max-min composition, we have

$$\mu_{\tilde{P}\circ\tilde{P}}(u,w) = \max_{v\in U}\{\min \mu_{\tilde{P}}(u,v), \mu_{\tilde{P}}(v,w)\}$$
$$\leq \mu_{\tilde{P}}(u,w)[\because \text{ by definition of max-min transitive}$$
$$\therefore \tilde{P} \circ \tilde{P} \subseteq \tilde{P}$$

Example 3.3.1. Show that a fuzzy relation $\tilde{P}$ is called max-min transitive if $\tilde{P} \circ \tilde{P} \subseteq \tilde{P}$.

Proof: Let $\tilde{P} = \begin{bmatrix} 1 & .7 & .7 \\ .7 & 1 & .7 \\ .7 & .7 & 1 \end{bmatrix}$ (5)

Now, we shall prove that $\tilde{P}$ is transitive.

$$\tilde{P} \circ \tilde{P} = \begin{bmatrix} 1 & .7 & .7 \\ .7 & 1 & .7 \\ .7 & .7 & 1 \end{bmatrix} \circ \begin{bmatrix} 1 & .7 & .7 \\ .7 & 1 & .7 \\ .7 & .7 & 1 \end{bmatrix}$$

$$\therefore \tilde{P} \circ \tilde{P} = \begin{bmatrix} 1 & .7 & .7 \\ .7 & 1 & .7 \\ .7 & .7 & 1 \end{bmatrix} \quad (6)$$

Comparing equation (5) and (6) we have

$$\tilde{P} \circ \tilde{P} = \tilde{P} = \begin{bmatrix} 1 & .7 & .7 \\ .7 & 1 & .7 \\ .7 & .7 & 1 \end{bmatrix}$$

i.e., $\tilde{P} \circ \tilde{P} \subseteq \tilde{P}$.

Hence, $\tilde{P}$ is a max-min transitive fuzzy relation.

Theorem 3.4. Let $\tilde{P}_1$ and $\tilde{P}_2$ be two fuzzy relation in $U \times V, V \times W$ respectively, then prove that $[\tilde{P}_1(U,V) \circ, \tilde{P}_2(V,W)]^{-1} = \tilde{P}_2^{-1}(W,V) \circ, \tilde{P}_1^{-1}(V,U)$.

Proof: We need to prove that

$\mu_{[\tilde{P}_1 \circ \tilde{P}_2]^{-1}}(u,w) = \mu_{[\tilde{P}_2]^{-1} \circ [\tilde{P}_1]^{-1}}(w,u)$ for all $u, \in U, v \in V, w \in W$.

By definition of max-min composition, we obtain

$$\mu_{\tilde{P}_1\circ\tilde{P}_2}(u,w)=\max_{v\in V}\min\{\mu_{\tilde{P}_1}(u,v),\mu_{\tilde{P}_2}(v,w)\}$$

$$\mu_{[\tilde{P}_1\circ\tilde{P}_2]^{-1}}(u,w)=\max_{v\in V}\min\{\mu_{\tilde{P}_2^{-1}}(w,v),\mu_{\tilde{P}_1^{-1}}(v,u)\}$$

$$=\max_{v\in V}\min\{\mu_{\tilde{P}_2}(v,w),\mu_{\tilde{P}_1}(u,v)\} \quad (7)$$

$$[\because \mu_{\tilde{P}_1^{-1}}(v,u)=\mu_{\tilde{P}_1}(u,v)]$$

$$\mu_{\tilde{P}_2^{-1}}(w,v)\circ\mu_{\tilde{P}_1^{-1}}(v,u)=\max_{v\in V}\min\{\mu_{\tilde{P}_2^{-1}}(w,v),\mu_{\tilde{P}_1^{-1}}(v,u)\}$$

$$=\max_{v\in V}\min\{\mu_{\tilde{P}_2}(v,w),\mu_{\tilde{P}_1}(u,v)\} \quad (8)$$

$$[\because \mu_{\tilde{P}_1^{-1}}(v,u)=\mu_{\tilde{P}_1}(u,v)]$$

From equation (7) and (8), we get

$$\mu_{[\tilde{P}_1\circ\tilde{P}_2]^{-1}}(u,w)=\mu_{\tilde{P}_2^{-1}}(w,v)\circ\mu_{\tilde{P}_1^{-1}}(v,u)$$

Hence, $[\tilde{P}_1(U,V)\circ\tilde{P}_2(V,W)]^{-1}=\tilde{P}_2^{-1}(W,V)\circ\tilde{P}_1^{-1}(V,U).$

Example3.4.1. Let

$$\tilde{P}_1=\begin{bmatrix}1 & .4 & .7\\ .3 & .9 & .5\\ .6 & .2 & 1\end{bmatrix},\ \text{and}\ \tilde{P}_2=\begin{bmatrix}.8 & .5 & .6\\ .7 & 1 & .4\\ .3 & .9 & .8\end{bmatrix},$$

Then prove that $[\tilde{P}_1\circ\tilde{P}_2]^{-1}=\tilde{P}_2^{-1}\circ\tilde{P}_1^{-1}$.

Proof: we need to prove that

$$[\tilde{P}_1\circ\tilde{P}_2]^{-1}=\tilde{P}_2^{-1}\circ\tilde{P}_1^{-1}.$$

Then by using max-min composition of fuzzy relation, we have,

$$\tilde{P}_1\circ\tilde{P}_2=\begin{bmatrix}1 & .4 & .7\\ .3 & .9 & .5\\ .6 & .2 & 1\end{bmatrix}\circ\begin{bmatrix}.8 & .5 & .6\\ .7 & 1 & .4\\ .3 & .9 & .8\end{bmatrix}$$

$$=\begin{bmatrix}.8 & .7 & .7\\ .7 & .9 & .5\\ .6 & .9 & .8\end{bmatrix}$$

$$\therefore\ [\tilde{P}_1\circ\tilde{P}_2]^{-1}=\begin{bmatrix}.8 & .7 & .6\\ .7 & .9 & .9\\ .7 & .5 & .8\end{bmatrix} \quad (9)$$

Then,

$$[\tilde{P}_2]^{-1}\circ[\tilde{P}_1]^{-1}=\begin{bmatrix}.8 & .7 & .3\\ .5 & 1 & .9\\ .6 & .4 & .8\end{bmatrix}\circ\begin{bmatrix}1 & .3 & .6\\ .4 & .9 & .2\\ .7 & .5 & 1\end{bmatrix}$$

$$=\begin{bmatrix}.8 & .7 & .6\\ .7 & .9 & .9\\ .7 & .5 & .8\end{bmatrix} \quad (10)$$

Hence, from equation (9) and (10) we get,

$$[\tilde{P}_1\circ\tilde{P}_2]^{-1}=[\tilde{P}_2]^{-1}\circ[\tilde{P}_1]^{-1}$$

IV. CONCLUSION

This paper study several properties of max-min composition, including symmetry, max-min transitivity, and inverse composition. These properties are mathematically proved and systematically verified by using numerical example of a 3×3 order of matrix.

REFERENCES

[1] Zadeh, L. A. (1965). Fuzzy Sets. *Information and control,* 8, 338-53.

[2] Dorugade Namdev H., Nhivekar, G.S. & Mudholkar, R.R. (2012). Application of fuzzy composition for electronics component. *International Journal of Advanced Engineering Research and Studies*, I(II), 138-141.

[3] Gowrishankar, C. Dharshinee, R. & Geetha, K.. (2020). Properties of composition of fuzzy relations and its verifications. *International Journal of Management and Humanities(IJMH),* 4(5), 1-7. DOI:10.35940/ijmh.E0514.014520

[4] Shakhatreh, M.A. & Qawasmeh, T.A. (2020). Associativity of max-min composition of three fuzzy relations, *Italian Journal of Pure and Applied Mathematics-N*. 44, 224-228.

[5] Mangijaobi, Ksh. (2025). Fuzzy relation and its max-product composition. *The Aligarh Bulletin of Mathematics,* 44(1), 57-65.

[6] Bezdek, J.C. & Harris, J.D. (1978). Fuzzy partitions and relations; an axiomatic basis for clustering. *Fuzzy Sets and Systems,* 1(2), 111-127. https://doi.org/10.1016/0165-0114(78)90012-X

[7] Kumar, S. & Gangwal, Chh. (2021). A study of Fuzzy Relation of Its Application in Medical Diagnosis. *Asian Research Journal of Mathematics*, 17(4), 6-11. DOI:10.9734/arjom/2021/v17i430289

[8] Li, D. & Zhang,Y. (2024). Aggregation of I-transitive fuzzy relations and fuzzy preference relations. *Computational and Applied Mathematics*, 1-21. DOI: https://doi.org/10.21203/rs.3.rs-2945730/v1

[9] Latha Devi, R.A. & Velammal, G. (2024). Application of Z-Fuzzy Relationship to Medical Diagnosis, *African Journal of Biological Sciences,* 6(9), 2034-2043.https://doi.org/10.33472/AFJBS.6.9.2024. 2034-2043

[10] Pundir, S. K. & Pundir, R. (2022). Fuzzy sets and their applications. *Pragati Prakashan tenth edition.*

[11] Zadeh, L.A. (1971). Similarity relations and fuzzy ordering. *Information Sciences: an International Journal,* 3(2), 177-200. https://doi.org/10.1016/S0020-0255(71)80005-1

[12] Zadeh, L.A. (1997). Toward a theory of fuzzy information granulation and its centrality in human reasoning and fuzzy logic. *Fuzzy Sets and Systems,* 90(2) 111-127. https://doi.org/10.1016/S0165-0114(97)00077-8

[13] Zimmermann, H.J. (2010). Fuzzy set theory. *Wiley Interdisciplinary Reviews Computational Statistics,* 2, 317-332. DOI:10.1002/wics.82

International Journal of Advanced Engineering Research and Science (IJAERS)
Peer-Reviewed Journal
ISSN: 2349-6495(P) | 2456-1908(O)
Vol-13, Issue-4; Apr, 2026
Journal Home Page Available: https://ijaers.com/
Article DOI: https://dx.doi.org/10.22161/ijaers.134.12

Coastal Heritage Conservation Methods, a Visual-Based Pathological Assessment for Historic Masonry; A case study of Fort Williams

Cephas Teyie, Han Weicheng*

College of Architecture and Art, Taiyuan University of Technology, Taiyuan, China
No. 79 West Yingze Street, Wanbailin District, Taiyuan, Shanxi Province, China
*Corresponding Author

Received: 25 Mar 2026,

Received in revised form: 22 Apr 2026,

Accepted: 26 Apr 2026,

Available online: 30 Apr 2026

Keywords*— *Architectural heritage conservation, coastal masonry deterioration, Fort Williams, ICOMOS standards, visual-based assessment, Ghanaian forts.

***Abstract*—*Ghana's coastal forts and castles, including Fort Williams, suffer from severe decay due to marine exposure, rising damp, salt crystallization, biological growth, and past improper repairs. Systematic, low-cost diagnostic methods are needed for resource-limited heritage contexts. To diagnose the principal deterioration mechanisms of Fort Williams using a non-invasive visual assessment aligned with ICOMOS standards, and to propose a phased, evidence-based conservation framework. A four-phase visual protocol was applied: (1) systematic photographic survey, (2) pathology taxonomy and causal analysis, (3) intervention design guided by conservation ethics, and (4) monitoring plan. Deterioration types were recorded across all architectural spaces. The key mechanism is a self-reinforcing cycle: capillary rise, rain, and sea spray introduce moisture that dissolves salts; evaporation causes sub-florescence, generating crystallization pressure that cracks bricks and mortars, allowing more moisture ingress. Persistent dampness also supports algae, fungi, and moss, which retain further moisture. The most severe decay occurs at wall bases and in areas with poor ventilation or roof leaks. Interrupting moisture sources is the only way to break the deterioration loop. A phased intervention is proposed: (1) source control and monitoring (0–12 months), (2) desalination and biological cleaning (12–24 months), (3) lime mortar reinstatement and brick replacement (24–48 months), and (4) perpetual maintenance. Systematic visual assessment alone can produce robust conservation decisions, offering a replicable model for other coastal forts in Ghana and similar tropical environments. Future work must include laboratory salt analysis, long-term monitoring, and socio-economic integration.*

I. INTRODUCTION

Ghana's coastal forts and castles, built between the 15th and 19th centuries, are UNESCO World Heritage sites of immense historical, architectural, and cultural significance. Among them, Fort William (originally Fort Anomabo, built 1753) is notable for its well-preserved layout and its later use as a state prison and community

library. However, centuries of exposure to a harsh marine environment, combined with deferred maintenance and inappropriate past repairs, have led to severe material decay.

Most previous studies on Ghanaian coastal heritage have focused on historical narrative, tourism, or adaptive reuse potential, but systematic, building-pathology-based conservation diagnostics remain rare. This gap is critical because interventions that do not address root causes such as rising damp and salt transport can accelerate damage.

This study therefore aims to diagnose the principal deterioration mechanisms affecting the masonry of Fort Williams using a non-invasive, ICOMOS-aligned visual assessment; classify and map the spatial distribution of pathologies; then propose a phased, material-compatible conservation framework that prioritizes moisture source control.

The significance of this study can therefore be identified in threefold. (1) Culturally preserving a key symbol of Ghana's colonial and post-colonial history. (2) Scientifically advancing an evidence-based, engineering-informed approach for coastal heritage in tropical climates. And (3) practically providing a low-cost, replicable diagnostic protocol for heritage professionals and policymakers in resource-limited settings.

II. THEORETICAL AND ETHICAL FOUNDATIONS.

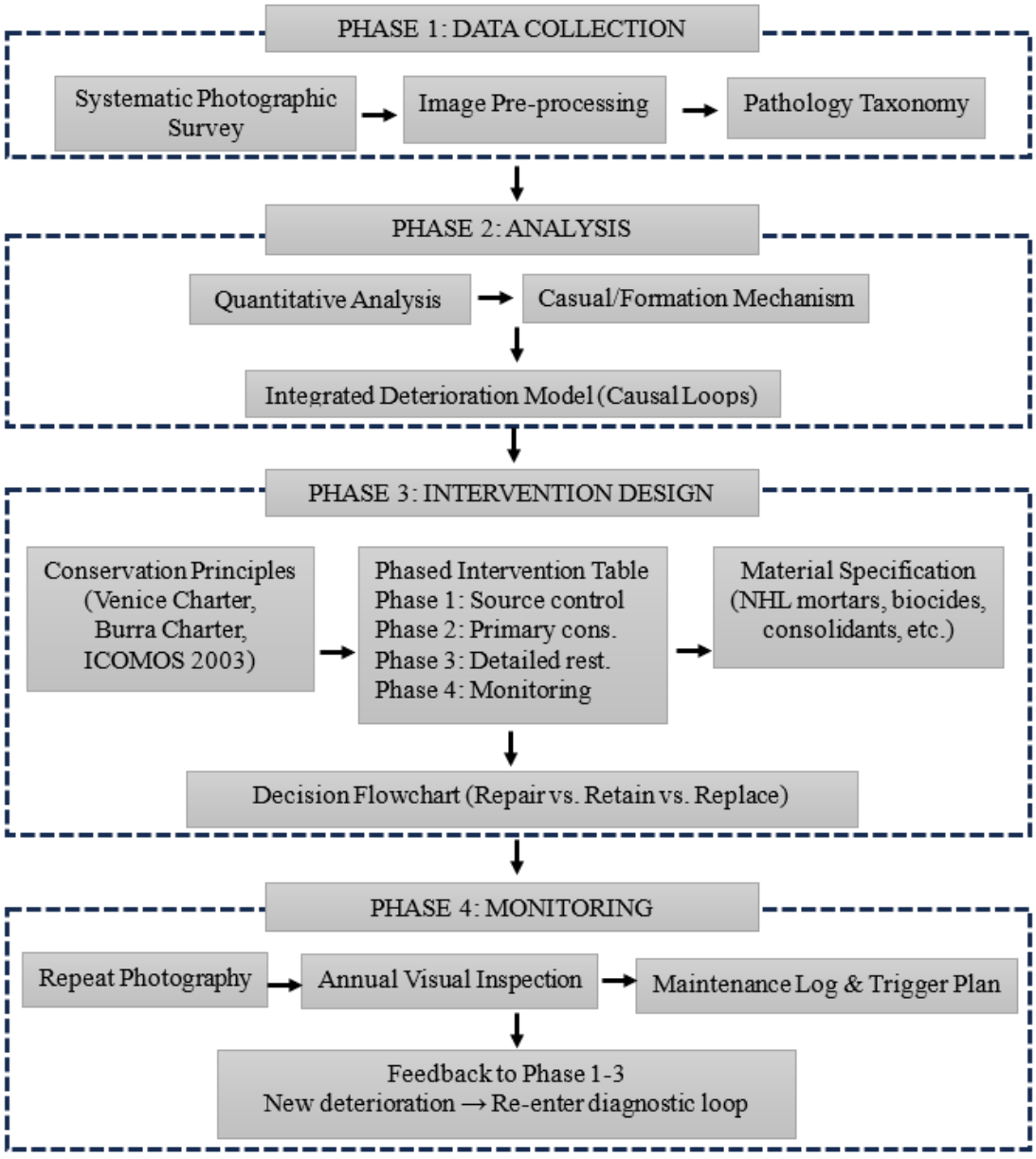

Fig.1. Conceptual Framework

This study is grounded in four interconnected bodies of knowledge:

1. ***Heritage Values Theory (Mason, 2002):*** Recognizes historical, aesthetic, informational, communal, and economic values. Any intervention must enhance rather than diminish these values.
2. ***Conservation Doctrine - Venice Charter (1964), Burra Charter (2013), ICOMOS Structural Restoration Charter (2003)***: Principles of minimal intervention, reversibility, authenticity, material compatibility, and root-cause treatment.
3. ***Building Pathology***: Focuses on understanding the physical, chemical, and biological mechanisms of deterioration (e.g., salt crystallization, capillary rise, biofilm formation).
4. ***Structural Assessment Theory***: Provides systematic inspection and documentation methods (visual, non-destructive).

These theories are operationalized through the conceptual framework as shown in Figure 1.

Table 1 summarizes the international standards aligned with the study.

Table 1. Summary of International Standards Aligning with the Study.

Standard	Year	Key principles aligned with the study
Venice Charter	1964	Authenticity, Minimal Intervention, Documentation.
ICOMOS Structural Restoration Charter	2003	Medical Approach, Root Cause Treatment, Material Compatibility, Reversibility.
Burra Charter	1979/2013	Cultural Significance, Retention of Fabric, Conservative Reconstruction
ICOMOS Timber Structures Principles	1999	Monitoring, Maintenance, Material Matching, Discreet Marking
Nara Document	1994	Culturally Relative Authenticity, Intangible Values
UNESCO World Heritage Operational Guidelines	Various	Reconstruction only with Documentation, No Conjecture
ICOMOS-ISCS Glossary	2008	Standardized Pathology Terminology

III. METHODOLOGY

3.1 Research Approach

The research adopted a visual-based, non-invasive diagnostic survey aligned with the ICOMOS medical model for structural restoration (ICOMOS, 2003). This model emphasizes systematic diagnosis of root causes before intervention, rather than ad hoc treatment of symptoms. No samples were taken from site, all assessments were based on systematic observation, photography, and mapping. The methodology was structured into four phases, as illustrated in the conceptual framework (Figure 1).

3.2 Case Study Area: Fort Williams, Anomabo

Fort William is located in Anomabo, Central Region, Ghana (5°10′N, 1°08′W). Built by the British in 1753 on the site of earlier Dutch and English forts, it was renamed in the 1830s after King William IV. Constructed almost entirely with local materials (stone, brick, lime mortar), it was inscribed as a UNESCO World Heritage site in 1979. After the abolition of the slave trade, it served as a state prison until 2001, then briefly as a community library. The fort's architectural form (see Figures 2–5) includes a courtyard, governor's chamber, dungeons, and defensive walls.

Architectural Form of Fort Williams.

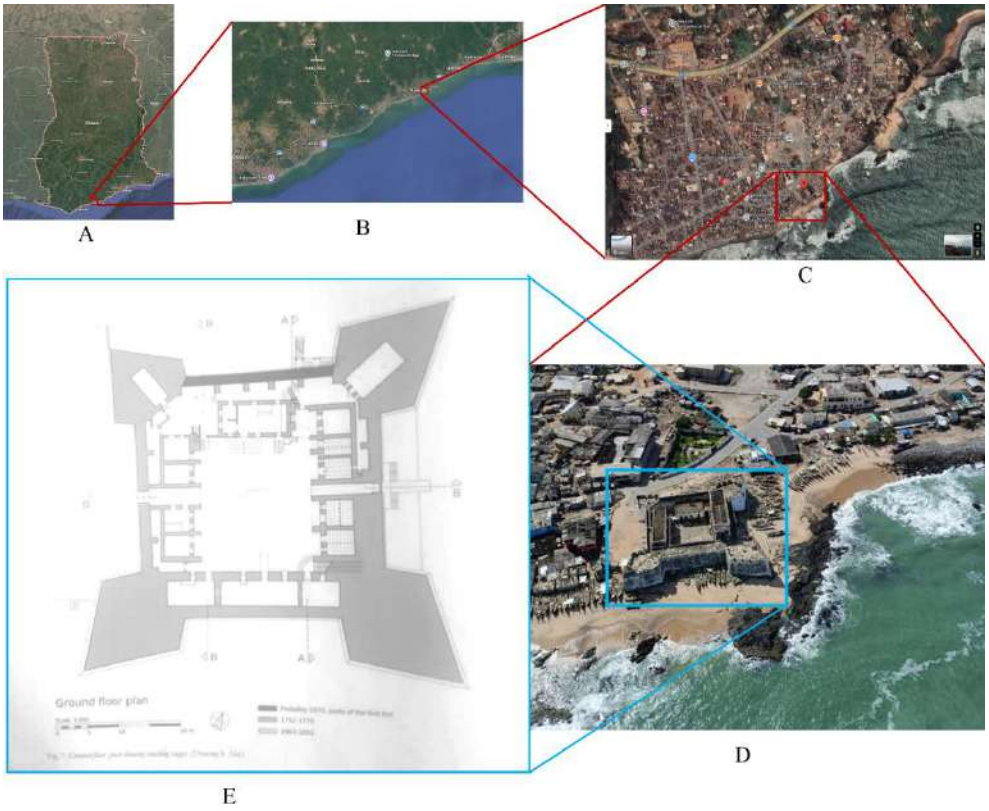

*Fig.2. Location of Fort Williams. (**A&B**) Map of Ghana (Google map, 2025), (**C&D**) Anomabo Township (Google map), (**E**) Fort Williams - Floor plan. (Source: Fort Williams Site Management.)*

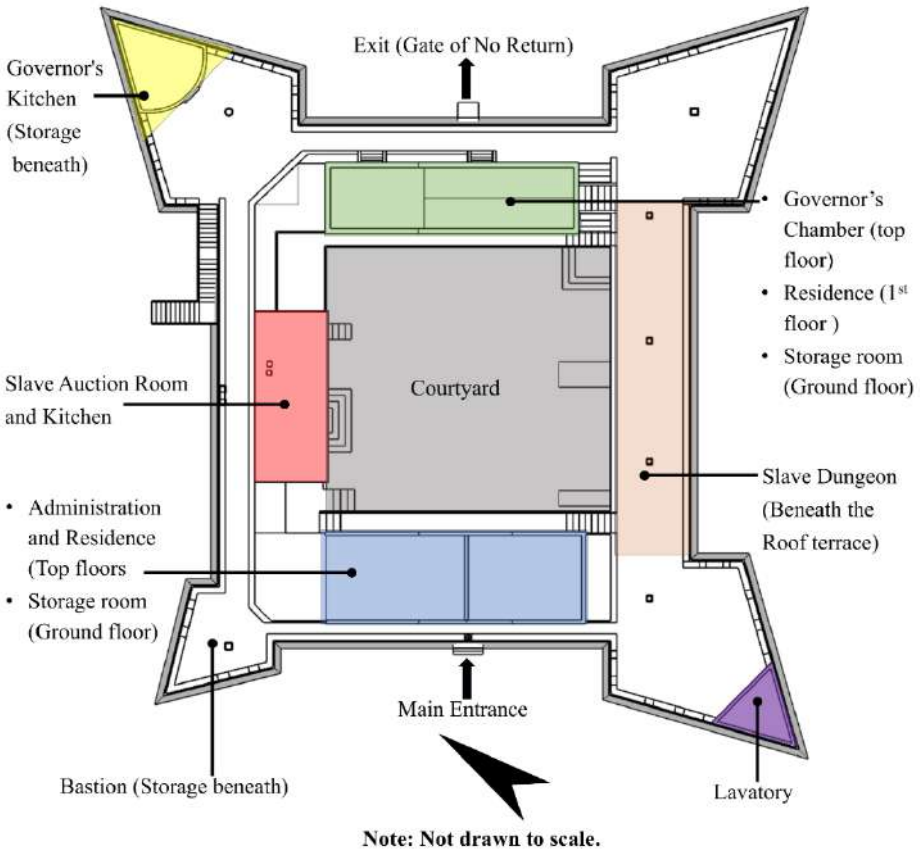

Fig.3. Spatial Organization from aerial view (Source: Drawn by author, 2025)

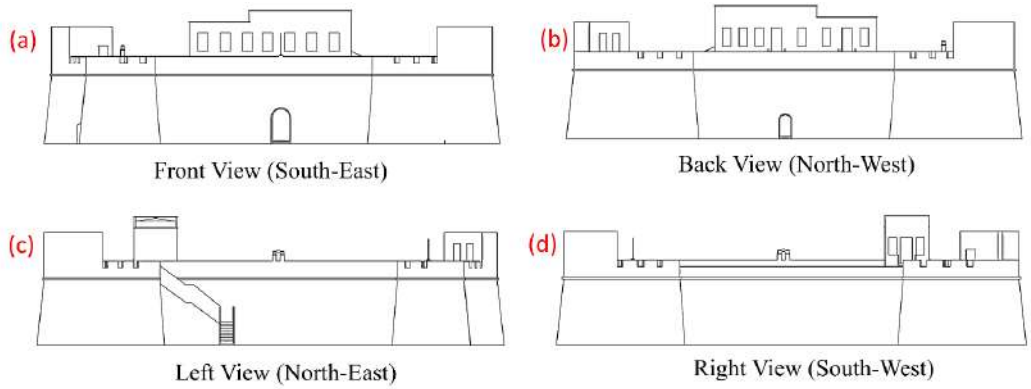

Fig.4. Elevations/Views of Fort Williams (Source: Drawn by author, 2025)

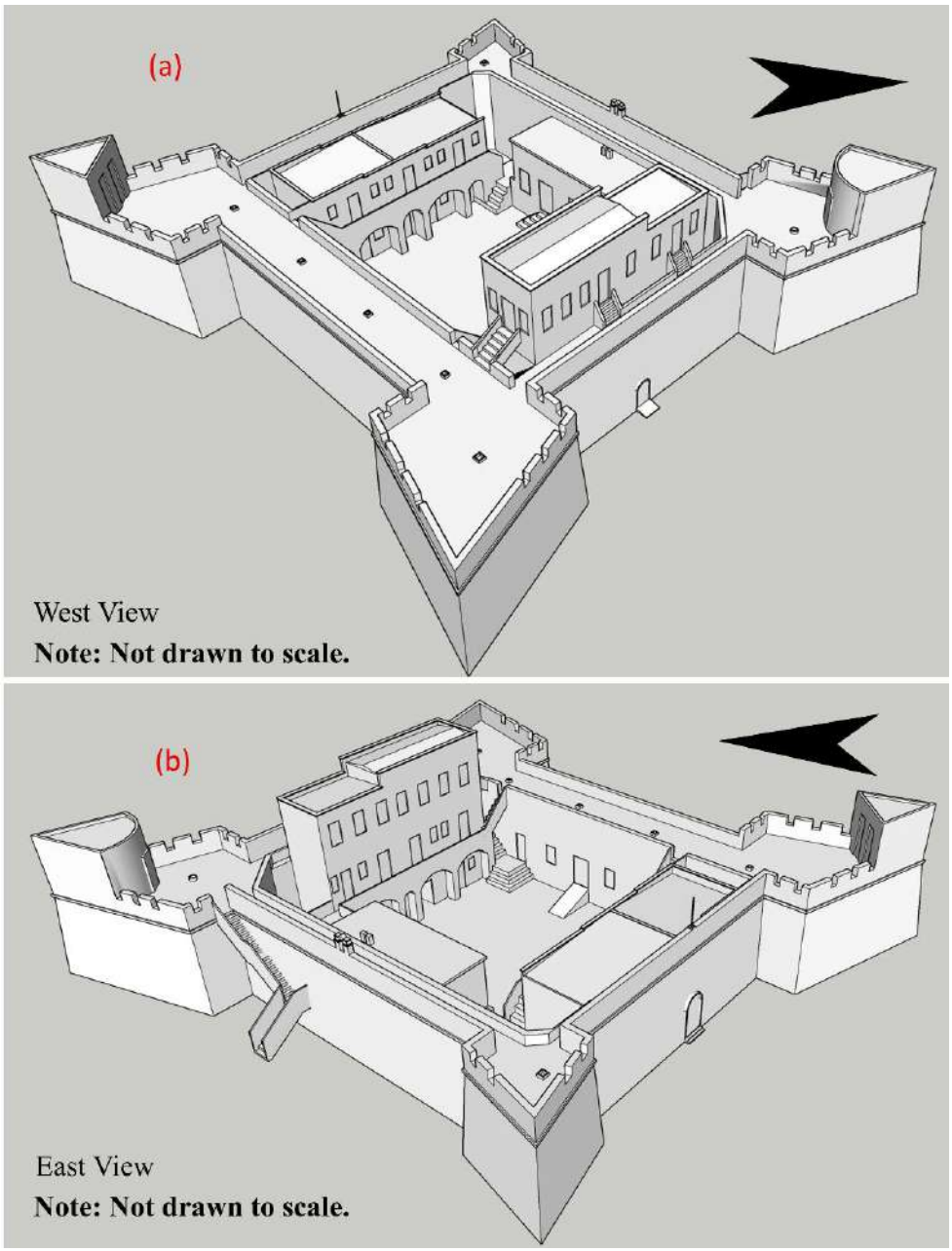

Fig.5. 3D Renderings of Fort Williams (Source: Drawn by author, 2025)

3.3 Environmental Context

Anomabo has a humid tropical coastal climate with a mean annual temperature of 24.1–27.3 °C. and relative

humidity of 80–88%. A bimodal rainfall from May–June and September–October with a persistent marine aerosols and salt-laden winds. Figure 6 gives the climate statistics of Anomabo from 1991 to 2021.

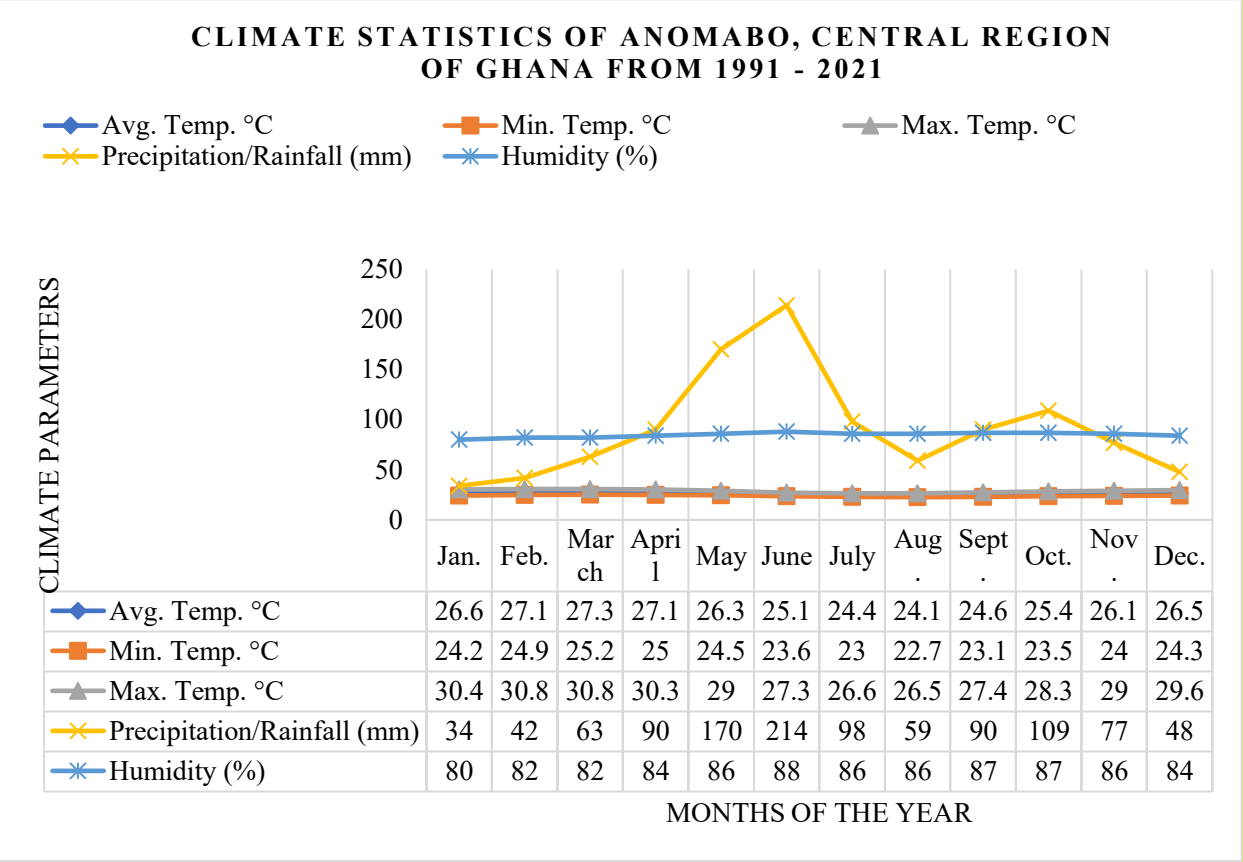

	Jan.	Feb.	March	April	May	June	July	Aug.	Sept.	Oct.	Nov.	Dec.
Avg. Temp. °C	26.6	27.1	27.3	27.1	26.3	25.1	24.4	24.1	24.6	25.4	26.1	26.5
Min. Temp. °C	24.2	24.9	25.2	25	24.5	23.6	23	22.7	23.1	23.5	24	24.3
Max. Temp. °C	30.4	30.8	30.8	30.3	29	27.3	26.6	26.5	27.4	28.3	29	29.6
Precipitation/Rainfall (mm)	34	42	63	90	170	214	98	59	90	109	77	48
Humidity (%)	80	82	82	84	86	88	86	86	87	87	86	84

Fig.6. Climate Statistics of Anomabo, Central Region of Ghana from 1991 – 2021.

Source: *Climate Data, 2025*

3.4 Visual Survey Protocol

The survey was conducted in January 2025. Each accessible space (courtyard, terrace, kitchen, auction room, dungeons, governor's chamber, kitchen, lavatory, staircase, storage rooms, administrative/residential rooms, exterior defense wall, upper exterior walls) was examined. The deterioration types were recorded using a standardized checklist derived from ICOMOS-ISCS (2008) terminology. Photographs were also taken with scale references and a causal loop diagram was developed to integrate the findings.

Salt-induced: surface efflorescence, sub-florescence (crypto-florescence), plaster delamination, plaster spalling/loss, brick/stone scaling/powdering, salt staining/discoloration.

Biological: algal biofilm (green), cyanobacterial colonization (black/green), fungal growth (mould), moss colonization, biological patina/soiling.

IV. RESULTS

4.1 General Observations

Externally, the fort's walls have been freshly painted, giving a superficial impression of good condition. However, the interior courtyard reveals extensive deterioration (Figures 7–8). Roofs show local failures, biological growth is widespread, and mortar joints are eroded. Despite this, the overall geometry and spatial hierarchy remain intact.

Fig.7. Exterior Walls of Fort Williams Source: Site investigation by author, 2025.

Fig.8. Courtyard within Fort Williams Source: Site investigation by author, 2025.

4.2 Deterioration Types and Distribution

Table 2 presents the observed deteriorations per location. The most affected areas are the wall bases, terrace, courtyard, governor's chamber, and areas with roof leaks or poor ventilation.

Table 2. Observed Deteriorations at Fort Williams.

Location	Deteriorations										
	Efflorescence & Salt Crystallization						Damp & Microbial Growth				
	Surface Efflorescence	Sub-florescence (Crypto-florescence)	Plaster Delamination Due to Salt	Plaster Spalling / Loss	Brick/Stone Surface Scaling / Powdering.	Salt Staining / Discoloration / Paint Loss	Algal Biofilm (Green)	Cyanobacterial Colonization (Black/Green)	Fungal Growth (Mold)	Moss Colonization	Biological Patina / Soiling
Courtyard	●	●	●	●	●	●		●	●	●	●
Terrace	●	●	●	●	●	●					●
Kitchen	●	●	●			●			●	●	●
Auction Room	●	●	●			●			●	●	●
Dungeons	●					●	●			●	
Governor's Chamber	●	●	●			●	●			●	
Governor's Kitchen	●	●	●			●					
Lavatory	●	●	●			●					
Staircase	●	●	●			●					●
Storage	●					●	●			●	

Rooms											
Admin./ Residential Rooms	●	●				●	●			●	
Exterior Defense Wall		●				●		●	●	●	
Upper Exterior Walls	●	●	●	●		●		●	●		

4.3 Efflorescence and Salt Crystallization

At Fort Williams, white powdery efflorescence is common on surfaces in the courtyard, terrace and most of the interiors. These deposits form where salt-laden moisture rising by capillary action evaporates at the masonry surface, leaving dissolved salts behind. More damaging is sub-florescence (crypto-florescence), where salts crystallize beneath the surface within the pore structure. This generates crystallization pressure that exceeds the tensile strength of historic bricks and mortars, causing plaster delamination, spalling, and brick scaling (Figure 9 a–e). Severe deterioration is concentrated at wall bases, matching the classic rising-damp salt zonation model. Plaster detachment and paint failure occur at material interfaces where impervious layers trap crystallizing salts. The most advanced damage shows complete loss of plaster and surface disintegration of brick, particularly in areas with chronic moisture exposure and no historic damp-proof course.

Fig.9a–e: Salt efflorescence, plaster failure and brick disintegration. Source: Site investigation by author, 2025.

4.4 Dampness and Biological Colonization

The results again show persistent dampness is widespread at Fort Williams, originating from rising capillary groundwater, wind-driven rain, sea spray, and roof leaks. This sustained moisture supports extensive biological colonization. Green-black algal biofilms cover interior walls and ceilings (Figure 10 a–d), while cyanobacteria and fungal growth appear on both interior and exterior surfaces. Moss colonization is visible on damp exterior walls and roof areas (Figure 10 e–f). Biological growth is most intense at wall bases, where capillary rise maintains continuous wetness, and in poorly ventilated spaces such as dungeons and storage rooms. The biofilms retain moisture, prolonging evaporation and creates favorable conditions for further

biological activity. Dark staining from photosynthetic pigments and metabolic byproducts is evident across multiple surfaces. No active intervention has been applied yet, allowing natural succession from pioneering algae to complex fungal and moss communities.

Fig.10a–f: biological colonization. Source: Site investigation by author, 2025.

4.5 Causal Loop Diagram

At Fort Williams, dampness caused by rising capillary moisture, rain penetration, and marine aerosols supplies the water that dissolves soluble salts within the masonry. As moisture moves toward evaporation surfaces, salt crystallization occurs initially as harmless surface efflorescence, then progresses into a destructive sub-florescence within the masonry pores. The crystallization pressure fractures mortar and brick, creating micro-cracks. These cracks pave way for more moisture which transports additional salts, intensifying the cycle. Persistent dampness or moisture also sustains biological growth (algae, fungi) that retains more moisture, prolonging evaporation and salt activity. The combined effect is accelerated plaster delamination, spalling, material loss, and rising damp-driven vertical zonation of decay. Interrupting moisture sources is therefore the only way to break this self-reinforcing loop as shown in figure 11 below.

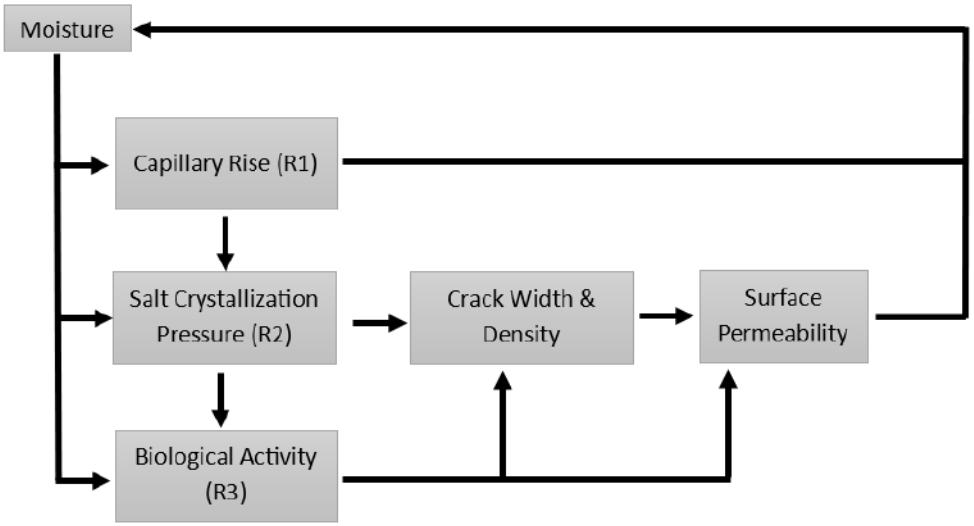

Fig.11: Causal loop diagram: Moisture-Driven Deterioration Cycles. (Source: Designed by author, 2025)

V. DISCUSSION

5.1 Formation Mechanisms.

Efflorescence and Salt Crystallization: The deterioration observed at Fort Williams is consistent with established models of salt decay in coastal masonry (Manohar et al., 2023; Woolfitt, 2019). The convergence of multiple salt sources such as marine sodium chloride from sea spray and aerosol deposition, plus sulphates, nitrates, and chlorides carried by rising groundwater, creates an exceptionally aggressive decay environment (Manohar et al., 2023; Franzoni et al., 2014). The absence of any historic damp-proof course allows uninterrupted capillary rise, drawing saline solutions from the moisture or water sources into the porous brick and lime mortar fabric (Franzoni et al., 2014).

The critical distinction between surface efflorescence and sub-florescence explains the spatial pattern of damage. Where evaporation occurs slowly at the masonry surface, salts precipitate as harmless white powdery deposits (Woolfitt, 2019; Wijnhorst et al., 2024). However, at Fort Williams, evaporation rates often exceed the rate of solution transport, forcing crystallization within the pore network just behind the surface (Wijnhorst et al., 2024). This sub-florescence generates crystallization pressure that can exceed the tensile strength of historic materials (Thaulow et al., 2004). Scherer demonstrated that this pressure arises from supersaturation required for crystal nucleation in confined pores, with magnitude depending on the supersaturation ratio and interfacial energy between crystal and pore wall (Manohar et al., 2023).

The concentration of severe damage at wall bases matches Charola's synthesis of Arnold's four-zone model of salt-affected walls (Charola, 2000). The lowest zone, closest to the ground, retains more soluble salts in solution and shows less damage. The most deteriorated zone occurs immediately above, where less soluble salts such as sodium sulphate precipitate, generating the expansive forces responsible for spalling, delamination, and material loss (Charola, 2000). This vertical zonation is clearly visible at Fort Williams (Figure 9 c–e).

The damage mechanism is intensified by phase transformations of salts in response to environmental fluctuations. Sodium sulphate, common in coastal groundwaters, undergoes repeated transitions between anhydrous thenardite and hydrous mirabilite forms under changing temperature and relative humidity (Thaulow et al., 2004). Each dissolution-recrystallisation cycle generates cyclical stresses that progressively fatigue the material structure (Franzoni et al., 2014). Research on heritage brick structures has documented that the simultaneous presence of sodium chloride and sodium sulphate produces complex deterioration patterns different from single-salt systems (Manohar et al., 2023). The observed progression from plaster staining (c) to render failure (b) to complete material loss (e) represents the temporal evolution of salt damage (Franzoni et al., 2014). Critically, delamination and paint failure at material boundaries occur when impervious layers trap crystallizing salts (Woolfitt, 2019; Charola, 2000). This explains why surface treatments applied to salt-laden masonry inevitably fail, because salts continue migrating toward drying surfaces and accumulate beneath any impermeable coating. Therefore, any sustainable conservation strategy must prioritize moisture source control before attempting desalination or re-plastering.

***Dampness and Biological Colonization*:** As identified earlier, persistent dampness is the primary driver of biological colonization at Fort Williams, and its sources are multiple: rising capillary moisture from saline groundwater, wind-driven rain penetrating exposed walls, marine aerosol deposition, and failed roof coverings. This combination creates a microenvironment where relative humidity remains elevated throughout much of the year, sustained by the bimodal rainfall pattern and coastal humidity (80–88%). Quantitative studies of fungal communities in heritage contexts have shown that humidity explains 19.2% of fungal community composition, the highest single variance factor (Li et al., 2020). This relationship underscores why the persistent dampness documented at Fort Williams has resulted in extensive biological colonization across multiple surface types and orientations.

The porous nature of brick masonry, with its inherent roughness and capillary structure, enables water retention within the material fabric, creating microenvironments where moisture remains available for extended periods even when surface conditions appear dry (Gregorini, 2020). Algae and cyanobacteria function as pioneering colonizers in the biodeterioration sequence, establishing the initial biological foothold on damp masonry surfaces. These microorganisms maintain metabolic activity only when appropriate combinations of dampness, warmth, and light coincide, yet they demonstrate remarkable tolerance to climatic variations, surviving dry periods through dormancy and resuming growth rapidly when moisture returns (Jan, 2020). This adaptive capacity explains the persistent green-black staining on interior walls (Figure 10 a–d), which reappears even after dry spells.

The distinction between interior and exterior colonization patterns arises from differences in moisture sources and microclimatic regimes. Exterior walls experience direct wind-driven rain, marine aerosol deposition, and cyclical wetting-drying driven by solar radiation (Jan, 2020). Interior colonization results primarily

from capillary moisture rising from foundations, condensation on cold surfaces, or leakage through failed roof membranes. These sources produce more sustained substrate dampness without the desiccating effects of direct sunlight and wind. The biological communities at Fort Williams represent a successional sequence beginning with algal pioneers and progressing toward complex assemblages including fungi, mosses, and potentially lichens. Algae establish first because they require only moisture, light, and minimal nutrients derived from atmospheric deposition or substrate dissolution (Cutler, 2019). Their photosynthetic activity produces organic compounds that accumulate on and within the masonry surface, creating nutrient-enriched conditions that support subsequent colonization by heterotrophic fungi and mosses (Jan, 2020).

The deterioration mechanisms accompanying biological growth operate through multiple pathways. Biochemically, microbial metabolic activities produce organic acids that dissolve mineral binders in mortars and plasters, while chelating agents complex with metal ions in the masonry matrix, accelerating material loss (Stewart et al., 2019). Physically, algal and fungal hyphae penetrate surface pores and expand during wetting-drying cycles, exerting mechanical stresses that loosen mineral grains and exacerbate existing micro-fractures (Jan, 2020). The preferential colonization at wall bases aligns with the vertical moisture gradient from capillary rise. Significantly, the dark staining observed results from both photosynthetic pigments within living organisms and the accumulation of metabolic byproducts and trapped atmospheric particulates within the biofilm matrix (Jan, 2020). The biological growth at Fort Williams both indicates and accelerates underlying material decay. While surface colonization alone may appear primarily aesthetic, the sustained presence of moisture-retaining biofilms prolongs surface wetness, creating self-perpetuating conditions that favor continued biological activity and progressively more severe material deterioration (Stewart et al., 2019). Therefore, as earlier emphasized; effective intervention must first eliminate the moisture sources that sustain biological communities; biocide treatment alone, without moisture control, will only provide temporary relief.

5.2 Implications for Conservation

The findings lead to a clear hierarchy of interventions:

1. **Source control** (drainage, roof repair, damp-proof course) must precede any aesthetic or surface treatment.
2. **Desalination** (poulticing) is essential before re-plastering; otherwise, salts will migrate into new plaster.
3. **Sacrificial lime plasters** (more porous than the original brick) are recommended to allow salts to concentrate in the plaster, which can later be replaced.
4. **Biocides** should be used sparingly and only after moisture reduction, with preference for low-toxicity products (e.g., benzalkonium chloride).

6. Proposed Conservation Framework

Based on the diagnosis, a phased, pathology-specific intervention framework as in table 3 is proposed.

Table 3. Phased Intervention Framework for Fort Williams

Phase	Timeframe	Primary Actions	Materials / Methods	Key Conservation Principle
Phase 1: Source control & monitoring.	0–12 months	•Moisture mapping (non-destructive meter) •Excavate around walls, install French drain •Insert breathable DPC (stainless steel or slotted) •Repair all roof leaks, gutters •Improve ventilation	Moisture meter, gravel + geotextile, stainless steel DPC, roofing materials and ventilation grilles.	Root-cause treatment.
Phase 2: Primary conservation (desalination + biocide).	12–24 months	•Dry brush efflorescence (no water washing) •Apply clay/cellulose poultices to salt-affected areas; repeat until conductivity low •Inject lime grout (NHL 2) where plaster delaminated but sound	Attapulgite/arbocel poultice, deionized water, conductivity meter, NHL 2 grout, benzalkonium chloride, soft brushes and HEPA vacuum.	Minimal intervention and reversibility.

		•Remove loose failed plaster •Apply biocide (benzalkonium chloride 0.5-2%) to biological growth, then rinse with deionized water		
Phase 3: Detailed restoration (lime plaster & brick replacement).	24–48 months	•Reinstate plaster with NHL 2 or 3.5 lime plaster (sacrificial, more porous than brick) •Consolidate friable bricks with limewater or ethyl silicate (test area first) •Replace bricks with >20% section loss using handmade, low-strength bricks bedded in NHL 2 mortar •Finish with breathable limewash (no impervious paints)	NHL 2/3.5 lime plaster, limewater or ethyl silicate, replacement bricks, NHL 2 mortar and limewash.	Authenticity and material compatibility.
Phase 4: Perpetual maintenance.	Ongoing	•Annual repeat photography (fixed points, end of wet season) •Annual moisture meter readings at baseline points •Inspect drains, roof, DPC annually •Spot biocide treatment only if growth returns •Maintain intervention log	Photographic reference, moisture meter, inspection checklist and maintenance log	Monitoring and feedback.

VI. CONCLUSION

This study demonstrates that a systematic, visual-based pathological assessment guided by ICOMOS principles can produce robust, actionable conservation decisions for coastal heritage masonry, even without characterization of mineral composition. The case of Fort Williams reveals a self-reinforcing deterioration cycle driven by uncontrolled moisture, leading to salt crystallization, cracking, biological growth, and material loss. Interrupting moisture sources is the only sustainable intervention.

Limitations.

The study lacked laboratory salt analysis (XRD, ion chromatography) therefore all formation mechanisms were inferential. Being a single-site study, findings may not fully represent research findings on other Ghanaian forts and castles. This is a proposed framework which has not been implemented yet and therefore no post-intervention monitoring data was available.

Recommendation for future research.

The absence of laboratory analysis means findings remain inferential and therefore future work should integrate field tests, targeted lab analysis and comparative assessments of other Ghanaian coastal forts. Additionally, sustainable management must integrate socio-economic considerations, adaptive reuse strategies, local stakeholder engagement, and respectful interpretation of the fort's complex historical legacy.

ACKNOWLEDGEMENTS

The authors thank the Ghana Museums and Monuments Board for access to Fort Williams, and the site management team for logistical support.

FUNDING

This research was supported by the Shanxi Provincial Foundation Research Program (Grant No. 202203021211171): Research on the Characteristics and Protection Methods of Salt Weathering Deterioration in Ming Dynasty City Walls in Northern Shanxi.

DISCLOSURE STATEMENT

The authors declare no conflict of interest.

DATA AVAILABILITY STATEMENT

The data (photographs and field notes) are available from the corresponding author upon reasonable request.

AUTHORS' CONTRIBUTIONS

Cephas Teyie[1]: Conceptualization, Methodology, Data collection and curation, Writing and editing, Original draft preparation.

Han Weicheng[2*]: Perfecting of research direction and Reviewing.

All authors read and approved the final manuscript.

REFERENCES

[1] Australia ICOMOS, The Burra Charter: The Australia ICOMOS Charter for Places of Cultural Significance 1999: With Associated Guidelines and Code on the Ethics of Co-Existence, Burwood, Victoria: Australia ICOMOS, pp. 23, 2000.

[2] Cape Coast Climate: Average Temperature by Month, Cape Coast Water Temperature, 2025a.

[3] Charola, A. E., SALTS IN THE DETERIORATION OF POROUS MATERIALS: AN OVERVIEW, May 15, 2000.

[4] Cutler, N., Greening of Masonry Walls Research Project - Why Do Algae Grow on Walls? Test Walls | School of Geography and the Environment, October 14, 2019.

[5] Fort William, Anomabu (1753) – Ghana Museums and Monuments Board, 2025b.

[6] Fort William, Ghana, in Wikipedia, February 19, 2026.

[7] Franzoni, E., Gentilini, C., Graziani, G. and Bandini, S., Towards the Assessment of the Shear Behaviour of Masonry in On-Site Conditions: A Study on Dry and Salt/Water Conditioned Brick Masonry Triplets, Construction and Building Materials, vol. **65**, pp. 405–16, accessed March 5, 2026, from https://www.sciencedirect.com/science/article/pii/S0950061814004747, August 29, 2014. DOI: 10.1016/j.conbuildmat.2014.05.002

[8] GhanaWeb TV, Anomabo Fort Williams, One Oldest Tourist Site in Ghana Left to Crumble, 2023.

[9] Gregorini, B., Facing the Biodeterioration of Construction and Cultural Heritage Materials: A Novel Approach to Predict Algae Growth on Fired Brick Surfaces, December 2020.

[10] INTERNATIONAL CHARTER FOR THE CONSERVATION AND RESTORATION OF MONUMENTS AND SITES (THE VENICE CHARTER 1964).

[11] Jan, E., RIBuild - Internal Insulation in Historic Buildings, RIBuild, 2020.

[12] Li, Y., Huang, Z., Petropoulos, E., Ma, Y. and Shen, Y., Humidity Governs the Wall-Inhabiting Fungal Community Composition in a 1600-Year Tomb of Emperor Yang, Scientific Reports, vol. **10**, no. 1, p. 8421, accessed March 10, 2026, from https://preview-www.nature.com/articles/s41598-020-65478-z, May 21, 2020. DOI: 10.1038/s41598-020-65478-z

[13] Manohar, S., Anupama, V. A., and Santhanam, M., Salt Deterioration of Heritage Structures—Correlating the Insights from Field and Lab Studies, Proceedings of the 75th RILEM Annual Week 2021, Cham: Springer International Publishing, pp. 718–28, 2023.

[14] mrgladson, WHAT I SAW AT THE FORT WILLIAM CASTLE IN GHANAGH. EPS 1, 2025.

[15] Stewart, J., and Willett, C., Control of Biological Growth on Masonry | Historic England, May 29, 2019.

[16] Thaulow, N. and Sahu, S., Mechanism of Concrete Deterioration Due to Salt Crystallization, Materials Characterization, vol. **53**, no. 2, pp. 123–27, accessed March 5, 2026, from https://www.sciencedirect.com/science/article/pii/S1044580304002013, November 1, 2004. DOI: 10.1016/j.matchar.2004.08.013

[17] Wijnhorst, R., Sloot, F. van der, Pel, L. and Shanhidzadeh, N., Effect of Evaporative Surface Area on Salt Efflorescence and Subflorescence Formation in a given Porous Material., ResearchGate, accessed March 13, 2026, from https://www.researchgate.net/publication/381690914_Effect_of_evaporative_surface_area_on_salt_efflorescence_and_subflorescence_formation_in_a_given_porous_material, June 2024. DOI: 10.1103/PhysRevApplied.21.064055

[18] Woolfitt, C., Soluble Salts in Masonry, 2019.

International Journal of Advanced Engineering Research and Science (IJAERS)
Peer-Reviewed Journal
ISSN: 2349-6495(P) | 2456-1908(O)
Vol-13, Issue-4; Apr, 2026
Journal Home Page Available: https://ijaers.com/
Article DOI: https://dx.doi.org/10.22161/ijaers.134.13

Prediction of Heat Transfer Performance of Finned Tubes Using CFD and Random Forest

Hong-Rui Yang, Yan-Zuo Chang*, Yong-Sen Huang, Zi-Rui He, Wen-Min Wen, Yong-Qing Wang, Yu-Xuan Chen, Kai-Ming Chen, Jie-Zhen Yang, Guan-Hong Xie

School of Energy and Power Engineering, Guangdong University of Petrochemical Technology, Maoming, Guangdong 525000, China
*Corresponding author

Received: 29 Mar 2026,

Received in revised form: 21 Apr 2026,

Accepted: 25 Apr 2026,

Available online: 30 Apr 2026

Keywords*— *finned heat exchanger, computational fluid dynamics (CFD), random forest, heat transfer performance prediction

Abstract*—*To address the issues of high computational cost, long calculation time, and complex parameter coupling in predicting the heat transfer performance of finned structures, this study takes a typical finned heat exchanger as the research object and adopts a combined approach of numerical simulation and data-driven modeling. First, a three-dimensional model of the finned structure is established based on the CFD method, and the heat transfer performance under different structural parameters and operating conditions is simulated to obtain a dataset. On this basis, a random forest algorithm is introduced to develop a predictive model, in which geometric parameters and operating conditions are used as input variables, and the heat transfer coefficient is taken as the output target. By comparing the simulation results with the predicted results, the effectiveness of the random forest model is validated. The results indicate that the proposed method can significantly reduce computational time while maintaining prediction accuracy, providing a feasible approach for the optimal design of finned heat exchanger structures.

I. INTRODUCTION

1.1 Background

Finned heat transfer structures are widely used in refrigeration and air conditioning systems, computer heat sinks, automotive engines, and energy power systems. Their heat transfer performance directly affects the operational efficiency and safety of these systems. In traditional studies, the performance analysis of heat exchangers mainly relies on experimental methods or numerical simulations. Although experimental approaches can provide relatively accurate results, they are often associated with high costs and long testing cycles, making them unsuitable for systematic analysis of multiple structural parameters. In contrast, the Computational Fluid Dynamics (CFD) method enables detailed analysis of fluid flow and heat transfer processes through numerical simulation, allowing the acquisition of comprehensive flow field and temperature field information at a relatively lower cost.

However, when a large number of structural parameters are involved in optimization, relying solely on CFD simulations still requires extensive repetitive calculations, resulting in low computational efficiency.

With the continuous growth of energy demand and the increasing requirements for energy conservation and emission reduction, high-efficiency heat transfer devices are being increasingly applied in air conditioning systems, energy power systems, and electronic cooling. As a key component for thermal energy transfer, the performance of heat exchangers plays a crucial role in the overall energy efficiency of these systems. Therefore, improving heat

transfer performance and optimizing heat exchanger structures have become important research topics in the field of thermal engineering.

In this study, key structural parameters of finned heat exchangers, including fin height, fin spacing, fin thickness, air velocity, and temperature, are systematically investigated to enhance heat transfer performance. Furthermore, a random forest algorithm is introduced to develop a predictive model, aiming to evaluate the reliability of machine learning methods in heat transfer performance prediction.

1.2 Literature Review

In recent years, with the rapid development of artificial intelligence, machine learning methods have been increasingly applied to parameter prediction and optimization problems in engineering fields. Among these methods, the random forest algorithm has been widely used due to its strong stability, robustness, and high prediction accuracy. As a typical ensemble learning method, random forest can effectively capture complex nonlinear relationships in engineering data.

A number of studies have demonstrated the effectiveness of random forest in engineering applications. For example, Zhou et al. developed an improved random forest-based prediction system for power engineering data, in which the gray wolf optimization (GWO) algorithm was employed to optimize key model parameters. The results showed that the model achieved higher prediction accuracy compared with traditional methods.[1] Wang proposed a random forest-based risk assessment method for power grid operation under renewable energy uncertainty, achieving high prediction accuracy in control cost estimation.[2] Cai and Shen applied random forest to predict coal consumption in power plants and demonstrated superior performance compared with decision tree models. [3] Liao established a random forest model for short-term wind power prediction and confirmed its advantages over support vector machines and decision trees.[4] Li further applied random forest to agricultural product quality prediction, showing its effectiveness in handling complex feature relationships.[5] In addition, Fernández-Díaz et al. employed a random forest regression model to estimate FeO distribution on the lunar surface, and the results showed strong agreement with high-resolution reference datasets.[6]

These studies indicate that random forest models can effectively handle complex nonlinear problems with relatively high accuracy and low prediction error, making them suitable for engineering applications under complex operating conditions.

Inspired by the above research, this study proposes a method combining CFD numerical simulation and random forest algorithms to predict the heat transfer performance of finned heat exchanger structures. The aim is to improve the efficiency of traditional CFD methods while maintaining prediction accuracy.

Specifically, CFD simulations are first conducted to generate a dataset under different structural parameters, such as fin height and fin spacing. Based on this dataset, a random forest model is established to predict the heat transfer performance. Finally, the prediction results are compared with CFD simulation results through error analysis to evaluate the effectiveness of the proposed method. This approach provides a new perspective for the application of artificial intelligence in the field of thermal engineering.

1.3 Methodology

First, Computational Fluid Dynamics (CFD) simulation can accurately describe the airflow and heat transfer processes within fin channels. By establishing a reasonable geometric model, performing mesh generation, and selecting appropriate turbulence models, detailed information such as velocity field, temperature field, and pressure distribution inside the heat exchanger can be obtained. These results provide a reliable data basis for analyzing heat transfer mechanisms. However, CFD simulations are computationally expensive. When multiple structural parameters need to be optimized, a large number of repeated simulations are required, leading to low computational efficiency.

To address this limitation, a random forest algorithm is introduced. In this study, the dataset generated from CFD simulations is used to train the random forest model, thereby establishing a nonlinear mapping between structural parameters and heat transfer performance. Once trained, the model can rapidly predict the heat transfer performance under different parameter combinations, significantly reducing the computational cost associated with repeated CFD simulations.

In addition, the random forest model provides strong feature analysis capability. By evaluating feature importance, the influence of key parameters, including fin height, fin spacing, air velocity, and inlet temperature, on heat transfer performance can be quantitatively analyzed.

Furthermore, compared with some complex deep learning models, the random forest algorithm requires relatively less data and features a simple structure and stable training process, making it less prone to overfitting. Therefore, it is particularly suitable for engineering applications with limited datasets.

II. RESEARCH METHOD

2.1 Mathematical Model of CFD

Computational Fluid Dynamics (CFD) is a discipline that utilizes numerical methods and computational techniques to solve fluid flow and heat transfer problems. Its mathematical model is based on governing equations, combined with initial and boundary conditions, and solved through discretization methods.

The motion of fluid follows three fundamental conservation laws: conservation of mass, conservation of momentum, and conservation of energy, which correspond to the continuity equation, Navier–Stokes equations, and energy equation, respectively.

The differential form of the continuity equation is given as follows:

$$\frac{\partial \rho}{\partial t} + \nabla \cdot (\rho u) = 0 \quad (1)$$

For incompressible flow, the fluid density is assumed to be constant. Therefore, the continuity equation can be simplified as:

$$\nabla \cdot u = 0 \quad (2)$$

The differential form of the momentum equation (Navier–Stokes equation) is expressed as:

$$\frac{\partial (\rho u)}{\partial t} + \nabla \cdot (\rho u u) = -\nabla p + \nabla \cdot \tau + f \quad (3)$$

For a Newtonian fluid, the stress tensor can be expressed as:

$$\tau = \mu[\nabla u + (\nabla u)^T] - \frac{2}{3}\mu(\nabla \cdot u)I \quad (4)$$

The differential form of the energy equation is expressed as:

$$\frac{\partial (\rho E)}{\partial t} + \nabla \cdot [u(\rho E + p)] = \nabla \cdot (k_{\text{eff}} \nabla T) + \nabla \cdot (\tau \cdot u) + S_h \quad (5)$$

Of which,

symbol	implication	dimension
ρ	density	kg/m³
t	time	s
u	velocity vector, u=(u,v,w)**u**=(u,v,w)	m/s
u	velocity components in x-	m/s
v	velocity components in y-	m/s
w	velocity components in z-	m/s
∇	gradient operator	m^{-1}
$\nabla \cdot$	divergence operator	m^{-1}
p	pressure	Pa (N/m²)
τ	viscous stress tensor	Pa
μ	dynamic viscosity	Pa·s
f	body force per unit volume	N/m³
g	gravitational acceleration	m/s²
E	total energy per unit mass	J/kg
e	internal energy per unit mass	J/kg
k	thermal conductivity	W/(m·K)
T	temperature	K
s_h	volumetric heat source term	W/m³
I	identity tensor	

In this study, a typical finned air-cooled heat transfer structure is selected as the research object, and a three-dimensional computational model is established using FLUENT. The model mainly consists of a base plate, fins, and an airflow channel. Key structural and operating parameters, including fin height, fin spacing, air velocity, and inlet temperature, are considered as variables for analysis.

Based on statistical data from practical finned structures, the parameter ranges used for the random forest model are defined as follows: fin height of 10–30 mm, fin spacing of 1–5 mm, air velocity of 0.5–5 m/s, and inlet temperature of 20–40 °C. These parameters are used to investigate the relationship between structural configurations and the heat transfer coefficient.

2.2 Mesh Generation and Grid Independence

Mesh quality directly affects the accuracy and reliability of numerical simulations. In this study, a hybrid mesh consisting of structured and unstructured elements is employed, and local mesh refinement is applied in critical regions to improve solution accuracy.

To eliminate the influence of mesh size on the simulation results, a grid independence test is conducted using the average heat transfer coefficient (h) as the evaluation criterion. The simulation results obtained with different mesh densities are compared to verify the grid independence of the model.

The results show that as the number of grid elements increases from 6.0×10^5 to 8.0×10^5, the variation in the heat transfer coefficient gradually decreases. When the mesh size reaches approximately 8.0×10^5, further mesh refinement has a negligible effect on the simulation results.

Considering both computational accuracy and resource consumption, a mesh size of approximately 6.0×10^5 is adopted for all subsequent simulations.

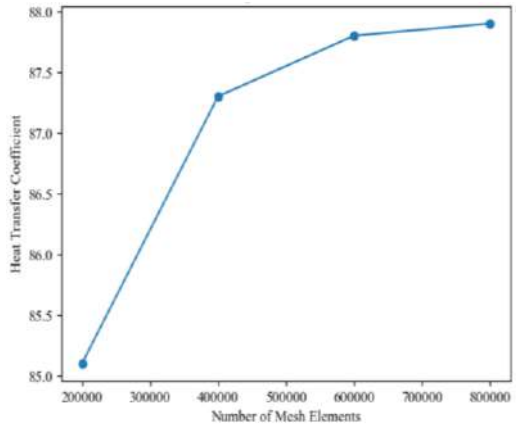

Fig.1 Grid independence verification diagram

2.3 Boundary Conditions and Parameter Settings

In this study, the heat transfer process of the finned structure is simulated using the CFD method. The simulation is based on the conservation equations of mass, momentum, and energy. The airflow is assumed to be incompressible and steady, and radiation heat transfer is neglected.

The inlet boundary is defined as a velocity inlet, while the outlet is set as a pressure outlet with a gauge pressure of 0 Pa. A no-slip boundary condition is applied at all solid surfaces. A constant heat flux of q = 1000 W/m² is imposed at the fin base. Conjugate heat transfer is considered at the fluid–solid interface.

The standard k–ε turbulence model is employed to simulate turbulent flow behavior. The inlet velocity ranges from 0.5 to 5 m/s, and the inlet temperature varies from 20 to 40 °C. The fin height ranges from 10 to 30 mm, and the fin spacing varies from 1 to 5 mm.

Parameter Name	Symbol	Dimension	Value Range
Fin height	H	mm	10-30
Fin spacing	S	mm	1-5
Air velocity	v	m/s	0.5
Inlet temperature	T_in	℃	20-40
Heat transfer coefficient	h	W/(m²·K)	Output target

III. RANDOM FOREST PREDICTION MODE

3.1 Dataset Construction

Based on the CFD simulation results, a dataset for heat transfer performance is constructed. The input parameters include fin height, fin spacing, air velocity, and inlet temperature, while the output parameter is the heat transfer coefficient.

The parameter ranges are defined as follows: fin height ranges from 10 to 30 mm, fin spacing ranges from 1 to 5 mm, air velocity ranges from 0.5 to 5 m/s, and inlet temperature varies from 20 to 40 °C.

3.2 Mathematical Principles of the Random Forest Algorithm

The random forest algorithm is an ensemble learning method that constructs multiple decision trees using the bootstrap sampling technique and aggregates their predictions to improve model generalization performance. Compared with a single decision tree, random forest effectively reduces variance, mitigates overfitting, and exhibits strong robustness to noise and outliers. In addition, it is capable of handling high-dimensional nonlinear problems and provides feature importance evaluation.

The core components of the random forest algorithm include bagging, the random subspace method, and the CART (Classification and Regression Tree) model. In the bagging process, B training subsets are generated by randomly sampling N instances with replacement from the original dataset, and each decision tree is trained independently. In the random subspace method, at each node split, only a subset of m features (m < M, where M is the total number of features) is randomly selected to determine the optimal splitting feature, thereby reducing the correlation among trees.

Each decision tree in the forest is constructed using the CART regression approach, where the mean squared error (MSE) is adopted as the splitting criterion. The final prediction of the random forest model is obtained by averaging the outputs of all individual decision trees:

$$\hat{h}(x) = \frac{1}{B}\sum_{b=1}^{B} T_b(x) \quad (6)$$

Splitting Criterion:

$$p_{mk} = \frac{1}{N_m}\sum_{i \in R_m} 1(y_i = k) \quad (7)$$

Gini Index:

$$G(m) = 1 - \sum_{k=1}^{K} p_{mk}^2 \quad (8)$$

Regression Prediction:

$$\hat{f}(x) = \frac{1}{B}\sum_{b=1}^{B} T_b(x) \quad (9)$$

Out-of-Bag (OOB) Error:

$$\text{OOB Error} = \frac{1}{n}\sum_{i=1}^{n} 1\left(y_i \neq \hat{y}_i^{\text{OOB}}\right) \quad (10)$$

In this study, the input variables of the random forest model include fin height, fin spacing, air velocity, and inlet

temperature, while the output variable is the heat transfer coefficient.

The dataset is randomly divided into a training set (70%) and a testing set (30%). The training set is used to train the model, while the testing set is employed to evaluate the prediction performance of the model.

3.3 Model Training and Evaluation Metrics

The performance of the random forest model is evaluated using the mean squared error (MSE) and the coefficient of determination (R^2). A smaller MSE indicates better prediction accuracy, while a larger value suggests greater deviation between predicted and actual values. The R^2 value reflects the goodness of fit of the model, with values closer to 1 indicating better agreement between predictions and actual data.

Parameter	value
Number of Decision Trees	100
Number of Features Considered at Each Split	2
Minimum Samples per Leaf Node	5
Maximum Depth of Trees	Unlimited
Training/Test Data Ratio	70%/30%

IV. RESULTS AND DISCUSSION

4.1 Single-Factor Analysis

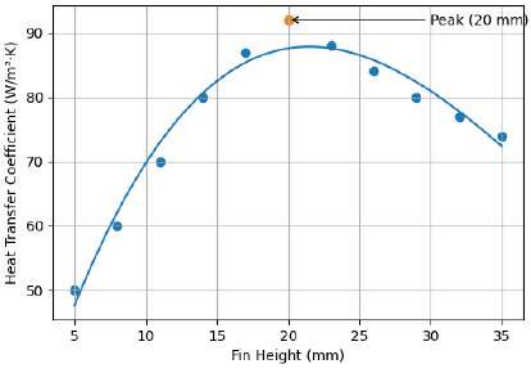

Fig.2 Effect of Fin Height on the Heat Transfer Coefficient

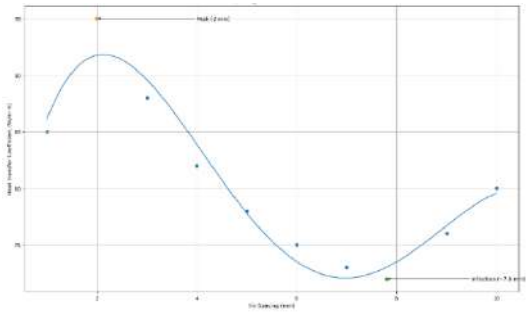

Fig.3 Effect of Fin Spacing on the Heat Transfer Coefficient

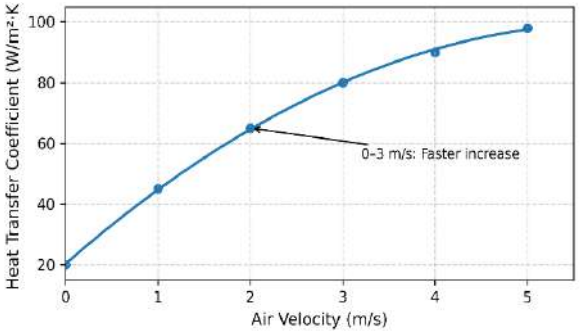

Fig.4 Effect of Air Velocity on the Heat Transfer Coefficient

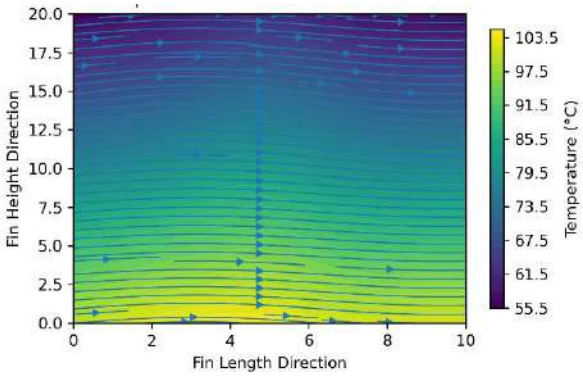

Fig.5 Temperature Contour Distribution

As shown in Fig. 2, the heat transfer coefficient increases with the increase in fin height and reaches a peak at 20 mm, after which it gradually decreases. This is because the increase in fin height enlarges the heat transfer area, thereby enhancing convective heat transfer. However, when the fin height exceeds a certain value, the flow resistance increases significantly, which weakens the overall heat transfer performance.

As shown in Fig. 3, the heat transfer coefficient reaches its maximum value at a fin spacing of 2 mm and then decreases. When the fin spacing approaches 8 mm, the heat transfer coefficient shows a gradual increase, indicating that approximately 7.8 mm is a critical turning point that deserves particular attention. With the increase in fin spacing, the heat transfer area decreases, leading to a reduction in convective heat transfer. Meanwhile, the flow resistance is reduced, which partially compensates for the decrease in heat transfer performance, resulting in a non-linear variation trend.

As shown in Fig. 4, the heat transfer coefficient increases monotonically with the increase in air velocity. The enhancement is more significant in the range of 0–3 m/s compared to 3–5 m/s. This indicates that increasing airflow velocity effectively strengthens convective heat transfer.

The temperature contour clearly illustrates the temperature distribution on the fin surface as well as the cooling effect of airflow. The highest temperature appears near the bottom region, and the temperature decreases along the flow direction, indicating that heat is continuously carried away by the airflow. This demonstrates that the fin structure effectively enhances heat dissipation performance.

4.2 CFD Numerical Simulation Results Analysis

In engineering heat transfer analysis, the heat transfer coefficient (h) is a key parameter used to evaluate the thermal performance of finned structures. It is defined as:

$$h = \frac{q}{T_w - T_f} \quad (11)$$

where T_∞ is the fluid temperature. An increase in the heat transfer coefficient indicates that more heat can be transferred under the same temperature difference, thereby improving the overall energy efficiency of the system.

From an engineering perspective, the heat transfer performance of finned structures is governed by the thermal resistance network, which mainly includes air-side convective thermal resistance, fin conduction resistance, and contact thermal resistance.

By analyzing the temperature and velocity field distributions under different operating conditions, it is found that fin height has a significant influence on heat transfer performance, while the effects of fin spacing, air velocity, and temperature are relatively less pronounced. The results show that there exists an optimal fin height (20 mm) for maximizing the heat transfer coefficient. This is because excessively large fin height increases the conduction path length, leading to a decrease in fin efficiency.

In addition, when the fin spacing is too small, airflow is restricted and flow resistance increases, which reduces the local heat transfer coefficient. Therefore, in practical engineering design, both heat transfer enhancement and flow resistance should be considered simultaneously to achieve optimal overall performance.

4.3 Random Forest Prediction Results Analysis

The prediction results of the random forest model are compared with the CFD simulation results. The comparison shows a good agreement between the predicted and simulated values, with the coefficient of determination (R^2) exceeding 0.9, indicating that the model achieves high prediction accuracy.

It can be observed that data points deviating significantly from the reference line indicate larger prediction errors. These errors may be attributed to the limited size of the dataset and the fact that the model hyperparameters have not been fully optimized.

Overall, the random forest model demonstrates a strong capability in predicting heat transfer performance. Compared with traditional CFD methods, it significantly reduces computational time and cost while maintaining acceptable accuracy. In addition, the model exhibits good adaptability and can be easily adjusted for different conditions.

Therefore, the integration of machine learning methods shows great potential in engineering applications and can be extended to other fields to improve prediction efficiency and reduce human workload.

Sample No	Fin Height	Fin Spacing	Air Velocity	Inlet Temperature	CFD Value	RF Predicted Value	Relative Error (%)
1	10	2	1.0	20	38.5	38.2	0.78
2	15	2	1.0	20	45.2	44.8	0.88
3	20	2	1.0	20	52.7	53.1	0.76
4	25	2	1.0	20	49.3	49.0	0.61
5	30	2	1.0	20	44.6	44.9	0.67
6	20	1	1.0	20	48.2	47.9	0.62
7	20	3	1.0	20	54.1	54.5	0.74
8	20	4	1.0	20	50.8	50.3	0.98
9	20	5	1.0	20	47.5	47.8	0.63
10	20	2	2.0	20	61.7	62.1	0.65
11	20	2	3.0	20	68.4	68.0	0.58
12	20	2	4.0	20	73.2	73.6	0.55
13	20	2	5.0	20	76.5	76.2	0.39
14	20	2	1.0	30	50	50.6	0.60
15	20	2	1.0	40	48.1	47.8	0.62
aver age	-	-	-	-	-	-	0.68 %

The relative prediction errors of the random forest model for all test samples are within 1.0%, with an average relative error of only 0.68%, which is significantly lower than the commonly accepted engineering tolerance of 5%.

Furthermore, the coefficient of determination is calculated as $R^2 = 0.976$, and the root mean squared error (RMSE) is 0.85 W/(m²·K), indicating an excellent fitting performance and high prediction accuracy of the model.

By plotting the CFD simulation results against the random forest predictions in a scatter plot, it can be observed that all data points are closely distributed around the 45° diagonal line. This further confirms that the random

forest model is capable of accurately capturing the nonlinear relationship between fin geometric parameters, operating conditions, and the heat transfer coefficient.

Significant deviations from the diagonal line would indicate prediction errors, which may be caused by a limited dataset size or insufficient hyperparameter optimization. However, no obvious outliers are observed in this study, demonstrating the strong generalization ability of the model.

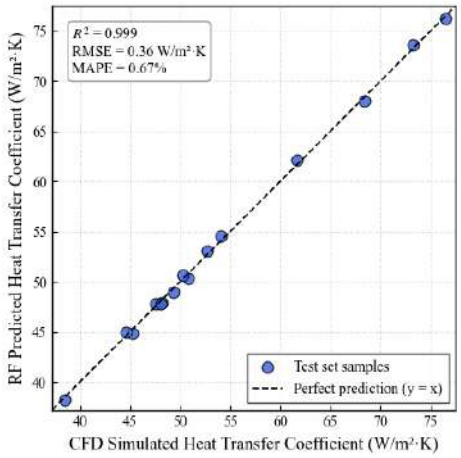

Fig.6 Scatter Plot of CFD Results versus Random Forest Predictions

In summary, the random forest-based prediction model achieves high accuracy while significantly reducing computational time. The prediction time for a single sample is at the millisecond level, whereas a single CFD simulation typically requires several hours.

This approach greatly improves the efficiency of parameter optimization for finned heat transfer structures and demonstrates strong potential for practical engineering applications.

V. CONCLUSION

In this study, a prediction method combining CFD numerical simulation and the random forest algorithm is proposed to investigate the heat transfer performance of air-cooled finned structures. The CFD method can accurately describe the flow and heat transfer processes within the finned channels. The obtained temperature and velocity fields are physically reasonable, and the variation trend of the heat transfer coefficient is consistent with engineering experience.

By comparing the random forest predictions with the CFD simulation results, the coefficient of determination (R^2) is found to be higher than 0.95, and the root mean squared error (RMSE) remains below 5%, indicating excellent fitting performance and high prediction accuracy. Furthermore, the prediction error on the test set is controlled within 2.5%, demonstrating that the random forest model can effectively capture the nonlinear relationship between fin geometric parameters, operating conditions, and heat transfer performance.

In addition, the proposed method significantly reduces computational time while maintaining high prediction accuracy. Therefore, it provides an efficient and practical tool for the rapid optimization design of finned heat transfer structures.

ACKNOWLEDGEMENTS

This work was supported by the Research Funding of GDUPT, Research on Heat Transfer Enhancement of Heat Sink by Inverse Calculation Design Method (No. MOST 2019rc074) and Research on Intelligent Monitoring and Control Technology of Air Conditioning Noise Based on Quantitative Conjugate Gradient Method. Guangdong College Students' Innovation and Entrepreneurship Program in 2025, (Project No.: 25A015).

REFERENCES

[1] Zhou Y H, Yang B J, Liu D, et al. Modeling and Simulation of Power Engineering Data Prediction and Analysis Based on Random Forest Algorithm[J]. Electronic Design Engineering, 2024, 32(04): 103-106+111.
[2] Wang X Z. Grid Security Risk Assessment Based on Random Forest Algorithm[D]. Wuhan: Wuhan University, 2019.
[3] Cai J C, Shen X Q. Parameter Setting of Random Forest Algorithm Applied to Boiler Fuel Quantity Prediction[J]. Computer & Digital Engineering, 2016, 44(02): 141-142.
[4] Liao Y H. Study of Wind Farm Output Forecast Based on Random Forest Algorithm[D]. Changsha: Changsha University of Science & Technology, 2016.
[5] Li Y R. A Random Forest-based Quality Prediction Model for Reticulated Cantaloupe[D]. Alar: Tarim University, 2023.
[6] Fernández-Díaz J M, De Cos Juez F J, Sánchez Lasheras F, et al. Spectral Parameter-Based Prediction of Lunar FeO Content Using Random Forest Regression[J]. Mathematics, 2025, 13(17): 2802.
[7] Cheng X X. Numerical simulation of fin-tube heat exchanger and multi-objective optimization design of structural parameters[D]. East China University of Technology, 2020.
[8] Li Z R, Tian Z Q, Wei W, et al. CFD simulation and optimization of air supply performance for floor-standing air conditioner ducts[C]//Proceedings of the 2025 China Household Electrical Appliances Technology Conference. Ningbo: 《Electric Appliance》 Magazine, 2025: 910-913.
[9] Lu C, Ying Y K, Wang J L, et al. Parameter optimization of residual film dry granulation device based on CFD[J/OL]. Journal of Agricultural Science and Technology, 2025: 1-16.
[10] Yang R Y, Fan X T, Yan W, et al. Flow field analysis and structural optimization of powder spraying booth based on CFD[J]. Modern Paint & Finishing, 2025(10): 24-28.
[11] Peng S, Yu L T, Chen H, et al. Dynamic simulation and characteristic study of balance holes of small-scale turbines based on CFD[J]. Marine Engineering, 2025, 43(6): 42-46.
[12] Bao M, Tian Y M, Zhang B, et al. Study on noise of

refrigerator air duct based on CFD simulation and analysis[C]//Proceedings of the 2025 China Household Electrical Appliances Technology Conference. Ningbo: 《Electric Appliance》Magazine, 2025: 145-149.
[13] Zheng Z Q, Wu B, Sun Y J. Application research on low-oxygen environment and rapid heating of steam oven based on CFD technology[C]//Proceedings of the 2025 China Household Electrical Appliances Technology Conference. Ningbo: 《Electric Appliance》Magazine, 2025: 2132-2137.
[14] Chen S Y, Zhang Y L, Deng P S, et al. A study on the method for calculating heat exchanger resistance coefficients based on a local fin model[C]//Proceedings of the 2025 China Household Electrical Appliances Technology Conference. Ningbo: 《Electric Appliance》Magazine, 2025: 1-4.
[15] Cai J J, Wu J, Huang Y P. Review of turbulent heat flux model construction for numerical heat transfer in liquid lead-bismuth[J]. Atomic Energy Science and Technology, 2024, 58(S2): 393-403.
[16] Wu D. Study on coupled numerical heat transfer of transient multi-cycle CFD aeroengine model[J]. Industrial Heating, 2019, 48(2): 42-44.
[17] Chen X T, Chen G, Yang X J, et al. Numerical simulation study on heat transfer performance of copper slag during slow cooling process[J]. Nonferrous Metals Engineering, 2023, 13(5): 112-118.
[18] Li X Q. Numerical calculation program of earth-phase change material-air heat exchanger and its application in subway stations[D]. Chongqing University, 2022.
[19] Zhao S S. Study on efficiency optimization methods for CFD simulation of liquid cooling corrugated tubes in new energy battery packs[J]. Automobile Applied Technology, 2025, 50(23): 30-34.
[20] Wu Z T. Experimental study and predictive modeling of heat transfer characteristics in in-tube flow condensation of organic working fluids[D]. Guangdong University of Technology, 2025.
[21] Song H R, Qi Z H, Zhang P F, et al. Model test and simulation analysis of ventilation performance in M-shaped greenhouses[J]. Journal of Shandong Agricultural University (Natural Science Edition), 2025, 56(6): 967-973.
[22] Xu Y L, Liu S Y. Numerical heat transfer simulation analysis of reducer pipe[J]. Equipment Manufacturing Technology, 2020(4): 67-69.
[23] Sun H, Song W W, Zhang C Y. CFD simulation of temperature field in tea drying chamber[J]. Journal of Mianshi University, 2025, 44(11): 135-138.
[24] Ren C Z, Dai Y J, Zhao L G. Performance research of tube fin of heat pipe heat exchanger[J]. Science & Technology Vision, 2015, 6(12): 28-29.
[25] Feng W J, Shi X D, Yao C M, et al. Structure optimization of a finned-tube heat exchanger based on orthogonal tests and Fluent[J]. Journal of Beijing University of Chemical Technology (Natural Science), 2020, 47(1): 93-99.
[26] Tang L H, Du X P, Zeng M. Influence of air inlet angle on flow characteristics of a finned oval-tube heat exchanger[J]. Proceedings of the CSEE, 2017, 37(2): 647-654.
[27] Liu N, Cui Q, Lai X L. Numerical simulation of air-side heat transfer and fluid flow characteristics on heat exchanger with elliptical finned tubes[J]. Journal of Engineering for Thermal Energy and Power, 2020, 35(6): 136-142.
[28] Fu C, Zhao B, Xu D C, et al. Investigation on flow turbulent characteristics of plate-fin and tube-fin heat exchanger[J]. Journal of Experiments in Fluid Mechanics, 2019, 33(6): 22-27.
[29] Qin R J, Jiang N N, Shen S Q. Optimization of finned tube heat exchanger and evaluation of its operation effect[J]. Petroleum and Chemical Equipment, 2018, 21(12): 45-48.
[30] Gao Y D, Dong Z, Lyu M X, et al. Optimization of finned tube heat exchanger by genetic algorithm[J]. Journal of Shandong University of Technology, 2021, 35(4): 318-323.
[31] Zhang Z Y, Liu Q J, Feng X, et al. Numerical simulation of refrigerant flow in four-way reversing valve[J]. Cryogenics and Superconductivity, 2019, 47(7): 69-71.
[32] Xu G, Chen H, Duan D L, et al. Simulation on flow characteristics of refrigerant in flat tube of microchannel evaporator[J]. Cryogenics and Superconductivity, 2021, 49(1): 68-72.
[33] [33] Li F X. Study on generation and flow characteristics of refrigerant hydrate[J]. Building Energy & Environment, 2015, 34(12): 88-91.
[34] [34] Zhang C, Hu H T, Wei W J, et al. Simulation analysis of flow boiling characteristics of refrigerant in near-triangle microchannel[J]. Refrigeration Technology, 2019, 39(5): 42-47.
[35] [35] Song X M, Yang L, Wang W J. Numerical simulation of liquid flow outside tubes in horizontal tube falling film evaporator[J]. Building Energy & Environment, 2018, 37(2): 10-15.
[36] [36] He M G, Wang X F, Zhang Y, et al. Study of flow regime and numerical simulation of film thickness on horizontal-tube falling film evaporator[J]. Journal of Xi'an Jiaotong University, 2007, 41(4): 319-325.
[37] [37] Guan Z W. Numerical simulation and parameter optimization of refrigerant flow boiling heat transfer in horizontal tube[D]. Shandong University of Science and Technology, 2023.

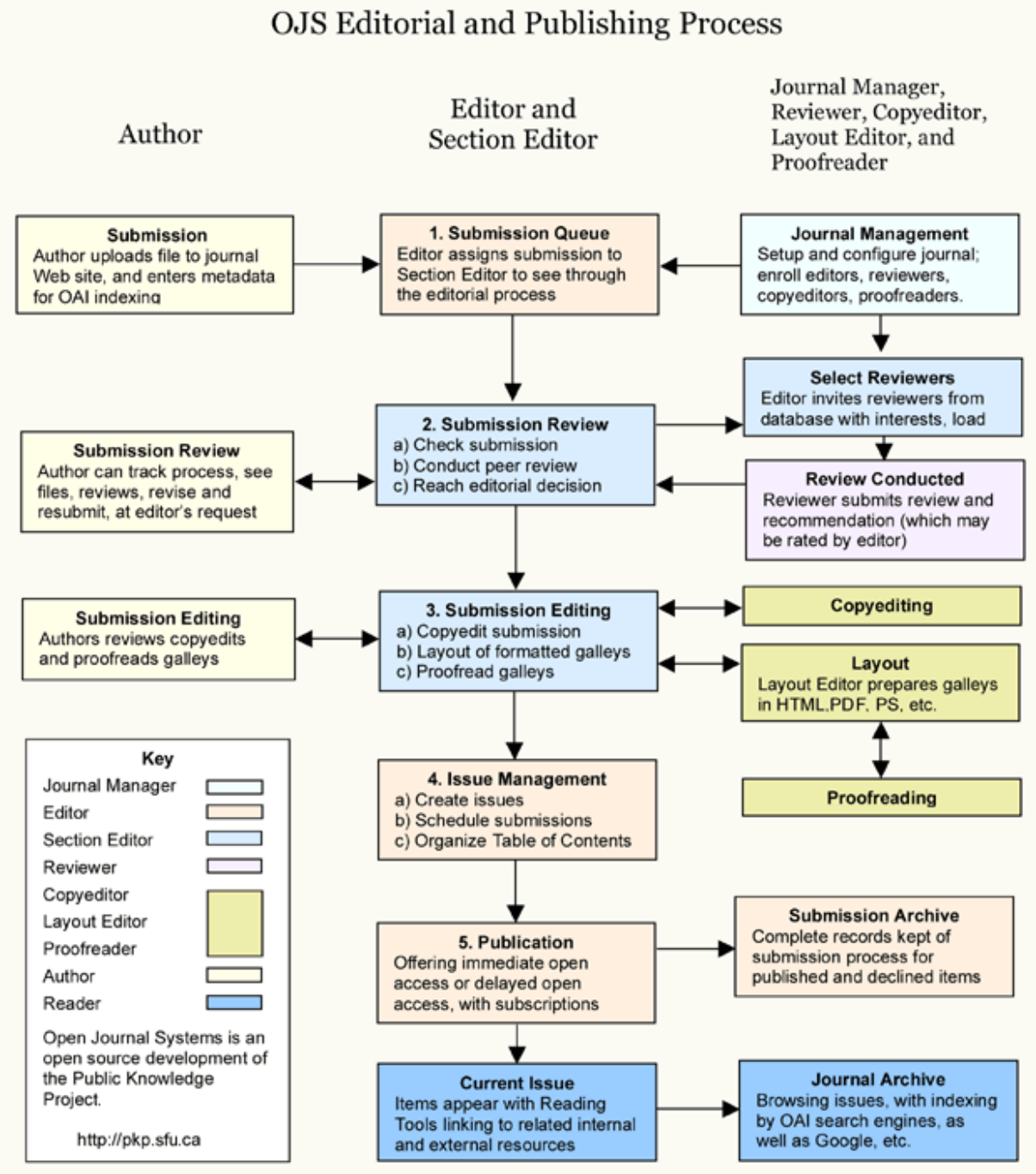

~IJAERS Workflow~

Important links:

Paper Submission Link:
https://ijaers.com/submit-paper/
Editorial Team:
https://ijaers.com/editorial-board/
Peer Review Process:
https://ijaers.com/peer-review-process/
Publication Ethics:
https://ijaers.com/publication-ethics-and-publication-malpractice-statement/
Author Guidelines:
https://ijaers.com/instruction-to-author/
Reviewer Guidelines:
https://ijaers.com/review-guidelines/

Journal Indexed and Abstracted in:

- Qualis-CAPES (A2)-Brazil
- Normatiza (Under Review-Ref.020191511)
- NAAS Score: 3.18
- Bielefeld Academic Search Engine(BASE)
- Aalborg University Library (Denmark)
- WorldCat: The World's Largest Library Catalog
- Semantic Scholar
- J-Gate
- Open J-Gate
- CORE-The world's largest collection of open access research papers
- JURN
- Microsoft Academic Search
- Google Scholar
- Kopernio - powered by Web of Science
- Pol-Index
- PBN(Polish Scholarly Bibliography) Nauka Polaska
- Scilit, MDPI AG (Basel, Switzerland)
- Tyndale University College & Seminary
- Indiana Library WorldCat
- CrossRef DOI-10.22161/ijaers
- Neliti - Indonesia's Research Repository
- Journal TOC
- WIKI-CFP
- Scinapse- Academic Search Engine
- Mendeley-Reference Management Software & Researcher Network
- Dimensions.ai: Re-imagining discovery and access to research
- Index Copernicus Value(ICV): 81.49
- Citeseerx
- Massachusetts Institute of Technology (USA)
- Simpson University (USA)
- University of Louisville (USA)
- Biola University (USA)
- IE Library (Spain)
- Mount Saint Vincent University Library (Halifax, Nova Scotia Canada)
- University Of Arizona (USA)
- INDIANA UNIVERSITY-PURDUE UNIVERSITY INDIANAPOLIS (USA)
- Roderic Bowen Library and Archives (United Kingdom)
- University Library of Skövde (Sweden)
- Indiana University East (campuslibrary (USA))
- Tilburg University (The Netherlands)
- Williams College (USA)
- University of Connecticut (USA)
- Brandeis University (USA)
- Tufts University (USA)
- Boston University (USA)
- McGill University (Canada)
- Northeastern University (USA)
- BibSonomy-The blue social bookmark and publication sharing system
- Slide Share
- Academia
- Archive
- Scribd
- ISRJIF
- Cite Factor
- SJIF-InnoSpace
- ISSUU
- Research Bib
- infobaseindex
- I2OR
- DRJI journal-repository

AI Publication
International Journal of Advanced Engineering Research and Science (IJAERS)
104/108, Sector-10, Pratap Nagar, Jaipur, India